Dual Species Atom Arrays for Quantum Simulation and Computation

A DISSERTATION PRESENTED
BY
KENNETH WANG
TO
THE DEPARTMENT OF PHYSICS

IN PARTIAL FULFILLMENT OF THE REQUIREMENTS
FOR THE DEGREE OF
DOCTOR OF PHILOSOPHY
IN THE SUBJECT OF
PHYSICS

HARVARD UNIVERSITY
CAMBRIDGE, MASSACHUSETTS
DECEMBER 2024

Dissertation advisor: Professor Kang-Kuen Ni Kenneth Wang

Dual Species Atom Arrays for Quantum Simulation and Computation

Abstract

Optical tweezer arrays of neutral atoms have emerged as a promising platform for studying quantum physics. These individual atoms can be carefully prepared in single quantum states, and easily manipulated with microwaves and lasers. MHz scale interactions are accessible at several micron scale distances by exciting these atoms to Rydberg states. These arrays can also be created in arbitrary 2D geometries with the use of a spatial light modulator. Adding the capability of a second species opens new possibilities in non-destructive measurement and quantum simulation of bipartite systems with widely tunable parameters.

In this thesis, we describe our efforts to build a flexible platform for studying quantum phenomena utilizing two species of atoms, sodium and cesium. In particular, we discuss the laser technology and setups required to create dual species optical tweezer arrays. These arrays are made defect-free with real-time rearrangement of atoms using a separate set of tweezers created with acousto-optical deflectors. We then describe how to excite these atoms coherently to the Rydberg state with coherence times in Cs as long as 20 microseconds. With these techniques established, we are able to probe an Ising critical point in 1D and 2D systems with up to 81 atoms. In particular, we measure and confirm the value of the universal critical exponent, η, via adiabatic preparation of the ground state at the critical point. Then, we measure the interactions between sodium and cesium atoms setting the stage for future experiments. Lastly, a theoretical proposal is presented where Rydberg atoms

can be used to enhance the interaction rates of ultracold polar molecules, as well as measure their states non-destructively.

Contents

Citations to previously published work

This thesis contains material originally distributed in the following publications:

1. Yu, Y.,* Wang, K.,*, Hood, J.D., Picard, L.R.B., Zhang, J.T., Cairncross, W.B., Hutson, J.M., Gonzalez-Ferez, R., Rosenband, T., Ni, K.-K. (2021). Coherent Optical Creation of a Single Molecule. *Physical Review X*, **11**, 031061

2. Wang, K., Williams, C.P., Picard, L.R.B., Yao, N.Y., Ni, K.-K. (2022). Enriching the quantum toolbox of ultracold molecules with Rydberg atoms. *PRX Quantum*, 3(3), 030339

3. Fang, F.,* Wang, K.,* Liu, V.S.,* Wang, Y.,* Cimmino, R., Wei, J., Bintz, M., Parr, A., Kemp, J., Ni, K.-K., Yao, N.Y. (2024). Probing critical phenomena in open quantum systems using atom arrays. arXiv:2402.15376 (submitted to *Science*)

*denotes authors who contributed equally to each work.

Listing of figures

List of Tables

To my parents, who gave me the opportunity to pursue my passion

Acknowledgments

Every PhD is a long and special journey and mine is no exception. Along the way, myriad experiences and people have shaped who am I today. I would like to take this opportunity to tell these stories and give the proper gratitude to those who mean the most to me.

The first person to contact me after my acceptance to graduate school at Harvard was Kang-Kuen. She quickly invited me for a lab tour and extended an offer to join the lab. For her belief in me from the very beginning, I am incredibly grateful. I have learned so much about the proper ways to do and think about science from her. I have learned to always strive for excellence and to be unwaveringly systematic. I have learned about how important it is to tell the right story and to highlight the key aspects of a scientific result. I also thank her for all her personal support over the years, ensuring that I was in the best position to do my best work.

I joined the NaCs 1.5 experiment (which became the true molecule making experiment) briefly in August 2017 before transitioning to the NaCs 1.0 team, where I spent nearly the entirety of my graduate school life. The two graduate students at the time were Lee Liu and Yichao Yu. The postdoc was Jon Hood. It is no understatement to say that most of the experimental skills and methods I learned came from Lee, Yichao and Jon. They were a joy to work with and we overcame many

challenges in creating weakly-bound molecules. I thank Lee for his friendship and his ability to lighten the mood in the lab. I will never forget his distinctive laugh. Jon was the wizard of calculations and simulations and I thank him for sharing many insights with me. Together, we learned all the ins and outs of intensity stabilization. A huge shoutout goes to Yichao, whom I overlapped with the most during the molecule-making years. I thank him for his patience, willingness and dedication to teach me everything he knew about, especially our computer control system. I thank him for his friendship and the random tangents we go on during our computer control sessions.

Near the conclusion of our molecule project, which took nearly three years, Kang-Kuen approached me to change directions on our apparatus. She proposed that we create a dual-species Rydberg atom apparatus. I welcomed the change, and the opportunity to learn something new! The start of our Rydberg project saw a new graduate student Yu Wang and postdoc Fang Fang join the team. The very next year, another new graduate student Ryan Cimmino joined the team. Our team of four marks the transition, for me, into the second half of my PhD. The next three years were focused on expanding our array and obtaining Rydberg capabilities on cesium atoms. Using these techniques, we undertook an extensive study on quantum criticality with the help of our theory collaborators led by professor Norm Yao. These included graduate students Vincent Liu, Marcus Bintz, and Julia Wei, as well as postdoc Jack Kemp. The criticality project saw many twists and turns with both pleasant surprises and disheartening dead ends. However, at the end of the day, we made it and measured features of criticality. This was truly a team effort, and I thank every member of this collaboration for their valuable contributions and perseverance to see the project through to the end.

In the last year and a half, I have had the pleasure of working extensively with Yu and Ryan, running the apparatus together as a team. We have added sodium Rydberg capabilities and seen the first signatures of truly dual-species operation with interactions between sodium and cesium Rydberg atoms: a dream of mine since my third year! Yu and Ryan are the ultimate team players and they

have grown so much in the years we have worked together. They transitioned from willing learners to truly independent, capable and creative thinkers. I thank them for putting up with my mood swings when running the experiment and their steadfast support and commitment to the experiment. I especially thank Yu for being much more than a labmate, but also a caring friend. We have enjoyed many conversations about all kinds of life topics and her sense of humor and adherence to logic are unparalleled. I also especially thank Ryan for his friendship over the years. I have greatly enjoyed all our conversations ranging from linguistics to policy to pedagogy. Just in the last few months, Hunter Kemeny has joined the team. Now that we have seen interactions between sodium and cesium Rydberg atoms, the fun truly begins. With Yu, Ryan and Hunter at the controls, I am sure the experiment will have a bright future.

The other experiments in the Ni group have also seen many members come and go, all of whom have contributed to the atmosphere of the group. On our "sister" experiment, the NaCs 1.5 team, I thank Jessie Zhang, Yen-Wei Lin, Eliot Fenton, Lewis Picard, Will Cairncross, Gabriel Patenotte, Annie Park, Sam Gebretsadkan and Youngshin Kim for always being willing to share knowledge and answer any questions I had about sodium and cesium. I especially thank Jessie and Yen-Wei for welcoming me into the lab. I also overlapped extensively with Lewis and have enjoyed his friendship and wisdom over the many years where we manned our respective machines. I especially thank Gabriel for his friendship and personal support over the years. I will remember the many nights spent playing Civilization and discussing life, although we never quite finished a single game of Civilization. I especially thank Annie for her friendship and support over the last few years. Annie was a joy to work with and had much wisdom to share with me about life.

On the other side of the "channel" was the KRb team. I thank Yu Liu, Ming-Guang Hu, Andrei Gheorghe, David Grimes, Lingbang Zhu, Matt Nichols, Yixiang Liu, Jeshurun Luke, Arfor Houwman, Mark Babin and Roy Shaham for sharing their knowledge and experiences. I especially thank Yu Liu for his friendship and personal support. Yu carries so much wisdom with him and I

will never forget our basketball games and Costco adventures. I especially thank Ming-Guang for his friendship and support as a sort of mini "father" figure in the lab. I especially thank Lingbang for his friendship and will remember all our conversations ranging from deep philosophical questions to gaming. I especially thank Yixiang for her friendship and conversations about life. I especially thank Jeshurun for our various chess battles and for his helpful attitude.

Recently, a new NaCs 2.0 team was formed. I thank Conner Williams and Christian Nunez for all the valuable discussions we have had. I especially thank Conner for being a willing and dedicated partner on the molecule toolbox paper, which would not have been possible without him. He has also been a valuable friend and I enjoy all our banter and bubble tea excursions.

Last but not least, a new ytterbium experiment has been created. I thank Dewei Gong, Lysander Christakis and Ziguang Lin for teaching me about alkaline-earth like atoms.

Finally, without a category to place him, I must thank our theorist in residence, David Wellnitz. In addition to discussing science, we have had many battles over the chessboard and discussions about life.

In addition to all the members of the lab, several professors have shaped my career in AMO physics. I thank John Doyle and David Patterson, who were the first professors to give me an opportunity to pursue research during my undergraduate years. I am grateful for their support and guidance. I thank Norm Yao, who has taught me so much about how to think systematically about science. He has also convinced me that no question is a stupid question. Without him, the Rydberg critical physics paper would simply not exist. I thank my thesis committee members, Subir Sachdev and Mikhail Lukin, for all their support over the years. I especially thank Subir Sachdev for teaching me quantum mechanics for the first time and igniting my passion for it.

The administrative and support staff help make the lab run smoothly. I thank Susan Kinsella, Felix Negron, Patricia McGarry and Gina Yildrim for their administrative support. I thank Mike Paterno and his team for ensuring our facilities are in tip-top shape. I thank Chris Perry and his

team for handling all our shipping problems and logistics. For technical support staff, I thank Jim MacArthur for his help in the electronics shop, Stan Cotreau and Steve Sansone for their help in the machine shop.

Outside of the lab, other members of Harvard physics have truly shaped my experience. The first shoutout goes out to Sooshin Kim. I thank him for being my dearest friend during my graduate school experience. We have gone through many trials and tribulations, shared many meals and I will never forget our travels to Europe and in Asia. I also thank Rémy Vatré, who joined the Ni group for a one year internship the same year I did. I thank him for his friendship and travels in Europe. I thank Hiromitsu Sawaoka, Christian Hallas, Yicheng Bao, and Muqing Xu for their friendship and personal support over the years.

Outside of physics, many friends have helped me through the personal ups and downs that are inevitable in life. For that, I thank Jon Lu, Cheng Xing, Amir Bitran, Jeffrey Ling, Sindy Tan, and Jimmy Jiang for their friendship and support through tough times.

I owe a tremendous debt of gratitude to my family for their support. My parents Tsukang and Wen made many personal sacrifices to ensure a better life for me and my brother. For that, I am eternally grateful. They were never pushy and simply encouraged me to pursue my passion. I thank my brother, Allen, for always paving the path for me and going through life four years earlier than me. He was always supportive and willing to share his wisdom. Finally, I want to thank my partner Maggie Dang for all her support. She is always caring, supportive and level-headed no matter my mood. Without her, this PhD adventure would not have ended on such a positive note.

1

Introduction

Over the last few decades, atomic, molecular and optical (AMO) physics has become an active and fruitful area of fundamental research ranging from high precision spectroscopy to quantum computing and simulation. Central to this effort has been crucial advances in the control of atomic and molecular systems to isolate them from unpredictable sources of noise and unveil their underlying quantum nature. It is precisely their underlying quantum behavior that makes these platforms especially useful for probing quantum phenomena.

Controlling atoms require getting all their degrees of freedom, including electronic, spin and translational, under control. For atoms, energy scales for electronic transitions are typically in the optical domain, which, in units of temperature, are at around tens of thousands of Kelvin. Thus, at typical temperatures in a laboratory, the atoms are predominantly in the ground electronic state. The translational degree of freedom was first tackled with the technique of doppler cooling[154]. Doppler cooling involves shining light that is red detuned from an atomic transition towards the atoms. Due to the Doppler effect, atoms traveling towards the laser beam view an up-shifted frequency and thus encounters a larger scattering cross-section (the laser is more on-resonant) compared to those traveling away from the beam. Thus, a net slowing effect is achieved due to the momentum kicks from the absorption of these counter-propagating photons. Putting laser beams along all six directions in space provides three dimensional cooling along all axes. The limit of laser cooling via this mechanism (known as Doppler cooling)

$$T_D = \frac{\hbar\Gamma}{2k_B} \tag{1.1}$$

is set by the natural linewidth of the atomic transition. When Doppler shifts are below this linewidth, the atom cannot easily distinguish which laser beam (co- or counter- propagating) to absorb from. Doppler cooling limits for alkali atoms are typically around a few hundreds of microkelvin. Combining red-detuned light with a magnetic field gradient (created in the lab with a pair of magnetic field coils running in the anti-Helmholtz configuration), a magneto-optical trap[154] of cold atoms can be formed. Temperatures in these MOTs were routinely found to be below the Doppler limit due to the multilevel nature of the atoms, which enables sub-doppler cooling mechanisms such as polarization gradient cooling[61]. Further cooling of these gases via evaporative cooling resulted in Bose-Einstein condensation[63,8], a distinctly quantum phenomenon, where a macroscopic population of atoms are found in the ground state. Cooling has also been performed on Fermions resulting

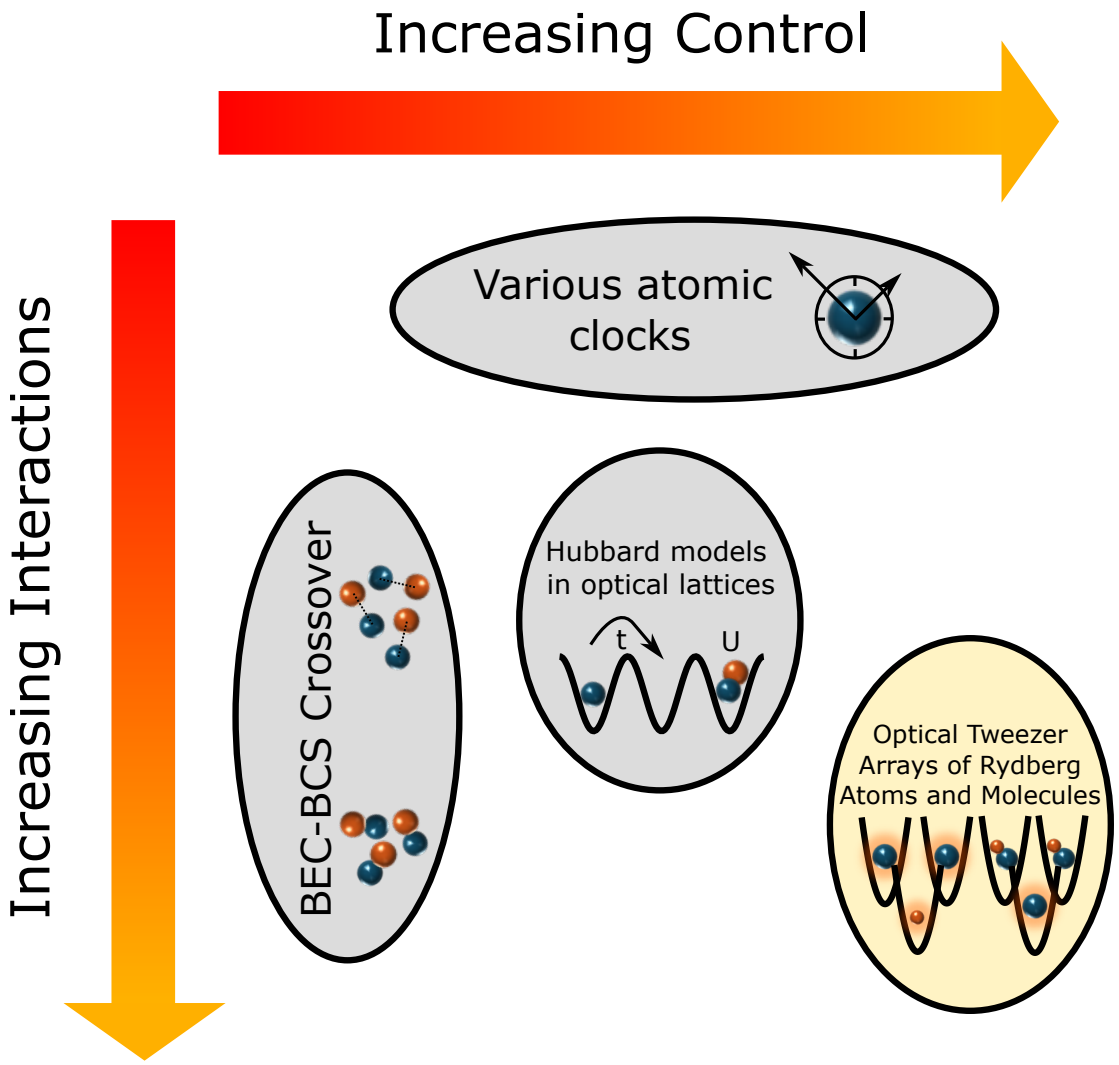

Figure 1.1: A non-exhaustive schematic overview of some characteristic systems in AMO physics along the dimensions of control (mostly spatial control) and interaction strength. Our system of interest, optical tweezer arrays of atoms or molecules, represents a system capable of large interaction strength and a high level of control.

in a degenerate Fermi gas[65], where obeying the Pauli exclusion principle, Fermionic atoms fill up all states below a Fermi surface.

This quantum gas[175] is the starting point for many additional studies utilizing ultracold atoms.

These studies can generally be categorized along two axes: the level of system control and amount of interactions as shown in figure 1.1. The lowest level of control starts from the quantum gas, where millions of atoms collide and interact freely. When interactions are suppressed, these fundamentally identical atoms are an ideal platform for an accurate clock [147]. On the other hand, these contact interactions are also highly tunable near a Feshbach resonance [52], making them valuable as a resource for studying quantum mechanics. These interactions predict features such as the so-called BEC-BCS crossover [167], where Fermions transition from condensation of delocalized Cooper pairs to tightly-bound Bosonic molecules [253,17]. These Fermionic atoms provide a controllable platform for studying superconductivity [25], a phenomena of Fermionic electrons. Superfluidity, the fluid equivalent of superconductivity has been successfully observed in ultracold gases [254]. Additional complexity is introduced with long-range interactions, present in magnetic atoms, that come from the dipole-dipole interaction

$$V_{\mathrm{dd}}(\mathbf{R}) = \frac{1}{4\pi\varepsilon_0}\left(\frac{\mu_1 \cdot \mu_2}{R^3} - \frac{3(\mu_1 \cdot \mathbf{R})(\mu_2 \cdot \mathbf{R})}{R^5}\right). \tag{1.2}$$

where μ_1 and μ_2 are the dipole operators for particles 1 and 2, and $\mathbf{R}$ is the distance between the dipoles, while $R = |\mathbf{R}|$ is the distance between them. Depending on the competition between the contact interaction (once again, controlled by a Feshbach resonance), and the dipole-dipole interaction, the so-called dipolar gas can be unstable [54]. The exact theories governing such systems are fundamentally quantum mechanical and not easily solvable, lending value to these dipolar gases as a quantum simulator.

Whereas gases offer large atom number, isolating individual atoms offers more control, where the Hamiltonian of the system can be meticulously engineered and rigorously studied. Trapping individual atoms require localized potentials which can be created by light. In a two level atom, light that is far red-detuned from an atomic transition shifts the ground state energy lower through

the AC Stark effect. This shift is proportional to the intensity of the light, so atoms experience a lower potential at intensity maxima of the light. A method of efficiently creating many traps, each trapping an individual atom, involves interfering counterpropagating laser beams creating an optical lattice[93]. These optical lattices naturally implement lattice models such as the Bose-Hubbard model[79,91] with the Hamiltonian

$$H = -t \sum_{\langle i,j \rangle} \hat{a}_i^\dagger \hat{a}_j + \frac{1}{2} U \sum_i \hat{n}_i (\hat{n}_i - 1) \tag{1.3}$$

where the first term (as a sum over nearest neighbors) represents the tunneling of atoms from one site to another and the second term represents a contact interaction present when there are multiple atoms on one site. $\hat{a}_i^\dagger$ and $\hat{a}_i$ are the creation and annihilation operators of a Boson on site i. $\hat{n}_i = \hat{a}_i^\dagger \hat{a}_i$ is the number operator for the number of Bosons on a single site. Lastly t and U represent the tunneling and interaction energies, both of which are tunable with the depth of the lattice and the scattering length (characterizing the contact interaction) between the atoms. With the microscopic resolution[92] available in these systems, the superfluid to Mott insulator transition* has been studied[12]. In the Fermionic version of the model (where the Pauli exclusion principle must be obeyed), aptly named the Fermi-Hubbard model, antiferromagnetic correlations have been observed resulting from an allowed superexchange process when nearby sites have opposite spin[173]. In the dipolar version of the model, where an additional dipole-dipole interaction is present (say from a magnetic atom), anisotropic dipolar solids have been observed[216] arising from the anisotropic dipole-dipole interaction.

While a wide variety of lattice geometries can be obtained with interfering laser beams[235], more flexibility can be achieved with optical tweezers[123]. Arrays of optical tweezers with arbitrary geometry can be formed using a spatial light modulator to imprint a phase on the laser beam, while

*A Mott insulator has a well-defined number of Bosons on each site.

those with rectilinear geometries can be formed from acousto-optical deflectors. Trapped atoms in tweezers can serve perfectly well as atomic clocks [166,1] or sensors [210], but a larger realm of possibilities open when the particles in the tweezers can interact. In the first half of my PhD, where much of the work has been documented in a previous thesis [243] and is highlighted in section 6.2, we explored the possibility of obtaining interactions between tweezer-trapped particles (in particular sodium and cesium atoms) by forming polar molecules. NaCs, the polar molecule in question, has a relatively large permanent dipole moment of around 4.7 Debye [136], among the largest of the bialkali molecules. This arises from the electronegativity difference between the two atoms that form the covalently bonded molecule. These dipoles interact with the dipole-dipole interaction (equation 1.2). On the way to forming molecules, we discovered that putting a sodium and cesium atom in a single tweezer already leads to measurable kHz scale interactions [106] that depend on the hyperfine states of the atoms. This close-range interaction, while technically arising from a full-blown molecular potential in the Born-Oppenheimer approximation, is well modeled with a contact interaction, known as the Fermi pseudopotential [41]

$$\hat{V}(\mathbf{R}) = \frac{4\pi\hbar^2 a}{\mu}\delta^{(3)}(\mathbf{r})\frac{\partial}{\partial r}r \tag{1.4}$$

where the standard delta function potential needs to be "regularized" due to a diverging bound state energy, which disagrees with a square well in the limit as the width of the well goes to zero. By attaching a $\frac{\partial}{\partial r}r$, which as an operator on a wavefunction ψ means $\frac{\partial}{\partial r}(r\psi)$, the eigenfunctions and eigenenergies agree with the limit of the square well. μ is the reduced mass of the two atom system, and a is the scattering length. This interaction was not only spectroscopically measured but was also critical for our method of molecule formation. We pursued a general molecule formation method, utilizing an optical state transfer via a Raman process from an unbound two-atom state in the tweezer to a weakly-bound molecular state [244]. The optical transfer method benefited greatly

from better wavefunction overlap of the two-atom trap state with the intermediate state, which was an excited molecular bound state. The large negative scattering length of a particular hyperfine combination of sodium and cesium enhanced the wavefunction at short distance resulting in enhanced optical transfer efficiency. We were able to achieve about 69% molecule-creation efficiency. Unsatisfied with the small kHz scale molecular interaction at tweezer distances of 2 microns and also due to the success of the more proven Feshbach association [247,213,52] in optical tweezers, we decided to search for a new pathway towards interactions. In particular, we sought to excite atoms to Rydberg states, which are high principal quantum number states, where MHz level interactions are available at the several microns scale. Our quest to improve a molecule-formation apparatus into a dual species Rydberg atom machine forms the main contents of this thesis, the main systems of which are schematically depicted in figure 1.2.

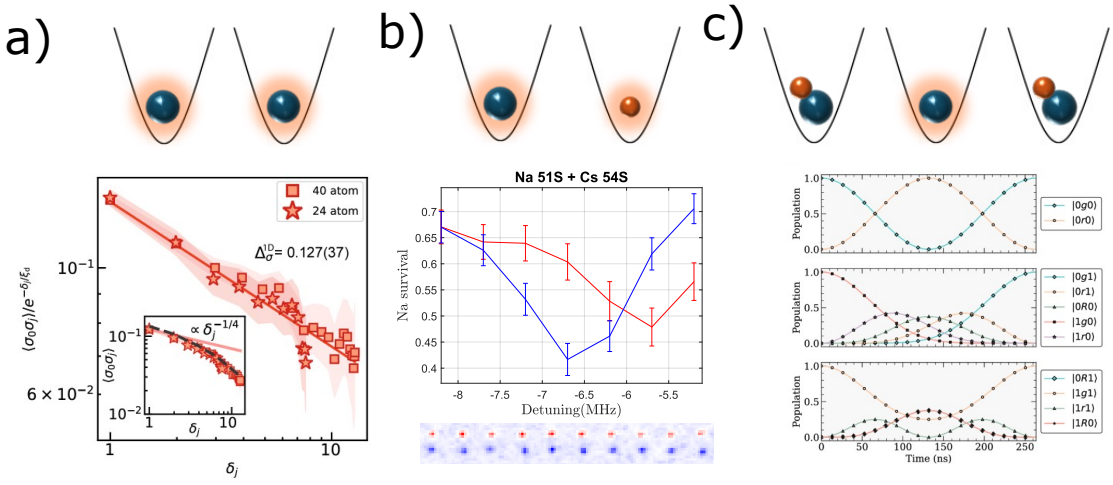

Figure 1.2: The main systems discussed in this thesis, all of which involve optical tweezer arrays. (a) The study of critical physics using a cesium Rydberg atom array interacting via the van der Waals interaction (see chapter 4). (b) The study of dual-species interactions and observation of interspecies interactions (see chapter 5). (c) The interaction between two molecules mediated by a Rydberg atom (see chapter 6).

In chapter 2, I give an overview of our machine with a focus on how we achieved large optical

tweezer arrays of sodium and cesium atoms. In chapter 3, we review Rydberg atoms and their interactions and demonstrate the successful excitation of cesium atoms to Rydberg states with large coherence times. In chapter 4, we combine the techniques of chapter 2 and 3 to study critical physics on a Rydberg atom array in both a circular and rectangular geometry. In chapter 5 I will describe the new features of a dual species apparatus and the successful excitation of sodium atoms and observation of interactions between sodium and cesium. Finally, in chapter 6, as a tribute to the early part of my PhD, I explore molecules again and describe a theoretical proposal to enrich the toolbox of molecular quantum computing with Rydberg atoms for faster interaction speeds and non-destructive measurement.

2

Experimental Apparatus

2.1 Introduction

As with many ultracold atom/molecule experiments, our apparatus rests on a floated optical table, which provides vibration isolation from the ground. The experiments take place under ultra high vacuum (UHV) which allows for the creation and trapping of sub millikelvin atoms, while limiting high energy collisions with background gas atoms. The details of the experimental cham-

ber are detailed in previous theses from the group [143,243], and the important parts are reproduced here for context. The experiment takes place in an epoxy-bonded 10 mm x 20 mm x 80 mm rectangular quartz cell from JapanCell. Each face is 4 mm thick and AR coated for < 4% reflection from 550 to 1100 nm at 0-45° angles of incidence. Light can also enter the cell from its open end (where atoms would enter as well) via an AR coated flange (MPF A8004-1-CF, coated for 550-1100 nm) and an in-vacuum 45 degree silver mirror (PF10-03-P01P). We believe the epoxy-bonding worsens the vacuum in our chamber and limits the vacuum-lifetime of atoms in our tweezers to approximately 5-6 seconds. Our atom sources are sodium and cesium metal dispensers from SAES Getters. These dispensers are constantly on and for dual-species operation, we run about 3.9 A of current in two dispensers, while the resistance is approximately 0.5 ohms. For experiments involving only Cs, we run 3.9 A through one dispenser and 2.1 A through the other. The current source is a standard laboratory benchtop power supply.

Surrounding the experimental apparatus are optics that control and direct laser beams into the glass cell to address the atoms. A potentially non-exhaustive list of lasers that are sent into our cell include: sodium and cesium optical tweezers, rearrangement tweezers, sodium and cesium MOT beams, sodium and cesium Raman beams, sodium and cesium optical pumping beams, and sodium and cesium Rydberg beams. Since we have so many beams, a judicious reuse of beampaths is required, and we often send multiple beams down the same path. Figure 2.1 shows all the various optical access paths currently built in the experiment. Co-propagating beampaths are typically combined either on the apparatus side with dichroic mirrors or prior to the output coupling fiber. Individual polarization control of the beams are accomplished via custom dual (or even triple) wavelength waveplates from Union Optic. The beampaths will be described in more detail in the sections that make use of the beams.

To create our tweezer traps, we use a custom microscope objective from Jenoptik with a numerical aperture of 0.55, aperture size of 18 mm and an effective focal length of 16 mm. The objective

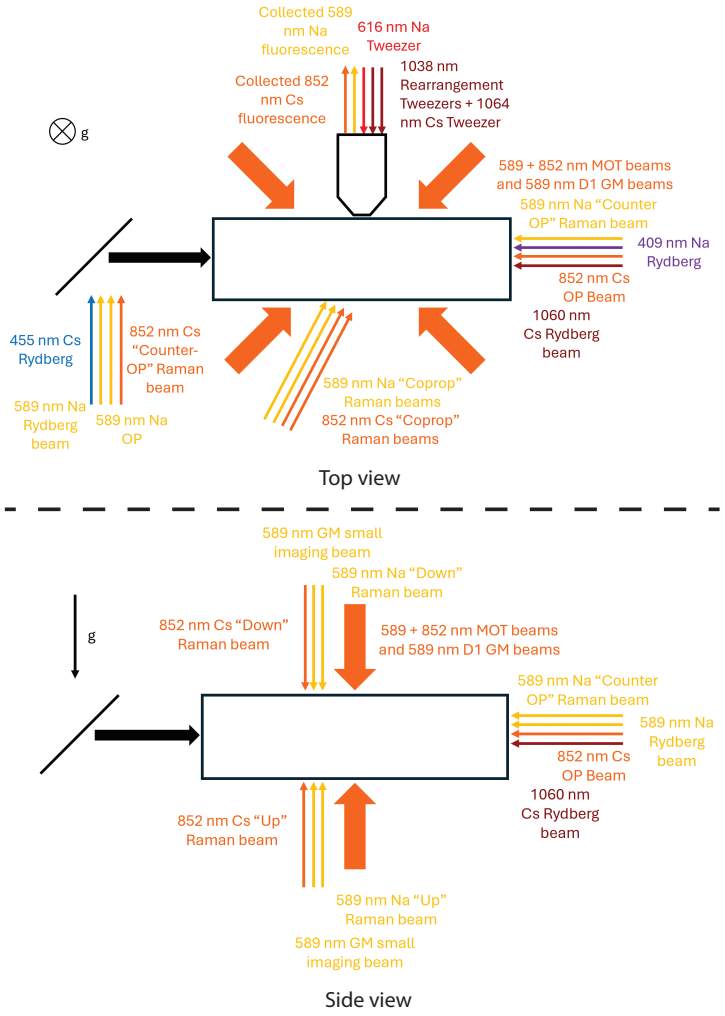

Figure 2.1: A top view and side view schematic of all the beams that impinge on the atoms. For clarity, co-propagating beams are drawn next to each other. For example, in the top view, there are 4 distinct MOT beam paths, a tweezer beam path, a skewed diagonal beam path (for the "coprop" Raman beams), a left going and right going beam path. In the bottom view, there are additionally up and down beam paths that co-propagate many beams.

is designed for 6 mm of glass (in our system, 2 mm of this is an ITO coated glass plate and 4 mm is the thickness of our cell wall). To image atoms, we collect light through the same microscope ob-

jective onto an Andor iXon Ultra 897 camera (Model number DU-897U-CS0-BVF). The collected light is focused onto the camera with a 400 mm lens. Filters that block our tweezer wavelengths are required for low background imaging.

In section 2.2, we discuss how we laser cool and image sodium, which has additional complexity due to large light shifts on the main cooling transition. In section 2.3, we discuss the how we laser cool and image cesium, which is comparatively simpler and more standard. Section 2.4 describes how we form optical tweezer arrays of both sodium and cesium. Section 2.5 describes the necessary software and hardware upgrades required to perform atom rearrangement, which is critical for forming defect free arrays. Lastly, section 2.6 describes our optical pumping procedure, which is used to prepare the atoms into a single quantum state after rearrangement.

2.2 Laser cooling and imaging of sodium

In this section, we describe the laser cooling and imaging of sodium used in our experiment. Sodium has nuclear spin $I = 3/2$, leading to two hyperfine ground states $F = 1$ and $F = 2$ in the $3S_{1/2}$ state. We form a magneto-optical trap (MOT) on the D2 line, which is the transition to $3P_{3/2}$ and contains a cycling transition from $F = 2$ to $F' = 3^*$. The laser system to create this light is described in a previous thesis [243] and involves a Raman fiber amplifier (VRFA-P-2000-589-SF from MPB Communications) which amplifies and subsequently doubles 1178 nm light from a ECDL seed from Timebase (ECQDL-1178). The laser is locked using modulation transfer spectroscopy [153] on the crossover of the $F = 1$ to $F' = 2$ and $F = 2$ to $F' = 2$ transition. A series of AOMs modifies the frequencies to drive desired resonances.

While the D2 line is the only line which has a viable cycling transition for the purposes of making a MOT, trapping sodium atoms in tweezers using cooling on the D2 line is non-trivial due to large

*Note primed quantum numbers indicate excited state quantum numbers.

transition light shifts from the trapping light[110]. To obtain sufficient cooling to cool atoms into the traps, the traps need to be strobed faster than the trap frequency but slower than the scattering rate (so that each dark period allows for a few photon scattering events). Strobing the tweezers decreases the available power for atom trapping and limits the number of atoms we can have in our arrays.

It turns out that there is an accessible magic wavelength[4] for the D1 ($3S_{1/2} \rightarrow 3P_{1/2}$) transition in sodium. A magic wavelength for a given transition is one that has zero transition light shift. Thus, with D1 cooling, it is possible to cool and trap atoms into DC tweezers, thus preserving tweezer power to trap more atoms. D1 light is produced from a second doubled Raman fiber amplifier seeded from a second ECDL seed from Timebase. The primary output of this laser is used for the NaCs molecule experiment in our lab. Upon request, these fiber amplifiers have an additional IR "dump" port for unconverted 1178 nm light. We separately double this unconverted IR with a magnesium-doped periodically poled lithium niobate (MgO:PPLN) crystal from Covesion (MSHG1180-0.5-40) which is 40 mm long. Operating the RFA at 2 W of 589 nm output yields approximately 5 W of IR. The conversion efficiency is approximately 4.4%/W saturating at about 16%. After the crystal, the light has repump sidebands added by an EOM from Qubig (PM-Na_1.7), and is frequency shifted by a single and double pass AOM. The beampath for creating the D1 light is shown in figure 2.2.

With the sodium D1 and D2 light generated, we now discuss how we deliver the light to the experiment. At the experimental apparatus, D1 and D2 light are needed along the "MOT beam paths" (two pairs of diagonals and a pair of vertical beams, see figure 2.1). The "MOT beam paths" on the apparatus table consists of 4 fiber outputs for the 4 diagonals and one fiber output for the down MOT beam (down here indicates that the beam propagates in the direction of gravity). The down MOT beam is retroreflected to create the up MOT beam. After the beams leave the fiber, it is collimated to approximately 5 mm in diameter. Polarization optics are used to convert them to the circular polarization required for a MOT.

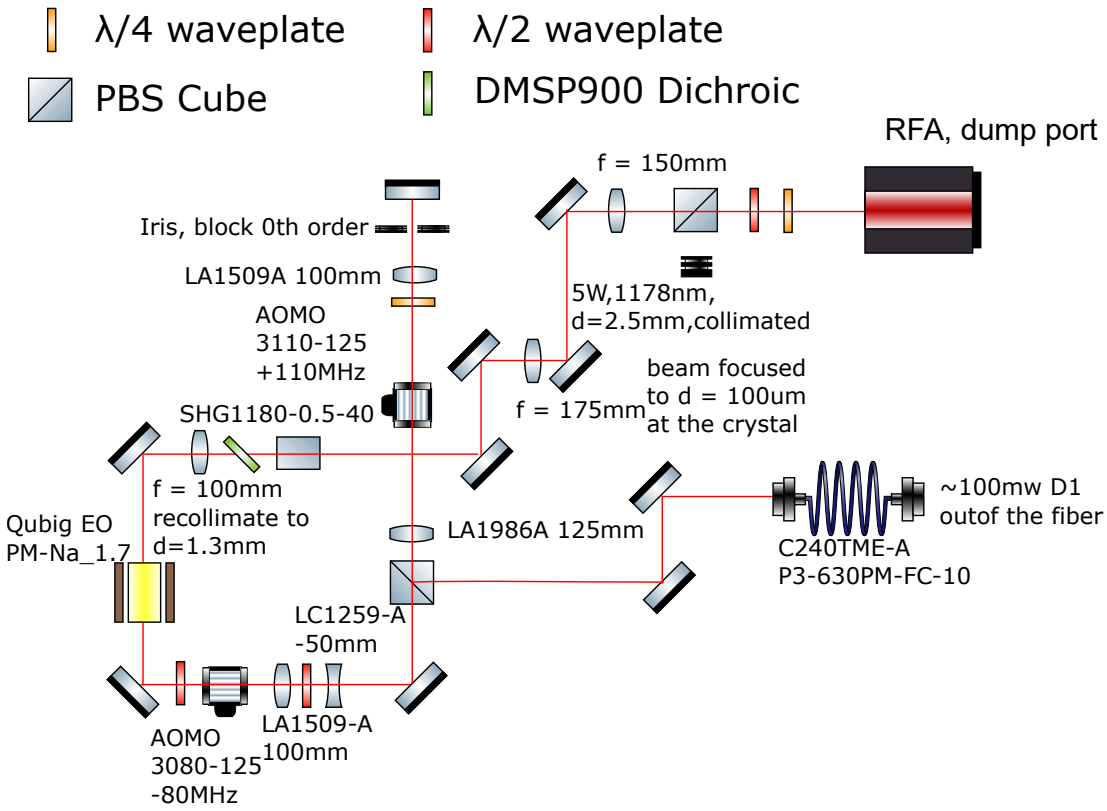

Figure 2.2: Our D1 light for gray molasses based atom loading is sourced from the dump port (unconverted IR at 1178 nm) of a doubled MPB Raman fiber amplifier. The output beam polarization is not very pure, so we need both a quarter and half waveplate to achieve good extinction on a PBS. This first PBS also acts as a dump to enable low power operation during alignment without needing to turn down the fiber amplifier. The beam also diverges out of this dump port, so a lens is empirically placed to collimate the beam. The beam is then focused into a Covesion doubling crystal and doubled to 589 nm. After the crystal, the unconverted IR is separated from the yellow light with a dichroic. In principle, this unconverted IR can be further used in another doubling stage. After the crystal, the yellow light passes through an EOM to produce the repump sidebands followed by a single and double pass AOM to shift the frequency away from the lock point. Frequency and amplitude control are accomplished with the double pass AO.

Each of these 5 fiber outputs need to have sodium D1, D2 and cesium D2 light. The distribution beampath shown in figure 2.3 combines sodium D1 and D2 light with cesium D2 light into these

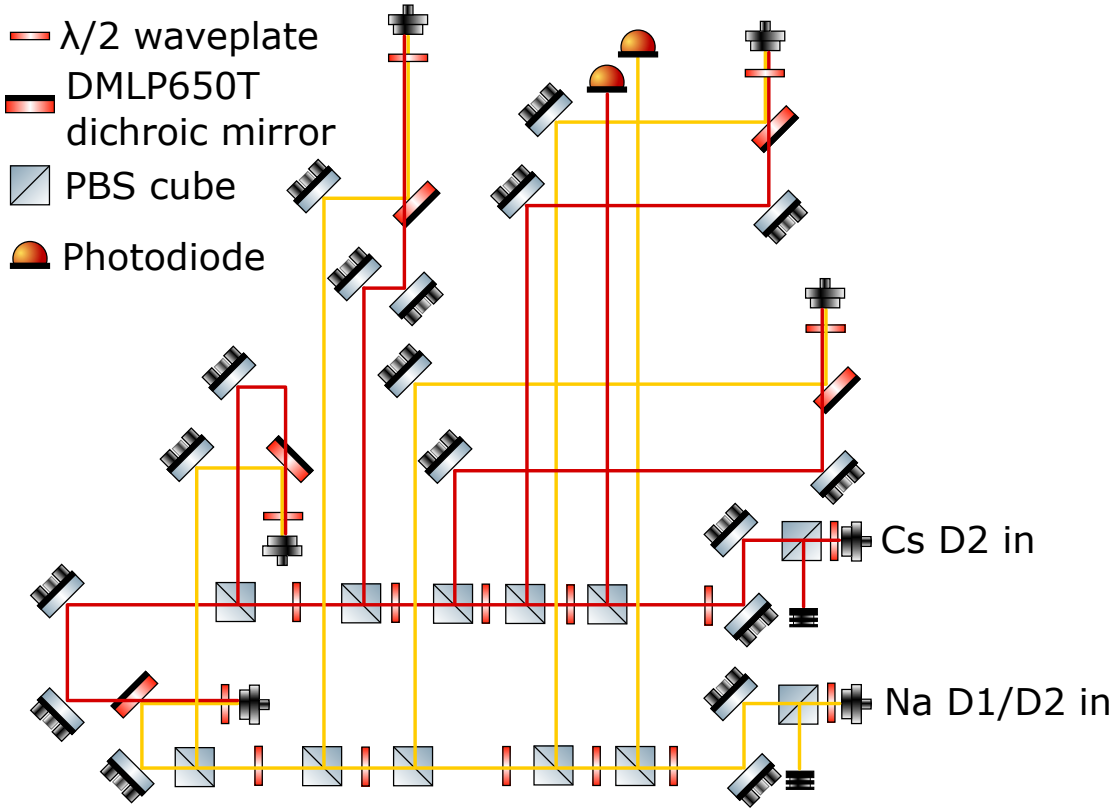

Figure 2.3: (Not to scale) This beampath distributes cesium D2 light (852 nm) and sodium D1/D2 light (589 nm) to 5 outputs which are sent to the experimental apparatus to serve as the MOT and sodium gray molasses beams. Frequency and amplitude control of the light is performed prior to this distribution beampath. The D1 and D2 light for sodium are already combined via a 2x2 polarization maintaining fiber optic coupler (Thorlabs PN635R2A2). Half waveplates and cubes allow for arbitrary control of the power into all 5 output beampaths. Sodium and cesium light is combined on long-pass dichroic mirrors. This design ensures that there are two mirrors before each output for each beam. We use PM630 fibers from Thorlabs and the C240TMD as the collimating asphere.

5 fibers with independent control of sodium and cesium beam alignment into each fiber as well as power balance into the 5 fibers. A key consideration in the design is dealing with the two different wavelengths involved. For instance, the beams diverge at different rates in free space (and out of the fiber) leading to a different spot size at the output fiber, and therefore different optima for the

collimating lens position for the cesium and sodium light. To minimize these issues, the distance from the inputs to a particular output should be similar for the cesium and sodium light and as small as possible. Alternatively, larger beam sizes also slow down the divergence of the two beams and the differences in that divergence due to their different wavelengths. With this setup, we deliver approximately 400 uW of sodium D2 light to the experiment (with a ratio of about 4:1 cooling to repump light), and 300 uW of cesium D2 light to the experiment (with a ratio of about 100:1 cooling to repump light) per beam. Note that the beam balance between pairs of beam needs to be about 10% or better to reliably obtain a MOT.

Our experimental sequence starts with loading MOTs of both sodium and cesium atoms. Here, we will discuss the sodium part of this sequence (but note it can happen in parallel with the cesium parts). A MOT using sodium D2 light is first formed over 100-200 ms. Then the B field and D2 light is turned off, while the sodium tweezers and D1 gray molasses light is turned on with approximately 1.5 mW in each beam. Recall that the D1 gray molasses beam are copropoagating with the MOT beams. Atoms are loaded into tweezers during this period.

To image atoms, we apply near resonant light and rely on the atoms to cycle photons. To determine whether an atom is present at a given location, we take a simple sum of the camera counts in a particular region and check if it is above a certain cutoff. Counts above this cutoff indicates an atom. For high imaging fidelity (the ability to distinguish between an atom and no atom), the histogram of camera counts over different experimental sequences should show two well separated peaks (see figure 2.4b). The number of scattered photons relies on the balance between heating from photon scattering and the cooling mechanisms. If the photon scattering causes so much heating that the atoms are quickly heated out of the trap, then not much fluorescence occurs. Therefore, a cooling mechanism (which scatters photons) must be present.

In our previous work, we performed imaging with our D2 MOT beams (at zero magnetic field, roughly under conditions of polarization gradient cooling), which has the advantage of automat-

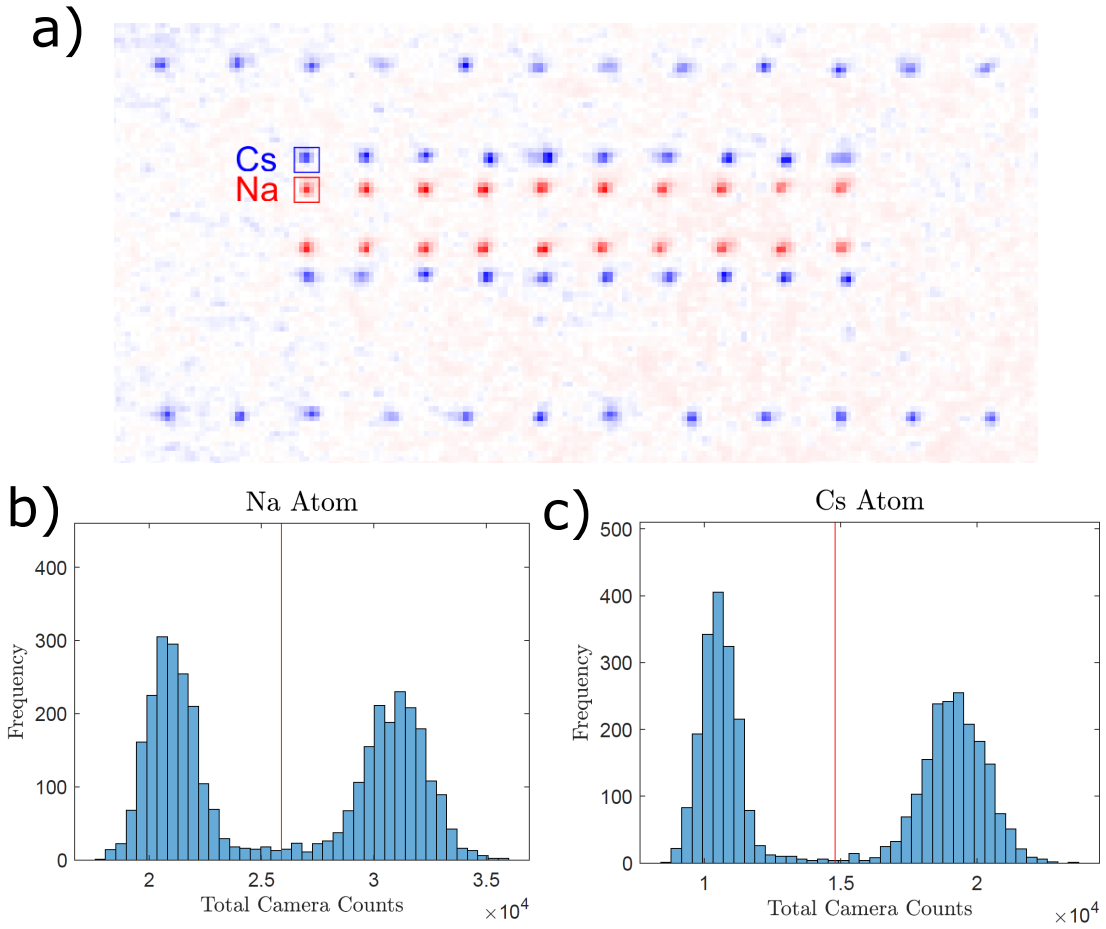

Figure 2.4: (a) An example of a dual species array of sodium and cesium atoms. Note that these two images are taken in series (not concurrently), but we have plotted the image results on top of each other to visualize the relative array locations. The box indicates the pixels which are summed to create the histograms in (b) and (c). (b) and (c) Histograms of the total camera count for sodium and cesium respectively. The red line discriminates between images with and without an atom at this site.

ically being aligned to our atoms. However, these large beams cause excess background scattering and lower the imaging fidelity. To combat this problem, we use a pair of small imaging beams (< 500μm at the atoms and typically < 1 mW of power in each beam) along the up and down directions. Furthermore, with our DC traps, D2 imaging is no longer possible, so we use D1 light pro-

viding cooling via gray molasses cooling. Only with both D1 loading and imaging can we completely remove our dependence on strobing tweezers and use our full tweezer laser power for larger arrays. Aligning the imaging beams is actually a bit tricky without atoms to reference the beams to. We found that by shining near-resonant light, we can align one of the beams to the atoms by destroying the MOT with as little power as possible. A decent starting point for the other beam is to fiber couple it into its counter-propagating counterpart.

2.3 Laser cooling and imaging of cesium

In this section, we describe the laser cooling of cesium used in our experiment. Cesium is a $I = 7/2$ atom leading to two hyperfine ground states $F = 3$ and $F = 4$ in the $6S_{1/2}$ state. We form a magneto-optical trap (MOT) on the D2 line, which is the transition from $6S_{1/2}$ to $6P_{3/2}$ and contains a cycling transition from $F = 3$ to $F' = 4$. The laser system to create this light is described in a previous thesis [143] and consists of two distributed Bragg reflector (DBR) laser from Photodigm (PH852DBR240TS) at 852 nm: one addresses the $F = 4$ hyperfine ground state and is considered the "cooling" laser, and the other addresses the $F = 3$ hyperfine ground state and is considered the "repump" laser. The repump laser from $F = 2$ to $F = 3'$ is approximately 9.2 GHz detuned from the cooling laser, and is locked to the crossover of the $F = 3$ to $F' = 3$ and $F = 3$ to $F' = 4$ transition using saturated absorption spectroscopy on a vapor cell. The cooling laser is then beat-locked to this repump laser, using a fast photodiode (Electro-Optics Technology ET-4000) to record the beatnote and a phase-locked loop (PLL) board (AD4159) to lock the beatnote to a reference DDS oscillator. The repump laser needs to be delivered to the MOT beampaths as well as the optical pumping beampath. Its frequency is controlled by a single double pass AOM with the actual beampath it goes to determined by shutters. The cooling light frequency is controlled by the reference frequency to the PLL board and the light is sent down the MOT and optical pumping beampaths. This setup is

shown in figure 2.5. Imaging is performed with near resonant light using the MOT beampaths.

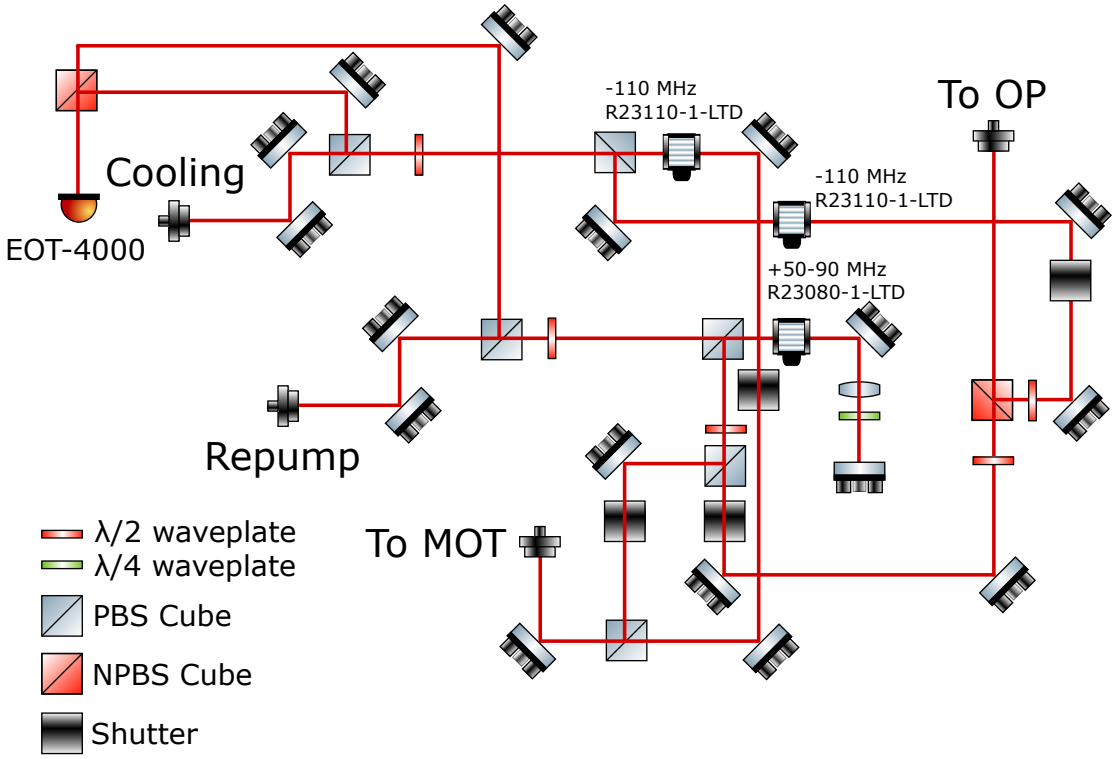

Figure 2.5: (Not to scale) This beampath distributes cesium cooling and repump light to the MOT and the optical pumping (OP) beampaths. The saturated absorption spectroscopy lock of the repump light is performed on another setup. The cooling light is combined on a NPBS (to allow for optical interference) with the repump light to create a beatnote that is measured on a fast photodiode. For the cooling light, the frequencies of the AOMs are not so critical, because its frequency can be controlled with the beatnote lock. Hence, these AOMs are in single pass configuration. The repump frequency is controlled by a double pass AOM and is thus tunable. Note that using it at 50 MHz (which is required for the MOT repump) is quite inefficient, but we do not need much repump to form a MOT. Shutters are used to eliminate leaked light for the cooling laser and to block the light from the undesired beampath.

2.4 Optical Tweezer Arrays

In our experiment, we use a static set of tweezers for sodium and cesium, and one set of rearrangement tweezers. The static tweezers are created with spatial light modulators [165], while the rearrangement tweezers are created with an acousto-optical deflector (AOD) [122].

The sodium static tweezer with a wavelength of 615.87 nm, which is magic for the sodium D1 transition [4], is created from a complete SFG system from Precilasers. This system consists of two fiber laser seeds at approximately 1534 and 1029 nm, which are then amplified by a ytterbium and erbium doped fiber amplifiers respectively. They are then passed through a nonlinear crystal where a SFG process creates approximately 4 W of 615.87 nm. The light is then intensity stabilized via an AOM (Gooch and Housego 3110-120) and coupled to a fiber for mode cleanup. This fiber is short (to handle higher powers) and delivers the light to the apparatus.

The cesium static tweezer is at approximately 1064 nm and is produced from a 50 W Precilasers ytterbium-doped fiber amplifier seeded by light from a Mephisto MOPA (Coherent Mephisto MOPA). The light is intensity stabilized with an AOM. To handle these high powers, we use a quartz AOM from AA Optoelectronics (MCQ68-A2.5-L1064-Z38-C35Sa) especially designed for high power. After the AOM, the light is delivered via an end-capped fiber to the experimental apparatus.

The AOD tweezer is at approximately 1038 nm and is produced from a 20 W Azur Light Systems ytterbium-doped fiber amplifier (ALS-IR-1040-20-A-SF). This light is intensity stabilized via an AOM (Gooch and Housego R23110-1-LTD). After the AOM, the light is delivered via an end-capped fiber to the experimental apparatus.

2.4.1 Spatial Light Modulators

The spatial light modulator consists of an array of liquid crystals. These liquid crystals, which contains long molecules, are anisotropic and thus are birefringent. An applied electric field tunes the principal axes, with the long molecules aligning to the field. Thus, an array of liquid crystals acts as a spatially dependent phase modulator of a laser beam, where this phase is controlled by an applied voltage. To obtain the largest filling fraction of individually-addressable liquid crystal pixels (addressed by a voltage), these devices employ liquid crystal on silicon (LCoS) technology. The liquid crystal is placed between a transparent conductive material, such as ITO coated glass, and a reflective array of electrodes, each of which can have its voltage adjusted. The drive electronics can then be placed directly behind these reflective electrodes. In this configuration, light is intended to pass through the conductive ITO coated glass, propagate through the birefringent liquid crystal, and reflect off the electrodes. Thus, these SLMs are used in reflection. Since the mechanism to change the phase modulation requires physically rotating these liquid crystal molecules, refresh rates are limited to the hundreds of Hz to kHz. These devices are also characterized by a settle time for the liquid crystals to align. For these reasons, spatial light modulators are typically left unchanged throughout an experimental cycle and are ideal as a static tweezer array. We note that there have been experiments which have successfully used dynamic changes of the SLM to move and rearrange atoms [135].

The phase modulation capability is used to create arbitrary tweezer arrays from a single input laser beam. To see how this is accomplished, we use the Fourier transform property of a lens, which we will derive here. We place the SLM a distance z_{SLM} away from a lens of focal length f. We are then interested in the electric field at a plane a distance z' after the lens. This setup is shown in figure 2.6.

We will use a scalar theory of light and ignore polarization [87]. We further assume that the medium in which the light propagates (characterized by index of refraction n) is homogeneous. In this case,

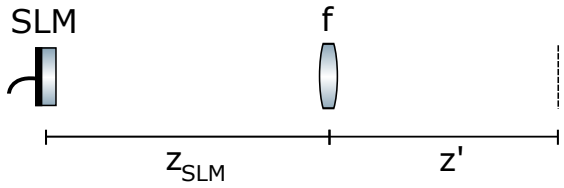

Figure 2.6: Setup for calculating the electric field of a SLM modulated beam after a lens.

the scalar field u satisfies the scalar wave equation

$$\nabla^2 u(x,y,z,t) - \frac{n^2}{c^2}\frac{\partial^2 u(x,y,z,t)}{\partial t^2} = 0. \tag{2.1}$$

We assume the light is monochromatic, namely that the time dependence of $u(x,y,z,t)$ is captured by $e^{-i\omega t}$, where $\omega = 2\pi\nu$ is the angular frequency of the light. Mathematically, we make the ansatz $u(x,y,z,t) = U(x,y,z)e^{-i\omega t}$ and substitute into equation 2.1 to obtain

$$\nabla^2 U + k^2 U = 0 \tag{2.2}$$

where $k = n\omega/c$ is the wavevector of the light. This equation is known as the Helmholtz equation. The Rayleigh-Sommerfeld solution relates the scalar field in one plane $z = z_0$ to another at $z = z_1$ in the following way:

$$U(x_1,y_1,z_1) = \frac{1}{i\lambda}\int_{-\infty}^{\infty}\int_{-\infty}^{\infty} U(x_0,y_0,z_0)\frac{z_1 - z_0}{r}\frac{e^{ikr}}{r}dx_0 dy_0 \tag{2.3}$$

where λ is the wavelength of the light and $r = \sqrt{(x_1-x_0)^2 + (y_1-y_0)^2 + (z_1-z_0)^2}$ is the distance from the observation point (x_1,y_1,z_1) to the source point (x_0,y_0,z_0). This equation is used to propagate the field from one plane to another. Let's work in the far field where $r \approx z_1 - z_0$. In this case, $(z_1 - z_0)/r \approx 1$, and we need to Taylor expand the exponent in e^{ikr} to lowest order in $(x_1 - x_0)/(z_1 - z_0)$ and $(y_1 - y_0)/(z_1 - z_0)$. We obtain

$$U(x_1, y_1, z_1) \approx \frac{e^{ik(z_1-z_0)} e^{\frac{ik(x_1^2+y_1^2)}{2(z_1-z_0)}}}{i\lambda(z_1-z_0)} \int_{-\infty}^{\infty}\int_{-\infty}^{\infty} U(x_0, y_0, z_0) e^{\frac{ik\left(x_0^2+y_0^2\right)}{2(z_1-z_0)}} e^{-ik\left(\frac{x_1x_0}{z_1-z_0}+\frac{y_1y_0}{z_1-z_0}\right)} dx_0 dy_0 \quad (2.4)$$

which is known as the Fresnel diffraction integral. Our plan of attack will be to propagate the field at the SLM (which is determined by the SLM) to the lens. Then, we apply the lens transmission function to the field. Finally, we will propagate it to the final plane of interest (such as the atom plane).

Let the field at the SLM be given by $U_{\text{SLM}}(x, y, z)$. Immediately before the lens, the field is given by

$$U_{\text{l-}}(x_1, y_1, z_1) = \frac{e^{ikz_{\text{SLM}}}}{i\lambda z_{\text{SLM}}} e^{\frac{ik(x_1^2+y_1^2)}{2z_{\text{SLM}}}} \int_{-\infty}^{\infty}\int_{-\infty}^{\infty} U_{\text{SLM}}(x_0, y_0, z_0) e^{\frac{ik\left(x_0^2+y_0^2\right)}{2z_{\text{SLM}}}} e^{-ik\left(\frac{x_0x_1}{z_{\text{SLM}}}+\frac{y_0y_1}{z_{\text{SLM}}}\right)} dx_0 dy_0. \quad (2.5)$$

The lens transmission function is given by $e^{-ik\frac{x^2+y^2}{2f}}$, where x and y are on the plane of the lens. The field immediately after the lens is then given by

$$U_{\text{l+}}(x_1, y_1, z_1) = \frac{e^{ikz_{\text{SLM}}}}{i\lambda z_{\text{SLM}}} e^{\frac{ik(x_1^2+y_1^2)}{2z_{\text{SLM}}}} e^{-ik\frac{x_1^2+y_1^2}{2f}} \int_{-\infty}^{\infty}\int_{-\infty}^{\infty} U_{\text{SLM}}(x_0, y_0, z_0) e^{\frac{ik\left(x_0^2+y_0^2\right)}{2z_{\text{SLM}}}} e^{-ik\left(\frac{x_0x_1}{z_{\text{SLM}}}+\frac{y_0y_1}{z_{\text{SLM}}}\right)} dx_0 dy_0. \quad (2.6)$$

Now, we finally propagate to our plane of interest, a distance z' away from the lens. Using the Fresnel diffraction integral once again, we obtain

$$U(x_2, y_2, z_2) = \frac{e^{ikz'} e^{\frac{ik\left(x_2^2+y_2^2\right)}{2z'}}}{i\lambda z'} \int_{-\infty}^{\infty}\int_{-\infty}^{\infty} U_{\text{l+}}(x_1, y_1, z_1) e^{\frac{ik\left(x_1^2+y_1^2\right)}{2z'}} e^{-ik\left(\frac{x_2x_1}{z'}+\frac{y_2y_1}{z'}\right)} . dx_1 dy_1 \quad (2.7)$$

The resulting integral integrates over 4 variables. We can evaluate the integral over x_1, y_1, thus relating x_2, y_2 directly to the SLM plane coordinates x_0, y_0. We collect all terms with x_1, y_1, which results in the integral

$$\mathcal{I} = \int_{-\infty}^{\infty}\int_{-\infty}^{\infty} e^{\frac{ik(x_1^2+y_1^2)}{2z_{\text{SLM}}}} e^{-ik\frac{x_1^2+y_1^2}{2f}} e^{-ik\left(\frac{x_0x_1}{z_{\text{SLM}}}+\frac{y_0y_1}{z_{\text{SLM}}}\right)} e^{\frac{ik\left(x_1^2+y_1^2\right)}{2z'}} e^{-ik\left(\frac{x_2x_1}{z'}+\frac{y_2y_1}{z'}\right)} dx_1 dy_1. \tag{2.8}$$

Instead of solving this integral in complete generality, let's consider a plane where $z' = f$. In other words, our final plane of interest is at the focus of the lens. This allows us to get rid of two terms in the above equation, and we can perform the integral after completing the square in the exponent. We obtain

$$\mathcal{I} = i\lambda z_{\text{SLM}} e^{-ik\frac{(x_0f+x_2z_{\text{SLM}})^2+(y_0f+y_2z_{\text{SLM}})^2}{2f^2z_{\text{SLM}}}}. \tag{2.9}$$

Substituting this result into equation 2.7, we obtain the final field at the focal plane

$$U(x_2,y_2,z_2) = \frac{e^{ik(z_{\text{SLM}}+f)}}{i\lambda f} e^{ik\frac{x_2^2+y_2^2}{2f}(f-z_{\text{SLM}})} \int_{-\infty}^{\infty}\int_{-\infty}^{\infty} U_{\text{SLM}}(x_0,y_0,z_0) e^{-ik\left(\frac{x_0x_2+y_0y_2}{z_{\text{SLM}}}\right)} dx_0 dy_0. \tag{2.10}$$

We notice that the field at the focal plane of the lens is the Fourier transform of the field on the SLM plane, with an additional quadratic phase factor, which vanishes when $z_{\text{SLM}} = f$. Thus, ideally, we would operate with $z_{\text{SLM}} = f$ to have this exact Fourier transform relationship between the two planes. However, if the SLM is not exactly on the back focal plane of the lens, there is additional phase curvature represented by this quadratic phase factor. If we are only interested in the intensity of the light, then this phase curvature does not impact the intensity distribution.

The problem of creating an arbitrary tweezer array on the focal plane of the lens thus reduces to calculating the inverse Fourier transform of our target pattern and projecting that on the SLM.

However, there is a slight complication since the SLM only has phase modulation capabilities and does not modulate the amplitude of the beam. If we have a plane wave (constant amplitude A_0 and phase) impinging on our SLM, the resulting field directly after the SLM is modified to be

$$U_{\mathrm{SLM}}(x_0, y_0, z_0) = A_0 e^{i\varphi_{\mathrm{SLM}}(x_0, y_0)}, \tag{2.11}$$

where $\varphi_{\mathrm{SLM}}(x_0, y_0)$ depends on the voltage applied to each pixel which can be controlled via a computer. Note that since the SLM can only phase modulate each part of the beam, it makes it difficult to specify both a desired phase and amplitude on the target plane. However, if one only constrains the intensity, and thus the amplitude, relatively efficient algorithms, such as weighted Gerchberg Saxton (WGS)[82,126] exist to calculate φ_{SLM}.

The WGS algorithm is an iterative algorithm. Suppose we want a target amplitude on the focal plane to be $\mathcal{T}(x', y')$. We start with a random initial guess phase $\varphi_0(x, y)$ on the SLM plane. Given an intensity distribution $I_{\mathrm{SLM}}(x, y)$, we can calculate the field

$$U_{\mathrm{SLM},0}(x, y) = \sqrt{I_{\mathrm{SLM}}(x, y)} e^{i\varphi_{\mathrm{SLM},0}(x, y)} \tag{2.12}$$

on the SLM plane. We assume that the effect of the lens is to perform a Fourier transform, so we can perform this numerically in software to obtain a field on the focal plane

$$\tilde{U}(x', y') = \tilde{A}_1(x', y') e^{i\tilde{\varphi}_1(x', y')}, \tag{2.13}$$

consisting of both an amplitude and phase part. The amplitude part is discarded and replaced with $\mathcal{T}(x', y') g_1(x', y')$, where $g_1(x', y')$ is a non-uniformity correction. This correction can be either calculated from $\tilde{A}_1(x', y')$ or can also be determined using feedback from a camera or from a measurement on the atoms. For instance, if there is some spatially dependent optical loss which reduces

transmission for a particular point, this correction allows our algorithm to artificially compensate and raise the target intensity of that point. The inverse Fourier transform is then applied to $\mathcal{T}(x', y')g_1(x', y')e^{i\tilde{\varphi}_1(x', y')}$ resulting in an SLM plane field of $A_1(x, y)e^{i\varphi_{\text{SLM},1}(x,y)}$. We then discard the amplitude part and replace it with $\sqrt{I_{\text{SLM}}(x, y)}$ resulting in

$$U_{\text{SLM},1}(x, y) = \sqrt{I_{\text{SLM}}(x, y)}e^{i\varphi_{\text{SLM},1}(x,y)}, \tag{2.14}$$

which is the next guess for the iterative algorithm. For the phase-fixed version of the algorithm [126], we no longer update $\tilde{\varphi}_i(x', y')$ at some N. In other words, when we perform the Fourier transform, we discard both the amplitude and phase beyond N, but note that we still have feedback from the $g_i(x', y')$. For our SLM phase patterns, we typically use around $N = 10$, and discretize our space into a 2048×2048 grid. We crop the central 1280×1024 region to use for our SLM. Padding the computational space with extra pixels helps the accuracy of the algorithm, allowing for the storage of higher frequency components in the Fourier transform.

Another nice feature of SLMs is that they can be used to correct for optical aberrations, which are deviations of the actual wavefront from the ideal one, say of a Gaussian beam. Deviations in a wavefront are a phase lag or phase lead relative to the ideal one. This setting is a perfect one for a SLM which can correct for these phase differences by applying its own phase modulation. Aberrations can be decomposed into a basis of Zernike polynomials [29], where each polynomial is a function of two variables x and y and is orthonormal on the unit disk. Each polynomial is characterized by its effect as seen after focusing by a lens, and include astigmatism, coma and trefoil. SLMs contain inherent imperfections mostly from the surface roughness on each pixel or an imperfect filling fraction. Thus, the manufacturer ships the SLM with a factory calibrated correction pattern that corrects the aberrations of the SLM itself. This correction pattern is critical to apply and without it a simple Gaussian beam can look quite distorted as shown in figure 2.7a. We find empirically that this

seemed to matter more for the cesium (1064 nm) SLM compared to the sodium (616 nm) SLM.

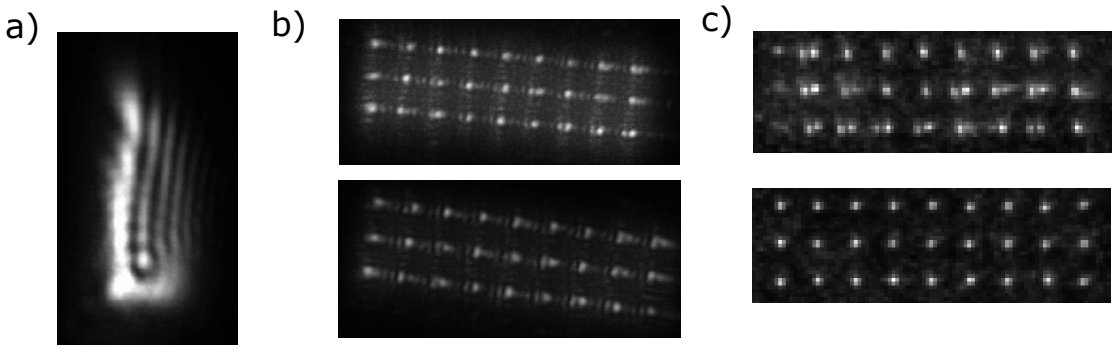

Figure 2.7: a) A single tweezer for our cesium SLM (1064 nm) without applying the factory calibrated correction. b) Upper: A 3 by 9 cesium array before wiping a mirror with some dust on it. Notice the haze around the array. Lower: The 3 by 9 array after cleaning the mirror. c) The corresponding arrays of cesium atoms before and after cleaning the mirror.

We note that while it is nice SLMs can in principle correct all aberrations (using infinitely high orders of Zernike polynomials), this power is not to be abused. It cannot easily compensate for high amounts of aberrations, nor is it easy to determine the exact Zernike decomposition to correct an arbitrary aberration. Care should be taken in the construction of the beampath to minimize the amount of aberrations. In fact, atom loading should be possible with zero aberration correction. In the upper panel of figure 2.7b, we show a picture of our atom array when a mirror in the beampath was dirty. The corresponding atom image in the upper panel of figure 2.7c shows misshapen traps. We worked hard to try to improve the array in this condition using Zernike polynomials, and while it was possible to make certain traps look better, it was impossible to make all traps look good using only the first 4 or so orders of Zernike polynomials. To solve this issue, we simply had to clean a particular mirror in the beampath, resulting in the light pattern in the lower panel of figure 2.7b. After cleaning, atoms loaded immediately (and at reasonable powers) with zero aberration correction.

While using cameras to emulate the atom plane (i.e. picking off the tweezer beam before the ob-

jective and focusing with a large focal length lens) are a reasonable tool for alignment and rough uniformity and aberration tweaking, we have not had great success at getting an exact 1 to 1 correspondence of the offline tweaks with the ideal conditions as determined by the atoms. For instance optimizing the uniformity of the trap depths offline on a camera only ensures actual trap uniformity to around the 10% level. Further optimization on the atoms is required to get the depths to be uniform beyond this level. Trap depths are measured by determining the transition frequency of the $3S_{1/2}F = 2, m_F = 2 \rightarrow 3P_{3/2}F = 3, m_F = 3$ ($6S_{1/2}F = 4, m_F = 4 \rightarrow 6P_{3/2}F = 5, m_F = 5$) in sodium (cesium). This transition light shift is related to the trap depth via the known polarizabilities for each state. For more precision, we can also determine the trap depth via the trap frequency. The trap frequency is most easily measured by locating the parametric heating resonance, which occurs at twice the trap frequency[81] (axial or radial). Typically trap depth information is also used to reduce optical aberrations based on the simple principle that optical aberrations reduce the peak intensity of the traps. Thus, by maximizing the trap depth as a function of Zernike polynomials applied on our SLM, we can minimize aberrations. We have found a 10-20% increase in our trap depths after correcting for aberrations[†].

Another known effect in SLMs is the presence of a "zero order" spot[186]. This spot arises from the imperfect anti-reflection coating on the SLM pixels, resulting in light that does not go through the liquid crystal medium. A rule of thumb is to avoid overlapping the diffracted beam spots (i.e. the portions of light that does go through the liquid crystal medium) with the zeroth order or points directly above and to the side of the zeroth order. Thus, the usable region of the SLM separates into 4 quadrants. We further block the zeroth order beam from making it to our atom plane by using a d-shaped mirror (which also blocks out two quadrants) on an intermediate focal plane, which will be described in section 2.4.2. The zeroth order spot is also stronger when we create arrays farther

[†]We have only scanned the weight of each Zernike polynomial more or less independently. There is great potential here to use machine learning to determine how to optimize this high dimensional parameter space.

away from the zeroth order. The diffraction efficiency of a trap is limited by a $\sin(r)/r$ envelope [186] resulting from the pixelated structure of the SLM, which causes diffraction into higher orders. This diffraction efficiency can be compensated for during array generation.

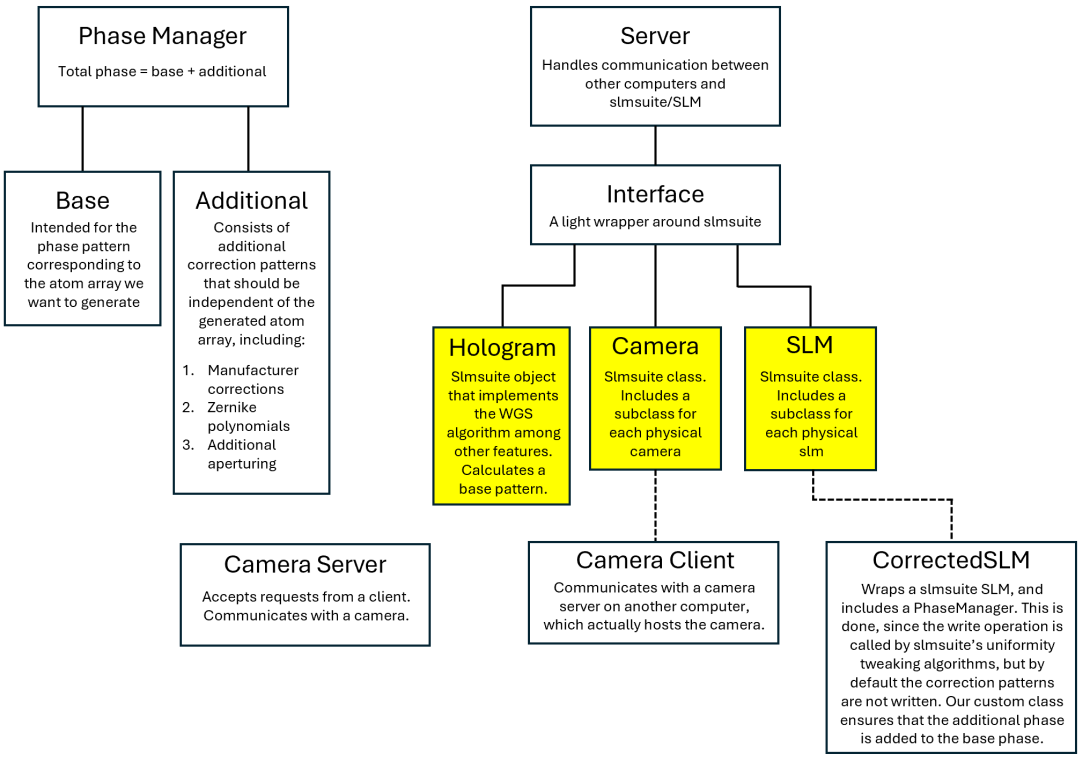

Figure 2.8: An overview of our SLM control software. The main additional abstraction to `slmsuite` is in the `PhaseManager`, which contains a base pattern (which is responsible for the atom array pattern) and an additional pattern (which includes all corrections that should be common for every atom array pattern). A `Server` manages connections to client computers. Highlighted boxes indicate classes from `slmsuite`, and the dashed lines indicate two custom camera and SLM classes we created. The `CameraClient` allows using cameras from a separate computer. The `CorrectedSLM` wraps a SLM with a `PhaseManager` so that the `write` function includes the additional corrections.

SLM Control Software

The goals of our control software are to be flexible and modular. Our software wraps around `slmsuite`[‡], which implements the WGS algorithm and builds in feedback capabilities. For instance, it is relatively well integrated with cameras in order to perform automatic uniformity feedback. It also automates the calibration between computational space coordinates and camera coordinates. It can also perform automatic wavefront calibration, where it can determine a correction pattern for the aberrations in your optical path and has recently implemented local Zernike polynomials, allowing for more local aberration correction.

Our Hamamatsu SLMs interface with a computer via a display adapter and thus gets treated as a monitor. `slmsuite` uses a generic class to deal with these SLMs, compared to more specific classes to deal with SLMs that have a dedicated SDK. Generically, `slmsuite` defines abstract camera and SLM classes, equipped with a standard set of functions such as writing to the SLM or taking a picture that need to be implemented for each new SLM or camera. As of this writing, `slmsuite` supports Thorcams, but not our Andor cameras.

The main abstraction our codebase adds is the concept of two separate "buckets" of phases, which in the code is often referred to as the "base" or "additional" pattern. Simply stated, the base pattern is all information that is specific to a given tweezer array pattern, while the additional pattern, at least conceptually, is all information that is independent of the pattern. The base pattern is calculated for each desired tweezer array pattern, which is specified by a list of x, y coordinates and amplitudes for each of these points. The additional pattern mostly consists of aberration correction (manufacturer calibrated and our own Zernike polynomials) and in principle should be the same regardless of the base pattern. The base and additional phases are set and manipulated in a `PhaseManager`, which upon calling the `get` method returns a sum of these two components. This

[‡]https://github.com/slmsuite/slmsuite

abstraction between "base" and "additional" also extends to data saving, where we can save and load base patterns separately from additional patterns and mix and match them for convenience.

Our codebase also adds a `Server` which can accept requests from a client in order to control the SLM remotely. This functionality is also critical for automated feedback. The `Server` interfaces with `slmsuite` via a class called `Interface`. Any users of `slmsuite` which want to use our additional abstractions/functionality but with a different server or any other program should use the `Interface`.

Lastly, our codebase adds two additional subclasses of `SLM` and `Camera`. For the `SLM`, we created a thin wrapper called `CorrectedSLM`. This is because the `slmsuite` `Hologram` class, for its feedback features, directly writes the newly calculated pattern to the SLM, without any additional phase corrections. This is not ideal for us, because we need these corrections in order to load atoms and these corrections may also affect uniformity. Our custom class takes any SLM as an input but also a `PhaseManager`. It overwrites the `write` method to treat the argument only as the "base" and the `PhaseManager` contains the additional phase to add to the base before displaying on the SLM. The custom `Camera` subclass we created implements all `Camera` methods to send network requests to a `CameraServer` which then routes those same commands to an actual camera. It is called `CameraClient`, and allows the actual physical camera to be located on a separate computer from the SLM computer.

2.4.2 SLM Beampaths

Figure 2.9 depicts our beampaths on the tweezer side of our apparatus, which includes the SLM beampaths. The goal of these beampaths is to deliver light that can be modulated by a SLM through an objective without optical aberrations. Thus, extra care is taken to center the beam on each lens and to ensure that the beam passes through the lens on its symmetry axis. We also use achromat lenses, instead of simple plano-convex lenses. If possible, we will use two inch optics, so inhomo-

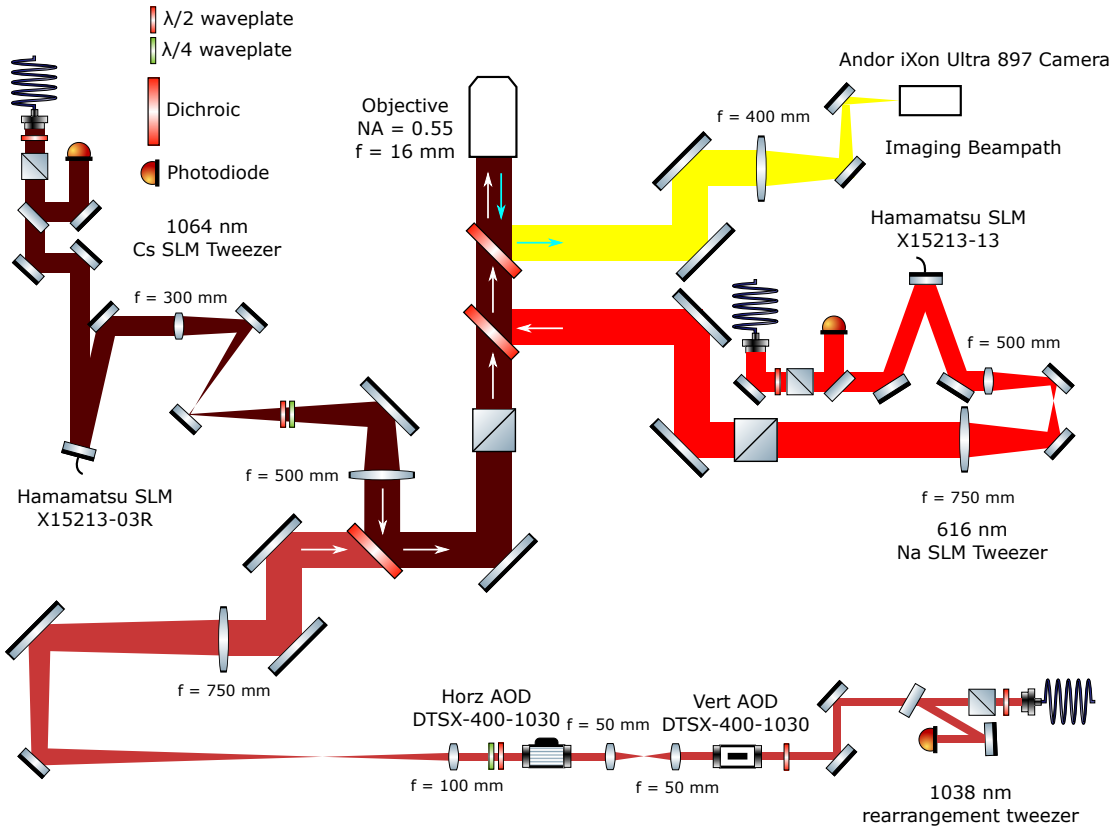

Figure 2.9: (Not to scale) Our tweezer and imaging beampaths. The brown is the 1064 nm cesium SLM tweezer. After the SLM, the beam is expanded to roughly 18 mm by a 4f telescope. A PBS cube is placed as far down the beampath as possible to remove any circular polarization which can cause vector light shifts between the hyperfine ground states. The maroon red is our 1038 nm rearrangement tweezer. The light first goes through a vertically deflecting AOD. The AOD location is imaged in a 4f system to a second horizontally deflecting AOD. Afterwards, the beam is expanded to about 18 mm by another 4f telescope. The red is the 616 nm sodium tweezer. After the SLM, the beam is expanded with a telescope, and the polarization is made linear with a PBS. This light is then combined with the other two aforementioned tweezers on a dichroic. The yellow represents the imaging beampath, which collects the fluoresced light (typically 589 and 852 nm for sodium and cesium) from the microscope objective. The light is directed to this beampath by a dichroic. The atoms are imaged in a 4f system to an Andor camera.

geneity of the optical surface near the edges of an optic can be avoided. Ideally, the beam should fill the entire surface of the SLM, so that all the pixels of the SLM can be used. At the objective, for the smallest waist at the focus, the beam should fill the entire aperture [§]. In our experiment, these constraints require a beam size of approximately 10 mm at the SLM plane and 18 mm at the objective entrance.

To navigate between these two sizes we use a $4f$ imaging system to expand the beam. In particular for sodium (cesium), we use a telescope with $f_1 = 500(300)$ mm and $f_2 = 750(500)$mm. Ideally, the SLM lies a distance f_1 before the first lens. The distance between the two lens is $f_1 + f_2$, and the objective is a distance $f_2 + f_{\text{obj}}$ from the second lens. For cesium, we are able to satisfy these relationships, but for Na, our SLM is not placed a distance f_1 from the first lens. According to equation 2.10, we see that the effect of this is to introduce additional phase curvature on the atom plane, which does not affect the intensity distribution.

Our cesium beam starts at about 10 mm out of an collimator from Oz Optics. Light is picked off with a beamsplitter and directed to a photodiode for intensity stabilization. After reflection off the SLM, it enters a 4f telescope for the purpose of expanding the beam. Within this telescope, there is an intermediate focus where we place a d-shaped mirror to reflect the zeroth order beam. Due to space limitations, to fit a distance of $f_1 + f_2$ between the two telescope lenses, we need to direct the beam upwards and back down. We find that Thorlabs damped posts provide sufficient stability. The beam is then combined with the rearrangement tweezer via a custom dichroic from Layertec. Since the wavelengths that need to be separated are very close in wavelength (1038 and 1064 nm), this dichroic only works well at a very specific angle up to a few degrees of tolerance, complicating alignment.

[§]There is also a school of thought that this technically results in an airy disk pattern, which can result in interference between nearby traps. To minimize this effect, a smaller beam that doesn't quite fill the aperture is preferred. Simulations can be performed to find the correct compromise between waist size and airy disk lobes that minimize interference.

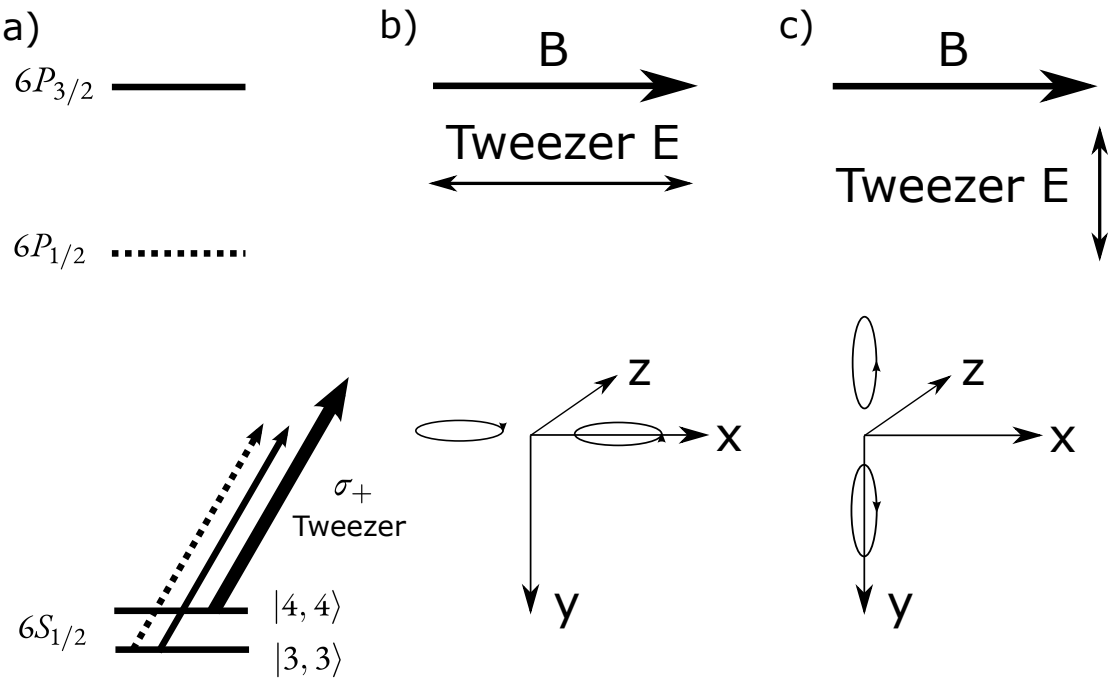

Figure 2.10: (a) An intuitive picture for the origin of the vector light shift in cesium. The circular polarization, σ_+, of the tweezer couples the $|4,4\rangle$ state only to a $|5,5\rangle$ state which is only available at the D2 line, which is at 852 nm. The $|3,3\rangle$ state couples to both the D1 line and the D2 line, which are at vastly different detunings. (b) The polarization [224] at the focus of a tweezer provided that the tweezer is at a horizontal polarization. The tweezer propagates in the z direction, and the effective B field from the circular polarization points in the y direction and the gradient is along the x direction. (c) Same as (b) but when the tweezer polarization is in the vertical direction. In this case, the effective B field is in the x direction, and the gradient is along the y direction.

After this dichroic, the polarization of the tweezer is cleaned up by a polarizing beam splitter cube. Polarization cleanup is critical for avoiding vector light shifts on the $|4,4\rangle$ to $|3,3\rangle$ transition in cesium. Figure 2.10a shows the level diagram for cesium. This light shift arises from the fact that with σ_+ light, the $|4,4\rangle$ state is only connected to the $6P_{3/2}$ state while the $|3,3\rangle$ state has matrix element with both $6P_{1/2}$ and $6P_{3/2}$. Thus, with the large fine structure present in cesium, there is a large detuning discrepancy with the states in each manifold and thus a large difference in the

contribution of each state to the AC Stark shifts on the ground state levels.

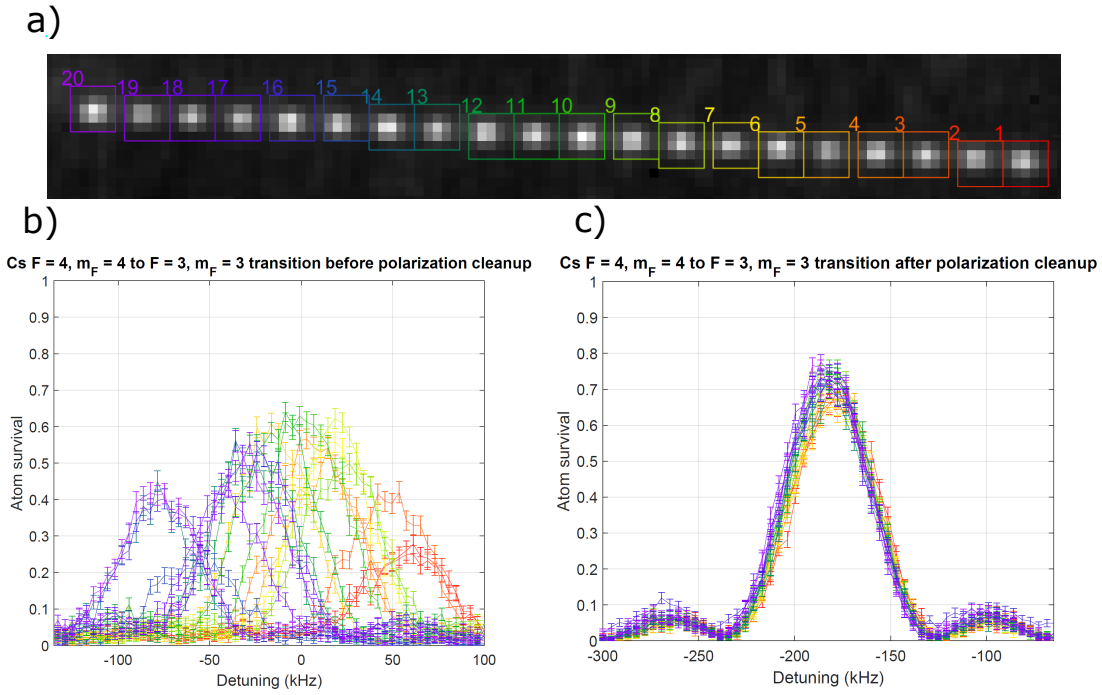

Figure 2.11: (a) An array created by an acousto-optical deflector with color-coded site labels. (b) The location of the $|4, 4\rangle$ to $|3, 3\rangle$ resonance in cesium as a function of the site. (c) The same data as (b) after cleanup of the tweezer polarization.

Figure 2.11 shows this light shift and its variance across an array formed from an acousto-optic deflector. This shift can be on the order of a few hundred kHz, and shows a clear gradient from one side of the array to the other. We believe this gradient of the circular polarization arises from some polarization changing optic that depends on angle. To avoid these issues, we cleanup the polarization as close to the microscope objective as possible, which greatly reduces the polarization variation across the array.

The use of horizontal polarization as the preferred polarization of our tweezer array is also important. The focus of a tweezer has a polarization gradient [224]. Suppose the tweezer propagates in

the z direction and has a linear polarization. The polarization gradient is along the direction of the linear polarization and the circular polarization is in the plane of the tweezer propagation and the linear polarization (so either xz or yz plane) as shown in figure 2.10b and c. We want the effective B field created from this circular polarization to add in quadrature (be perpendicular) to the bias field. This minimizes the state dependent energy shift within the tweezer by reducing the effect the tweezer focus has on the overall local polarization. This condition is satisfied with a horizontally polarized tweezer but not with a vertically polarized tweezer. We note that this allows one to combine the SLM and AOD tweezer light using a polarizing beam splitter cube as long as the SLM tweezer is on the transmission port of the cube. This requirement is most important for the tweezers in which we perform Raman sideband cooling which are the SLM ones. It matters less for the AOD tweezers, which are used only for atom rearrangement. In our experiment, we are geometrically constrained, so we choose to combine the cesium SLM and AOD tweezers using the aforementioned dichroic.

After the polarization cleanup, the light then proceeds through a combining dichroic (DMLP900L) from Thorlabs which allows through our 1038 and 1064 nm tweezers while reflecting 616 nm, our sodium SLM tweezer wavelength. Then, the light proceeds through a custom imaging dichroic from Layertec which allows 1038, 1064 and 616 nm through while reflecting 589 and 852 nm which are our two imaging wavelengths.

The sodium SLM tweezer light starts from a C40APC-A fiber collimator from Thorlabs at approximately 10 mm. The polarization is cleaned and the light is picked off by a beamsplitter and sent to a photodiode for intensity stabilization. The light is then sent to the SLM which operates in reflection and sent through a 4f telescope to get expanded. The light is combined with the Cs SLM and AOD tweezers and then sent through our microscope objective.

2.4.3 AOD Beampaths

An acousto-optical deflector consists of an optically transparent crystal, in which a sound wave propagates through it. The sound wave creates a spatially periodic variation in the refractive index. This effect creates a grating which can diffract an incident laser beam according to the formula

$$\theta = \frac{\lambda f}{v} \tag{2.15}$$

where λ is the wavelength of the laser beam, f is the RF frequency of the acoustic wave and v is the acoustic velocity. To obtain larger deflection angle, we typically use shear mode acousto-optic deflectors (AA Optoelectronics DTSX-400-1030) which is a lower velocity mode (650 m/s) compared to typical longitudinal mode AOMs (4200 m/s). These shear mode deflectors require a particular linear polarization and rotates the polarization by 90 degrees.

Figure 2.9 shows our AOD tweezer beam path in maroon red. The AOD tweezer light starts from a custom collimator from Oz Optics with a beam diameter around 2 mm. The beam has its polarization cleaned up and then is picked off for intensity stabilization. The light then passes through two acousto-optical deflectors placed along each direction to deliver deflection in the vertical and horizontal direction. In order for the effect of the first AOD to purely be a deflection (and thus a position change after the objective lens), we place a $4f$ telescope (using 50 mm lenses) to image the beam from the vertical to the horizontal AOD. This beam is then expanded using another $4f$ telescope ($f_1 = 100$ mm, $f_2 = 750$ mm). This $4f$ telescope which expands the beam by a factor of 7.5 also reduces the angular deflection by this same factor. This limits our total angular deflection and thus the range of positions our AOD traps can access.

These AODs need to be carefully aligned for high diffraction efficiency across a large bandwidth. If it is aligned for high diffraction efficiency at a single frequency, it may not have high efficiency at another frequency. Thus, it should be aligned with a frequency ramp and the light (whose deflec-

tion is changing) subsequently focused onto a photodiode.

2.5 Atom Rearrangement

Loading atoms in optical tweezers is stochastic, due to light assisted collisions[197,196] which eject atoms pairwise. Red-detuned cooling light (such as light typically used in atomic MOTs) will cause atom pairs to be excited to a molecular state, which can roll down a potential well causing pairwise loss and a loading rate around 50%. However, by using blue-detuned light, the light excites the atom pair to a dissociative potential where the energy release can be carefully controlled with the laser detuning. These techniques have yielded loading rates beyond 80%[94,37,4,116,205,26]. In either case, stochastic loading poses a challenge for experiments in quantum computing and quantum simulation which require defect-free arrays. This problem has been solved by real-time imaging of atoms and subsequently moving atoms with mobile traps, created from an acousto-optical deflector, to the desired locations[75,135,14]. Atom rearrangement requires fast atom-imaging as well as the ability to dynamically determine the required atom moves in real time. Any time that the atom spends while interpreting an image and deciding what to do is wasted time where the atom is vulnerable to background gas collisions. Our approach attempts to minimize this time while maintaining as much flexibility as possible.

2.5.1 Hardware

To move atoms dynamically and quickly, we use the aforementioned shear-mode acousto-optical deflector (AOD). Driving the acousto-optical deflector requires inputting multiple frequencies. As documented in a previous thesis of our group[243], our computer control system's RF generation capabilities consist of a FPGA which controls DDS chips that output single frequencies. Combining the outputs of multiple DDS chips can quickly become cumbersome and is a poor allocation of

resources on our control system. Hence, we use an arbitrary waveform generator (AWG), the Spectrum Instrumentation M4i.6622-x8, to generate our AOD control signal. We operate the AWG in first-in-first-out (FIFO) mode. In this mode, the AWG continuously runs through a buffer, outputting 16-bit samples at its sampling rate. We need to continually fill this buffer with new samples. This allows the greatest flexibility in the programmed waveforms, and allows them to be determined arbitrarily in real time. However, the computational cost is quite hefty. At the maximum sampling rate of 625 MS/s, we need to generate and transfer over a gigabyte of data a second. We describe our software architecture in section 2.5.2.

Another challenge that using the AWG presents is synchronization. For our experiment, the primary clock of the experiment is determined by the FPGA. The FPGA maintains the timing of all DDS and TTL pulses, which it itself controls, and it clocks our National Instruments analog output device (PCI-6733). We need to synchronize the output of the FPGA with the AWG. Precisely, the AWG needs to know which sample in its buffer corresponds to the FPGA $t = 0$ for a given sequence.

To do this, we use the AWG's feature to output a sample clock, where each cycle corresponds to an output of a new sample[¶]. The goal is to use a counter to keep track of each sample of the AWG, and to synchronize the sample count with a FPGA trigger. The counter we use is within an Arduino Nano which also allows simple interfacing with a computer via a serial connection. The details of the circuit are described and shown in figure 2.12.

In our case, at our maximum sample rate of 625 MHz, the clock signal is divided down by 128 to approximately 4.88 MHz, which can be counted by our Arduino Nano (16 MHz clock speed). This limits the theoretical synchronization accuracy to about 200 ns. Once the start trigger is successfully mapped to a buffer sample, the FPGA and the program agree in advance that $t = 0$ of the sequence

[¶]Precisely, according to the manual of the device, this output clock is sample rate/8, if the sampling rate is greater than 71.68 MHz, and is sample rate/4 if less.

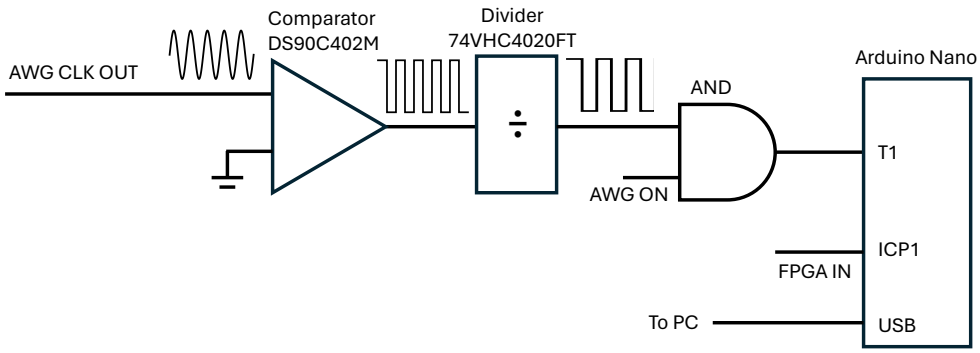

Figure 2.12: This circuit synchronizes the Spectrum Instrumentation AWG with our FPGA via an Arduino. The clock signal out of the AWG is a sine wave that is about 800 mV peak-to-peak at a frequency of 625 MHz/8 = 78.125 MHz. We convert this into a "digital" signal with a comparator. Then, a clock divider (or counter) divides the signal by a factor of 16, so that it is slower than the clock speed of the Arduino. To count edges on the Arduino, we configure hardware Timer 1 (T1) to perform the counting in hardware and not in software. The FPGA start trigger is sent to the ICP1 pin, which latches the current value of T1 (while allowing T1 to continue counting), and runs an interrupt service routine in software. The interrupt service routine then writes the clock count to the serial port which is connected to the computer. An interrupt service routine is also run each time the 16 bit hardware counter overflows to increment a software counter. The software variable allows for an arbitrary number of bits in our counter, and for us we use a 32 bit integer.

will be x ms after the trigger. We call x the synchronization latency of our system. x cannot be zero, since this would require the AWG program to begin outputting the real sequence immediately upon receipt of the trigger. The latency is determined by two factors: the serial communication time between the Arduino and the program that populates the FIFO buffer of the AWG, and the computational time required to pre-fill the buffer as much as possible to prevent buffer underrun. The first

limitation is fundamental and is on the order of 5 ms. However, faster methods than serial communication may be used to speed this up. The second limitation depends on the complexity of the sequence, and the computational capabilities of our AWG computer. In practice, we use latencies of around 25-100 ms for most rearrangement tasks described in this thesis.

2.5.2 Software on the AWG side

The software additions required to implement rearrangement consists of two major components: code to operate the AWG device itself, and code to program rearrangement sequences in a user-friendly and efficient way on the frontend. We first discuss the code that operates the AWG device. This code runs on an Ubuntu system, which has the AWG installed on a PCIe slot, and the aforementioned synchronization Arduino connected via serial port.

We parameterize our arbitrary waveforms as composed of virtual channels, each of which has a frequency, amplitude and phase. These frequencies, amplitudes and phases can be ramped or simply just set at specific times. Each virtual channel is calculated using AVX512 instructions, and thus are calculated in parallel 64 bytes (32 samples) at a time. Virtual channels that are calculated on the same CPU thread compose a `Stream`. Multiple streams are summed together in a `StreamManager` and delivered to a single physical output via a `Controller` class. Our device has 4 physical output channels. Using multiple output channels requires faster data generation capabilities, so we have used at most 2 physical output channels in the experiments of this thesis.

Now, we describe the data flow in our program. The `Controller` configures the AWG's internal hardware buffer and also a separate software buffer that the AWG driver automatically extracts from. The `StreamManager` has a buffer where it adds up results from its constituent `Stream`s. Each `Stream` also has a buffer where it stores its results. The sum of all these buffers sets a lower bound on the synchronization latency. In other words, since it is unknown when a trigger might arrive, these buffers are constantly filled (to prevent underrun) and thus any "real" sequence data

needs to follow after the already computed data. Notice that during a sequence, the needed samples are completely known, which allows us to arbitrarily fill the buffer without any latency issues. We do allow a larger buffer to be filled during a sequence, but throttle the filling of this buffer in software when awaiting a sequence. When we operate with 25(100) ms latency, the total relevant buffer size is 8(40) megasamples per physical output, which is a theoretical latency of 13.4(67.1) ms.

To communicate with the `Stream`s, especially from a remote computer, we run a `Server` written using ZeroMQ as the main network communication library. The server accepts sequences, which are a list of commands, and then passes these commands through the `Controller`, which distributes them to the correct `StreamManager`. The `StreamManager` then shuttles them to the correct `Stream`. The `Server` also alerts the requesting computer when a sequence is finished. The key components of this software package are summarized in figure 2.13.

Currently, as mentioned above, we calculate the entire waveform in real-time. At the very least, for every sample, the phase of each channel needs to be advanced (according to its current frequency) and its value calculated. If we program a channel to perform an arbitrary frequency or amplitude ramp, we also need to calculate the new value of the frequency and amplitude at each sample. Thus, the highest computational costs occur when channels need to be ramped, and buffer underrun is more likely to occur during longer ramps. When we do not ramp any channels, on our Intel Core i9-9980XE processor, we can output approximately 64 frequencies on a single output with a total of 16 threads at max buffer size. In typical daily operation, we operate with two outputs[‖], with around 12 frequencies on one and one frequency on the other. To reduce the latency to 25 ms, we find it helpful to reduce the sampling rate to 500 MS/s.

Now, we will discuss future improvements to this system. A hybrid approach involving precomputing and on-the-fly computing can save some resources for truly dynamic situations. For instance, if particular tones just need to be on, these can use precomputed waveforms while dynamically de-

[‖]One for a horizontal rearrangement tweezer and the other for our cesium Rydberg beam

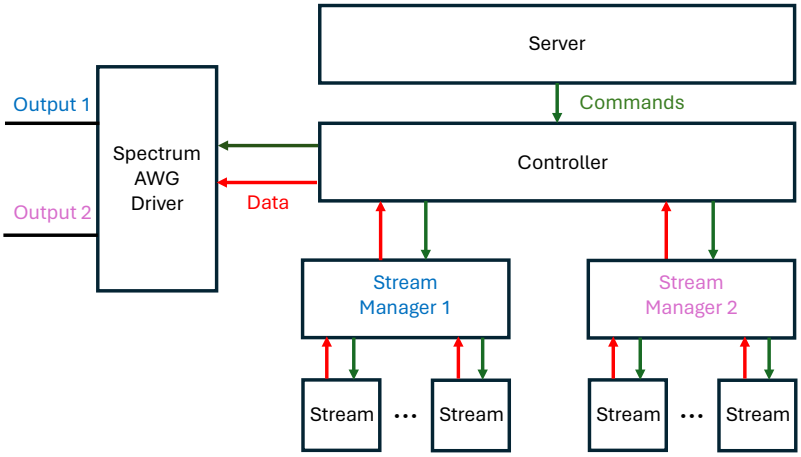

Figure 2.13: Architecture of the AWG Control Software. The `Server` receives commands over a network, and sends them to the `Controller`. The `Controller` distributes configuration commands directly to the Spectrum AWG Driver, and sequence commands to `StreamManagers` which correspond to each physical output. The `StreamManager` sums up data generated by `Streams`. Data is then sent by the `Controller` to the Spectrum AWG Driver which handles output.

termined ramps are computed on the fly. Spectrum Instrumentation has implemented DDS cores on their AWGs which can also be utilized to relieve the load on the CPU. Lastly, a GPU is ideal for these sort of repetitive parallelizable computational tasks. However, the main concern with using a GPU is the required communication bandwidth between the CPU and GPU. As we will discuss in the next section, arbitrary frequency and amplitude ramps are currently calculated on the CPU, and these results will need to be sent to the GPU for each sample, requiring gigabyte per second transfer speeds. Similar in spirit to the hybrid precomputation approach, the GPU may be reserved for non-ramps, while the CPU continues to handle ramps.

2.5.3 Software on the user side

Our full control system and user interface has been detailed in a previous thesis in our group[243]. I will briefly summarize the interface here. An experimental sequence is a collection of pulses on all the channels of our experiment. Channels include the frequency and amplitude of DDS pulses, the analog output of a National Instruments DAC, or the frequency, amplitude and phase of a virtual channel on the AWG. A pulse can be a simple instantaneous change of the value or a complicated ramp that extends over a certain amount of time.

Previously, sequences were fully deterministic, so they would be written and then converted into commands for the various devices. These commands would be executed independent of MATLAB and controlled by the FPGA for synchronization and precise timing. However, with atom rearrangement, each sequence will now depend on the exact configuration of stochastically loaded atoms. It would be infeasible to calculate a sequence for every configuration of loaded atoms, so the sequence will need to receive feedback in real time on what it should do. To do this, we introduce the concept of a "basic sequence". A full experimental sequence may comprise of multiple basic sequences. Between each basic sequence, program control is returned to MATLAB, so MATLAB code can run during this time. Note that since MATLAB code does not run completely predictably (from our perspective), the timing between basic sequences is not strictly controlled and cannot be relied on. If the AWG is involved, each basic sequence must be separated by at least the synchronization latency of the AWG. For us, the return to MATLAB is necessary in order to grab images from the camera and communicate with the National Instruments DAC**, both of which currently interface with MATLAB.

In this case of atom rearrangement, images are grabbed in between basic sequences, and then the

**This is certainly unnecessary, and in fact some 20-30 ms of latency arises from using MATLAB to communicate with the National Instruments card. Using the FPGA to directly interface with the camera is also being explored.

rearrangement algorithm is calculated in MATLAB and the rearrangement sequence is determined. In principle, the rearrangement sequence can then be created, compiled and ran much like any other sequence, without any significant change in the user interface. However, in this paradigm, sequence creation and compilation occurs in between basic sequences, while atoms are sitting idly in traps. Thus, we need to prioritize speed in between basic sequences to prevent atom loss or heating.

To do this, we note that most components of the sequence are already known regardless of the loaded atom configuration. For instance, if we are performing a Rydberg experiment, Rydberg excitation pulses after rearrangement are known and can be precompiled already. In other words, we would like to precompile everything that we already know before any atom loading as much as possible. We introduce the concept of a "global", which is a dynamic variable that can be set in between basic sequences. Globals can represent a variety of concepts, such as the length of pulses, the set value of pulses, parameters of a ramp or a switch for whether a pulse occurs. In this paradigm, the user needs to create a scaffold of all possible rearrangement sequences, and the appropriate globals are filled after the image is obtained.

For the implementation, globals are assigned to particular memory addresses in a piece of precompiled object code, which is compiled and managed by LLVM. This object code also precompiles any ramp functions, which is much faster than interpreting them on the fly. Note that LLVM supports compiling for a non-host target system. For the AWG, the code is compiled on the host computer (which is typically a Windows computer), and then sent over the network to the AWG computer (typically an Ubuntu computer), which executes it when needed. The complete implementation details and a detailed API is out of scope for this thesis.

2.6 Optical Pumping

In our experiments, we often need to perform state preparation. For instance, to perform Raman sideband cooling, the atoms need to be prepared in a particular hyperfine state. Our Rydberg excitation scheme is also hyperfine-state selective requiring high fidelity state preparation. Our optical pumping schemes have been described in previous theses and are relatively standard, but I'd like to reiterate here for completeness and to also provide some practical tips on how to optimize the procedure.

Typically, we want to perform F and m_F level pumping; in other words, we'd like to prepare the atoms in a single F, m_F state, typically $|F = 4, m_F = 4\rangle$ for cesium and $|F = 2, mF = 2\rangle$ for sodium. This can be achieved by shining σ_+ light on the $F = 4$ to $F' = 4$ and $F = 2$ to $F' = 2$ transition in cesium and sodium respectively along with a repumper to address the $F = 3$ and $F = 1$ states. Due to the lack of a $m_F = 5 (m_F = 3)$ state in cesium (sodium), the $|4, 4\rangle$ and $|2, 2\rangle$ states are dark states to this drive. Hence, we would expect accumulation of cesium and sodium atoms in these states. While these conditions can technically be achieved on both the D1 and D2 transitions in sodium and cesium, the D1 transition always leads to better results, due to its lack of a $F' = 5$ and $F' = 3$ state, which contains $m_F = 5$ and $m_F = 3$ that limit how dark the final state is. In both these atoms on the D2 line, this transition is detuned. However, the detuning is smaller in sodium (only about 60 MHz) compared to cesium (about 250 MHz), so this is a limitation in sodium but not cesium. Thus, in sodium, we perform optical pumping on the D1 line, while providing repump on the D2 line.

This procedure requires a quantization magnetic field to well-define these states and also purely polarized light. We use a roughly 8.8 G bias field along the long direction of our glass cell. Good optical pumping thus relies on both the circularity of the light and the alignment of the light propagation axis to the direction of the bias field. The circularity is achieved using a good polarizer (such

as a Glan Taylor) followed by a quarter wave plate (sometimes a half waveplate is also used to be able to account for more generic polarization changes caused by subsequent optical surfaces such as the glass cell itself). Alignment of the beam can be done with mirrors, but it's easiest to change the bias field slightly with our other bias coils.

Any sort of alignment or optimization procedure requires a metric to optimize on. We can perform hyperfine state selective detection by applying resonant light with the $F = 4$ to $F' = 5$ and $F = 2$ to $F' = 3$ transitions in cesium and sodium. In this case, the light can heat up atoms in $F = 4$ and $F = 2$ and push them out of the trap. Atoms in $F = 3$ and $F = 1$ are left untouched. A subsequent (non) hyperfine-state selective image can determine whether there was an atom in $F = 4$ or $F = 2$. The absence of an atom is interpreted as an atom in the $F = 4$ ($F = 2$) state in cesium (sodium), while the presence of an atom is interpreted as an atom in $F = 3$ ($F = 1$).

The first coarse diagnostic that can be performed is to determine whether atoms are being lost under application of optical pumping light. If atoms are lost, this implies that there is no dark state the atoms are being pumped into, and the continual photon cycling leads to heating and ejection from the trap. The next diagnostic is to perform a depumping measurement. In this case, atoms are first optically pumped into some state (hopefully the correct one!), and then are exposed to optical pumping light again without repump. In the ideal case, there will be no excess depumping out of $F = 4$ or $F = 2$ by the optical pumping light. Upon hyperfine state selective detection, all atoms remain in $F = 4$ or $F = 2$. However, if the polarization is not correct or any parameter of the optical pumping is not ideal, there will be accumulation of population in the $F = 3$ and $F = 1$ levels. The time scale of such depumping can be optimized.

This time scale of depumping depends on factors such as the exact power being used in the optical pumping procedure, thus as a quantity on its own, it does not hold much value. We compare it to the time scale of depumping when the atoms are prepared in $|F = 4, m_F = 3\rangle$ and $|F = 2, m_F = 1\rangle$ instead. In this case, some of the atoms should quickly depump without any repump light. State

preparation into $|4,3\rangle$ and $|2,1\rangle$ is achieved with two Raman pulses transferring atoms from $|4,4\rangle$ ($|2,2\rangle$) to $|3,3\rangle$($|1,1\rangle$) and subsequently to $|4,3\rangle$ and $|2,1\rangle$. The ratio of these two quantities is called the *depumping ratio*, and we achieve around 10,000 for both species.

Note that these above metrics only work if the initial state preparation is good enough at preparing most of the atoms into $|4,4\rangle$ and $|2,2\rangle$. The detection method of pushing out $F = 4$ and $F = 2$ can only determine whether our atoms are in the $F = 4$ or $F = 2$ manifold but not specifically which hyperfine state the atoms are in. To effectively perform m_F state resolved imaging, we use a pair of Raman beams to transfer atoms out of $|4,4\rangle$ ($|2,2\rangle$) into $|3,3\rangle$ ($|1,1\rangle$). This can be achieved, since in a magnetic field, the various transitions between the hyperfine states are frequency resolved. Subsequently $F = 4$ and $F = 2$ pushout is performed, and surviving atoms must have come from the $|4,4\rangle$ and $|2,2\rangle$ states[††].

Another technical note of interest is that when setting the polarization of the optical pumping beams, it is sometimes hard to distinguish whether σ_+ light or σ_- light is being utilized. In the former case, atoms are prepared in $|4,4\rangle$ ($|2,2\rangle$) while in the latter case, atoms are prepared in $|4,-4\rangle$ ($|2,-2\rangle$). To distinguish between these possibilities, one can measure the optimal blast detuning (pushout from $|4,4\rangle$ to $|5,5\rangle$ or $|2,2\rangle$ to $|3,3\rangle$ in cesium and sodium respectively) as a function of the magnetic field. Depending on whether the state that the atoms are pumped to are aligned or antialigned with the field, the optimal blast detuning either goes to higher or lower frequency.

2.7 Summary and Outlook

In this chapter, we discussed the basic setup of our apparatus, and detailed our efforts to scale up our optical tweezer arrays from single atoms to a hundred and more. In particular, while cesium was more or less a straightforward task, sodium required the implementation of D1 gray molasses and

[††]Technically, these atoms could also be coming from other m_F levels in $F = 3$ and $F = 1$ not including $m_F = 3$ and $m_F = 1$.

a magic wavelength tweezer to avoid deleterious light shifts. Larger tweezer arrays also required the use of new (to us) technology including SLMs and shear mode AODs. The SLM is quite a robust device but a flexible codebase is required to unleash all its capabilities. The shear mode AODs were an absolute pleasure to work with, due to their high efficiency and ease of alignment. With larger arrays, inhomogeneities became a serious problem. Special care of the polarization and careful tuning of the spot intensities (aided by experimental measurements) are required to acquire accurate collective statistics. Lastly, such larger arrays can only be taken advantage of with the successful implementation of atom rearrangement. Rearrangement requires real-time feedback and thus entirely new fast hardware (AWG) and new software paradigms to implement flexibly and efficiently.

Although our apparatus has served us and my PhD quite well, there are many possible upgrades that can be implemented in the future. Our vacuum lifetime of 6 seconds is quite a limitation especially for larger arrays. A 100 ms sequence times results in a per-atom loss probability of $e^{-0.1/6} = 0.9835$ resulting in defects in our array. Longer vacuum lifetimes have been achieved by using two-chamber designs, where the higher pressure source chamber is separated from a science chamber where atoms are trapped. The atomic source, which is created in the source chamber, is a 2D MOT[69], where it can be pushed along the non-confining axis into the science chamber. Further sputtering of all metal surfaces with titanium from titanium sublimation pumps can achieve 23 minute vacuum lifetimes at room temperature[150]. Titanium is very reactive so it is able to bind with residual gas in the vacuum chamber resulting in very low pressures. Cryogenic cooling of the vacuum chamber further reduces outgassing and can result in 100 minute vacuum lifetimes[202]. A two-chamber design for our apparatus can greatly improve the vacuum lifetime.

Now, we have the scene set for observing quantum phenomena with arrays of individually trapped atoms! In the next chapter, we will excite these atoms to the Rydberg state and observe their coherent interactions.

3

Coherent Rydberg Excitations of Cs

3.1 Introduction

Neutral atoms in optical tweezers have been used to study a range of quantum phenomena from tunneling [122] to spin-exchange interactions [121]. Both these studies required bringing two tweezers very close to each other or merging two atoms into the same tweezer. A wealth of additional phenomena can arise when these atoms have long-range interaction, and furthermore, if the geometries

of these tweezer arrays can be varied. As we saw in the previous chapter, we have extensive capabilities of creating arbitrary-geometry optical tweezer arrays. However, atoms have minimal long-range interaction unless they are excited to highly polarizable Rydberg states, where there are (typically) van der Waals interactions between the atoms. In section 3.2, we lay out some of the key properties of Rydberg atoms and their interactions. Subsequently in section 3.3, we discuss the lasers required to excite cesium atoms to the Rydberg state. In section 3.4, we present data exhibiting coherent excitation of cesium atoms to the Rydberg state and the technical challenges involved in such an excitation. Finally, in section 3.5, we probe the interactions between two cesium Rydberg atoms, and set the stage for many-body experiments with Rydberg atom arrays.

3.2 Rydberg Atom Theory

Rydberg states are highly excited electronic states of atoms. For alkali atoms, they are labeled as nL_j, where n is the principal quantum number, $L = S, P, \ldots$ is the angular momentum quantum number, j is the total angular momentum quantum number, where $\mathbf{J} = \mathbf{L} + \mathbf{S}$. Note that hyperfine structure is typically negligible in Rydberg states. The energies of Rydberg states scale as roughly $-1/n^2$, given by the approximate formula

$$E_{n,l,j} = -\frac{\mu e^4}{8\varepsilon_0^2 h^3 c}\frac{1}{(n-\delta_{n,l,j})^2}, \tag{3.1}$$

where μ is the reduced mass between the nucleus and the electron, e is the elementary charge, ε_0 is the permittivity of free space, h is Planck's constant and c is the speed of light in vacuum. $\delta_{n,l,j}$ is the quantum defect [180] which depends on the atom and characterizes the effect of the core electrons of the alkali atom on the valence electron. The quantum defect itself can be expanded into powers of $1/(n-\delta)^2$

$$\delta_{n,l,j} = \delta_0 + \frac{\delta_2}{(n-\delta_0)^2} + \frac{\delta_4}{(n-\delta_0)^4} + ..., \tag{3.2}$$

and subsequently fit to experimental data [146].

The wavefunctions for these Rydberg states are separable into radial and angular parts. The angular part, neglecting spin-orbit coupling, is given by spherical harmonics, and thus the matrix elements between these states for operators such as the dipole operator are given by Clebsch-Gordan coefficients or Wigner symbols. The reduced radial wavefunction, $u(r) = rR(r)$, for a hydrogen atom, satisfies

$$\left(-\frac{\hbar^2}{2\mu}\frac{d^2}{dr^2} + \frac{\hbar^2 l(l+1)}{2\mu r^2} - \frac{e}{4\pi\varepsilon r}\right) u(r) = Eu(r). \tag{3.3}$$

To account for core electrons, the radial equation is modified to the following form [152]

$$V(r) = -\frac{1}{4\pi\varepsilon_0}\left(\frac{Z_l(r)}{r} - \frac{\alpha_c}{2r^4}\left(1 - e^{-(r/r_c)^6}\right)\right), \tag{3.4}$$

where α_c is the core polarizability, r_c is a cutoff radius determined by a fit and $Z_l(r)$ is an effective charge given by

$$Z_l(r) = 1 + (z-1)e^{-a_1 r} - r(a_3 + a_4 r)e^{-a_2 r}, \tag{3.5}$$

where z is the nuclear charge, and a_1, a_2, a_3, a_4 are given by fits. This radial equation can be numerically solved and luckily, packages like the Alkali Rydberg Calculator (ARC) [208] or PairInteraction [232] automate these calculations for us. In this thesis, we primarily use the ARC package to perform calculations.

3.2.1 Single Rydberg Atom Properties

With these radial wavefunctions, we can calculate a slew of useful quantities, such as how the transition strength between states, the DC polarizability and the lifetime of Rydberg atoms scale with principal quantum number. All these properties rely on the calculation of dipole matrix elements and depend on the energies of the various states, obtainable via equation 3.2. We can use a semiclassical argument to determine the scaling of the dipole matrix element with principal quantum number.

For roughly determining how the size of the atom scales with principal quantum number, we assume that the electron is in an orbit at a distance r from the nucleus. Equating the centripetal force to the Coulomb force results in

$$\frac{mv^2}{r} = \frac{e^2}{4\pi\varepsilon_0 m r^2}, \tag{3.6}$$

from which we can see that $v \propto \frac{1}{\sqrt{r}}$. Then, we apply semiclassical quantization of the angular momentum

$$mvr = n\hbar, \tag{3.7}$$

which results in $r \propto n^2$. Dipole matrix elements between highly excited Rydberg states with $\Delta l = \pm 1$, are roughly proportional to r, so they should exhibit a n^2 scaling as shown in figure 3.1a.

An external electric field couples to a dipole via the following Hamiltonian

$$H_{\text{DC Stark}} = -\mathbf{d} \cdot \mathbf{E} \tag{3.8}$$

which is an odd operator in space. Thus, states of definite parity, i.e. with definite angular momentum quantum number, have no first-order response to the field, since

$$\langle nlm|H_{\text{DC Stark}}|nlm\rangle = 0. \tag{3.9}$$

The lowest-order response to an external electric field is quadratic, arising from 2nd order perturbation theory. The polarizability α is defined as the coefficient of this quadratic response in the following way

$$\Delta E = \frac{1}{2}\alpha E^2 \tag{3.10}$$

where we note in slightly confusing notation that the E on the left hand side means "energy" and the E on the right hand side means electric field strength as in equation 3.8. The polarizability can be calculated from second-order perturbation theory and thus has the form

$$\alpha \sim \sum_{n'l'm'} \frac{\langle nlm|H_{\text{DC Stark}}|n'l'm'\rangle^2}{E_{nlm} - E_{n'l'm'}} \tag{3.11}$$

consisting of a squared matrix element and an energy denominator. The squared matrix element is a dipole matrix element squared so it will be proportional to $(n^2)^2 = n^4$, while the energy denominator is proportional to $1/n^3$ (since it is the difference or derivative of a energy which scales as $1/n^2$). Thus, the polarizability should scale as n^7, as shown in figure 3.1b.

The polarizability calculations in figure 3.1b were not perturbative in the form of equation 3.11, but rather involve a "full diagonalization" of the $-\mathbf{d}\cdot\mathbf{E}$ Hamiltonian, as a function of E. Subsequently, the energy eigenvalues are fit to a quadratic dependence on E at low fields. Since these methods are numerical in nature, the state space is limited to only those states $|n'l'j'\rangle$ with $|n'-n| \leq 5$, and $l' \leq 20$, where these values are chosen to ensure convergence.

The next important scaling we turn to is Rydberg lifetime. For a two level system, the spontaneous emission rate can be calculated from the interaction of this system with the electromagnetic

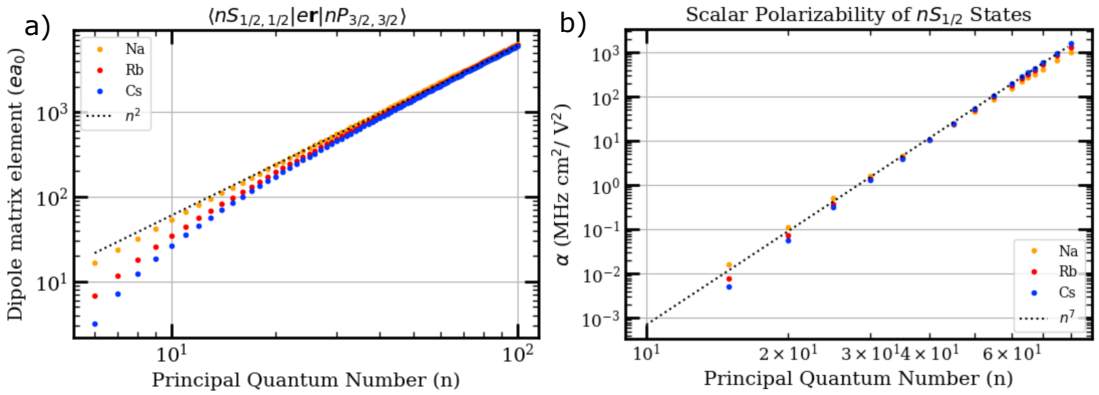

Figure 3.1: (a) The transition dipole moment between Rydberg states $nS_{1/2}$ and $nP_{3/2}$ in units of ea_0, where e is the electron charge and a_0 is the Bohr radius, as a function of principal quantum number n for sodium, rubidium and cesium. Note that this is the full transition dipole moment and is calculated on the stretch transition from $m_J = 1/2$ to $m_j' = 3/2$. The n^2 line is a guide to the eye. (b) The scalar polarizability of different $nS_{1/2}$ states in the alkali atoms sodium, rubidium and cesium. See the text for the details of the calculation. The n^7 line is a guide to the eye.

field modes of vacuum [234], resulting in

$$\Gamma = \frac{\omega^3}{3\pi\varepsilon_0\hbar c^3} |\langle i|e\mathbf{r}|f\rangle|^2. \tag{3.12}$$

Importantly, this spontaneous emission rate contains a ω^3 dependence partially coming from the density of states of vacuum modes and a $|\langle i|e\mathbf{r}|f\rangle|^2$ dependence. In a multi-level system, spontaneous emission can occur via equation 3.12 between the initial state and all states at lower energy. For Rydberg states, the largest transition dipole moments exist between nearby Rydberg states (see Figure 3.2a), whose energy spacings are much smaller than the typical optical frequency scales of the lower principal quantum number states. Hence, somewhat counterintuitively, the lifetime gets longer at higher Rydberg states, exactly due to the decreasing transition frequency with the nearby states (and the frequency enters with a cubic dependence in the transition rate). One way to obtain a scaling is to notice that for transitions to nearby states, $\omega \propto 1/n^3$, while the matrix element

$\langle i|e\mathbf{r}|f\rangle \propto n^2$, resulting in $\Gamma \propto 1/n^5$ and the lifetime $\tau = 1/\Gamma$ proportional to n^5. However, direct calculations indicate that this scaling only holds for so-called "circular" Rydberg states [109] which are those with $l = n - 1$ and only have limited decay pathways, since $\Delta l = \pm 1$. The lifetime of these states can approach several tens of ms, which is ideal for quantum computing applications [56]. The lifetime of non-circular states such as $l = 0$ states tends to scale more like n^3 due to effects from transitions to a large range of principal quantum number states. These lifetimes were calculated by summing up all the transition rates to all lower energy states and is shown in figure 3.3.

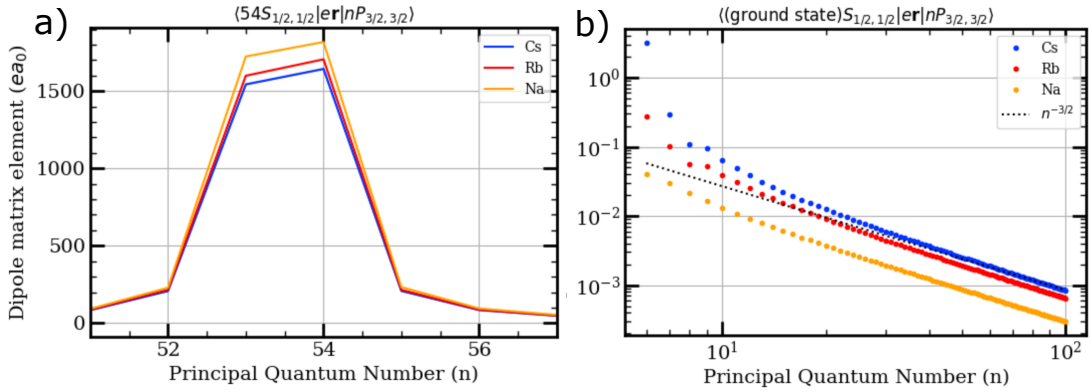

Figure 3.2: (a) Dipole matrix elements between the $54S_{1/2}$ state to $nP_{3/2}$ states in cesium, rubidium and sodium. These matrix elements are much stronger between the nearest two principal quantum numbers. The sodium, matrix element is a bit larger due to its smaller quantum defect, indicating it being a "higher" excited state. (b) Dipole matrix elements between the ground states of cesium ($6S_{1/2}$), rubidium ($5S_{1/2}$) and sodium ($3S_{1/2}$) and their Rydberg states. The high n scaling follows roughly $n^{-3/2}$, which is plotted as a guide to the eye.

In addition to spontaneous emission, electromagnetic modes in space are often populated by blackbody radiation photons, where the power density per unit frequency, area and solid angle, is given by

$$B_\nu(T) = \frac{2h\nu^3}{c^2} \frac{1}{e^{h\nu/k_B T} - 1}. \tag{3.13}$$

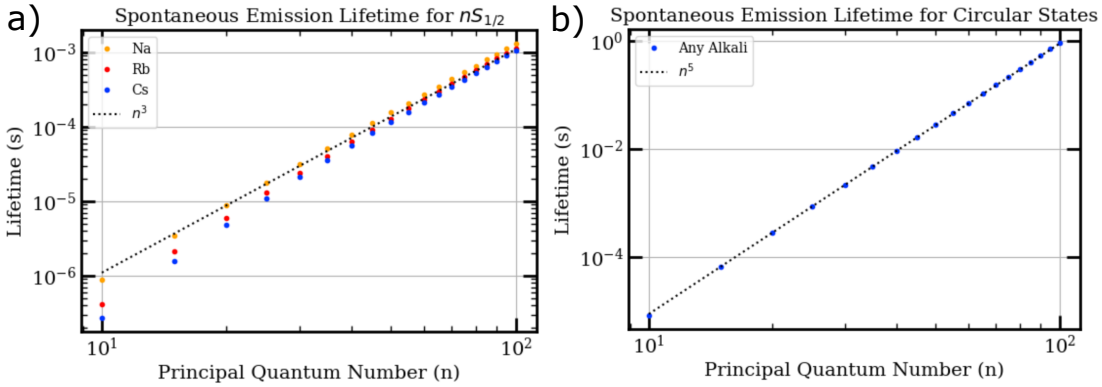

Figure 3.3: (a) The spontaneous emission lifetime for $nS_{1/2}$ states. The n^3 line serves as a guide to the eye. (b) The spontaneous emission lifetime for circular Rydberg states, which are states with $l = n - 1$. These scale with n^5, and in general are more longer lived than their non-circular counterparts due to the fact that its decay channels are all to nearby states with lower frequency differences. Note that in ARC's model, the circular states are no different between different alkali atoms, emphasizing that so far away from the core, the number of core electrons and protons do not matter. In other words, these states are the most hydrogenic, and are independent of exactly which alkali we are discussing. Thus, the calculated lifetimes are the same for any alkali atoms.

Stimulated transitions due to blackbody radiation also affect the lifetime, especially for Rydberg states, where the transitions start entering the GHz regime. We can include transitions (both absorption and emission) stimulated by the blackbody radiation in our calculations. We consider absorption up to 20 principal quantum numbers above the state of interest. We see from figure 3.4 that at higher n, the effect of blackbody radiation is larger, and experiments have introduced cryogenics [202] to mitigate this effect.

Another important matrix element that is useful to understand is the matrix element connecting the ground state to an excited Rydberg state. This matrix element is relevant for the excitation of the atom from the ground state to the Rydberg state. It scales roughly as $n^{-3/2}$ and is shown in figure 3.2b.

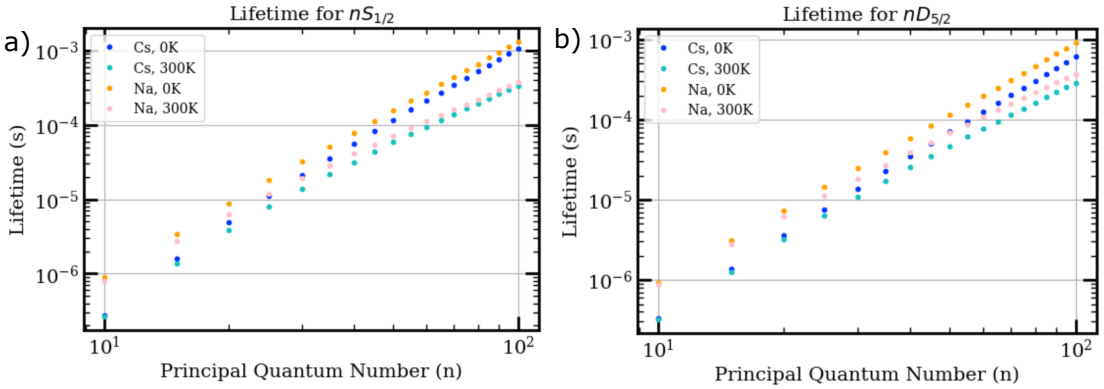

Figure 3.4: (a) The lifetime of the $nS_{1/2}$ states at $T = 0$ K (spontaneous emission lifetime) compared to $T = 300$ K in sodium and cesium. We see that 300 K blackbody radiation is a bigger effect at higher principal quantum numbers. (b) The lifetime of the $nD_{5/2}$ states at $T = 0$ K and $T = 300$ K. The same qualitative trend exists for this state as the $nS_{1/2}$ states.

3.2.2 Interactions of Rydberg Atoms

The lowest order contribution to the long-range interactions between two atoms comes from the dipole-dipole interaction

$$V_{\mathrm{dd}}(\mathbf{R}) = \frac{1}{4\pi\varepsilon_0}\left(\frac{\mu_1 \cdot \mu_2}{R^3} - \frac{3(\mu_1 \cdot \mathbf{R})(\mu_2 \cdot \mathbf{R})}{R^5}\right), \tag{3.14}$$

where μ_1 and μ_2 are the dipole operators for atom 1 and atom 2, and $\mathbf{R}$ is the internuclear distance. Note that for this to be valid, we assume that the electron clouds of the atoms do not overlap, so that each atom is completely independent. At shorter distances, interactions between the electrons and both nuclei lead to rich molecular physics that this model would fail to capture. Nonetheless, this model is a good description for pairs of atoms at the micron separation level.

The full Hilbert space of our two atom system can be written in the pair state basis, where atom 1 is in the state $|n_1 l_1 j_1\rangle$ and atom 2 is in the state $|n_2 l_2 j_2\rangle$. For convenience, we will label states of atom 1 with a single Roman letter such as $|a\rangle$ and $|b\rangle$, and states of atom 2 with a single Greek letter such

as $|\alpha\rangle$ and $\beta\rangle$. The dipole-dipole interaction couples the pair state $|a;\alpha\rangle$ with all pair states $|b;\beta\rangle$, where a is dipole-connected to b and α is dipole connected to β, i.e. $\langle a|\mu_1|b\rangle \neq 0$ and $\langle\alpha|\mu_2|\beta\rangle \neq 0$. In general, a full interaction matrix needs to be diagonalized, and software, such as ARC, will allow the user to specify the bounds of the Hilbert space to consider, such as a minimum and maximum n and l quantum numbers.

However, in many situations, and for gaining an intuition on the effect of the interaction, it is useful to consider the effect of a single interacting pair state $|b;\beta\rangle$ that interacts with $|a;\alpha\rangle$. In the basis $\{|a;\alpha\rangle, |b;\beta\rangle\}$, the Hamiltonian can be written as

$$H = \begin{pmatrix} 0 & U_{\mathrm{dd}}(\mathbf{R}) \\ U_{\mathrm{dd}}(\mathbf{R}) & \hbar\delta \end{pmatrix}, \tag{3.15}$$

where $U_{\mathrm{dd}}(\mathbf{R}) = \langle a;\alpha|V_{\mathrm{dd}}(\mathbf{R})|b;\beta\rangle$ is the matrix element for the dipole-dipole interaction between these two states, and $\hbar\delta = E_{\alpha\beta} - E_{ab}$ is known as the energy defect of the pair state. We define the C_3 coefficient through the relation

$$U_{\mathrm{dd}}(\mathbf{R}) = \frac{C_3}{R^3}. \tag{3.16}$$

Thus, the C_3 coefficient is proportional to the radial matrix elements $\langle a|r|b\rangle$ and $\langle\alpha|r|\beta\rangle$, which can be calculated from the wavefunctions described previously. This Hamiltonian can be easily diagonalized yielding the eigenstates and eigenenergies of the interacting system. The eigenenergies are

$$E_{\pm} = \frac{\hbar\delta}{2}\left(1 \pm \sqrt{1 + \frac{4C_3^2}{\hbar^2\delta^2 R^6}}\right). \tag{3.17}$$

This energy shift associated with nearby interacting Rydberg atoms is the origin of the Rydberg blockade, and has been used in the implementation of quantum gates and performing quantum

simulation. Specifically, for an interaction strength $V(r)$ (shift from a non-interacting pair state) and drive Rabi frequency Ω, the Rydberg blockade radius is the r such that $V(r) = \Omega$. A cutoff radius[207] (also known as the van der Waals radius)

$$R_c = \left(\frac{C_3^2}{\hbar^2 \delta^2}\right)^{1/6} \tag{3.18}$$

separates two distinct regimes for this interaction energy. When $R \ll R_c$, then the second term dominates the square root and the eigenenergy is proportional to C_3/R^3. Note that when $\delta \to 0$, $R_c \to \infty$, and we are always in this resonant regime, where the interaction energy is proportional to C_3/R^3. When $R \gg R_c$, we can Taylor expand the square root and the energy shift is given to first order by

$$-\frac{C_3^2}{\hbar \delta R^6} = -\frac{C_6}{R^6} \tag{3.19}$$

where we have now defined the C_6 coefficient as $C_3^2/(\hbar\delta)$. This $1/R^6$ regime gives rise to the so-called van der Waals interaction. From this analysis, we see that the van der Waals interaction simply arises from the perturbative regime ($R \gg R_c$ or $U_{\text{dd}}(\mathbf{R}) \ll \delta$) of the dipole-dipole interaction. However, when $R \ll R_c$ or $\delta \ll U_{\text{dd}}(\mathbf{R})$, there is a "resonant" regime, where the interaction scales as $1/R^3$. This resonant regime is the only regime at a Förster resonance, where $\delta = 0$. These resonances can arise more easily in interactions between two different species and the energy defect can be tuned with electric fields. Note that this resonance naturally occurs as an exchange interaction in a single-species context between pair states $|a; b\rangle$ and $|b; a\rangle$. This regime has been accessed in experiments where the spin states are encoded in dipole-connected Rydberg levels as well as experiments with molecular rotational states.

In real Rydberg atoms, there will be many pair states which interact with a particular state of interest. If all interacting pair states enter perturbatively, a C_6 coefficient can be calculated by sum-

ming over all connected pair-states k that are dipole-connected to $|a;\alpha\rangle$ in the following way,

$$C_6 = \sum_k \frac{C_{3k}^2}{\hbar\delta_k}. \tag{3.20}$$

However, the most accurate result for the interaction energy will require a full diagonalization. In some cases, especially at high principal quantum number, different $1/R^6$ branches from distinct pair states may cross resulting in a "spaghetti" of levels at small distances.

The two-level model already yields intuition and is predictive of the long range interaction strengths, where a single state is likely to dominate the interaction. First, we can deduce the sign of the interaction from the sign of the defect. If the defect is positive (negative), then C_6 is positive (negative), and the resulting shift is negative (positive). For a pair state consisting of the same S state in an atom ($|nS_{1/2}, nS_{1/2}\rangle$), the nearest strongly dipole connected pair state consists of going to two P states with principal quantum number within 1 of the original principal quantum number, since this yields the strongest dipole moments (see figure 3.2a). Namely, the pair state $|nP, (n-1)P\rangle$ will shift the energy of $|nS_{1/2}, nS_{1/2}\rangle$ the most. There are 4 possible fine structure components, and the defects are shown in figure 3.5a. The defects in all cases are negative, indicating that the $|nP, (n-1)P\rangle$ state is lower in energy than the $|nS_{1/2}, nS_{1/2}\rangle$ state. This makes sense intuitively, since in a typical Rydberg ladder, going down in principal quantum number releases more energy than is gained when going up in principal quantum number. When the defect is negative, the energy shift is positive and the interaction is then repulsive. This leads to the general rule of thumb that interactions between the same species atom (in the same state) are repulsive. As we will see, it is easier to engineer attractive interactions in a dual-species context in section 5.2.

Second, we can deduce the scaling of the interaction strength with principal quantum number. The C_3 coefficient is proportional to a squared dipole moment. As discussed previously, the dipole moment is proportional to n^2 so the C_3 coefficient is proportional to n^4. The energy defect is, to

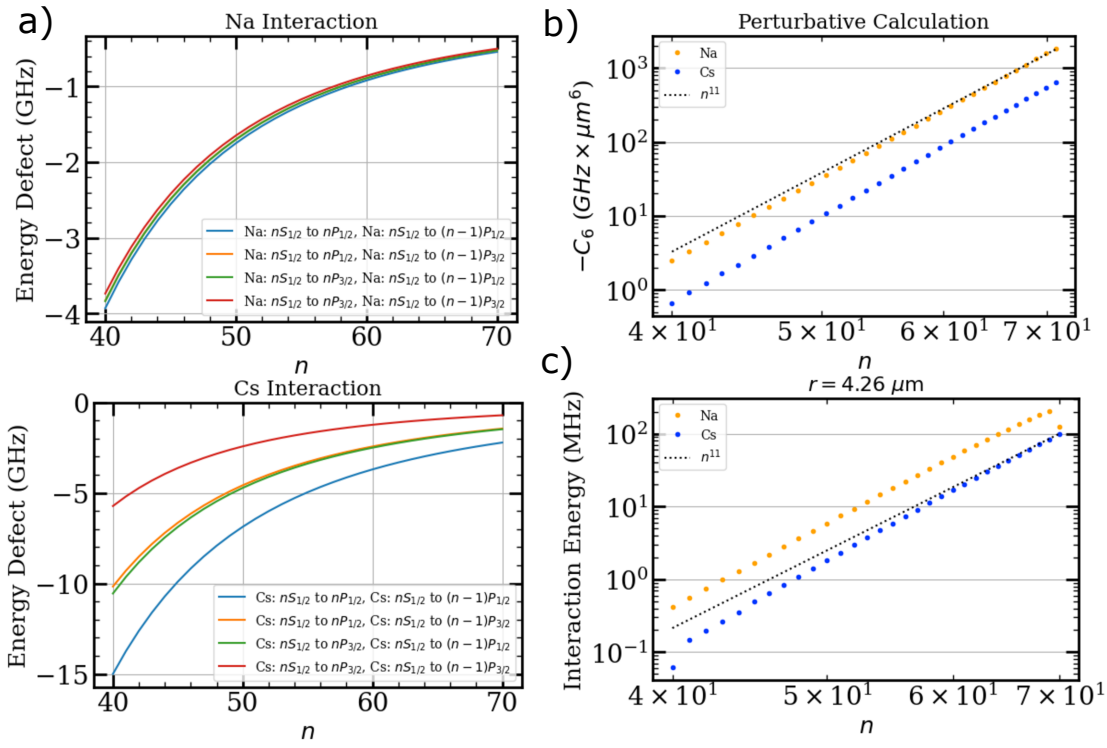

Figure 3.5: (a) The energy defect for a $|nS_{1/2}, nS_{1/2}\rangle$ state to a $|nP, (n-1)P\rangle$ for all 4 fine structure components in cesium and sodium. Fine structure is larger in cesium compared to sodium, but in all cases, the defect is negative. (b) The result of a perturbative C_6 calculation including states with principal quantum number within 10 of the initial state, and within 100 GHz of energy for sodium and cesium. As a guide-to-the-eye, the n^{11} scaling is plotted with gray dots. The C_6 coefficient is negative, so we plot $-C_6$ on this log scale. (c) The result of a full diagonalization at a distance of 4.26μm utilizing states with principal quantum number within 10 of the initial state, and within 10 GHz of energy for sodium and cesium. Once again, the gray dots represent a n^{11} scaling.

first approximation, at the scale of the energy level spacing at a particular n, which scales as $1/n^3$. Thus, the C_6 coefficient scales as n^{11}, which is quite significant! The results of a perturbative calculation are shown in figure 3.5b, and are quite consistent with the n^{11} scaling from the simple scaling arguments. The results from a full diagonalization are shown in figure 3.5c, and also shows good agreement with the n^{11} scaling. The rough dependencies of the quantities discussed in this section

with principal quantum number is summarized in table 3.1.

Quantity	Scaling	Reasoning
Atom size	n^2	Semiclassical argument
$\langle r\|d\|r'\rangle$	n^2	Proportional to atom size
$\langle g\|d\|r\rangle$	$n^{-3/2}$	Calculation
ΔE	n^{-3}	Rydberg energy spacing $\propto n^{-2}$
DC polarizability	n^7	Proportional to $d^2/\Delta E$
Circular Rydberg state lifetime	n^5	Proportional to $1/(d^2\Delta E^3)$
Typical Rydberg state lifetime	n^3	Calculation
C_3 coefficient	n^4	Proportional to d^2
C_6 coefficient	n^{11}	Proportional to $C_3^2/\Delta E$

Table 3.1: Scaling of important Rydberg atom quantities with principal quantum number n. d refers to either the dipole operator or dipole matrix element depending on context. ΔE refers to the energy spacing between nearby Rydberg states.

3.3 Rydberg Lasers

Figure 3.6 shows the possible Rydberg excitation pathways we can use for cesium. Ideally, a single laser is used to excite atoms from the ground state to the Rydberg state. However, a single photon excitation requires a 319 nm laser. Furthermore, since the radial wavefunctions of the ground and Rydberg state are very different, high powers are required for appreciable Rabi frequencies. High power lasers and compatible optics at these wavelengths are technically challenging. Thus, two photon excitation has been predominantly used in the field.

In a two-photon coherent excitation, we typically connect two states ($|g\rangle$, $|r\rangle$) (between which a dipole transition is forbidden) via an intermediate state $|e\rangle$. The intermediate state is typically lossy with loss rate Γ_e, and thus to minimize loss, we detune from the intermediate state by an amount Δ. The single photon Rabi frequency between $|g\rangle$ and $|e\rangle$ is Ω_{ge} and between $|e\rangle$ and $|r\rangle$ is Ω_{er}. Any deviation of the summed laser frequency and the energy difference between $|g\rangle$ and $|r\rangle$ is denoted as δ. This scenario is depicted in figure 3.7.

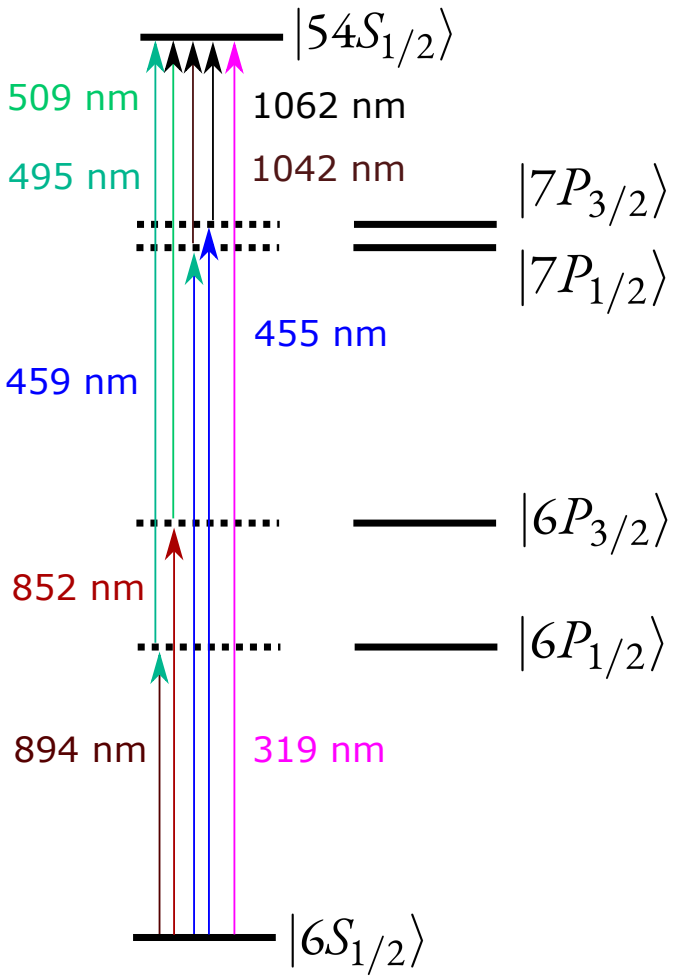

Figure 3.6: The possible transitions to use for exciting cesium to the Rydberg state. Fine structure in cesium is significant and depicted.

If we are detuned far enough away from the intermediate state, it can be adiabatically eliminated[33], and we can drive between the ground state and the excited state as if it were simply a two level system. The effective Rabi rate of this process is given by

$$\Omega_{\text{eff}} = \frac{\Omega_{ge}\Omega_{er}}{2\Delta}. \tag{3.21}$$

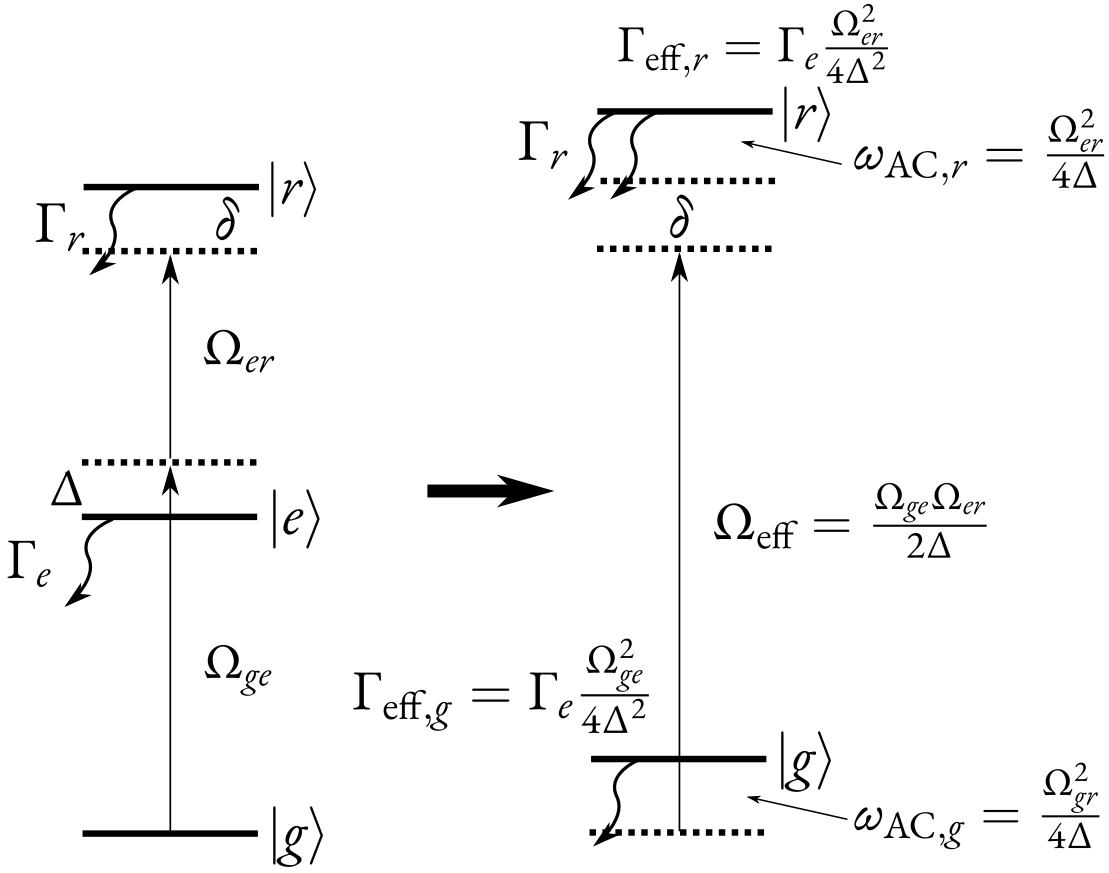

Figure 3.7: The initial three level system describing a two photon excitation process from the ground state $|g\rangle$ to the Rydberg state $|r\rangle$ via an intermediate state $|e\rangle$. Upon adiabatic elimination [33] of the intermediate state, an effective two level system can be used to describe the two photon process.

Each laser imparts an AC Stark shift on the state that they couple with magnitude $\Omega^2/4\Delta$. Due to the mixing with the intermediate state, each state now has some loss given by $\Gamma\Omega^2/(4\Delta^2)$. Notice that since the effective Rabi rate is proportional to $1/\Delta$ and the scattering rate is proportional to $1/\Delta^2$, the ratio of the two gets better at larger detuning. Thus, if one has infinite power (to compensate the overall decrease in the Rabi frequency with detuning), then detuning further reduces the scattering more. This model breaks down when one detunes so far that other intermediate states

start coming into play. In systems of alkali atoms, these states are typically other hyperfine states, while in molecules, other vibrational states can limit how far one can detune. At a fixed detuning, the ratio of the Rabi frequency to the scattering (which comes from both beams) is

$$\frac{\Omega_{ge}\Omega_{er}}{\Omega_{ge}^2 + \Omega_{er}^2}. \tag{3.22}$$

For fixed Ω_{ge}, Ω_{er} should be equal to Ω_{ge} in order to maximize the ratio of the Rabi frequency to scattering. Under these considerations, the best conditions for obtaining coherent Rabi oscillations from the ground to Rydberg state arise from using more power, which allows us to use larger detuning and reduce scattering. Furthermore, we'd like to balance the two individual single transition Rabi frequencies as much as possible.

The Rabi frequency comes from both the transition matrix element and the power of the laser. The second leg of the two photon Rydberg transition has a smaller matrix element due to the large mismatch in the size of the electron wavefunction. Thus, more power is required for this second leg. The now-standard approach of obtaining higher Rabi frequency is to use the so-called inverted scheme. Here, the first photon connects the ground state $nS_{1/2}$ to the $(n+1)P_{3/2}$ state, instead of connecting $nS_{1/2}$ to $nP_{3/2}$, which is the standard D line transition. The advantage of this is that the second photon which connects the intermediate P state to the Rydberg state is at a lower frequency and for many atoms, it falls in the infrared range of the electromagnetic spectrum. For example in cesium, this second leg changes from 509 nm to 1060 nm when using the inverted scheme. From a technical standpoint, it is much easier to produce high power infrared light than green or blue light. Thus, in cesium, we drive our two photon Rydberg transition with a 455 nm laser addressing the transition from $6S_{1/2}$ to $7P_{3/2}$, and an approximately 1060 nm laser addressing the transition from $7P_{3/2}$ to the Rydberg state.

Coincidentally, another advantage of the inverted scheme is that the linewidth of the interme-

diate state tends to be narrower reducing the intermediate state scattering. However, doppler effects tend to be worse in the inverted scheme. The doppler effects are minimized in a two-photon Rydberg transition when the beams are counter-propagating. In this case, a photon absorption from both beams result in a momentum kick that partially cancels. However, the difference in the wavelengths of the two beams results in a non perfect cancellation. This difference is larger for the inverted-scheme compared to the standard scheme resulting in larger doppler shifts.

Now, we will discuss the lasers we use to drive the transition. Our 455 nm laser is a doubled Ti-Sapphire laser from MSquared. The Ti-Sapphire laser is inherently low noise[67] and provides several watts of power, making it an ideal source for Rydberg excitation. In our system, we pump the Ti-Sapph with 15 W of 532 nm light from various sources* producing at maximum around 3.3 W of 910 nm. After doubling with a MSquared ECDX, we have about 1.4 W of 455 nm light. We noticed that the doubling efficiency exhibits large thermal effects and we were rarely able to maintain our maximum power output. To control the frequency and amplitude of the light, we use a double-passed AOM (AA Optoelectronics MQ180-A0,25-VIS) centered at 180 MHz, where we take care to focus the beam into the AOM to achieve a fast rise time of around 10-20 ns. This AOM requires a particular polarization to work most efficiently. We found a roughly 25% difference between the diffraction efficiencies of S and P polarization. Thus, to ensure that the same polarization traverses through the AOM on both passes, we use a Faraday rotator (Crystalaser FR-457-04) which rotates a linear polarization by 45 degrees regardless of the direction of the beam propagation. The setup is shown in figure 3.8. The polarization starts as horizontal, which is then rotated to approximately 45 degrees with a half waveplate. Then, it passes through the Faraday rotator which converts the polarization to vertical. It traverses through the AOM twice maintaining its vertical polarization before rotating to diagonal (but opposite the previous diagonal) after the Faraday rotator. The half

*Over the years, we really tried to use a MSquared Equinox to not much success. Our most reliable pump ended up being a Coherent Verdi, which unfortunately could not survive a power dip.

waveplate then changes this polarization to vertical which then reflects off the input cube.

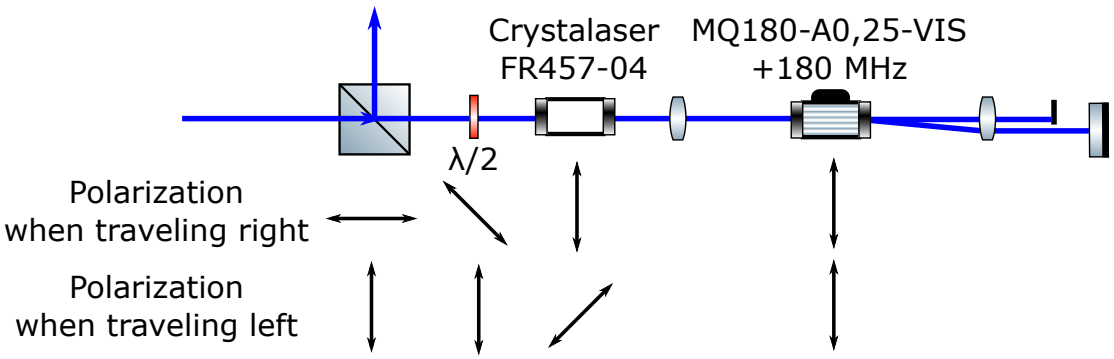

Figure 3.8: The setup for frequency and amplitude tuning our 455 nm Cs Rydberg beam. The AA Optoelectronics MQ180-A0,25-VIS AOM requires a particular polarization, so we use a Faraday rotator to perform the total 90 degree rotation (45 degree on each pass) before the AOM. This 90 degree rotation allows us to separate the double-passed beam from the incoming beam.

This light is then delivered to our experiment using an end-capped fiber from Schafter and Kirchoff (PMC-E-400Si-3.5-NA011-3-APC.EC-500-P). The output light is collimated on our experimental table with a beam size determined by our target size at the atoms. For intensity stabilization, the light is picked off by a beamsplitter and focused onto a photodiode. There is a shutter located after the beamsplitter. The light is focused with a 500 mm lens onto the atoms and combined with various other beams at 589 and 852 nm. The detailed beampath is depicted in figure 3.9.

Our 1060 nm laser is a diode laser based on an Innolume gain chip (GC-1030-160-TO-200-B) constructed commercially by Timebase (part number: ECQDL-200FC). We found that the Timebase current driver that the laser came with was noisy, so we had to replace it with an Agendile (CS500) current driver. We still use the Timebase driver for temperature control. In our first experiments, this laser directly seeded a fiber amplifier (we have used one from Azur Light Systems and Precilasers). The fiber amplifier can in principle supply up to 50W of light. After the fiber amplifier, the light goes through a single-pass AOM (Neos 23080-2-1.06) in order to control the amplitude of

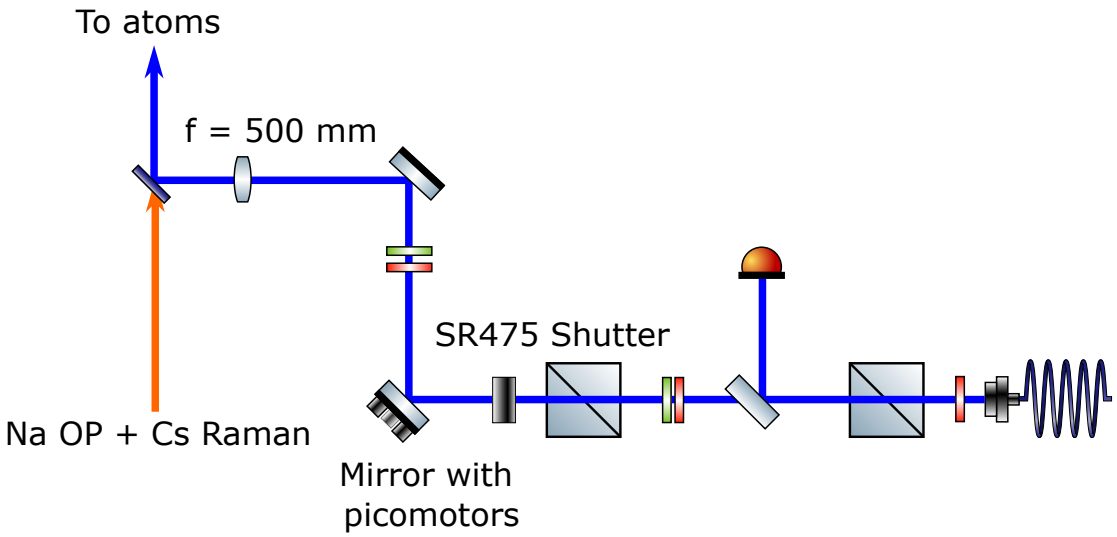

Figure 3.9: The setup on our experimental table for our cesium 455 nm beam. A beam-splitter pickoff onto a photodiode is used for intensity stabilization. Importantly, the shutter is placed after the pickoff, so during the relatively long sample and hold period (see details in text), the light does not impinge on the atoms. There is also a mirror with a picomotor allowing for automated or remote realignment. Typically we use a beam several mm in waist so that we obtain a spot of under 50 micron waist. The light is combined with sodium OP and cesium counter-op Raman beams. For more general context, see figure 2.1

the light. We are limited in the amount of light we can use by the delivery fiber (end-capped from Oz Optics) from our laser table to the experiment table. On the experiment table, the light is recollimated, picked off for intensity stabilization, and then shaped to a beam size of around a few mm. After focusing through a 600 mm lens, it impinges on the atom with a size of around 100 microns.

Both lasers need to be phase coherent with each other and frequency locked. To do this, we use a monolithic optical cavity made with a ultra low thermal expansion coefficient material and high reflectivity mirrors. The system needs to be temperature stabilized to the zero-crossing of the thermal expansion coefficient. The cavity is also held under vacuum to prevent pressure fluctuations from changing the index of refraction of the air which can change the resonance frequency of the cavity. The system was commercially manufactured by Stable Laser Systems.

It is challenging for a single cavity mirror to have high reflectivity at such both 455 and 1060 nm, which are quite different, so we instead coat the cavity mirrors at 910 nm, the pre-doubled wavelength of the 455 nm light. Therefore, we need to pick off part of the 910 nm light to send to the cavity for locking purposes.

The locking paradigm is a standard Pound-Drever-Hall (PDH) locking scheme[24], where a fiber EOM is used to create the frequency sidebands. Special care needs to be taken to use dichroics to combine the different wavelengths and mode-match them to the cavity. In order to be able to scan the frequency of our lasers, in addition to using AOMs, we apply two sets of locking sidebands to the EOM. We lock to a "large" frequency sideband via a set of "small" frequency sidebands. By changing the large frequency sideband, the lock point can be varied despite the cavity resonance being fixed. This is especially convenient when we want to change the intermediate state detuning significantly. The details of the electronics and exact optics will be documented in a future thesis.

3.4 Driving Coherent Rydberg Excitations

Now, we are ready to drive coherent Rydberg excitations. In order to drive this two-photon transition coherently, we need to ensure that the Raman Rabi frequency is larger than the rate of any decoherence or scattering processes. To maximize the Raman Rabi frequency, the lasers need to be aligned well to the atoms. We now discuss how we align the two beams to the atoms.

The 455 nm beam addresses the $6S_{1/2}$ to $7P_{3/2}$ transition. Thus, when the beam is shined on the MOT, it disrupts the cooling processes in the MOT and is able to destroy it. This provides us with a coarse alignment tool, where the goal is to find the alignment that destroys the MOT with the least amount of power. While this is not a perfect alignment to the atom, it does provide good enough alignment to get an initial in sequence signal on atoms trapped in the tweezer. Since our 455 nm light only addresses the $F = 4$ hyperfine state, to blast atoms from the tweezer, we need to

turn on a $F = 3$ repump light typically on the standard D2 line. We can then find the alignment that blasts the atoms in the shortest time possible. Another very sensitive method for aligning the beam is to perform state preparation into $F = 4$, and then use the blue beam to depump atoms into $F = 3$. A destructive hyperfine-state-selective measurement can then be used to maximize the rate of depumping, which will be correlated to the best beam alignment.

For a more sensitive and quantitative probe, one can detune the laser by less than the ground state hyperfine splitting of approximately 9.2 GHz. In this case, there would be a different scalar light shift on the $F = 4$ and $F = 3$ state, leading to a measurable differential light shift. This light shift can be measured by a frequency measurement, where the $|6S_{1/2}, F = 4, m_F = 4\rangle$ to $|6S_{1/2}, F = 3, m_F = 3\rangle$ hyperfine transition frequency is measured with and without the blue beam on. We are able to easily see shifts on the order of a few tens of kHz at a GHz blue detuned from the $|6S_{1/2}, F = 4\rangle$ to $|7P_{3/2}, F = 5\rangle$ transition. At shifts much larger than this, we begin to see significant depumping obscuring the frequency shift. An alternative method that allows us to measure the light shift corresponding to larger blue powers is to perform a Ramsey measurement, where we first start in $|6S_{1/2}, F = 4, m_F = 4\rangle$ and then perform a $\pi/2$ pulse on the $|6S_{1/2}, F = 4, m_F = 4\rangle$ to $|6S_{1/2}, F = 3, m_F = 3\rangle$ transition, creating an equal superposition of the two hyperfine states. Then, the blue light is turned on for a variable amount of time, and due to the differential Stark shift between the two states due to the blue beam, the two hyperfine components develop a relative phase. Applying a final $\pi/2$ pulse (at the phase of the original $\pi/2$ pulse) after the blue beam is turned off and a measurement of the hyperfine state reveals the famous Ramsey fringes as a function of time. The frequency of these fringes yields the differential light shift, and we have measured light shifts of up to 3 to 4 MHz with this method. Note that the light shift also depends on the polarization of the light due to the relatively large hyperfine (on the order of tens of MHz) and fine structure (on the several nm scale) of the excited state. Thus, the polarization can also be aligned through the measurement of this light shift.

While the blue beam is easier to align because it directly addresses the ground state, the IR second leg is more difficult. Thankfully (see figure 2.10) Cs has large vector light shifts, so we can observe a light shift of the $|6S_{1/2}, F = 4, m_F = 4\rangle$ to $|6S_{1/2}, F = 3, m_F = 3\rangle$ transition in the presence of the IR light, as long as we ensure the light is circularly polarized. We can see tens of kHz of shift when we provide several watts of IR to our atom. This is a difficult signal to observe upon first setup, so we recommend the standard techniques of aligning the beam to other easier to align beams (such as resonant light sources) or even sending resonant light down the same beam path and then accounting for chromatic shifts.

These two alignment methods also allows one to independently measure the single photon Rabi frequencies for each of these lasers. In a typical experiment exciting to the $|54S_{1/2}\rangle$ Rydberg state, we find single photon Rabi frequencies of $2\pi \times 80$ MHz for the blue beam and $2\pi \times 42$ MHz for the IR beam. At a $2\pi \times 1.06$ GHz detuning, this results in a Rabi frequency of $2\pi \times 1.58$ MHz. We have used Rabi frequencies ranging from 1 to 2.5 MHz, and detunings as close as 500 MHz.

To observe Rabi flopping, we need a method to detect whether an atom had been excited to the Rydberg state. In our experiment, detection always measures the presence or lack of atom fluorescence. Thus, a single image can only reveal a single bit of information, which reveals whether a trap holds an atom or not.

In the case of Rydberg excitations, the states we want to distinguish are $|g\rangle$, a ground state atom, from $|r\rangle$, an atom in the Rydberg state. We will map the ground state to atom present and the Rydberg state to atom absent. The way we are able to remove Rydberg atoms is to use the property that the Rydberg state is anti-trapped by the tweezer light. Hence, strong tweezer light should retain and trap a ground state atom but expel a Rydberg atom. We note that this effect requires us to turn off the tweezer before performing any Rydberg excitation, since we do not want to suffer from any tweezer antitrapping effects during the Rydberg dynamics. Furthermore, in addition to tweezer antitrapping, we find that using a microwave pulse can also help expel Rydberg atoms. While the

exact mechanism is unclear, it appears that the microwave may help drive and ionize the Rydberg atoms. We find that this additional microwave pulse can help at the $< 10\%$ level, and is relatively frequency agnostic. Thus, we use our microwave setup for ground state hyperfine manipulation of cesium atoms, which can produce microwaves from about $7-10$ GHz. To summarize, our sequence to perform Rydberg excitations is shown in figure 3.10. In brief, tweezers are lowered adiabatically and then dropped during the Rydberg excitation to prevent the antitrapping effect of the tweezers on the Rydberg atoms. Then, the blue light is pulsed on and off to excite the atoms, while the IR is constantly on during this entire period. Lastly, the tweezers are turned on along with microwaves to detect the atoms.

There are two general types of error in this detection procedure. First, a false positive error[†], where a ground state atom has been lost, and is misinterpreted as a Rydberg atom. Second, a false negative error, where a Rydberg atom has decayed to the ground state and is interpreted as a ground state atom. False positive error can be measured in a release-recapture experiment, where without any Rydberg excitation, the loss of ground state atoms can be determined as a function of time. The detailed procedure for determining the false negative error is outlined as follows. We first define three quantities:

- $1 - \eta_0$: False positive detection error where a ground state atom is detected as a Rydberg atom.
- p: Rydberg excitation probability after a π pulse.
- ε: False negative detection error where a Rydberg atom is detected as a ground state atom.

We determine $\eta_0 = 0.980(8)$ via a release-recapture experiment. To further determine ε, we additionally perform two experiments. In the first experiment, we apply a Rydberg π pulse and then

[†]Note that positive here refers to detection of a Rydberg atom.

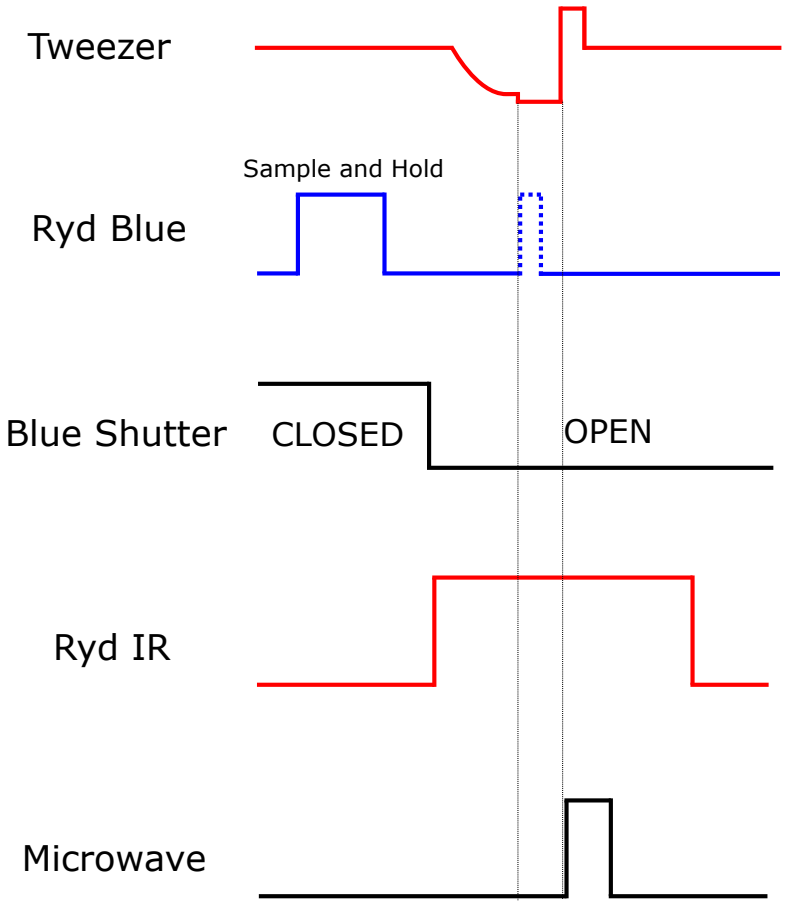

Figure 3.10: Our typical cesium Rydberg excitation sequence. The tweezers are adiabatically lowered in about 100 μs, before being shut off completely during the Rydberg excitation process. The excitation is controlled by the first leg blue light, which requires fast drive electronics. The fast drive is incompatible with our servo electronics, so we use a sample and hold prior to the Rydberg pulse to perform some low frequency stabilization. During this sample and hold period, a shutter is used to prevent the light from entering our vacuum chamber while allowing it onto our stabilization photodiode. The second leg IR light, in contrast, is controlled by slower electronics and its timing does not need to be precisely determined. After the Rydberg excitation is performed, detection occurs by anti-trapping the Rydberg atoms out of the trap. This is performed by pulsing on the tweezer and using a microwave pulse.

detect the ground state population $n_{g1} = 0.053(14)$. In the second experiment, we apply two Rydberg π pulses and then do the same detection for the ground state population $n_{g2} = 0.86(1)$. With the three quantities defined above, we end up with two equations:

$$\eta_0(1-p) + \varepsilon p = n_{g1} \tag{3.23}$$

$$\eta_0(p^2 + (1-p)^2) + 2\varepsilon p(1-p) = n_{g2} \tag{3.24}$$

where the equations arise from carefully consideration all pathways of observing ground state atoms. For example, the two terms in equation 3.24 arise from detecting a ground state atom successfully and from a false detection of a Rydberg atom.

We then solve the above equations (containing two unknowns) to estimate ε. The errors in ε are done by propagating the standard deviation of the known quantities η_0, n_{g1} and n_{g2}. This calibration procedure yields our estimate of the error, which is less than 0.015. We note that to achieve a good calibration of η_0, n_{g1} and n_{g2}, the above experiments are repeated by more than 10000 times.

With this detection procedure, we observe characteristic Rabi flopping in figure 3.11b. The Rabi flopping clearly does not proceed forever, and begins to show an exponential decay envelope due to decoherence. We can categorize decoherence processes into fundamental and technical sources. Fundamental sources include lifetime of the Rydberg state (from both spontaneous and simulated absorption/emission) and intermediate state scattering, which is determined by the current powers and detunings of the lasers. These sources provide fundamental limits to our Rydberg excitation under fixed two-photon excitation parameters. The lifetime limit can be improved by reducing the amount of blackbody radiation, but ultimately will be limited by spontaneous emission.

Technical sources of decoherence include global effects such as laser phase noise, electric field noise, as well as those at a site-to-site level such as beam inhomogeneity. These technical sources can also include shot-to-shot fluctuations in time such as laser intensity noise. We now discuss our

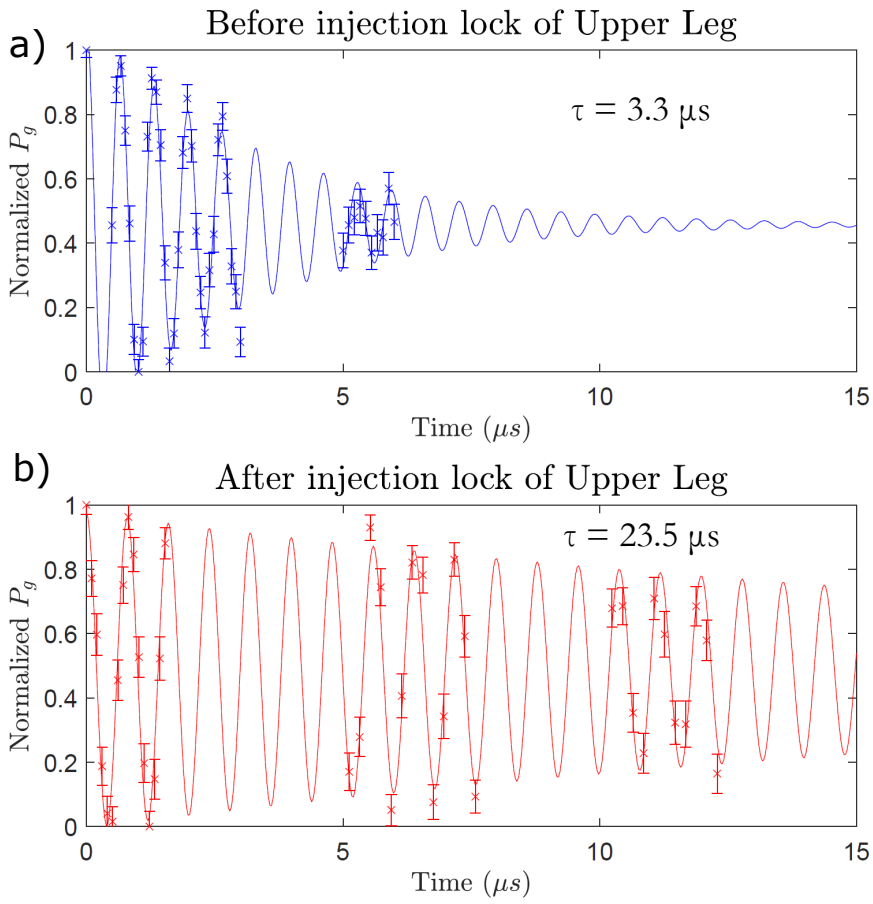

Figure 3.11: Comparison of the Rabi oscillations before and after applying the injection lock technique to reduce the phase noise of the upper leg IR laser. Both datasets have some error where Rydberg atoms are not properly detected and ground state atoms are lost. Thus, both datasets have been normalized to exclude these errors. (a) Data before applying the injection lock technique with a measured time constant of $\tau = 3.3\,\mu$s. (b) Data after applying the injection lock technique with a measured time constant of $\tau = 23.5\,\mu$s.

mitigation efforts for all of these various factors.

Rydberg lifetime. We would like to work at higher principal quantum number Rydberg states to increase the Rydberg lifetime. However, more highly excited states are more sensitive to electric

field (see Electric field noise point below) and also result in lower Rabi frequencies (at fixed laser power) due to a smaller matrix element. Ideally with no electric field noise, and infinite laser power, higher principal quantum number is preferred. Using a circular Rydberg state can also enhance the lifetime.

Intermediate state scattering. As discussed in section 3.3, intermediate state scattering rate relative to coherent Rydberg excitation rate is minimized (for a fixed Rydberg Rabi frequency) when the two beams have equal single photon Rabi frequency. Since the second leg has a smaller transition dipole matrix element, more power is required to achieve this condition. For us, we are power limited by the upper leg, so more power can mitigate decoherence from intermediate state scattering.

Laser phase noise. Reduction of laser phase noise greatly improves the coherence time of Rydberg Rabi oscillations with decay time constants of up to 20 μs. Phase noise is a property of the laser source and is also impacted by the locking of the lasers to the high-finesse ultra-low-expansion cavity. Thus, it depends on the locking electronics and lock parameters. We find the best phase-noise performance when the proportional gain of the PDH lock is as low as possible while being able to maintain lock. However, servo-bumps arising from when the phase delay of the feedback loop results in positive feedback will always be present on the laser light. These bumps are mitigated when one uses the transmitted light from the cavity, which has been filtered to the linewidth of the cavity. Since our cavities are high-finesse, these linewidths are kHz scale. The main difficulty in using the cavity-transmitted light is its low power (typically 100s of μW at most), which is limited by keeping the built-up power inside the high-finesse optical cavity manageable. However, this light can be used to injection lock a free-running diode, stimulating its emission into the frequency mode of the injected light and thus inheriting its linewidth. This can boost the power into the 10s of mW, which is sufficient to seed a fiber amplifier. As far as we can tell, the fiber amplifying process does not introduce any additional frequency noise. The details of this setup will be documented in a future thesis.

The cleaned cavity-filtered light increases the coherence time from 3.3 to 23.5 μs, as shown in figure 3.11.

Electric field noise. Rydberg atoms have large polarizability and thus are quite susceptible to electric fields. As discussed in section 3.2, polarizability scales with n^7, meaning that higher Rydberg states as more susceptible to electric fields. Electric field noise resuling in detuning fluctuations that have similar time scales to the Rabi frequency would cause decoherence. Our chamber consists of a glass cell which is nominally a dielectric material, and thus can result in buildup of charge on its surfaces. These charges, especially if they change dynamically, can affect the coherence of our Rydberg excitations. We found empirically in our setup, that it is difficult to drive Rydberg transitions to states with $n \geq 60$. Thus, we have mostly used $n = 54$ for the studies in this thesis. Turning on UV LEDs that shine on our glass surfaces impacts the location of our resonance for higher n (such as $n = 66$). We turn on 3 different UV LEDs impinging on the top, side and bottom surfaces of our glass cell and keep them continuously on. We find that this stabilizes the electric field conditions experienced by the atoms.

Beam inhomogeneity. At the moment, we drive our atoms with Gaussian beams, which per their name, has a Gaussian spatial profile. This leads to Rabi frequency variation across our array if the beam is too small. Thus, focusing the beam increases the peak Rabi frequency, while resulting in more spatial inhomogeneity. An example of data where there is variation across the array is shown in figure 3.12. We typically aim for a Gaussian waist size such that there is at most 90% Rabi frequency variation across our array. Another technique to increase the homogeneity of our beam is to shape it with an airy beam shaper (Asphericon ASM25-10-D-Y-355) or a SLM to create a tophat or plateau like structure. However, we found the airy beam shaper to be difficult to work with. The beam's intensity profile as a function of the beam propagation axis is quite unintuitive and thus hard to align. A SLM is a good solution, but is expensive for this task. We note that beam inhomogeneity, for single atom data, only affects "coherence" on averaged quantities. In fact, for the plots shown in

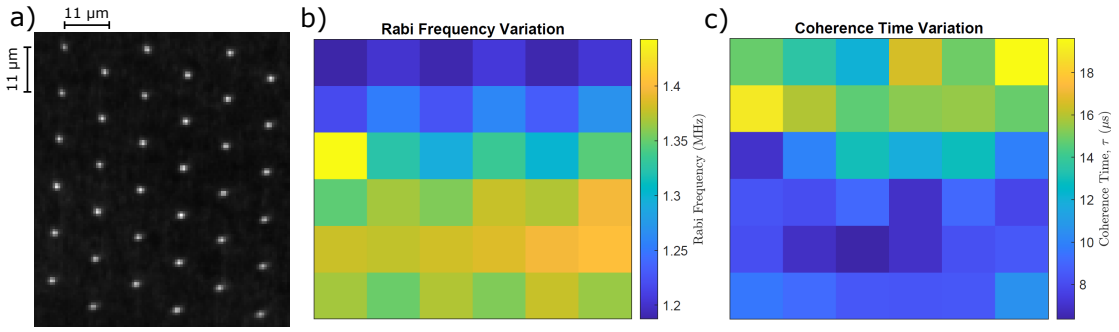

Figure 3.12: (a) The large test array of cesium atoms for observing site-to-site decoherence effects. Note the large spacing eliminates the need for rearrangement to acquire data free of interactions. We can use single atom data or average data in different spatial regions. The Rydberg excitation beams traverse the array from left to right (or right to left, the two beams are counterpropagating). Thus, the horizontal direction has smaller beam intensity variation than the vertical direction. (b) Rabi frequency as a function of position in the array of (a). The top of the array is experiencing lower Rabi frequencies, likely due to beam misalignment. (c) The corresponding coherence times of these sites. The lower Rabi frequency sites have larger coherence time, indicating the presence of intensity noise.

this chapter, we either use single-site data or an average of nearby sites so that the decoherence is not explained by site-to-site variation. Depending on what one can measure, site-to-site variation may be called decoherence, but since we have the resolution to resolve single sites, the effect can be nicely isolated out. However, when it comes to many-body phenomenon, site-to-site variation plays an important role.

Laser intensity noise. Intensity stabilizing a fast pulse (sub-microsecond) of our blue light is non-trivial. The bandwidth of the intensity servos which feedback on AOMs are typically limited by the AOM bandwidth. We find that using our servo to control the light results in slower ramps and also oscillations in light intensity. Thus, we need to bypass the servo completely when performing these Rydberg pulses and rely on fast modulation of the RF source. We have both used our home-built DDS (which has a minimum pulse time of 500 ns) and our AWG (minimum pulse time 1.6 ns, which is unachievable on an AOM) to drive this AOM. However, we'd still like to engage our servo

for its shot-to-shot stabilization and control of the DC value. The servo helps stabilize intensity noise from fiber coupling drifts or polarization drifts. To retain DC control while shutting off the higher frequency control that results in slower pulses, we use a sample and hold circuit. This sample and hold circuit is placed on the output of the servo before it reaches the control voltage input of the mixer. When the circuit is on sample mode, the servo output reaches the mixer and active stabilization is enabled. When the circuit is on hold mode, the servo will not be able to feedback to the laser power. Immediately before the Rydberg pulse is required, we engage the servo (and put the sample and hold circuit to sample mode) to hold the laser power at a certain value for 10 ms. The shutter is closed during this period to not disturb the atoms. Near the end of this period, we switch the sample and hold circuit to hold mode, holding a control voltage input that corresponds to the power setpoint. Further changes or pulse shaping on our Rydberg light is performed directly with the RF power, and the shutter will be opened when the light is needed on our atoms. This technique is able to stabilize our blue power to about 1%. We note that this method cannot stabilize fast frequency fluctuations, where we need to rely on stable cavity parameters on our ECDX doubling cavity. Unlike the blue laser, the Rydberg IR laser does not need to be turned on very quickly. It can stay on throughout the pulse, since the actual atom dynamics are governed by the blue pulse. Thus, for this laser, we use a standard intensity servo without any need for a sample and hold circuit.

3.5 Measuring Interactions Between Rydberg Atoms

Now that we have characterized our single atom Rydberg excitations, we want to observe interactions between our atoms when they are close to each other. As discussed in section 3.2.2, Rydberg atoms typically have a $1/r^6$ van der Waals interaction at the tens of MHz scale at 4 microns. Let's now consider a two atom system using a basis for our two atom states consisting of $|gg\rangle$, $|gr\rangle$, $|rg\rangle$, $|rr\rangle$. With a laser drive (actually two-photons) at effective Rabi frequency Ω and on resonant with the

single atom $|g\rangle \rightarrow |r\rangle$ transition, the Hamiltonian is given by

$$H = \frac{\hbar\Omega}{2} |gg\rangle \langle gr| + \frac{\hbar\Omega}{2} |gg\rangle \langle rg| + \frac{\hbar\Omega}{2} |gr\rangle \langle rr| + \frac{\hbar\Omega}{2} |rg\rangle \langle rr| + V_{rr} |rr\rangle \langle rr| . \tag{3.25}$$

where V_{rr} is the Rydberg-Rydberg interaction. Now, we make the following definition

$$|+\rangle = \frac{1}{\sqrt{2}}(|gr\rangle + |rg\rangle). \tag{3.26}$$

With this definition, we can rewrite the Hamiltonian as

$$H = \frac{\hbar}{2}\sqrt{2}\Omega |gg\rangle \langle +| + \frac{\hbar}{2}\sqrt{2}\Omega |+\rangle \langle rr| + V_{rr} |rr\rangle \langle rr| . \tag{3.27}$$

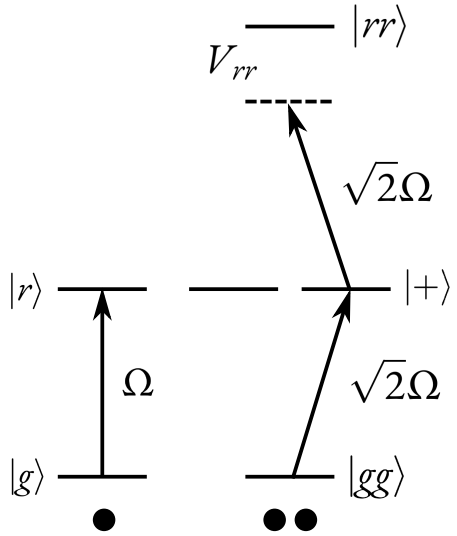

Figure 3.13: Comparison of the single atom and two atom states under a laser drive. In the two atom case, only of the two states with a single Rydberg excitation is populated. This state is populated at a $\sqrt{2}$ enhanced rate. The Rydberg state is shifted from the energy of two independent Rydberg excitations by the interaction energy.

What this Hamiltonian tells us is that with two atoms, because of the symmetry of the drive addressing each atom in the same way, the $|gg\rangle$ state is only coupled to one particular combination of $|gr\rangle$ and $|rg\rangle$, namely the $|+\rangle$ combination. This coupling has an enhanced Rabi frequency of $\sqrt{2}\Omega$. Now, when $V_{rr} = 0$, this $|+\rangle$ state is subsequently coupled to $|rr\rangle$, and the resulting dynamics are equivalent to two independent Rabi flops. However, when $V_{rr} \gg \Omega$ (distances where atoms are within a blockade radius), we can assume that the $|rr\rangle$ state is energetically forbidden to access, and a residual two-level system between the states $|gg\rangle$ and $|+\rangle$ emerges with the aforementioned enhanced Rabi frequency $\sqrt{2}\Omega$. In fact, a π pulse in this two-level system results in the creation of an entangled state $|+\rangle$ which has been enabled by the interaction V_{rr}. Hence a signature of interactions is to measure an enhanced Rabi frequency with 50% Rydberg population when atoms are within the blockade radius and to otherwise (when atoms are far apart) obtain full contrast Rabi oscillations with a slower frequency.

Figure 3.14 illustrates the aforementioned features. Panel a) compares the standard single atom oscillations between the ground and Rydberg state, which occurs at a Rabi frequency of $2\pi \times 1.05$ MHz, with those oscillations of a two atom system. When two atoms are within a blockade radius (i.e. V_{rr} is shifted away by an energy much larger than a Rabi frequency), the state $|gg\rangle$ oscillates with the state $\frac{1}{\sqrt{2}}(|gr\rangle + |rg\rangle)$. Hence, with two atoms the P_{gg} population should exhibit full contrast oscillations and as explained above will oscillate with a $\sqrt{2}$ enhancement in the Rabi frequency. The P_{gg} oscillations in the two atom case are fit to a Rabi frequency of $2\pi \times 1.46$ MHz. Taking the ratio of the two oscillation frequencies in the two cases, we obtain $1.46/1.05 \approx 1.39$, which is not far from $\sqrt{2}$. Figure 3.14b shows the other 3 measurement results when there are two atoms, namely P_{gr}, P_{rg} and P_{rr}. As expected, P_{gr} and P_{rg} only display half contrast oscillations, consistent with populating the $\frac{1}{\sqrt{2}}(|gr\rangle + |rg\rangle)$ state. The P_{rr} state is only minimally populated. Residual population in this state can result from finite interaction strength and imperfect blockade as well as detection error, such as atom loss, which would be interpreted as Rydberg population. Further-

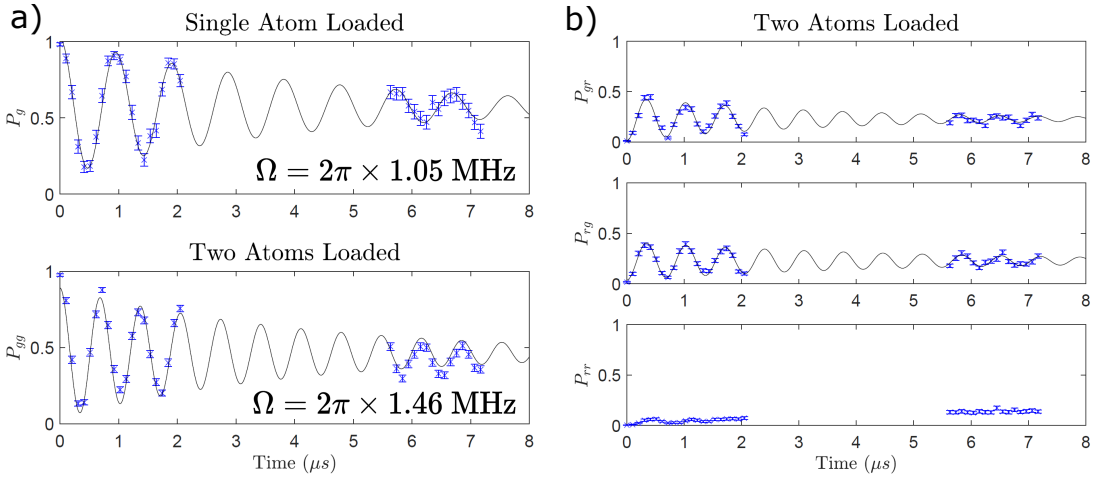

Figure 3.14: (a) Comparing oscillations of a single atom with two atoms that are interacting. The interacting atoms oscillate faster than the single atom indicating blockaded oscillations as described in the text. By looking at P_{gg}, full contrast oscillations are allowed. (b) The P_{gr}, P_{rg} and P_{rr} populations when two atoms are loaded. Due to the Rydberg blockade, only one Rydberg atom can be excited at a time. The presence of two Rydberg atoms, P_{rr}, indicate blockade violation, which are small at these interaction strengths.

more, any atom loss during the sequence will also encourage Rydberg excitation, due to the removal of the blockade effect. In other words, when an atom loss event occurs, full contrast oscillations of the remaining atom is allowed.

Observing enhanced frequency blockade oscillations is relatively clear evidence of interactions, but it does not allow us to quantitatively measure the strength of the interaction. In fact, it is an effect which is robust to the exact interaction strength and hence blockade phenomena have been used in the implementation of high fidelity quantum gates [112,158,114,138,77,148,199,47]. To measure the interaction strength, one can use a π pulse on two interacting atoms to obtain the state $\frac{1}{\sqrt{2}}(|gr\rangle + |rg\rangle)$ followed by another π pulse, but at a different laser detuning (figure 3.15a). This is achieved with a frequency change in our double-passed AOM. If the laser frequency matches the one of the first pulse, then atoms will return to the $|gg\rangle$ state. However, if the new laser frequency takes into

account the interaction energy V_{rr} then two Rydberg atoms can be created. Locating this frequency is, in effect, a measurement of V_{rr}.

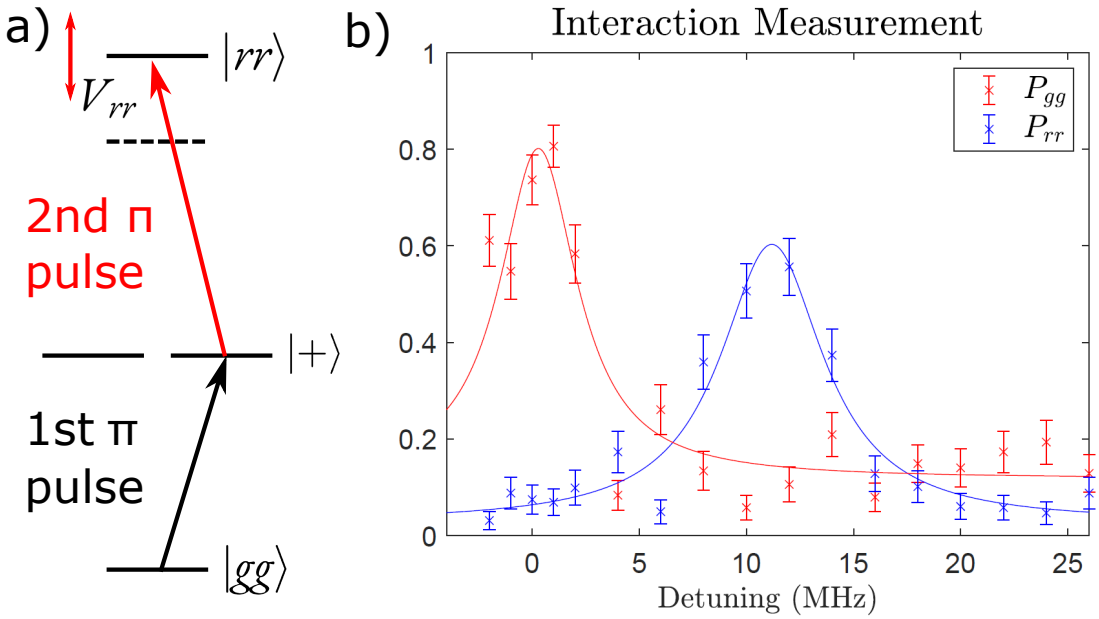

Figure 3.15: (a) The measurement scheme for determining the Rydberg-Rydberg interaction strength V_{rr}. A π pulse is used to bring atoms from $|gg\rangle$ to the $|+\rangle$ state. The second π pulse frequency is scanned across the $|rr\rangle$ resonance. (b) An example of such a measurement. When the detuning of the second pulse is the same as the first, the atoms are returned to the $|gg\rangle$ state. Otherwise, when the frequency difference matches the interaction V_{rr}, the $|rr\rangle$ state is populated.

Figure 3.15b shows an example of such a measurement. A peak in the $|gg\rangle$ population is found at 0 detuning (from the first pulse), while a peak in the $|rr\rangle$ population is found at approximately 11 MHz, which is the interaction strength of this particular pair of atoms. We note that at higher interaction strengths, the resonance tends to be broader due to finite temperature effects. Larger interaction strengths correspond to smaller distances, where position fluctuations due to finite temperature play a larger role in changing the interaction strength. The interaction measurement, and its dependence on distance, is our best measurement of the atoms' relative positioning. It can also

track any differences in the z (axial) positioning of the atoms (discussed more in section 5.4). Along with the numerically determined C_6 value, these measurements provide a calibration of the relative positions of the atoms.

3.6 Summary and Outlook

In this chapter, we reviewed the properties of high principal quantum number states (Rydberg states) and in particular discussed their sensitivities to external fields and their interactions. At principal quantum numbers of $n = 54$, we can observe tens of MHz scale interactions at around 3.5-4 microns, which are reasonable distances for SLM created tweezer arrays. Realizing these properties in the lab requires coherent excitation of ground state atoms, which we achieved with a two photon excitation via the $7P_{3/2}$ state using lasers at 455 nm and 1060 nm. We have achieved Rabi frequencies of up to 2.5 MHz, and coherence times of individual atoms of up to 20 μs. These Rabi frequencies require tight focusing, and the long coherence times require careful attention to control all sources of noise, including DC electric fields, laser intensity and phase noise. With coherent excitation in our toolbox, we can observe interactions between Rydberg atoms either through enhanced frequency blockaded Rabi oscillations or through direct spectroscopy of the $|rr\rangle$ state.

The critique of Rydberg platforms, especially for the purposes of quantum computing, typically revolve around the fundamental limitation of the Rydberg lifetime. Unlike molecules [66,163,13,104,176] and trapped ions [38], for instance, which have long-lived interacting states, neutral atoms need to be excited to high principal quantum number states in order to achieve usable interaction scales (relative to the lifetime). Thus, improvements focus on two fronts: increasing the effective lifetime of the atoms and increasing the Rabi frequency which governs the Rydberg dynamics used in computing and simulation applications.

As discussed in section 3.2, the lifetime of Rydberg states increase at higher principal quantum

number. However, to use these states, precise electric field control is required. Our experiment currently lacks the in-vacuum electrodes required for this control. At these higher principal quantum numbers, stimulated absorption and emission of blackbody radiation [20] plays a larger role as well, motivating the use of cryogenic setups [202,178,46]. Another possibility is to make use of circular Rydberg states [161,56]. Since they have the largest possible angular momentum for a given principal quantum number, optical decay channels are suppressed leading to lifetimes at the milliseconds level. Furthermore, these decay channels are in the microwave regime, where microwave cavities can be built to further suppress spontaneous emission rates through modification of the electromagnetic field modes of vacuum [237]. Creating circular Rydberg states has been achieved with circularly polarized microwave and RF fields [46] and arrays of circular Rydberg atoms have been trapped in repulsive pondermotive traps created from hollow optical bottle beams [182]. These capabilities would need to be integrated into our system, but have been demonstrated before.

In our typical experiments with cesium, other time scales come into play before the Rydberg lifetime. For instance, in a two-photon transition, the intermediate state scattering poses another limitation. This effect can be completely eliminated by using a single photon excitation, which is technically challenging since it would be require a coherent 319 nm laser source. Electric field stabilization, better beam uniformity and intensity stabilization will also help to increase the coherence time, which is also shorter than the lifetime.

Increasing the Rabi frequency of the Rydberg beams allows for more coherent dynamics within a coherence time. In our system, this can be achieved in various ways. Currently, our power for the 2nd leg IR is limited by the fiber delivery and not our fiber amplifier. We can switch out the end-capped fiber for a photonic crystal fiber, with a larger mode field diameter. Another improvement we can make is to use a SLM to shape our Rydberg beams into a tophat, utilizing our power more efficiently while maintaining uniformity.

The quantum science of these two atom systems is relatively simple and well understood. How-

ever, from chapter 2, we have developed all the techniques necessary to create large defect-free tweezer arrays of many atoms. Observing Rydberg physics on these large arrays will be the focus of the next chapter.

4

Interacting Arrays of Rydberg Atoms - Probing Critical Phenomena

4.1 Introduction

Tweezer arrays of Rydberg atoms have been used to study many models in condensed matter physics [35] including SSH models [64], dipolar XY models [51], XXZ models [200], XYZ models [200,215] and long-range

Ising models [19,74,198,248]. Confronted with this alphabet soup of models, we will briefly review what these models are and then discuss their implementation in Rydberg systems.

An XYZ model has anisotropic spin-spin interactions in all 3 spatial directions

$$H = \sum_{i<j} (J_{xx}(i,j) S_i^x S_j^x + J_{yy}(i,j) S_i^y S_j^y + J_{zz}(i,j) S_i^z S_j^z) \tag{4.1}$$

where i and j are site labels and x, y and z label the spatial directions. When $J_{xx} = J_{yy}$, the resulting model is called an XXZ model, where the interactions are isotropic in the two transverse directions. When $J_{zz} = 0$, but $J_{xx} = J_{yy} \neq 0$, then the resulting model is called a XY model. When $J_{xx} = J_{yy} = 0$, and $J_{zz} \neq 0$, this is known as an Ising model. Note that for all of these models, the strength coefficients J_{xx}, J_{yy} and J_{zz} can have a non-trivial dependence in space. For example, XY models often are found in systems with dipole-dipole interactions, where the dipole operator can flip spin states. If the dipole-dipole interaction is the cause of J_{xx} and J_{yy}, then these coefficients will have a $1/r_{ij}^3$ dependence. Hence, a XY model with this $1/r_{ij}^3$ distance dependence is known as a dipolar XY model. The Ising model also typically is a nearest neighbor model only, namely $J_{zz}(i,j) = 0$ for all i,j that are not nearest neighbor. To be more explicit, one can also call this the nearest-neighbor Ising model.

In addition to these two-body interaction terms, a "field" term can be applied that has the form

$$H = \sum_i (J_x S_i^x + J_y S_i^y + J_z S_i^z). \tag{4.2}$$

For instance, a transverse-field Ising model has $J_x \neq 0$, and $J_{zz} \neq 0$. Lastly, the SSH model [217] is a lattice model with nearest-neighbor hopping of alternating strength

$$H = v \sum_{i=1,3,5,\ldots} (a_i^\dagger a_{i+1} + a_i a_{i+1}^\dagger) + w \sum_{i=2,4,6,\ldots} (a_i^\dagger a_{i+1} + a_i a_{i+1}^\dagger) \tag{4.3}$$

where v, w are hopping strengths and a_i and $a_i^\dagger$ are the annihilation and creation operators for a particle on site i. This model is one of the simplest ones that exhibits topological features [10].

We now turn to the implementation of these models with tweezer arrays of Rydberg atoms. Rydberg interactions have been described in section 3.2.2 and arise from diagonalizing the dipole-dipole interaction in a pair-state basis that could involve an infinite number of states. Typically, these interactions are in one of two regimes, a non-resonant $1/r_{ij}^6$ regime and a resonant $1/r_{ij}^3$ regime. Let's consider a spin-1/2 encoding where our two spin states are a ground state $|g\rangle$ and a Rydberg state $|r\rangle$. In this basis, the Rydberg interactions are described by the operator $n_i n_j$, where $n_i = |r\rangle_i \langle r|_i$. This interaction, in the spin-language and encoding, acts like a $S_i^z S_j^z$ term. Adding a laser drive at a particular detuning Δ and Rabi frequency Ω yields a long-range transverse-field Ising model

$$H = \sum_i \left(\frac{\hbar\Omega}{2} \sigma_i^x - \hbar\Delta n_i \right) + \sum_{ij} V_{ij} n_i n_j \tag{4.4}$$

where $\sigma_i^x = |g\rangle_i \langle r|_i + |r\rangle_i \langle g|_i$ and $V_{ij} \sim 1/r_{ij}^6$ and arises from the long-range van der Waals interaction. This Hamiltonian is one of the easier Hamiltonians to engineer, only requiring arrays of atoms with Rydberg excitation.

Another encoding (basis) that we can use for our studies is a Rydberg-Rydberg encoding where our two spin states are two Rydberg states, $|r\rangle$ and $|r'\rangle$, which are dipole connected. In this case, the dipole-dipole interaction couples the $|rr'\rangle$ pair state resonantly with the $|r'r\rangle$ state leading to a Hamiltonian of the form [34]

$$H = \sum_{i<j} \frac{d^2(3\cos^2\theta_{ij} - 1)}{r_{ij}^3} (\sigma_i^+ \sigma_j^- + \sigma_i^- \sigma_j^+), \tag{4.5}$$

where d is the transition dipole moment between $|r\rangle$ and $|r'\rangle$, θ_{ij} is the angle between the $\mathbf{r}_{ij}$ vector and the quantization axis, and the $\sigma_i^\pm = \sigma_i^x \pm i\sigma_i^y$ are the raising and lowering operators in this spin-

1/2 encoding. The raising and lowering operators essentially perform a resonant exchange from the $|rr'\rangle$ state to $|r'r\rangle$ state. This dipole-dipole interaction is also anisotropic, which is illustrated with the $3\cos^2\theta_{ij} - 1$ dependence. This Hamiltonian for a linear 1D chain, or a 2D system where the quantization axis is perpendicular to the array, directly implements the dipolar XY model which has been studied experimentally [51]. However, an effect that needs to be accounted for is the residual van der Waals interaction of $|rr\rangle$ and $|r'r'\rangle$ which arises from off resonant coupling to other pair states. These effects add additional ZZ terms in the Hamiltonian. Utilizing the dipolar interaction in this basis with an arbitrary starting state requires site-selective excitation using microwaves between these Rydberg states. Typically, this is achieved with site-dependent light shifts with a laser beam.

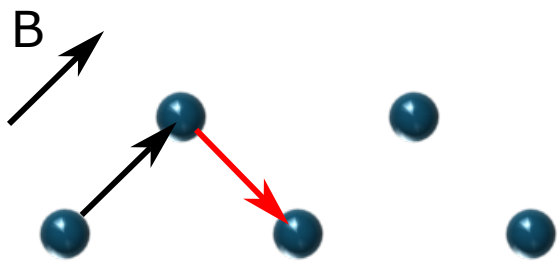

Figure 4.1: Geometry for implementing the SSH model with a Rydberg-Rydberg encoding. The anisotropic nature of the dipole-dipole interaction leads to alternating interaction strengths between atoms that form the chain. The two types of bonds are indicated in black and red.

This dipolar XY model can be used to implement the SSH model [64]. Consider atoms organized in a way such that the distances between any nearest neighbor atoms is the same, but the angle between the vector connecting odd numbered atoms to the next even numbered atoms differs from the vector connecting even numbered atoms to the next odd numbered atoms (shown in figure 4.1). This can be achieved by first placing the atoms in a line and then shifting all the even numbered atoms out of the row of atoms, resulting in a zig-zag shape. Then, due to the anisotropy of the dipolar XY model, the couplings between nearest neighbor sites exhibit an alternating pattern due to the

angular dependence of the dipole-dipole interaction.

Another way to engineer the interaction is to use the idea of Floquet physics[98,226,85,53], where the Hamiltonian is periodically modulated at a timescale much faster than the time dynamics one wants to observe. In this case, at these slower time scales, an effective Hamiltonian is implemented. In the Rydberg case, microwaves driving between $|r\rangle$ and $|r'\rangle$ can be applied periodically to effectively change the basis of the instantaneous interaction and all the parameters of a XYZ Hamiltonian can be controlled[200]. Floquet engineering can also be applied in the $|g\rangle$, $|r\rangle$ basis to realize a modified Ising interaction[248].

A disadvantage of using a Rydberg atom in the encoding is the finite lifetime of these Rydberg states. By changing the laser detuning, Δ, from the Rydberg state, one can control the admixture or dressing of the Rydberg state into the ground state. This dressing of the ground state can thus engineer interactions between ground state atoms but with longer lifetimes. Ensuring that the laser mostly only dresses one of two hyperfine ground states yields a model, once again with ZZ-like interactions. This technique is known as Rydberg dressing[118,105]. Despite the familiar interaction, this scheme produces an interaction strength with a non-trivial dependence on distance. The distance dependence of the dressed-state energy arises from the distance dependence of the Rydberg-Rydberg interaction itself. At distances where $\Delta \gg V_{ij}$, changes in distance do not significantly change the admixture of the Rydberg state in the ground state, but it does shift the energy of the dressed state proportionally. However, when $V_{ij} \gg \Delta$, corresponding to lower distances, the $|rr\rangle$ state is shifted farther out of resonance and the admixture of the state rapidly drops even if the interaction increases. The result is a relatively flat dependence of the dressed state energy as a function of distance for small distances. The short-range behavior of this potential is known as a "soft-core" potential. The dynamics of an Ising model with this soft-core potential has been experimentally studied[245]. Utilizing multiple Rydberg dressing lasers for both hyperfine states, one can engineer XYZ Hamiltonians[83,215].

For the work in this thesis, we will use a ground Rydberg encoding of states and study the long range transverse field Ising model of equation 4.4. In section 4.2, we discuss the salient features of the model with a focus on the quantum critical point (Ising) present in this model. Sections 4.3 to 4.6 focus on our experimental efforts to probe the critical point in both one and two physical dimensions.

4.2 The Long Range Transverse Field Ising Model using Rydberg Atoms

Our goal is to study the ground state physics of this Rydberg model. We first consider a 1 dimensional system consisting of all atoms in a line. As a thought experiment, let's first consider what happens when $\Omega = 0$, such that product states of $|g\rangle$ and $|r\rangle$ are eigenstates of the full Hamiltonian*. In this case, at large negative detuning, there is an energy cost to having Rydberg excitations. Thus, the many-body ground state, $|gg...\rangle$, consists of all atoms in the ground state. As the detuning increases towards positive detuning, Rydberg atoms lower the total energy of the state, encouraging the presence of Rydberg atoms in the ground state. However, the distance dependent repulsive interaction V_{ij} between Rydberg atoms disfavors exciting nearby atoms to the Rydberg state. If the so-called blockade radius includes nearest neighbors, then the ground state becomes ordered states, $|grgr...\rangle$ or $|rgrg...\rangle$ that staggers the Rydberg excitations spatially, satisfying both the detuning and interaction terms. We call the resulting states as $\mathbb{Z}_2$ ordered states, since they only obey the symmetry of translation by *two* lattice sites, instead of states that are fully translationally symmetric. As the interaction increases, it becomes costly for even next-nearest neighbors to be in the Rydberg state (i.e. the next-nearest neighbors are within a blockade radius). Thus, the ground state consists of so-called $\mathbb{Z}_3$ ordered states $|ggrggr...\rangle$, $|grggr...\rangle$, and $|rggr...\rangle$. In 2 dimensions, more interesting states

*This scenario is meaningless physically because the Δ term only arises from the laser drive. When $\Omega = 0$, tuning Δ is impossible and non-sensical. Nevertheless, as a Hamiltonian, we can still theoretically consider its properties.

can arise in addition to the simple $\mathbb{Z}_2$ checkerboard state as a function of the interaction strength. Using arbitrary geometries, finding the ground state of this Hamiltonian at a particular blockade radius results in a "packing problem", where one wants to pack as many Rydberg atoms as possible while reducing any unwanted repulsive interactions from putting the atoms too close to each other. In graph theory, this problem maps exactly to the NP-hard maximum independent set problem, and a Rydberg atom quantum simulator has been used to tackle this problem efficiently[73]. The experimental platform is prepared in the ground state and then a measurement is performed to determine what is the densest packing of Rydberg atoms possible that obey the blockade constraint.

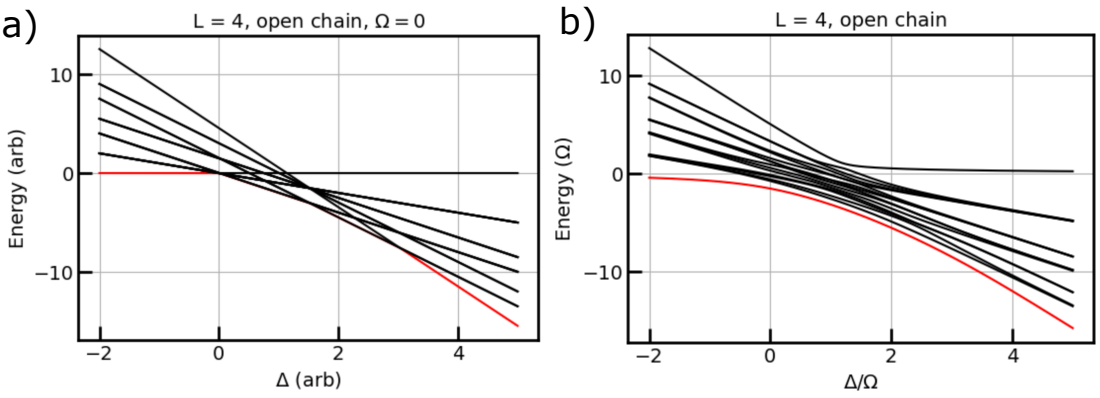

Figure 4.2: Exact diagonalization for the Rydberg model (equation 4.4) at a system size of $L = 4$. Calculations are performed for a nearest neighbor interaction strength of 1.5 in arbitrary units. The eigenenergies are plotted against the detuning, and the red line illustrates the ground state energy. In (a), $\Omega = 0$ (which is nonphysical) for illustrative purposes, while in (b), $\Omega = 1$.

Now, equipped with an understanding on the basic features of this Hamiltonian, we now need to add the important effect of the $\frac{\Omega}{2}\sigma_i^x$ term. Without the drive term, the total excitation number $\sum_i n_i$ is a conserved quantity, and as a function of Δ, states will cross as shown in figure 4.2a. In particular for a blockade radius that would lead to a $\mathbb{Z}_2$ state, the ground state at large negative detuning $|gg...\rangle$ will eventually cross with the $\mathbb{Z}_2$ ordered states. However, with the drive term

present, a gap opens and this crossing becomes an avoided crossing (see figure 4.2b). As the system size grows (shown in figure 4.3b), this gap closes signaling the presence of a quantum phase transition [191,230,212]. The location of the gap closing is known as the critical point. The quantum phase transition is called such since our entire framework strictly describes a $T = 0$ phenomenon, i.e. it is a ground state phenomenon. Classical phase transitions are driven by thermal fluctuations, while quantum phase transitions are driven by quantum fluctuations caused by the non-commuting[†] $\frac{\Omega}{2}\sigma_i^x$ term. The theory of quantum phase transitions can be extended to finite temperatures.

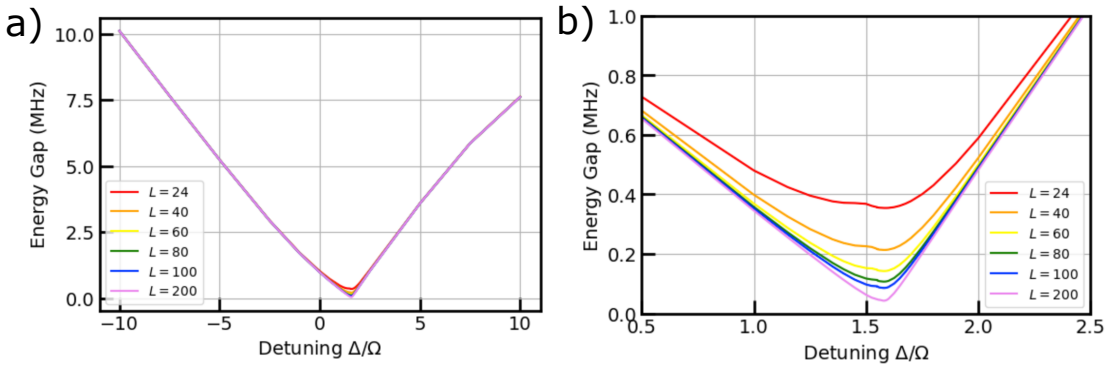

Figure 4.3: (a) The energy gap between the first excited state and ground state of the Rydberg model (equation 4.4) as a function of detuning Δ for different system sizes on a ring. (b) Zoom in of (a)

At the critical point of a quantum phase transition, much like its classical counterpart, the correlation time and subsequently the correlation length diverges, leading to scale invariance. A diverging correlation length means that fluctuations exist across all length scales so the system looks the same, no matter which scale the system is viewed at. Since the physics of our system must look the same upon a scaling transformation, its properties must be described by self-similar functions, which have the following property

[†]Non-commuting here means with respect to the other terms of the Hamiltonian. This leads to an effective Heisenberg uncertainty principle which disallows a simple ground state that is a product state.

$$f(bx) = b^{\alpha} f(x) \tag{4.6}$$

for arbitrary b and some α. In other words, scaling a system's coordinates by a factor b, results in the exact same functional form, where we allow the y-axis or function result to be scaled as well by b^{α}. Functions that satisfy this relation consist of power law functions $f(x) = x^{\alpha}$. A graphical depiction of this special feature of self-similarity is shown in figure 4.4 contrasting a quadratic function with an exponential function. At the two different scales, the quadratic looks exactly the same while the exponential clearly changes shape.

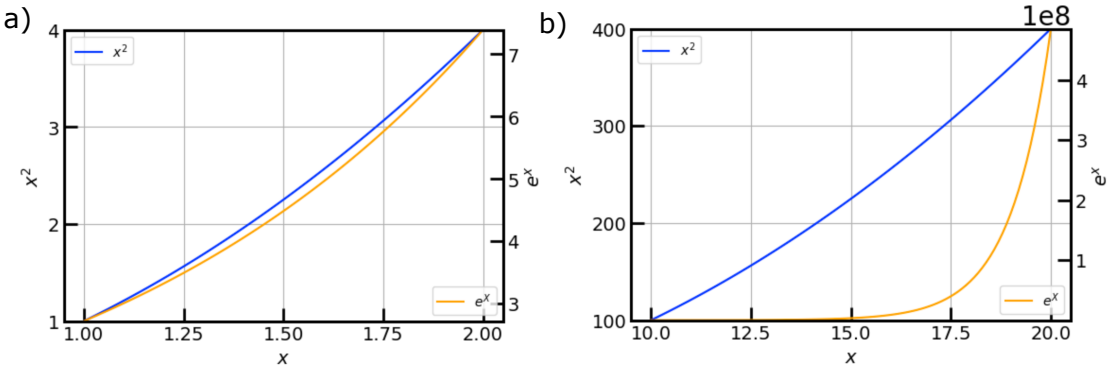

Figure 4.4: Comparing a quadratic function (power law) with an exponential at two different scales in (a) and (b). The shape of the exponential function changes dramatically compared to the power law.

Another key feature of the critical point is universality[214,242], beautifully observed in 1945[95] showing the universality of the critical point of a liquid-gas transition across many different chemical compounds. In this system, the liquid-gas density difference $\rho_l - \rho_g$ becomes zero at the critical point, but upon approach to the critical point, the density is a power law function of the deviation from the critical point

$$\rho_l - \rho_g \propto \left(-\frac{T - T_c}{T_c}\right)^{\beta} \tag{4.7}$$

with a so-called critical exponent β. The temperatures and densities of 8 fluids near the critical point were shown to collapse on each other when normalized with the non-universal critical temperature T_c and density ρ_c, i.e. when T/T_c was plotted against ρ/ρ_c. A critical exponent of approximately $\beta = 1/3$ was found. The same critical exponent was found for a ferromagnetic-paramagnetic critical point [102] and a critical point in a mixture of CCl_4 and C_7F_{16} [223]. A simple explanation for universality is as follows: since the correlation length diverges, properties of the state cannot depend on the microscopic details of the Hamiltonian but only on the symmetry and dimension of the system. In these cases, a choice between two phases means that these critical point belong to the $\mathbb{Z}_2$ Ising universality class [242].

The $\mathbb{Z}_2$ Rydberg phase transition also belongs to this universality class and its critical exponents has been studied both in 1D [124] and 2D [74] in atom arrays previously utilizing the Kibble-Zurek mechanism [125,252]. The Kibble-Zurek mechanism is a dynamical method that monitors the final correlation length of the system as a function of ramp speed and gives access to the dynamical exponent z and critical exponent ν. If the ramp speed is infinitely slow, then the correlation length can grow to infinity, but if it has finite speed, then correlations will only have enough time to build up to a finite value. However, the scaling of the correlation length with ramp speed depends universally on the critical exponent combination $z\nu$. The Kibble-Zurek mechanism has also been used in other quantum simulators such as trapped-ion systems [60,139], atomic-gases [9] and superconducting circuits [72] to measure critical exponents.

In our work, we want to probe the critical point using a more direct method: namely preparation of the ground state at the critical point. We seek to directly observe power-law behavior of the correlations of observables and spatial scale-invariance. It turns out for our system, there is a more

powerful symmetry at play. The Rydberg model critical point exhibits conformal invariance, where the system is invariant under conformal transformations which locally preserves angles. Thus, the Ising conformal field theory (CFT) describes the low energy physics at the critical point[211]. The Ising CFT is described by two primary fields, the σ and ε fields, which can then be used to calculate all critical exponents. These continuous fields need to be placed on a lattice, which depends on the geometry, dimension and boundary conditions of the lattice.

In a 1D Rydberg atom array with periodic boundary conditions, the primary field σ, known as the spin field, is represented, at leading order[211], by the microscopic lattice operator

$$\sigma_i = (-1)^i (n_i - \langle n \rangle). \tag{4.8}$$

In the quantum critical ground state, $\langle \sigma_i \rangle = 0$ on each site, but its two-point correlator $\langle \sigma_0 \sigma_j \rangle$ decays as a power law,

$$\langle \sigma_0 \sigma_j \rangle \propto \delta_j^{-2\Delta_\sigma^{1D}}, \tag{4.9}$$

where $\delta_j/a = \frac{N}{\pi} \sin\left(\frac{\pi j}{N}\right)$ is an effective spatial separation (chord distance) that accounts for the periodic boundary condition[211]. The exponent of this power law, also known as η, is twice the scaling dimension, $\Delta_\sigma^{1D} = 1/8$, of the (1+1)d Ising CFT[‡].

The other primary field ε, known as the energy field, can be similarly represented, at the leading order in 1D, by a microscopic lattice operator[211]

$$\varepsilon_{i+1/2} = (n_i + n_{i+1}) - \langle n \rangle. \tag{4.10}$$

[‡](1+1)d is the conventional naming scheme for quantum phase transitions[191]. Here, the two 1s refer to a single spatial and time dimension.

The two-point correlator $\langle \varepsilon_{1/2}\varepsilon_{j+1/2}\rangle$ decays as a power law

$$\langle \varepsilon_{1/2}\varepsilon_{j+1/2}\rangle \propto \delta_j^{-2\Delta_\varepsilon^{1D}}, \tag{4.11}$$

where $\Delta_\varepsilon^{1D} = 1$, predicted by the (1+1)d Ising CFT.

Nicely, these microscopic operators for the CFT primary fields are entirely in the Z basis, allowing for just measurements of the Rydberg population to be enough to experimentally measure these correlations. The main novel result of our work will be to directly measure these scaling dimensions via adiabatic preparation of the ground state wavefunction at the critical point. In section 4.3, we will detail how we prepare defect-free arrays in the geometries we want and how to prepare the atoms for excitation. In section 4.4, we describe how to experimentally locate the critical point. Next, in section 4.5 we measure a critical exponent in one dimension, consistent with theoretical expectations, while overcoming the challenges brought upon by decoherence. Finally, in section 4.6, we make measurements in two dimensions, where boundaries emerge as a major challenge but also provide an opportunity to observe the physics related to boundary phase transitions.

4.3 Experimental Parameters

For these experiments, we use cesium atoms. Critical exponents are most easily extracted in systems with periodic boundary conditions[211]. In 1D, this can be accomplished by arranging atoms in a ring. The ring needs to be large enough so that interactions between farther neighbors are negligible. If these interactions are not negligible, then there will be a significant difference between the geometry of a ring and true linear chain with periodic boundary conditions. Nevertheless, for all our numerical simulations, we are able to place the atoms in their true locations and confirm that we can still theoretically observe the correct critical phenomena.

We place the atoms on the ring such that the interaction strength is on average about 12 MHz.

However, we measure a static interaction homogeneity (standard deviation/mean) to be 26% for a 24 atom ring and 20% for a 40 atom ring. The true interaction inhomogeneity can also be incorporated into numerical simulations. For 2D experiments, since we cannot easily create periodic boundary conditions, we perform our experiments on rectangular geometries with open boundaries.

For our experiments, it is very important to create and use data from defect free arrays. We perform atom rearrangement as described in section 2.5. During rearrangement, we grab atoms using AOD tweezers at approximately twice the trap depth of the static SLM tweezers. The AOD tweezers are turned on and off in about 200 μs and moved at about 110 μm/ms.

We design our rearrangement algorithms to operate on grids. The sequence of atom moves and ejections must be tailored to the geometry of the SLM tweezers. Each SLM array includes both 'target' sites belonging to the desired defect-free pattern and 'reservoir' sites supplying additional atoms to fill unloaded target sites. In both 1D and 2D, we are careful to minimize the number of grab and drop events (which can lead to loss) of the atoms.

1D rearrangement procedure. For our 1D experiments on a ring, we load additional atoms into rows and columns of traps situated around and inside the ring to serve as a reservoir. This reservoir is designed to maximize connectivity along a row/column, reduce redundancies, and enforce a minimum spacing between traps (see figure 4.5). The reservoir choice, and its subsequent success rate, can be simulated. The simulation guides the reservoir design. While the AOD is capable of simultaneously producing multiple tweezers, we only use a single mobile tweezer to rearrange atoms on a ring. This minimizes atom heating due to beat-note frequencies of adjacent tweezers moving over a non-uniform grid, which would otherwise cause trap depth modulations on the order of our trap frequencies. The detailed rearrangement procedure is illustrated for a particular example in figure 4.5.

First, row by row, we shuffle atoms horizontally to columns that need additional atoms to reach their targets (refer to figure 4.5a). Green arrows denote atoms that are moved in order to fill the

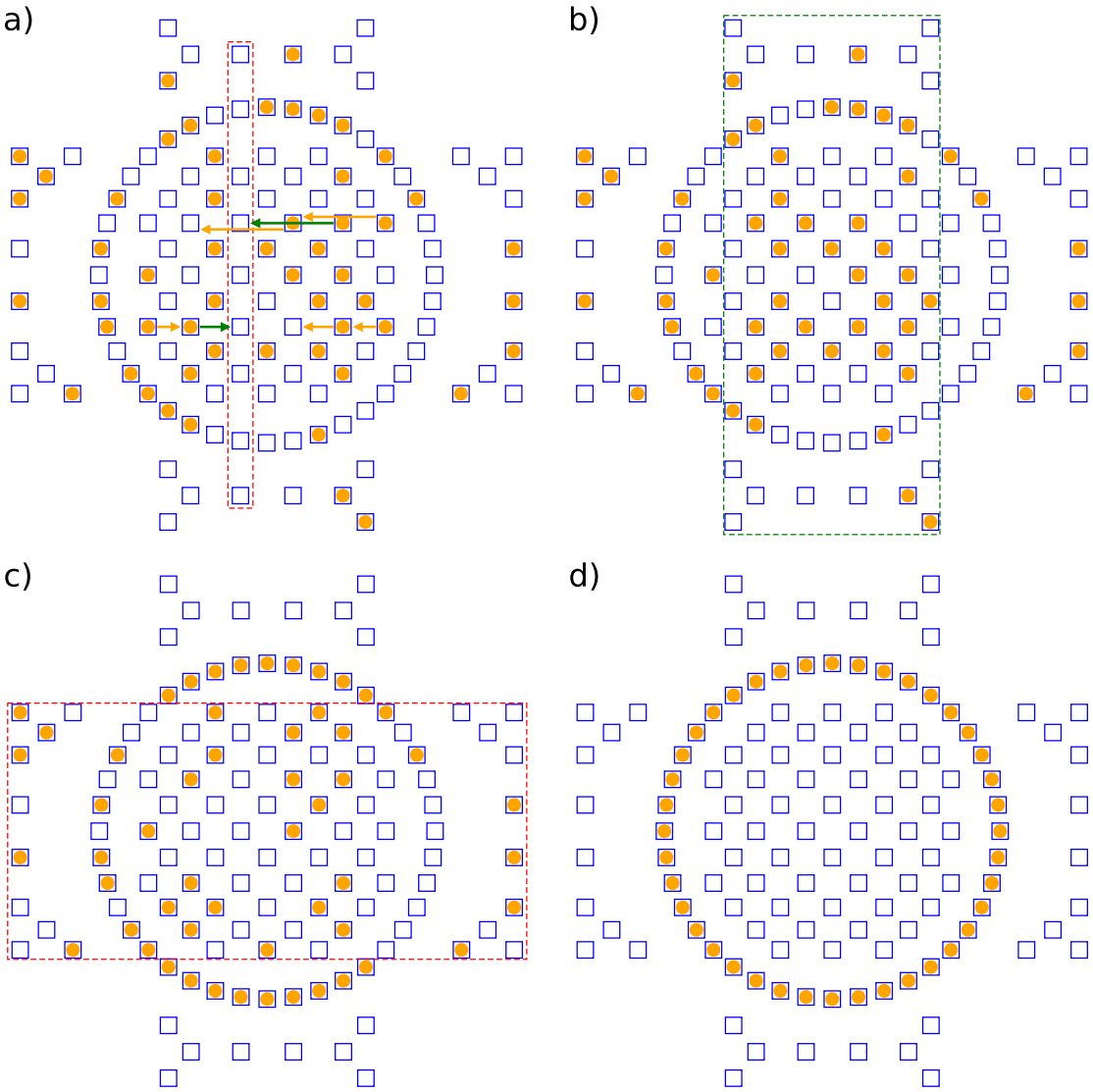

Figure 4.5: Rearrangement procedure in 1D for a 40-atom ring. Blue squares denote locations of SLM traps, and orange circles denote the locations of atoms. Each target site on the ring is associated with a reservoir row or column. The details of the procedure are in the main text.

deficient red column. Orange arrows denote atoms that are moved to more central columns to contribute more atoms to the next step. We note that if all columns have a sufficient number of atoms,

this step can be skipped. Furthermore, not all rows will be moved. The result of such movements is shown in figure 4.5b. Then, column by column (within the green rectangle in figure 4.5b), we shuffle atoms vertically to their target sites, ejecting any unneeded atoms and also filling rows that need additional atoms. Importantly all atoms are now in the central rows (see figure 4.5c) which will be targeted in the next step. Next, row by row (within the red rectangle in figure 4.5c), we place the remaining atoms into the target sites, while ejecting unneeded atoms. After the previous rearrangement steps, a defect free ring (see figure 4.5d) is achieved.

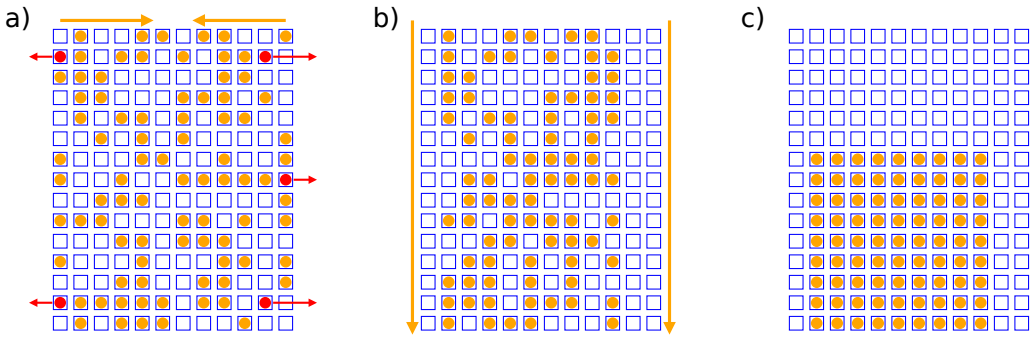

Figure 4.6: Rearrangement procedure in 2D for a 9x9 rectangular array. Blue squares denote locations of SLM traps, and orange circles denote the locations of atoms. (a) Row by row, we shuffle atoms horizontally to columns that need additional atoms and eject unnecessary atoms (red arrows). Note that atoms in the final target region are moved as little as possible (b) We move all atoms downward to the bottom of the array (c) After the previous rearrangement steps, a defect free rectangular array is achieved.

2D rearrangement procedure. For our 2D experiments, we rearrange over a rectangular array. Because of the regular geometry, atoms of a given row or column can be simultaneously rearranged by AOD tweezers without low frequency beatnotes, allowing us to move atoms in parallel without substantial heating. The detailed procedure is in the caption of figure 4.6.

Following rearrangement, we optically pump atoms to the ground state $|6S_{1/2}, F = 4, m_F = 4\rangle$ in an 8.8 G magnetic field. We perform 3D Raman sideband cooling to reduce the average motional

quantum number $\overline{n}$ to less than 0.1 [144], taking approximately 100 ms. Following Raman sideband cooling, we adiabatically lower the trap in about 100 μs before turning it off completely during the Rydberg excitation. Although releasing the atom from a lower trap depth results in lower kinetic energy, the position distribution is wider resulting in greater sensitivity to static positional disorder. However, at a higher trap depth, releasing the atom results in greater kinetic energy, so the atom will move more during the Rydberg excitation. The optimal trap depth for release is numerically determined to be $2\pi \times 1.4$ MHz with radial and axial trap frequencies of $2\pi \times 30$ kHz and $2\pi \times 4.7$ kHz, respectively, by minimizing the atom position distribution $\sigma_r + \sigma_v \times t_{evolve}$ during state evolution, where σ_r and σ_v is the spread of the initial atom position and momentum upon trap release.

When the atoms are in the dark, we coherently excite atoms to the Rydberg state using a two-photon transition via the intermediate state $7P_{3/2}$, with counter-propagating laser beams at 455 nm and 1062 nm to the $54S_{1/2}$ state. The Rydberg excitation beams are shaped into elliptical Gaussian beams to improve their intensity uniformity across the array, with $(\omega_x, \omega_y)_{455} = (87, 137)$ μm and $(\omega_x, \omega_y)_{1062} = (64, 208)$ μm at the position of the atoms. In a typical experiment, the powers of each laser are chosen to achieve single-photon Rabi frequencies of $(\Omega_{455}, \Omega_{1062}) \approx 2\pi \times (80, 42)$ MHz. We operate at an intermediate state detuning of 1.06 GHz, and the two-photon Rabi frequency ranges from 1 to 1.6 MHz. For details of the laser system, see section 3.3.

4.4 Locating the Critical Point

Before we can observe critical exponents at the critical point, we need to determine the location of the critical point experimentally. First, it is important to note that at finite system sizes, different metrics (such as location of the minimum gap between ground state and first excited state, maximum entanglement entropy, or maximum susceptibility $\frac{dn_{\text{ryd}}}{d\Delta}$) for the critical point may differ from each other. However, these metrics all converge to a single value in the thermodynamic limit. In 1D,

and at our experimental system sizes larger than 24 sites, we find that all these metrics are reasonably close, from the perspective of finding the right critical exponent. The critical exponent itself varies smoothly but relatively quickly (at the 10% level with a 5-10% uncertainty in the critical point location) as a function of the detuning. Experimentally, the easiest of these metrics to measure directly is the susceptibility, or derivative of the Rydberg population with respect to detuning. Ideally, if we can adiabatically prepare the ground state at every detuning, the average Rydberg population will grow the fastest at the critical point. Thus, we perform the following experiment: we start with all atoms (24 or 40 atoms in a 1D ring) in the ground state, which corresponds to the many-body ground state at infinite negative detuning or when $\Omega = 0$. Then, we ramp up the Rabi frequency[§] at a finite negative detuning. At larger negative detunings, faster ramps can be used, since the scale that sets the many-body gap at these negative detunings is the detuning itself. However, starting at larger negative detunings requires more frequency to be traversed to arrive at the final detuning, thus requiring longer time for the ramp. A tradeoff between the two for small system sizes can be found numerically, and the Rabi frequency ramp can be determined to be adiabatic by minimizing the amount of Rydberg population after the ramp. After the Rabi frequency ramp, we use a linear detuning ramp, stopping at various points to make a measurement of the Rydberg population. Characteristic data of the population as a function of the stopping detuning is shown with the red dots in figure 4.7a.

The immediate numerical derivative of the raw data is very noisy, and thus the peak determined from such an explicit derivative is not particularly robust and requires copious amounts of experimental data. Thus, we need to use data processing tools such as smoothing (averaging together nearby points) and interpolation (a polynomial fit of nearby points) to achieve robust results. The 4-step procedure is as follows:

1. Smooth the data for $\langle n \rangle$ as a function of Δ/Ω using the Savitsky-Golay filter [194]. A relatively

[§] We choose to ramp up linearly for simplicity, but more complicated ramp profiles can be used.

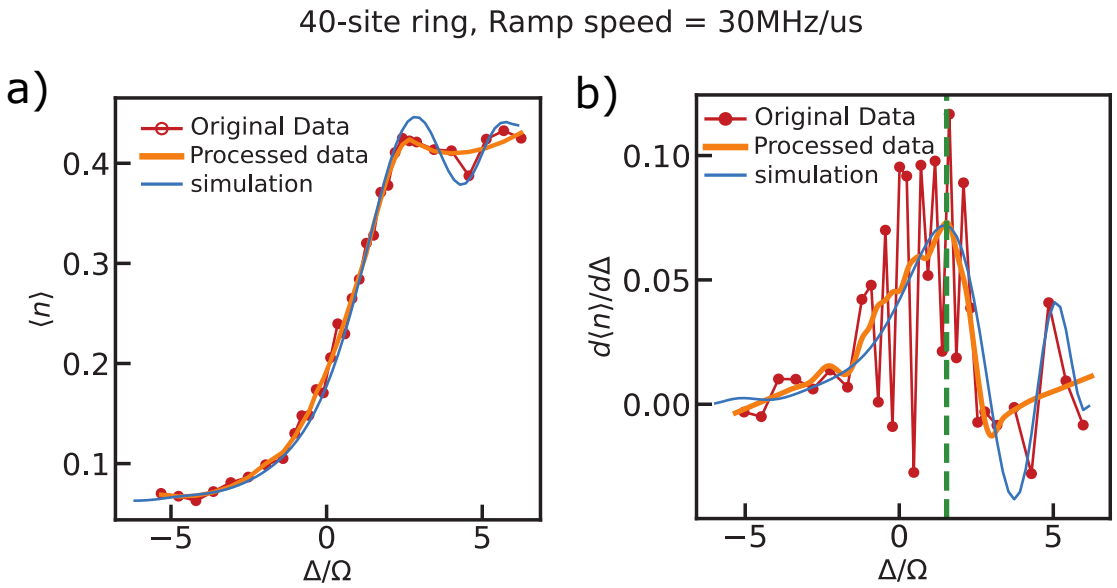

Figure 4.7: Exemplary dataset for determining the critical point location from a linear detuning ramp experiment (in this case, 30 MHz/μs). (a) Red circles: The raw data for the measured Rydberg population as a function of detuning (in units of Rabi frequency). Orange line: The data after processing with smoothing and interpolation. Blue line: The results of a numerical simulation that takes into account decoherence and initial atom loss. (b) Red circles: The numerical derivative of the measured Rydberg population. Orange line: The numerical derivative of the smoothed and interpolated orange data from (a) along with additional smoothing. Blue line: The numerical derivative of the simulation blue line from (a). The green dashed vertical line shows the location of the critical point, extracted from the peak of the orange line. The location is in good agreement with the one determined from the numerical simulation (blue line).

small window size is chosen to retain local features.

2. Intepolate the smoothed data (orange curve in figure 4.7a), which increases the resolution of determined critical point location, and allows us to better identify the critical point even if we don't take a data point exactly at the critical point.

3. Numerically differentiate with the central difference method to obtain the susceptibility.

4. Smooth the obtained susceptibility (orange curve in figure 4.7b) again with the Savitsky-

Golay filter and identify the location of the maximum value as the estimate for the maximum susceptibility for this dataset. In this case, we use a large window size for the filter in order to achieve robustness to noise-induced oscillations.

In order to choose the correct parameters and to fine tune this procedure, we applied this exact procedure to data from numerical simulations (blue curves in figure 4.7). The numerical results had contained about 300 points in Δ/Ω, but we only use about the 50 points we measure in experiment. This procedure works well and the extracted maximum susceptibility, $\Delta_{\max}$ is in good agreement from the nearly exact one determined from numerical simulations.

To determine whether our ramp is adiabatic enough, and thus providing data that can be used to estimate the critical point, we use linear ramps of different speed and measure $\Delta_{\max}$ in each case as a function of time[¶]. If the ramp is too fast, the system will not be able to follow the ground state completely and the resulting Rydberg population will lag behind the ground state expectation [22], as shown in the red data in figure 4.8. A similar effect is expected for first preparing the ground state at positive detuning (the antiferromagnet) followed by backward ramps at different rates. In this case, the lag of Rydberg state depopulation (or ground state population) will result in a peak that is shifted towards negative detuning as shown in the blue data in figure 4.8. The difference in the locations of these peaks for forward and backward ramps has been shown [22] to display universal features and can be used to extract the critical exponents z and ν. Although we do not quantitatively determine these critical exponents from these measurements, we do observe the correct qualitative features. Nevertheless our $\Delta_{\max}$ data as a function of sweep rate indicates that our slowest ramp speeds are adiabatic enough for a reliable determination of the critical point. We note that our method improves from previous approaches [74] involving cubic polynomial fits, since our method does not assume anything about the shape of the susceptibility curve. As can be seen in the blue simulation data in figure 4.7, the theoretical susceptibility is not symmetric leading to a systematic bias in the

[¶] The time maps linearly onto the detuning in a linear ramp.

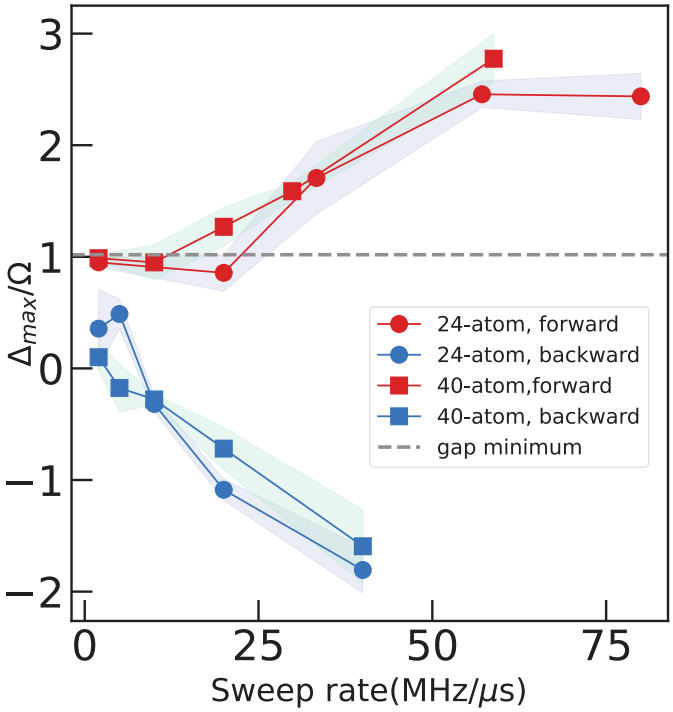

Figure 4.8: The extracted maximum susceptibility location, $\Delta_{\max}/\Omega$, as a function of linear sweep rate. Squares show data for 40 atom rings, while circles show data for 24 atom rings. Red data points indicate the extracted critical point, when performing forward ramps at different rates. Blue points indicate the extracted critical point when first adiabatically preparing an antiferromagnetic state (ground state at positive detuning) and then performing various backward ramps. For forward (backward) ramps, the maximum susceptibility is found at higher (lower) detunings for faster ramps. The horizontal dashed gray line indicates the location of the numerically calculated gap minimum location.

determination of the critical point using a cubic fit method. By using our slowest linear ramp data, we determine the critical point on our 1D ring to be located at $\Delta_c/\Omega = 0.97(5)$, where the errorbar is determined from bootstrapping (see Appendix A.2).

4.5 Extracting Critical Exponents in 1D

With our critical point now determined, we turn our attention to preparing the ground state at the critical point. The challenge of adiabatic preparation to a critical state arises from the vanishing gap (scales as $1/L$) at the critical point. However, at our finite system sizes, we can make use of the finite-size gap present in our system. To make the best use of our limited coherence times, we optimize the detuning ramp profile by taking into account the instantaneous energy gap and going slower when we have to and faster when we can afford it. We call our ramp profile the local linear adiabatic ramp (LILA).

Consider a system with the Rydberg Hamiltonian (equation 4.4) that is evolving in time according to a time-dependent detuning $\Delta(t)$ that starts at $\Delta(0) = \Delta_0$. According to the adiabatic theorem, the system will remain in the ground state of $H(t)$ at a later time t, provided that the evolution of the Hamiltonian is slow enough to satisfy [184,5,185]

$$\min_{t\in[0,T]} \left| \frac{E_g(t)^2}{\dot{\Delta}(t)} \right| \gg 1. \tag{4.12}$$

Here $E_g(t)$ denotes the time-dependent gap between the ground state and the first excited state of the instantaneous $H(t)$. Our goal is to maximize $\min_{t\in[0,T]} \gamma(t)$, where $\gamma(t) = \frac{E_g^2}{\dot{\Delta}}$ for a fixed time T, which is realized when $\gamma(t) = \gamma$ is a constant. Therefore, our task is to find a ramp profile $\Delta(t)$ that fulfills the condition

$$\frac{d\Delta}{dt} = \frac{E_g^2(\Delta(t))}{\gamma}. \tag{4.13}$$

with two boundary conditions $\Delta(0) = \Delta_0$ and $\Delta(T) = \Delta_c$. We solve this problem on a equal-spacing discretized grid in detuning with N points. We set $\Delta_{k=0} = \Delta_0$ and $\Delta_{k=N} = \Delta_c$, and $(\Delta_{k+1} - \Delta_k)T \ll 1$, where T is the total time. The corresponding time spacings can be solved for,

and we obtain

$$\Delta t_k = \frac{T}{E_g^2(\Delta_k) \sum_{k=0}^{n} 1/E_g^2(\Delta_k)}, \tag{4.14}$$

$$\gamma = \frac{T}{d\Delta \sum_{k=0}^{n} 1/E_g^2(\Delta_k)}. \tag{4.15}$$

This formula allows us to numerically evaluate an optimal ramp profile $\Delta(t)$ given a known gap profile $E_g(\Delta)$, an initial detuning Δ_0 and final detuning Δ_c, and a fixed total time T.

However, this solution requires knowledge of the gap at all detunings, which can be computationally expensive. To reduce the computational cost, we approximate the gap profile as linear around the critical detuning Δ_c:

$$E_g(\Delta) = E_0 + \frac{E_c - E_0}{\Delta_c - \Delta_0}(\Delta - \Delta_0). \tag{4.16}$$

We can see from figure 4.3a that this is a decent assumption. This results in an analytic solution:

$$\Delta(t) = \frac{E_0 \Delta_c t + E_c \Delta_0 (T - t)}{E_0 t + E_c (T - t)}, \tag{4.17}$$

$$\gamma = \frac{E_0 E_c T}{\Delta_c - \Delta_0}, \tag{4.18}$$

which is the optimized ramp profile that we call the LILA ramp. To determine this ramp, one now only needs two numerically calculated values: the gap at the critical point and the gap at some initial start detuning. The time is still a free parameter that can be used to ensure the adiabaticity of our ramp.

Utilizing the LILA ramp and our experimentally extracted critical points, we can now prepare critical states. We follow a similar procedure to locating the critical point which is summarized in

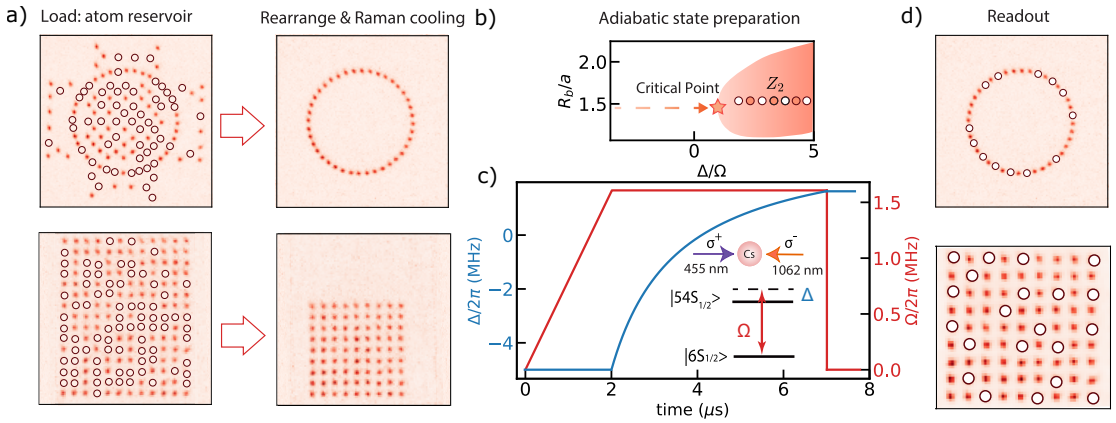

Figure 4.9: Experimental scheme for measuring critical correlations via adiabatic preparation. (a) First, we rearrange stochastically loaded atoms into either rings or square arrays to study 1D and 2D physics respectively. Raman sideband cooling is also performed on the arrays to ensure atoms are in their ground motional state. (b) A schematic of the quantum phase transition we are studying, which contains an Ising critical point. (c) The pulse sequence for an adiabatic preparation experiment. The detuning follows a LILA ramp. (d) Example of readout of $|g\rangle$ and $|r\rangle$ states after an experiment. Atom loss is interpreted as the $|r\rangle$ state.

figure 4.9. The adiabatic preparation procedure is shown in figure 4.9c, where we once again need to first perform an intensity ramp to ensure adiabaticity followed by a frequency ramp that now follows the LILA profile. Data arrives in the form of atom images (figure 4.9d), where Rydberg atoms are interpreted as atom loss, indistinguishable from actual atom loss. Upon postselection (detailed in appendix A.1) of reliable data, we obtain the σ field correlations as a function of chord distance δ_j depicted in figure 4.10a (star data) at the critical point. While the initial decay of the correlation appears to be scale-invariant and display power law decay, there is clearly a second non-universal length scale at play at longer distances. This suggests the presence of a mechanism that inhibits the formation of long-distance correlations.

To investigate this, we adiabatically prepare and characterize states away from the critical point, keeping the total preparation time fixed. In the antiferromagnetic phase, one analytically expects the

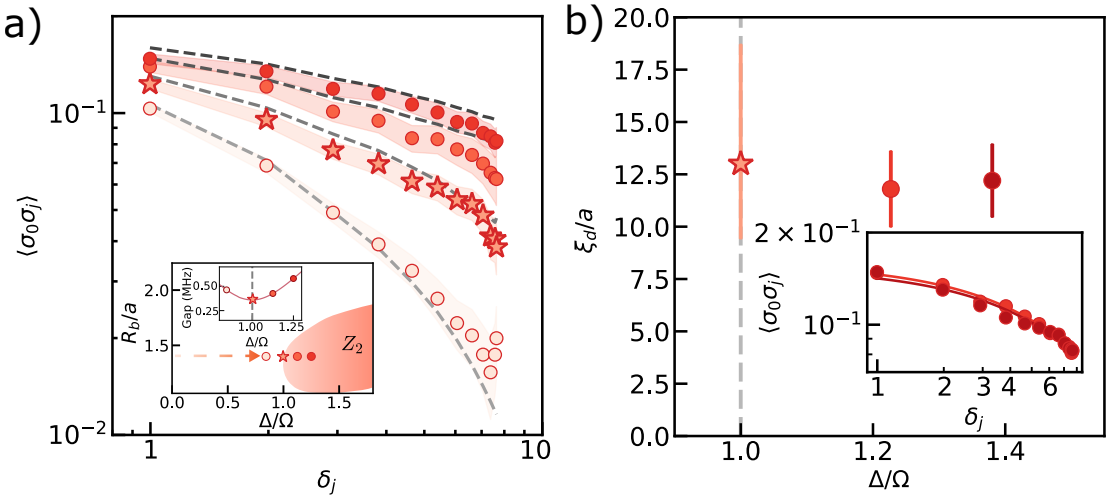

Figure 4.10: (a) The measured σ field correlators $\langle\sigma_0\sigma_j\rangle$ as a function of chord distance δ_j when performing the LILA ramp to different detunings. Darker shades of red indicate further detunings into the antiferromagnetic $\mathbb{Z}_2$ phase. Data with stars indicate data at the nominally extracted critical point. Shading indicates the errorbars for the correlator measurement as determined from bootstrapping (see Appendix A.2). The gray lines correspond to numerical simulations including the effect of decoherence. Inset: Schematic of the various stopping points in which we take data as well as where the phase boundary is located on a phase diagram of interaction strength (in units of blockade radius R_b over the lattice spacing a) and detuning (in units of Rabi frequency). The inset of the inset depicts the calculated gap profile for our 24 atom system and experimental parameters. (b) Extracted correlation lengths from the corresponding datasets in (a). The circular points located in the antiferromagnet have correlation lengths extracted with a simple exponential fit, depicted in the inset. For the critical point (star), the correlation length is fit from a power law times exponential as discussed in the text.

correlator, $\langle\sigma_0\sigma_j\rangle$, to exhibit a plateau at large distances, corresponding to long-range order. However, as shown in figure 4.10a (dark red curves), we again observe the rapid decay of correlations; in particular, we find that the σ field correlator exhibits an exponential decay with length scale $\xi/a = 12.0(13)$ (inset figure 4.10b). This raises the question: what is the microscopic origin of this length scale?

There are two natural possibilities. First, despite our best efforts, the long-distance correlations

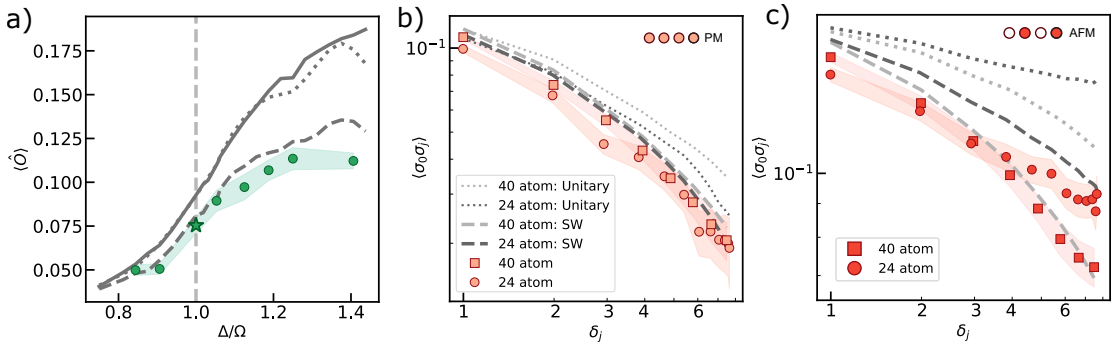

Figure 4.11: (a) The growth of the order parameter $\langle \hat{O} \rangle$ as a function of the different end points of our LILA ramp. The green points represent our data with the shaded region representing bootstrapped error bars (see Appendix A.2). The solid line represents the order parameter expected from the numerical simulation of the ground state of the system at these various detunings. The dotted line represents unitary evolution of the system under our LILA ramp and experimental parameters elucidating non-adiabatic effects. The dashed line represents a stochastic wavefunction simulation of our system including decoherence mechanisms. The vertical dotted gray line indicates the critical point location. (b) The $\langle \sigma_0 \sigma_j \rangle$ correlator when preparing a state in the paramagnetic phase. Circles represent data for a 24 atom ring, while squares represent data for a 40 atom ring (error bars in shading once again). The dotted and dashed lines once again represent the results of unitary and stochastic wavefunction simulations. (c) The same as (b) but for the preparation of a state in the antiferromagnetic phase. The 40 atom system begins to be limited by non-adiabaticity.

could still be cut-off by diabatic errors. Second, decoherence arising from the openness of our quantum system could also limit the growth of correlations. To distinguish these possibilities, we consider the order parameter

$$\langle \hat{O} \rangle = \frac{1}{N^2} \sum_{i,j} \langle \sigma_i \sigma_j \rangle, \tag{4.19}$$

where N is the total number of atoms. Compared to the ground state expectation (solid gray curve, figure 4.11a), we find that the data (green circles, figure 4.11a) exhibit smaller values of the order parameter, with a difference that becomes more pronounced after the critical point. Moreover, we observe that time-dependent simulations (dotted gray line, figure 4.11a), which account for non-

adiabatic errors, yield an order parameter that is quite close to the ground state value, indicating that non-adiabaticity is not a dominant factor for these 24 atom systems. However, we can see the effect of non-adiabaticity in larger 40 atom systems. In these systems, the larger system sizes result in smaller gaps where adiabaticity poses a stricter constraint on our experiment. In preparation of states in the paramagnetic phase (figure 4.11b), where the gap has not closed, non-adiabatic effects are minimal. The σ field correlator for both 24 and 40 atom systems more or less lie on top of each other. However, in preparation of states in the antiferromagnetic phase (figure 4.11c), we clearly see that the correlators of the 40 atom system decays faster than the 24 atom system. This result is also predicted from comparing unitary to stochastic wavefunction simulations. The details of how the simulations are done are detailed in Appendix B. This suggests that for our 24 and 40 atom ring systems at the critical point, the length scale suppressing the correlations originates from decoherence.

To confirm our reasoning, we posit that the decoherence length scale (unlike adiabaticity) should not depend on system size. The system size does not increase deleterious effects like laser scattering or phase noise. Repeating the adiabatic preparation experiment for a 40 atom system, we observed that the σ field correlator behaved similarly as the 24 atom system with short range power law behavior followed by a second length scale which was consistent with the one observed for 24 atoms. Now that we have determined the origin of the second length scale, the question turns to whether we can still extract critical exponents from this non power law behavior at the critical point.

A broad theoretical understanding of quantum criticality in the presence of decoherence is still being actively developed. A simple and likely scenario is when decoherence (or unitary noise) acts similarly to a finite-temperature bath. This has previously been shown to be the case in a variety of open and noisy quantum systems [155,70,149,174,72]. Then, one can gain intuition from known results of quantum criticality at finite temperatures. For example, in a (1+1)d conformal field theory at

finite temperature T[48], the exact form of the correlation function is

$$\langle \sigma_0 \sigma_j \rangle \propto \left(\frac{T}{\sinh(\pi T j)} \right)^{-2\Delta_\sigma^{1D}}. \tag{4.20}$$

This has two key features that are generic to weakly-perturbed critical points: (i) power-law decay at short distances, featuring the true critical exponents, and (ii) a crossover to an exponential decay at long distances. This does not dictate the precise form of the correlation decay profile, but the simplest function with the right features is $C(r) \sim r^{-2\Delta} e^{-r/\xi}$. We note that a direct multiplication by an exponential decay has previously been used to study the preparation of the Ising critical point in the presence of noise[72].

Thus, we simultaneously fit our 24 and 40 atom correlator data to a decay profile of the form

$$\langle \sigma_0 \sigma_j \rangle \propto \delta_j^{-2\Delta_\sigma^{1D}} e^{-\delta_j/\xi_d}. \tag{4.21}$$

We extract a decoherence-induced length scale $\xi_d/a = 13.2^{+5.7}_{-3.6}$, which matches that observed in the AFM (figure 4.10b). As depicted in figure 4.12, by accounting for this exponential decay, we observe the characteristic power-law decay of critical correlations, with $\Delta_\sigma^{1D} = 0.127(37)$, in excellent agreement with the CFT prediction of $1/8$.

Our observations suggest that the principal effect of decoherence on quantum criticality is to introduce a single length scale into an otherwise scale-invariant state[72]. This provides a simple conceptual framework for extracting the universal scaling dimensions from open quantum systems at criticality. To investigate the generality of this framework, we directly tune the amount of decoherence in our system, by either increasing the total ramp time (figure 4.13a) or the intermediate-state scattering rate (figure 4.13b). From the adiabaticity perspective, increasing the ramp time is strictly a positive effect. However, we see a shorter decoherence length scale arising from the longer time

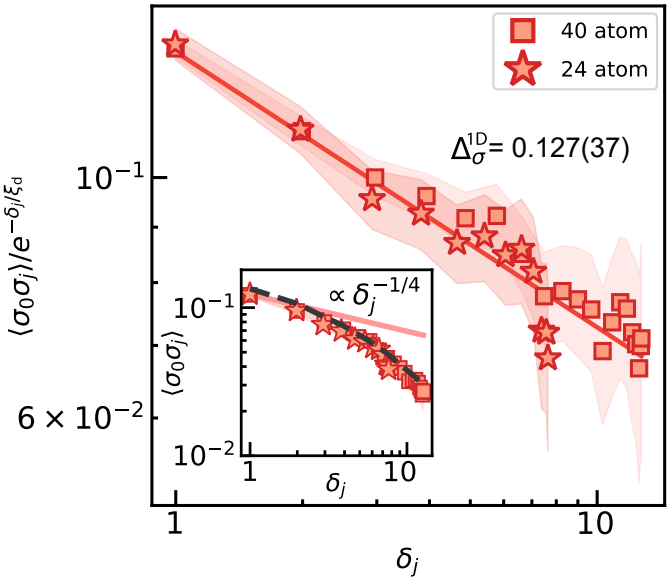

Figure 4.12: The σ field correlator divided by a fitted exponential length scale. The circles (squares) represent the 24 (40) atom system. Shaded region represents the bootstrapped error bars (see Appendix A.2). The exponential length scale and scaling dimension Δ_σ^{1D} are obtained from a simultaneous fit of both the 24 and 40 atom systems to a single scaling dimension and length scale. Inset: The raw data before dividing out by the exponential length scale. The solid pink line is a guide-to-the-eye for the expected power law decay of the (1+1)d Ising model.

that deocherence is allowed to act. Intermediate state scattering can be increased by unbalancing the Rabi frequencies of the two beams (see section 3.3). To hold effects from time constant, we change both beam powers at the same time in order to maintain the same two-photon Rabi frequency. We observe that with more unbalanced beams, the decoherence length scale indeed shortens.

In all cases, the correlations decay as in equation 4.21, but with different decoherence length scales (figure 4.13a,b). Despite a relatively large range of values for ξ_d, the extracted scaling dimension remains unchanged. This is evinced by the collapse of the data onto the universal Ising CFT power-law (across both ramp times and scattering rates) once ξ_d is accounted for (figure 4.13c).

With the scaling dimension of the σ field measured, we would have all the information of the

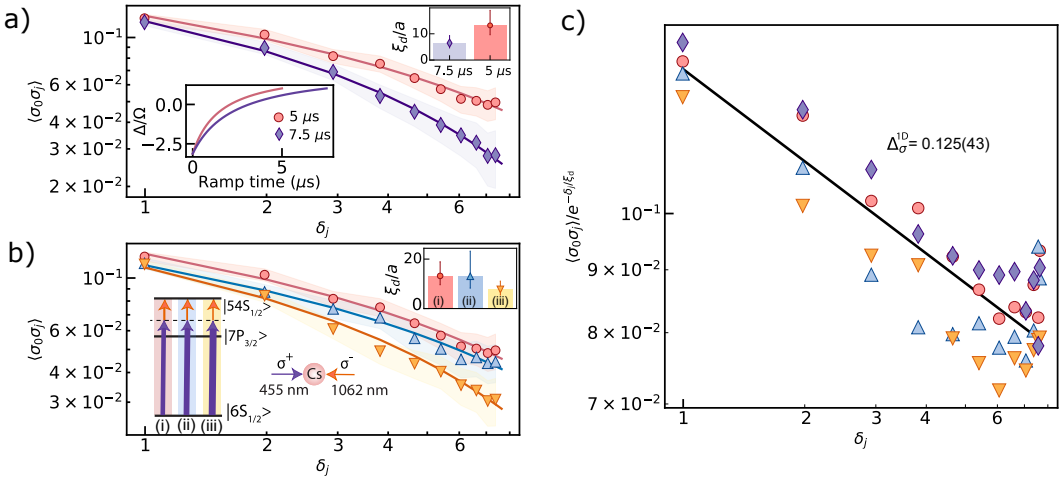

Figure 4.13: Tuning quantum criticality in an open system. Markers (24-atom) with different shapes are experimental measurements at the critical point under different experimental conditions, with shaded regions denoting the 1-σ bootstrap errors. Error bars in fitted ξ_d/a include 1-σ bootstrap error and fitting error. (a) σ field correlation measurements at two different ramp times. Upper inset: Fitted ξ_d/a. Lower inset: Corresponding ramp profiles. (b) σ field correlation measurements at three different intensity configurations at fixed Ω. Upper inset: Fitted ξ_d/a. Lower inset: A schematic showing the single photon rabi frequencies Ω_{455} and Ω_{1062} for each configuration. (c) Correlation measurements in (a) and (b) divided by the exponential $\exp(-\delta_j/\xi_d)$, displaying a collapse onto a power-law decay with an exponent of $2\Delta_\sigma^{1D}$ (solid black line), acquired via a simultaneous fit to the power-law exponential model for all scenarios. The uncertainty in Δ_σ^{1D} includes both 1-σ bootstrap error and fitting error.

Ising CFT by also measuring the scaling dimension of the ε field. However, the predicted scaling dimension for the ε field is Δ_ε^{1D} is 1, which would lead to a fast decay exponent of -2. The measured data is shown in figure 4.14. Without better measurement resolution, we cannot quantitatively extract this exponent. Qualitatively, the ε field correlator decays much faster than the σ field correlator.

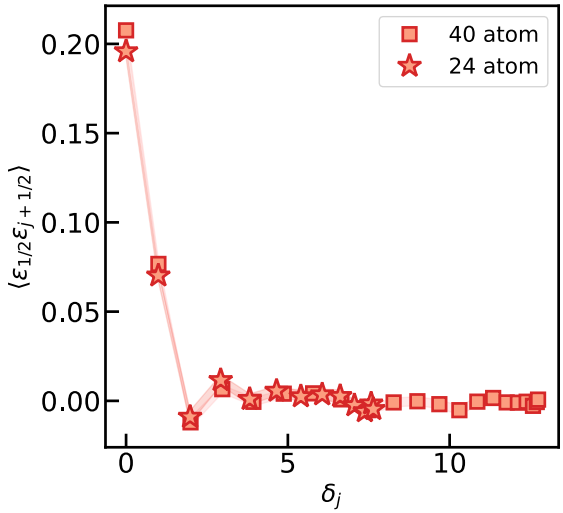

Figure 4.14: Measurement of the ε field correlator $\langle \varepsilon_{1/2}\varepsilon_{j+1/2} \rangle$ as a function of chord distance δ_j for 24 and 40 atom systems. The correlator quickly decays into the noise floor.

4.6 Critical Exponents in 2D and Boundary Effects

We now turn to the exploration of quantum criticality in two spatial dimensions. Working with a square lattice and a blockade radius of $R_b/a = 1.25$ (figure 4.15a), our model exhibits two phases analogous to the 1D case: at low detuning, a trivial paramagnet, and at high detuning, a $\mathbb{Z}_2$ checkerboard state that spontaneously breaks translation symmetry[78,19]. The transition between these two phases is in the (2+1)d Ising universality class[‖]. The CFT's primary σ field can be associated with a microscopic operator residing on the lattice bonds (inset, figure 4.15a). Namely, between two neighboring lattice sites at coordinates (x_i, y_i) and (x_j, y_j), the operator is given by

$$\sigma_{i,j} = (-1)^{x_i+y_i}(n_i - n_j). \tag{4.22}$$

[‖] This notation once again refers to two spatial dimensions and one time dimension.

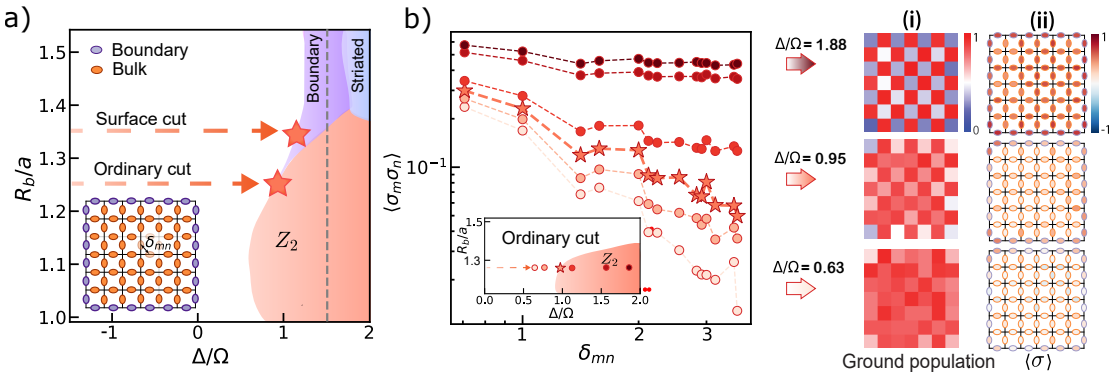

Figure 4.15: Probing critical Ising correlations and surface transitions in a 2D square lattice. Circles (7 x 7), stars (7 x 7 at the critical point) and squares (9 x 9) denote experimental measurements, with shaded regions representing 1-σ bootstrap errors (see Appendix A.2). (a) A schematic for the 2D phase diagram, adapted for finite system size. The shaded area labeled *boundary* marks the region of a boundary-ordered phase with a disordered bulk. Red stars indicate the location of the critical point along two different cuts. Gray dashed line indicates $\Delta/\Omega = 1.5$. Inset: The σ fields live on lattice bonds, both along the boundary (purple) and within the bulk (orange). δ_{mn} denotes the Euclidean distance between two nearest σ fields. (b) σ field correlation measurements around the critical point along the ordinary cut, with measured ground state population (i) and σ field (ii) across the phase transition. The critical spatial correlation is highlighted by the star marker. Inset: 2D phase diagram schematic with markers indicating the measurements' locations.

This field measures the "staggeredness" of a configuration. In a single checkerboard, the field is 1 on all bonds, while in the other checkerboard, it is -1 on all bonds. We begin by utilizing our optimized LILA ramps to prepare the ground state (on a 7×7 array) at various detunings (inset, figure 4.15b). Due to the odd-length, open-boundary condition geometry, there is a unique ground state in the ordered phase with $\langle\sigma\rangle \approx +1$ (panel (ii) in figure 4.15b), which exhibits a checkerboard pattern of $\langle n_i\rangle$ (panel (i) in figure 4.15b).

Next, we employ the same Kibble-Zurek-like procedure to experimentally locate the critical point, finding $\Delta_c/\Omega = 1.03(11)$ (figure 4.16a). The (2+1)d Ising CFT predicts that correlations at the critical point should decay as $\langle\sigma_m\sigma_n\rangle \propto \delta_{mn}^{-2\Delta_\sigma^{2D}}$, where δ_{mn} is the Euclidean distance between

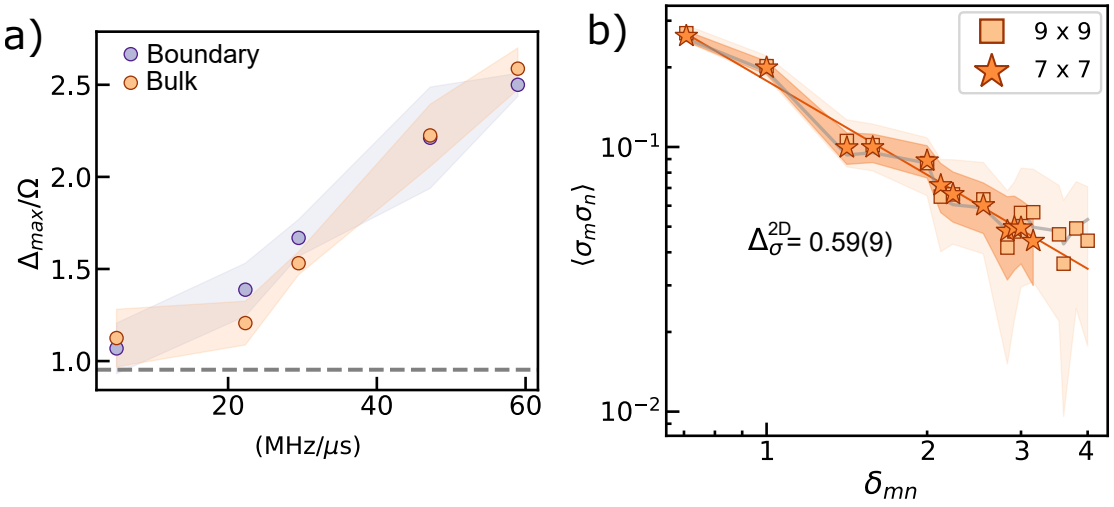

Figure 4.16: (a) Peak location of susceptibility χ along the ordinary cut at different sweep rates with boundary and bulk analyzed separately. Gray dashed line marks the location of gap minimum. (b) The measured critical σ field correlation within the bulk exhibits a power-law decay with an exponent of $2\Delta_\sigma$, shown by the orange solid line. The gray solid line represents the ground state simulation using experimental parameters.

bond centers m and n. Unlike in the 1D case, the 2D critical exponent $\Delta_\sigma^{2D} \approx 0.518149$ is not known exactly, but has been estimated to high precision using conformal bootstrap techniques [130].

We adiabatically prepare the critical ground state for both 7×7 and 9×9 square arrays. In this setting, we are able to directly observe real-space power-law correlations unimpeded by decoherence (figure 4.16b). This is enabled by two facts: (i) the larger scaling dimension causes power-laws to manifest at shorter distances, and (ii) the previously-extracted decoherence length scale, $\xi_d \approx 13$, exceeds our linear system size. A simultaneous fit of both system sizes yields $\Delta_\sigma^{2D} = 0.59(9)$; note that in order to minimize boundary effects, we only include σ fields within the bulk (inset, figure 4.15a). While our measured scaling dimension is slightly larger than the CFT prediction, it agrees with ground state DMRG calculations. In fact, the correlation function matches the simulations within statistical error for all distances; this suggests that the discrepancy with the CFT prediction is

a finite-size effect.

We note that there are also very strong corner effects from the parity of the system's length in 2D. For odd system sizes, there is a unique classical checkerboard pattern in the AFM phase that energetically satisfies both the Rydberg blockade condition and the positive detuning δ, with Rydberg excitations on all four corners. For even system sizes, there are instead two degenerate checkerboard patterns, each with Rydberg excitations on two corners. The exact functional form of the correlation decay in such a (2+1)d CFT with finite boundary conditions is unknown theoretically, and in light of this, it is difficult to make quantitative claims about critical exponents even in numerics.

While we have focused thus far on bulk criticality, the boundary (and especially our open boundary) itself can also exhibit rich physics in two dimensions. At $R_b/a = 1.25$, we observe that the bulk and boundary order simultaneously (figure 4.16a)—a so-called ordinary transition [31,40,84]. However, this is not the only possibility. In an alternative case, known as a surface transition, the boundary orders independently prior to the bulk phase transition [31]; for example, this is expected to occur when $R_b/a = 1.35$ (figure 4.15a) [119].

To investigate this, we prepare states at various detunings along both the ordinary ($R_b/a = 1.25$) and surface ($R_b/a = 1.35$) cuts depicted in figure 4.15a. This is achieved by changing the Rabi frequency, which effectively changes the blockade radius. We measure the order parameter (equation 4.19), but now separately average over bonds either within the bulk, $\langle \hat{O} \rangle$, or at the boundary, $\langle \hat{O} \rangle_\partial$. Note that the bulk and boundary are defined in the inset of figure 4.15a. Along the surface cut (figure 4.17b), the growth of $\langle \hat{O} \rangle$ exhibits a discernible lag behind $\langle \hat{O} \rangle_\partial$, particularly when compared to the growth observed along the ordinary cut (figure 4.17a). This is consistent with the expected surface transition [119].

The Ising CFT also has predictions for the decay of the two-point correlator $\sigma_{i,j}$ (equation 4.22) for the ordinary and surface transitions. As $\sigma_{i,j}$ is odd under the $\mathbb{Z}_2$ Ising symmetry of the transition, we should thus expect that asymptotically its decay is governed by the scaling dimension the most

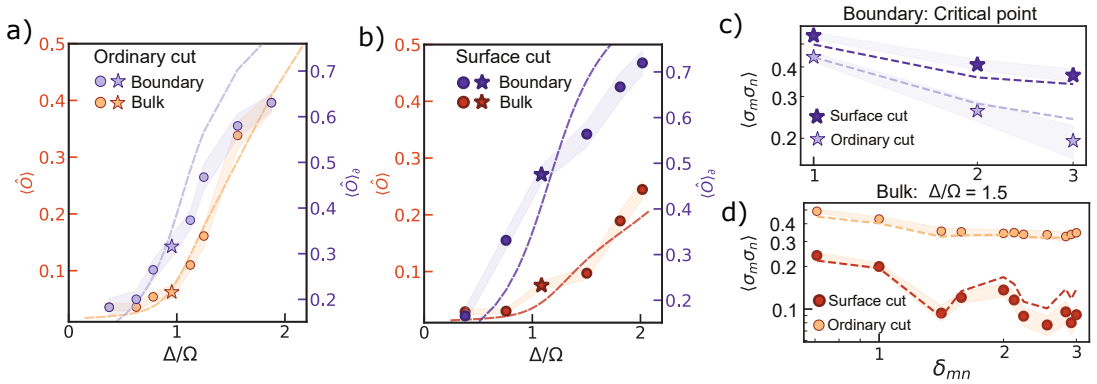

Figure 4.17: (a) and (b) The order parameter, analyzed separately for the bulk ($\langle\hat{O}\rangle$) and boundary ($\langle\hat{O}\rangle_\partial$), is shown across the phase transition for the ordinary cut (a) and the surface cut (b). Solid blue lines represent ground-state numerical simulations using experimental parameters. (c) and (d) Measured spatial correlations of the σ field along the boundary (c) at the critical point for both cuts, and within the bulk (d) at $\Delta/\Omega = 1.5$. Dashed blue lines are ground-state numerical simulations with the experimental parameters. Shaded regions in all data represent the error bar determined from bootstrapping (see Appendix A.2).

relevant odd CFT field on the boundary. For the surface transition, this is just the scaling dimension of the usual (1+1)d Ising universality class spin field, $\Delta_\sigma^{1D} = 1/8$. By contrast, for the ordinary transition the scaling dimension for the most relevant odd boundary field has instead been calculated via conformal bootstrap to be much greater: $\Delta_{\partial_z\hat{\sigma}} = 1.276(2)$ [84].

Now we examine the boundary correlations, $\langle\sigma_m\sigma_n\rangle_\partial$, in the experimental data at the ordinary and surface critical points (stars, figure 4.15a). At the surface transition, $\langle\sigma_m\sigma_n\rangle_\partial$ exhibits a slower decay with larger absolute values compared to the ordinary transition, which is in qualitative agreement with the theoretical prediction. However, our ability to quantitatively determine this scaling dimension is constrained by the presence of strong corner effects.

For contrast, we also analyze the bulk correlations $\langle\sigma_m\sigma_n\rangle$ along $\Delta/\Omega = 1.5$ (dashed gray, figure 4.15a), which lies within the ordered phase for the ordinary cut, but should only have boundary

order for the surface cut. Indeed, as shown in figure 4.17d, the ordinary cut exhibits a plateau in the spatial correlations at large distances indicative of an ordered bulk, while the surface cut exhibits rapidly decaying correlations, indicative of a yet to be ordered bulk.

4.7 Summary and Outlook

We have seen that a driven Rydberg system using a spin-1/2 system encoded in the $|g\rangle$ and $|r\rangle$ states implements a long range transverse field Ising model, where the transverse field strength and interaction strength can be tuned. Combined with a tweezer array, these systems can study many-body physics in arbitrary geometries. In particular, we study the Ising critical point in a 1D system with periodic boundary conditions (ring) and a 2D system with open boundary conditions via adiabatic preparation of the wavefunction at the critical point. We were able to extract the correct critical exponents in 1D by carefully accounting for decoherence. In 2D, we obtained a result consistent with the predicted critical exponent, but open boundaries complicate the procedure. However, the boundary of a 2D system can host distinct boundary phase transitions, which we were able to observe qualitatively by modifying the blockade radius.

In principle, our procedure of locating the critical point and then performing adiabatic preparation of the critical state is generalizable to other systems. However, other systems, such as frustrated ones, will present additional challenges. Let's take for example the recent Z_2 spin liquid work[204], where Semeghini et al. use quasi-adiabatic evolution to explore the many-body phases in their geometrically-frustrated Rydberg array. In this case the transition points and critical behavior are known theoretically, but the following general issues arise. First, due to frustration the energy scales of excitations are smaller, and so adiabatic preparation is more challenging (within a Kibble-Zurek framework, one needs slower dynamics to push the critical correlations out to long distances). Second, the magnitude of the correlations are weaker, and the power-laws can be faster. The latter issue

is because local operators create pairs of the topological anyon excitations, and so one needs to effectively probe 4-body correlations, which have faster decay. Third, there are often competing phases with expanded unit cells (i.e. valence bond solids), which necessitates larger system sizes, i.e. so that a sufficiently large number of unit cells fits within the cluster.

Larger system sizes necessitate longer adiabatic state preparation times. This, in turn, requires us to minimize decoherence in our system. A fundamental limit is the Rydberg lifetime, which can be extended by using higher Rydberg states or mitigated through post-selection based on erasure detection. Reducing intermediate state scattering can be achieved by increasing the intermediate state detuning and compensating with optical power to maintain the Rabi frequency. Alternatively, it can be eliminated by using a single-photon scheme.

In cases where the critical exponents are not known, benchmarking the experimental system at small system sizes with known numerical results could be helpful for designing the adiabatic ramp trajectory and understanding potential sources of decoherence. In terms of locating the critical point, a similar approach to our current work, where peaks in susceptibility are extracted at different sweep rates, could be adapted. This would require a careful analysis of convergence as a function of sweep rate without prior knowledge of the critical point location. The Kibble-Zurek mechanism also offers a complementary approach that can help verify at least some of the exponents we find using our method.

Our work also lays the foundation for several other directions. First, producing larger square arrays and improving coherence times should allow direct access to various boundary universality classes (surface, ordinary, and extraordinary) in experiment. Second, bulk ground state physics is enriched by the presence of geometric frustration: odd-length rings support a W-state in the ordered phase [168], and in two dimensions one can find 3D XY critical points with an associated novel extraordinary-log boundary universality class [169] as well as transitions into gapless and topological spin liquids [204]; each of these should be possible to study using the same adiabatic preparation

framework. Finally, quantum critical states are expected to display rich dynamics when out of equilibrium [43,18], including holographic signatures of emergent gravitational physics [192]. Such topics have been extensively studied theoretically in (1+1)d CFTs. The extension to (2+1)d is non-trivial, and would benefit greatly from experimental study.

5

Dual-Species Tweezer Arrays of Rydberg Atoms

5.1 Introduction

In the last chapter, we combined our capabilities of creating large defect-free atom arrays and coherent Rydberg excitations to measure the critical exponents of the Ising critical point. Another

important unused capability of our apparatus is the presence of a second atomic species, sodium. Born out of a former molecule apparatus, as detailed in chapter 2, we have all the machinery to laser cool and trap large arrays of sodium atoms. Thus, our experiment is uniquely positioned to explore the physics of dual-species atom arrays.

The main feature of dual-species atom arrays[209,206] is independent addressability and readout of the two atomic species. Having two different types of physical qubits results in crosstalk free addressing and measurement of each species individually. Sodium and cesium atoms respond to very different frequencies, and thus, sodium atoms can be driven or measured completely independently of cesium atoms and vice versa. This feature has already been used experimentally in ground state atoms, where real time measurement of one species is used to sense the local magnetic field environment and thus correct for field-induced errors in the other species[210].

In section 5.2, we first highlight the key differences in the types of interactions that can be engineered in dual-species atom arrays. Section 5.3 then describes our experimental efforts towards developing Rydberg capabilities in Na atoms. Section 5.4 details our observation of interaction between sodium and cesium Rydberg atoms. Lastly, section 5.5 describes future prospects of our dual-species array for applications in both quantum computing and simulation.

5.2 Interspecies Interactions -Theory

The theory of interspecies interactions[21,111] for different species is exactly the same as single species interactions that was laid out in section 3.2.2, which we briefly summarize here. The states that were discussed in that section included pair states $|a;\alpha\rangle$ and $|b;\beta\rangle$ which were connected by the dipole-dipole interaction and had an energy difference $\hbar\delta = E_{\alpha\beta} - E_{ab}$, known as the energy defect. When the dipole-dipole interaction (which depends on distance) is much stronger than the energy scale set by the energy defect, then the pair states shift as $1/r^3$. Otherwise, when the dipole-dipole interaction

energy is much weaker than the energy defect, the pair states exhibit a $1/r^6$ shift. The sign of the energy defect controls the sign of the shift. In the formalism of that section, the states $|a;\alpha\rangle$ and $|b;\beta\rangle$ were completely general, and could have come from different species! Thus, the formalisms used to describe intraspecies and interspecies interactions are mathematically equivalent. However, there are some new interesting features that arise in the dual-species case.

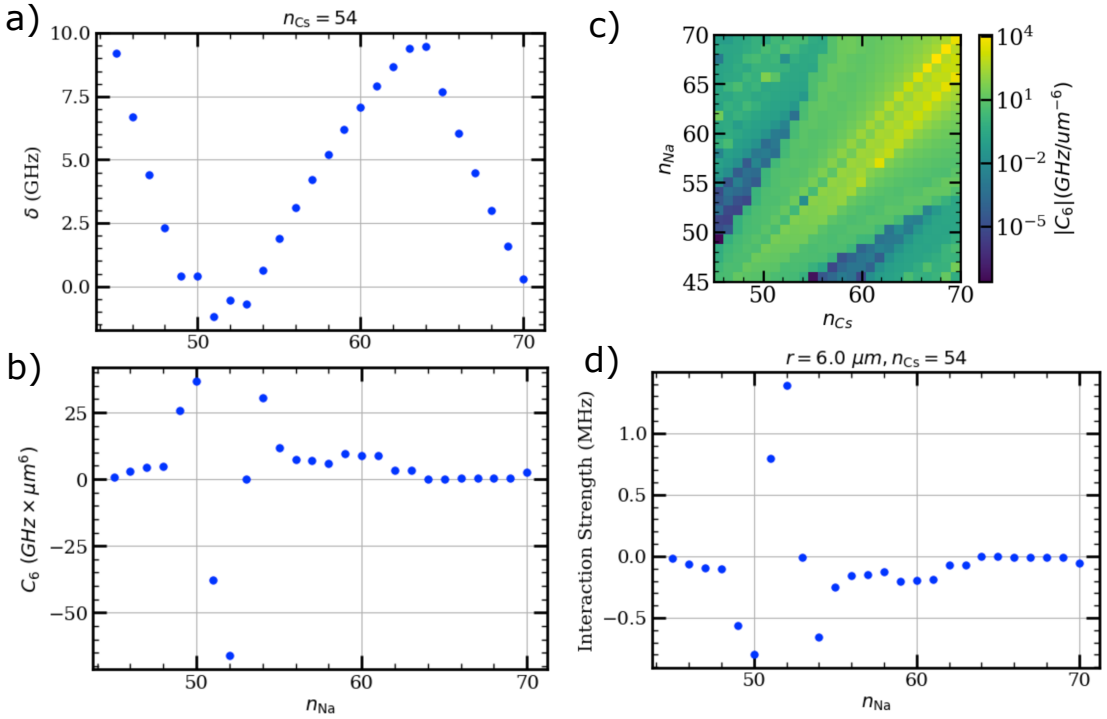

Figure 5.1: (a) The energy defect in GHz for a pair state with $n_{Cs} = 54$ as a function of n_{Na}. (b) The C_6 coefficient for a pair state with $n_{Cs} = 54$ as a function of n_{Na}. (c) The C_6 coefficient as a function of both n_{Na}, n_{Cs}. The colorbar is on a log scale. (d) The resulting interaction energy from a full diagonalization at $r = 6\,\mu$m for a dual species system with $n_{Cs} = 54$ as a function of n_{Na}.

We argued, on the basis of figure 3.5, that intraspecies Rydberg interactions tend to be repulsive. In the interspecies case, there is no natural reason to require the two states $|a\rangle$ and $|\alpha\rangle$ to be the

same Rydberg state. This leads to a greater variety of interactions that can even change sign when the defect changes sign. Holding the principal quantum number of cesium, n_{Cs} fixed at 54, figure 5.1a depicts the energy defect of the highest contributing state to the C_6 as a function of the principal quantum number of sodium, n_{Na}. The corresponding C_6 is shown in figure 5.1b. We see that the C_6 exhibits a resonance, corresponding to when the energy defect is near zero. In fact, there are highly interacting repulsive and attractive C_6 coefficients, corresponding to when the defect changes sign. The highest interaction strength occurs at $n_{\mathrm{Na}} = 52$, which is 2 less than $n_{\mathrm{Cs}} = 54$. This difference in 2 is close to the difference in quantum defects of Na and Cs of being about 3. At high n_{Na}, it appears the defect gets smaller again. However, the dipole moments between the pair states that make up this defect are small, since the principal quantum number of sodium likely changes by quite a bit to match the energy change in cesium. This results in a small C_6 despite the small defect. The interaction energy resulting from a full diagonalization along the $n_{\mathrm{Cs}} = 54$ cut is shown in figure 5.1d, showing good agreement with the perturbative C_6 result.

Full diagonalizations are expensive calculations that require far more time than a perturbative C_6 calculation. Hence, we map out the entire two-dimensional landscape of interspecies interactions only via the C_6 coefficient and the results are shown in figure 5.1c. We see a huge variation in C_6 coefficients, partially owning to the n^{11} scaling. We note that the majority of C_6 coefficients are quite small when the principal quantum numbers of sodium and cesium are quite mismatched, leading to large energy defects. Thus, it is quite easy to have weak interspecies interactions but relatively strong intraspecies interactions. This is quite counterintuitive to simple classical reasoning, when the van der Waals interaction are simply a function of the sizes of the atom, and not any sort of "matching" of their sizes.

Engineering strong interspecies interactions relative to intraspecies one is more difficult. The intraspecies interactions (between two same species atoms in the same state) have the benefit of always having reasonable defects. Thus, high ratios of interspecies interactions over intraspecies in-

teractions tend to occur at smaller principal quantum number. An alternative approach is to bring the interspecies interaction into resonance with an electric (or magnetic) field. This is known as a Förster resonance and has been experimentally observed in both the single-species [181] and dual-species contexts[6].

This formalism can also be extended to dipole-dipole interactions between any two species with a dipole moment, including polar molecules. In these cases, the dipole moment of a polar molecule is typically far smaller than the transition dipole moment of a Rydberg atom. Thus, Förster resonances are far more important in these molecule-atom systems and has been observed experimentally[249,115,251]. These resonances are utilized extensively in chapter 6, where we discuss a novel approach of speeding up molecular gates and performing non-destructive measurement on molecules with Rydberg atoms.

5.3 Na Rydberg Excitation

Figure 5.2 depicts the possible excitation pathways for exciting sodium to the Rydberg state. The wavelengths in sodium are all shorter than cesium, indicating that the valence electron is more bound in sodium compared to cesium. A single photon excitation, which would eliminate all intermediate state scattering, requires a 241 nm laser, which is technically challenging. Even the so-called "inverted" scheme (exciting from $3S_{1/2}$ to $4P_{3/2}$ in the first leg instead of to $3P_{3/2}$), where the second leg laser is more in the infrared would require a 330 nm first leg laser. Due to these technical challenges of a short wavelength laser, for sodium, we use the standard scheme of exciting the atom from the $3S_{1/2}$ state to the $3P_{3/2}$ state with a 589 nm laser, followed by a Rydberg excitation with a laser at around 409 nm.

We create 589 nm by doubling 1178 nm light. Our 1178 nm laser is a commercial ECDL from Timebase (ECQDL-200S_1178) that can output around 180 mW of light. It then is doubled by a

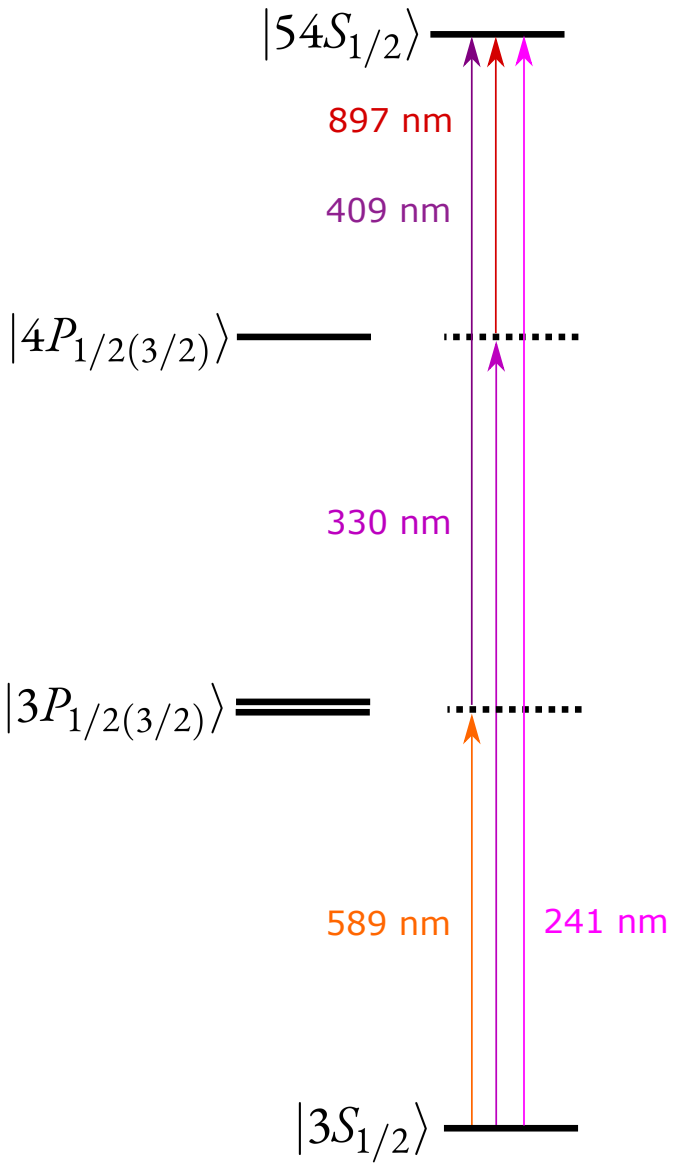

Figure 5.2: The possible transitions to use for exciting sodium to the Rydberg state. Fine structure in sodium is insignificant and not depicted.

waveguide doubler from NTT Electronics (WH-0589-000-A-B-C) to 589 nm, resulting in around

10 mW of 589 nm light*. The Rydberg excitation is controlled by this 589 nm laser (the blue 409 nm is kept constantly on), so it needs to be pulsed on quickly. When we perform detuning scans, we also change the frequency of this laser. Thus, this laser goes through a double-passed AOM before being delivered to the experiment. On the experiment table, this laser is focused to around 300 μm on the atom plane resulting in a Rabi frequency of up to around $2\pi \times 50$ MHz. The 589 nm light is σ^+ polarized to connect to a single state in the excited $3P_{3/2}$ state manifold after preparing the atom into the $|F = 2, m_F = 2\rangle$ stretched hyperfine state.

The 409 nm light needs to be high power and tunable. Thus, we use a TiSapph laser from MSquared (pumped by a 10W Sprout laser at 532 nm) that is then doubled by a commercial bowtie cavity from Agile Optic. Due to the degradation of the TiSapph used to perform these experiments, we have used at most 1 W of 818 nm light that is doubled to about 400 mW of 409 nm light. To preserve as much of our 409 nm light as possible, we currently do not use an AOM and simple switch the light on and off via a mechanical shutter before the delivery fiber. To handle high powers of blue light, we deliver the light to the experiment table using a photonic crystal fiber. The light is focused to approximately a 50 μm diameter, once again to maximize the power onto the atoms. The 409 nm light is σ^- polarized in order to connect to the $nS_{1/2}$ state.

The two laser beams are frequency stabilized by locking to a ULE cavity (the same one as described in section 3.3) which has been coated with high reflectivity at 1060 nm and 910 nm for the Cs Rydberg lasers. Once again, to reduce the technical complexity of the coating, we lock the fundamentals (pre-doubled) wavelengths of both lasers, namely 1178 nm and 820 nm. To summarize, our ULE cavity has been designed to have high reflectivity at 820, 910, 1060 and 1178 nm.

To align the 589 nm beam to the atoms, we can make use of the fact that this light does indeed address the ground state, and we can use the same technique to align the beam as we do for the ce-

*This doubling efficiency can definitely be improved. We suspect some of the loss to come from fiber coupling. However, the 589 nm transition has a large dipole moment, so we don't need as much power on this leg.

sium 455 nm beam. We make use of the differential scalar light shift present between the $F = 2$ and $F = 1$ hyperfine ground states when the detuning of the beam from the $F = 2$ state is smaller than the ground state hyperfine energy scale of about 1.7 GHz.

The 409 nm beam alignment is trickier, since it does not directly address the sodium ground state. In the case of cesium, we were able to align the second leg beam via large vector light shifts, due to the large D1 and D2 line separation in cesium. In sodium, we unfortunately do not have the same luxury, and vector light shifts are expected to be small. However, with a dual species apparatus, we chanced upon a very nice feature. Our cesium atoms are actually pushed out with the combination of D2 line light at 852 nm and 409 nm. We hypothesize that this is due to the two beams providing enough energy to ionize the cesium atoms. Thus, for coarse alignment of the 409 nm beam, we can attempt to destroy the cesium MOT with as little 409 nm power as possible. As a more precise target, we can also push single cesium atoms out of their optical traps, and place the cesium atoms near sodium atoms. This signal is also particularly nice to use, since it can be time broadened and is not frequency sensitive at all. Thus, the laser does not need be locked when performing this alignment.

Another challenge for the beam delivery and alignment of this 409 nm beam is due to the reflective glass cell and viewport interfaces separating the vacuum chamber from atmosphere. As discussed in section 2.1, these components were AR coated for the MOT wavelengths to prevent background scattering during imaging. However, Rydberg excitation was not in the initial plans. We measure an intensity transmission coefficient of approximately 55% per surface that is polarization independent for both the glass cell and viewport. This reflection not only reduces the power that can be transmitted through the glass cell, but also creates deleterious interference effects that complicate alignment.

The two reflective surfaces that make up the glass cell support multiple reflections and transmissions which can interfere (as shown in figure 5.3a), when the angle of incidence is small or the beam

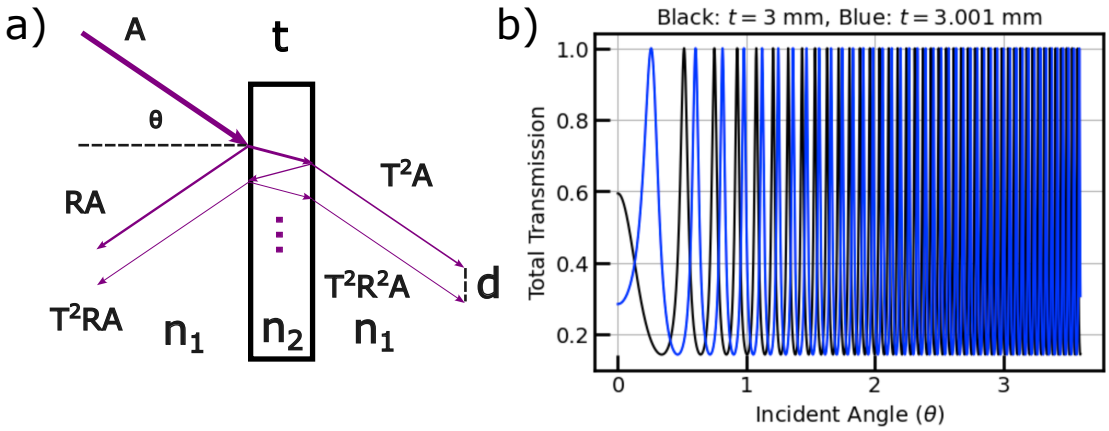

Figure 5.3: (a) A ray optics model of our viewport or glass cell. An incident beam with amplitude A impinges on the first surface with angle of incidence θ. Multiple (an infinite number in this model) reflections and transmissions appear with amplitudes designated by the thickness of the ray representing the beam. The thickness of the glass is given by t, and the indices of refraction are n_1 and n_2 outside and within the glass respectively. (b) The total transmission (of all beams) as a function of the incident angle at fixed wavelength and reflectivity as a function of incident angle for two different thicknesses.

is large. When we model the incoming rays as plane waves, all beams interfere completely and the intensity transmission function is analytically known to be [193,238]

$$T = \frac{1}{1 + F\sin^2(nkt\cos(\theta))} \tag{5.1}$$

where $F = 4R/(1-R)^2$ is the coefficient of finesse which is related to the intensity reflection coefficient, R, of a surface. n is the index of refraction of the material between the two surfaces, t is the thickness of the etalon and θ is the angle of incidence. This function is plotted in figure 5.3b as a function of incident angle and for two different thicknesses. There are "resonances" of unity transmission, but they are not stable to slight changes in thickness. The black and blue traces in figure 5.3b plot the total transmission when the thickness differs by only a micrometer. At larger

angles of incidence, the total transmission is a more rapidly varying function of angle.

One way to intuitively understand the resonances is to realize that for $\theta = 0$, the two coated surfaces of the glass cell or viewport essentially form a (poor) optical cavity, known as a Fabry-Perot etalon [193]. The optical cavity's supported modes depend on the cavity length. As a function of incident angle, the effective cavity length can be changed to match the wavelength of the light exactly! However, if one is to utilize these resonances to obtain perfect transmission through lossy surfaces[†], the cavity length needs to be stabilized to the scale of the wavelength. This can be accomplished using monolithic spacers of low temperature coefficient of expansion materials, but is certainly not expected for a generic viewport or glass cell.

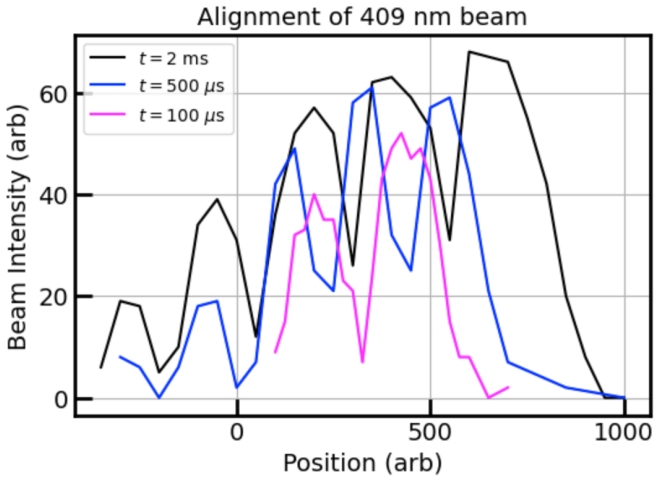

Figure 5.4: The beam intensity, as measured by a two photon excitation of trapped sodium atoms, as a function of the position of a horizontal picomotor controlling the beam. The three colors represent three different times of excitation. x-axis and y-axis units are arbitrary. The presence of hysteresis and slight differences in vertical alignment between the different attempts causes a displacement in the x-axis between the different excitation times.

Any interference effect would intimately depend on the exact cavity length (which can change

[†]This is exactly what one tries to do when locking a laser to a high-finesse cavity.

from temperature), frequency of the laser or incident angle, so we seek to eliminate any interference and contend with the reduced transmission. This can be achieved by using a large angle of incidence, where the different rays (which have finite extent in Gaussian beams), do not overlap and interfere. Using these large angles, the beam intensity can be stable. An alternative understanding of this effect arises from using equation 5.1. It appears that larger angles result in a more rapidly varying and unstable transmission. However, finite size beams contain a finite spread of incident angles[‡]. The transmission is then averaged over these incident angles, and due to the transmission's fast variation with angle, smaller beams sufficiently average over angles in order to have stable transmission. In fact, our first observation of this effect resulted from noticing these interference fringes in a large collimated beam, but not in a focusing beam. In our experiment, we can send our beam either through the viewport or the glass cell. Since the glass cell surface is much closer to the atoms (which lie in the center of the glass cell) than the viewport, delivering the beam through that surface allows for a larger angle of incidence.

Experimentally, we know our incident angle is large enough when we can see distinct peaks in the beam intensity when we displace the beam along the direction of the incident angle. The appearance of distinct beams rules out interference effects. Figure 5.4 depicts a successful alignment attempt at around 3 degrees angle of incidence. The key feature is the presence of multiple peaks but only in one direction. Once we see all the peaks, we can align to the furthest (and thus highest intensity) peak. With the beams aligned, we are ready to observe Rydberg excitation of sodium atoms.

In order to obtain the highest Rabi frequencies, we work at the close intermediate state detuning of 120 MHz blue-detuned at the expense of higher scattering rates. We also choose a relatively low Rydberg state, $38S_{1/2}$. We load and trap sodium atoms into a large and sparse array to avoid any

[‡]Plane waves can have a single incident angle, but any finite size beam must be composed of a finite spread of incident angles.

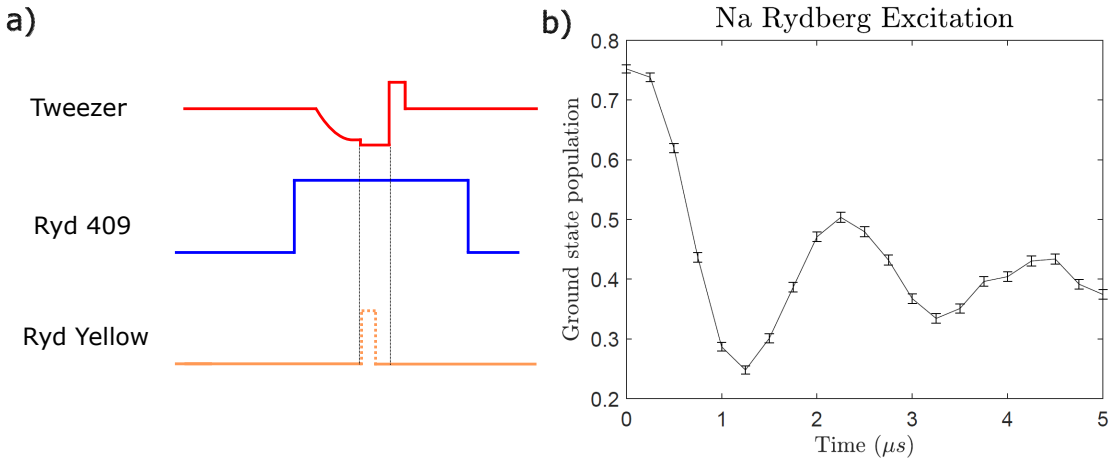

Figure 5.5: (a) The pulse sequence used to excite sodium atoms to the Rydberg state. The Rydberg yellow beam controls the time of the dynamics, with the second leg 409 nm on at all times. (b) Coherent Rabi oscillations between the ground and Rydberg state with Na atoms.

interactions. Note that with a low Rabi frequency, the blockade radius is larger. After loading the atoms, we optically pump them to the stretched $|F = 2, m_F = 2\rangle$ hyperfine state. Then, figure 5.5a shows the pulse sequence we use to excite sodium atoms from the ground state to the Rydberg state. The sodium tweezer needs to be turned off before the Rydberg excitation, since it antitraps the Rydberg state. The same antitrapping effect is used to push out Rydberg atoms for state detection. Any finite sodium tweezer depth also causes a light shift on the Rydberg transition, which we have observed in experiment. Once again, we note that the 409 nm light beampath only has a mechanical shutter, so we use the 589 nm yellow beam to control the pulse time.

The resulting Rabi oscillations are depicted in figure 5.5b. These oscillations leave much room for improvement. Firstly, the ground state population at $t = 0$ is not quite at 100%. This loss of contrast arises from atom loss either from imaging or the tweezer ramp down. Both of these procedures can be further optimized. Secondly, there is too much decoherence for high fidelity preparation of the Rydberg state. Higher fidelity can be achieved either through higher Rabi frequency or

reduced decoherence. The decoherence can be mitigated by improving the phase noise of the 1178 nm diode laser. This can be achieved either in a similar way to the cesium 1060 nm laser via an injection lock system or via feedforward [141,50] using the clean transmission of the optical cavity. The scattering time scale under these experimental conditions is around 5 μs, which is a major limitation on the excitation fidelity. This can be improved by detuning further from the intermediate state, but would require higher laser intensities at the atoms.

5.4 Interspecies Interaction - Data

With the successful excitation of sodium atoms, we can now combine this capability with our cesium excitation capability. Exciting both atoms at the same time will allow us to observe interspecies interactions between the two atoms and confirm some of the theoretical ideas outlined in section 5.2. An experiment to measure this interaction energy is described in figure 5.6. After a cesium atom is excited to the Rydberg state, the location of the sodium resonance is measured.

The shift in the location of the sodium resonance when a cesium atom is excited compared to when it's not determines the Rydberg-Rydberg interaction strength. Figure 5.7 illustrates data acquired with the scheme in figure 5.6. Figure 5.7a depicts the results when sodium is excited to the 51S state and cesium is excited to the 54S state, a combination which is expected to interact strongly (see figure 5.1d and surrounding discussion). The red and magenta curves show a clear difference in the sodium excitation probability between when a cesium atom is present and excited (red curve) and when a cesium atom is not subject to the excitation pulse. In particular, the sodium atom fails to be excited in the presence of the cesium Rydberg atom due to the shift in the resonance location caused by the Rydberg-Rydberg interaction. In the language of blockade, a cesium Rydberg atom blockades the excitation of a sodium atom. Moreover, an additional advantage of our tweezer array platform is the individualized imaging of each atom in the tweezer. Thus, to confirm that this ef-

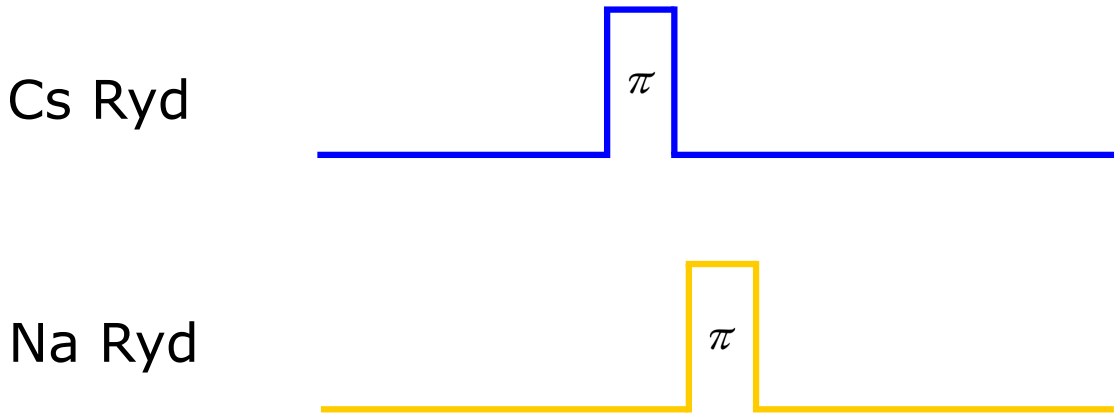

Figure 5.6: To observe an interaction between a sodium and cesium Rydberg atom, we first excite cesium to the Rydberg state (by pulsing the blue 455 nm light on resonance for a π time), and then attempt to locate the sodium Rydberg resonance by pulsing the 589 nm yellow light at different frequencies. Note that the other leg of the two-photon Rydberg excitation is on throughout this entire procedure. The tweezers are also lowered during the Rydberg excitation and detection is performed on both sodium and cesium atoms.

fect is coming from Rydberg physics, we can post-select our data in various other conditions. For instance, due to our pre-experiment image, we can post-select on the presence of a cesium atom in the array to begin with before the experiment commences. This dataset is shown in blue, and we see that the sodium atom is excited in the exact same way as the magenta curve, when there is no cesium excitation pulse. A more interesting post-selection can be performed on the state of the cesium atom, which is also measured at the end of the experiment. The green curve is acquired when the excitation pulse has "failed" to excite the cesium atom, and we observe the cesium atom as being in the ground state at the end of the experiment. This failure of excitation can also be viewed as the result of a projective measurement of the cesium atom state. In this case, the sodium excitation curve is equivalent to when no cesium excitation pulse is performed and when no cesium atom is present. The aforementioned red curve is post-selected for the presence of and successful excitation of the cesium atom. This is the only case which shows successful blockade of the sodium atom excitation.

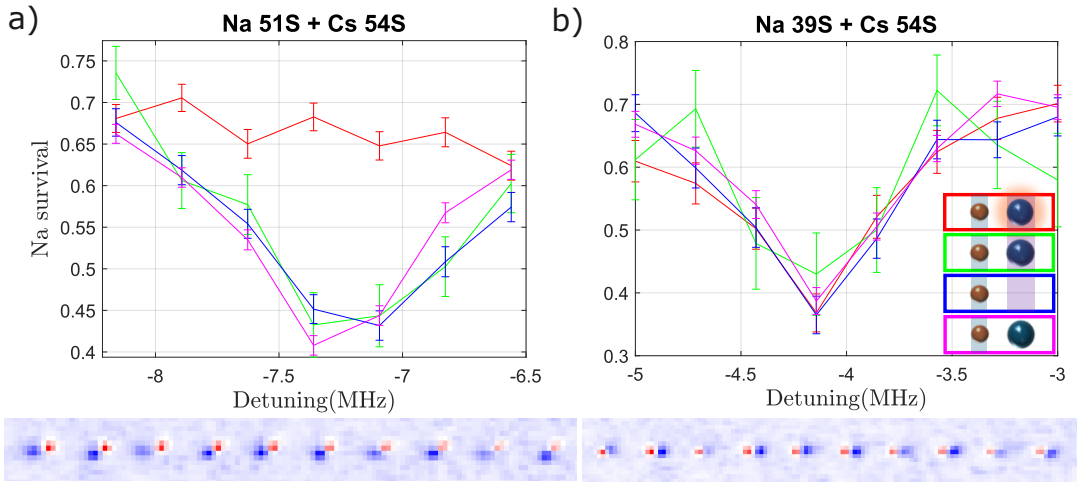

Figure 5.7: A measurement of the interspecies interaction according to the scheme in figure 5.6. The data shows the survival of sodium atoms (a proxy for sodium Rydberg population) after an attempted π pulse as a function of frequency. For all figures, a legend for the conditions different curves is provided in the lower right of b), all of which are acquired via post-selection and are described in more detail in the main text. The atom geometry for each dataset is pictured below the graphs. For each image, red indicates the locations of sodium atoms, and blue indicates locations of cesium atoms. (a) Data for when the sodium atom is excited to the 51S state and cesium atom is excited to the 54S state. The lack of excitation in the red curve illustrates interaction between the two species (b) Data for when the sodium atom is excited to the 39S state and cesium atom is excited to the 54S state. The collapse of all 4 curves on top of each other indicates that the atoms do not interact strongly in this configuration.

In these experiments, we measure the state of the cesium atom (which allows us to perform post-selection and acquire cleaner datasets), but we remark that one does not need to measure the state of cesium to observe the effects on sodium. In fact, the measurement of the state of the sodium atom performs a projective measurement of the cesium atom state! The ability for an ancillary qubit to non-destructively read out information about other data qubits is a key ingredient in many quantum error correction schemes and is elaborated on in section 5.5. While the demonstration here is not particularly useful, since the cesium atom is collapsed into a classical state and is easily readout

on its own, an extension where a measurement can still result in an entangled state (of multiple cesium atoms) is elaborated on in section 5.5.1. This procedure can also be used to readout the state of a molecule (which is hard to readout on its own!) and is described in section 6.6.

One of the more non-intuitive results from section 5.2 was that the interaction strength (for a fixed cesium principal quantum number) exhibited "resonances" as a function of the sodium principal quantum number (see figure 5.1d). The interaction strength does not simply grow monotonically larger as each atom orbital grows in size. Our experiment can verify this quantum mechanical feature by exciting the sodium atom to a different principal quantum number. For a sodium principal quantum number of 39*S*, the data are shown in figure 5.7b. When exciting sodium to this non-interacting state, all conditions of the cesium atom result in the exact same sodium excitation curve. The sodium is completely agnostic to the presence of or state of the cesium atom.

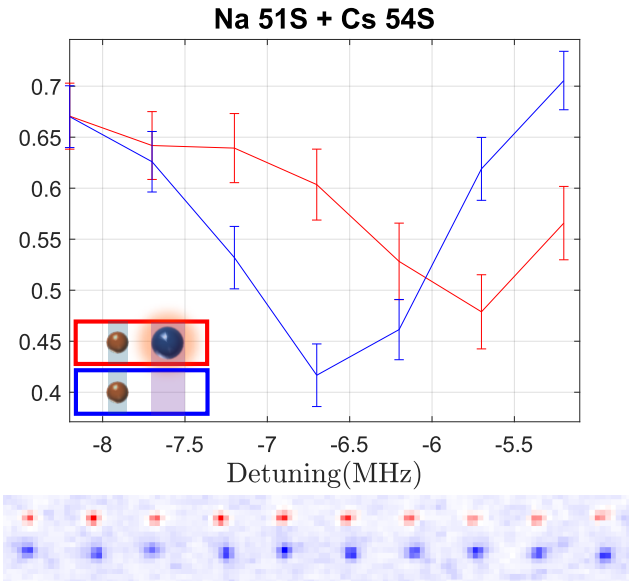

Figure 5.8: Measurement of the excitation of the sodium atom to the 51*S* state when cesium is excited to the Rydberg state or when it is not loaded in the atom geometry (red is sodium, blue is cesium in the atom image) depicted below the graph. The excitation of the cesium atom induces a shift in the resonance location of the sodium atom.

While the observation of blockade may be sufficient for quantum measurement, a more quantitative analysis of the interaction strength can be far more useful for calibration of atom distances or quantum simulation. However, at the large interspecies interactions present in the small distances of figure 5.7a, the interaction strength is difficult to measure. A technical constraint lies in the bandwidth of our double-passed AOM which we use to scan the frequency. A more physical limitation arises from finite temperature effects and static variation in the interspecies atomic distances, both of which result in a broadened interaction resonance. Thus, to reliably measure the interaction strength at a particular distance, which can yield metrics such as the C_6 coefficient, we bring the atoms farther apart such that the interaction strength is around the MHz scale. Under this condition, a resonance shift can be quantitatively measured and is shown in figure 5.8. While the camera image of the atom locations do yield a calibration of the interatomic distance, an interaction strength measurement is perhaps the most accurate determinant of the interatomic spacings (given that we trust the theoretical interaction strength calculations). We have found that the measured interaction strength disagrees strongly with the expectation from the camera image. We attribute this discrepancy to axial displacement of our two arrays, which our camera is unable to distinguish. In fact, this interaction measurement allows us to calibrate the axial displacement of a given pair of arrays.

5.5 Summary and Outlook

Through the work of the previous 4 chapters, the stage has been set for experiments involving dual-species optical tweezer arrays capable of Rydberg excitations. Large sodium arrays can be created and coherent Rydberg excitation has been achieved. Technical improvements largely center around better control of phase noise of the 1178 nm laser and higher power for the 409 nm laser. In addition to using a 15 W pumped TiSapph laser, a glass cell change to one without AR coating would

also greatly improve the intensity of 409 nm light on the atoms, which would increase the coherence of a π pulse. Changing the glass cell would also eliminate complications, such as etalon, that we had to contend with for this thesis. A new chamber is currently being designed, also equipped with in-vacuum electrodes. In-vacuum electrodes can be used to either stabilize the electric field environment which can affect the Rydberg coherence time or tune the interspecies interaction to a Förster resonance[6].

Future scientific directions center around efforts in quantum computing and quantum simulation. We now discuss each in turn.

5.5.1 Future Prospects in Quantum Computing

For quantum computing, dual-species atom arrays naturally implement the two qubit classes typical in quantum circuits, ancillary and data qubits[164]. In our case, for instance, sodium atoms can be the ancillary qubits while cesium atoms can be the data qubits. In addition to quantum circuits, readout of stabilizers in quantum error correcting codes[88] typically require ancilliary qubits. For example, in the standard surface code geometry[80], ancilliary qubits are placed at the centers of plaquettes consisting of data qubits with connectivity to the data qubits to efficiently read out the stabilizers. Additionally, in a typical error-corrected quantum computer, multiple rounds of readout need to be performed on the ancilliary qubits without disrupting the data qubits (other than through the measurement result). Crosstalk free readout of the ancillary qubits can also be used to efficiently prepare long range entangled states[227]. Currently in single-species atom arrays, atoms need to be transferred to spatially separated readout zones[27], which is slower than imaging in place. Furthermore, any leak light of the resonant readout light can induce error in the data qubits.

The natural gateset for a dual-species atom array will likely be different from single species atom arrays. In a single species atom array, the focus has been on performing gates with global driving pulses, since the Rydberg lasers simultaneously address all atoms. Although challenging, multi-

qubit gates have been successfully solved by carefully tracking the evolution phases of all relevant qubit states [138,77,47]. Furthermore, combining these global driving pulses with atom rearrangement has led to quantum processors with all-to-all connectivity [28] along with error correction [27]. Compilers [220,59] have also been developed specifically with these reconfigurable atom arrays in mind. Nevertheless, free individual addressing of subclasses of atoms should add to the toolbox of available gates and is easier to implement than global gates for the dual-species array. This is because global gates will require pulse synchronization between the independent lasers driving the two species. However, there are proposals to utilize global pulses for dual species atom arrays [49].

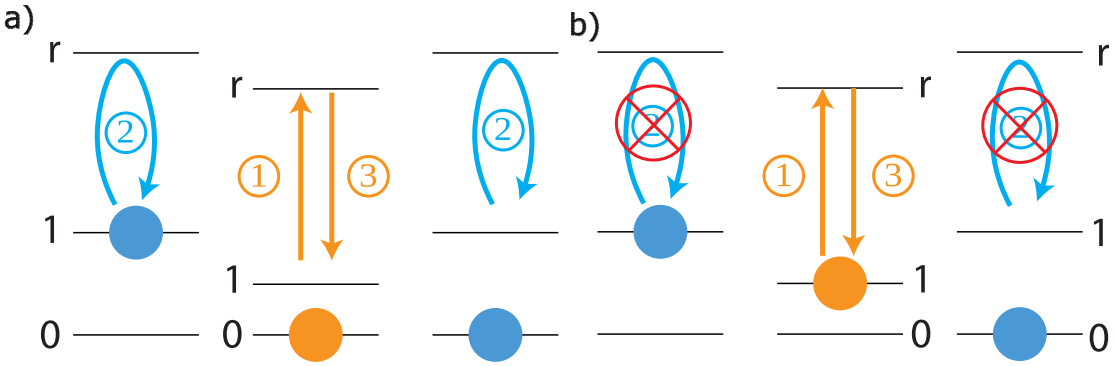

Figure 5.9: Setup for a multi-qubit dual-species gate. A sodium atom (orange) is placed between two cesium (blue) atoms. Each atom has two hyperfine ground states and a Rydberg state. The protocol involves a π pulse on sodium, followed by a global 2π pulse on cesium, and another π pulse on sodium. Ideally, the sodium Rydberg state blockades the cesium Rydberg state, but the cesium Rydberg states do not blockade each other. (a) Depicts the action of the protocol when sodium is in state $|0\rangle$. Here, all dynamics of cesium are allowed. (b) Depicts the action of the protocol when sodium is in state $|1\rangle$. Here, the dynamics of cesium are completely blockaded.

One of the first gate proposals [112] based on Rydberg atoms actually has a natural implementation in dual-species atom arrays instead of single species atom arrays. We summarize its working principle here, and discuss its generalizations to larger systems. Consider two atoms, sodium (orange) and cesium (blue) (see figure 5.9 but ignoring the right most cesium atom) within a blockade radius.

The atoms have two hyperfine ground states $|0\rangle$, $|1\rangle$ which form the qubit basis. Rydberg lasers which connect only hyperfine state $|1\rangle$ to Rydberg states for each species are also available. Now, we consider the following 3 step protocol.

1. Apply a π pulse on the sodium atom from hyperfine state $|1\rangle$ to $|r\rangle$.
2. Apply a 2π pulse on the cesium atom from hyperfine state $|1\rangle$ to $|r\rangle$.
3. Apply a π pulse on the sodium atom from $|r\rangle$ back to hyperfine state $|1\rangle$.

When the sodium atom is in state $|0\rangle$, steps 1 and 3 do not affect the state at all, and the 2π pulse in step 2 succeeds with a π phase shift (negative sign) if the cesium atom is in state 1. When the Na atom is in state $|1\rangle$, steps 1 and 3 result in a full 2π pulse on the Na atom, but step 2 fails due to the Rydberg-Rydberg interaction shifting the cesium atom Rydberg state out of resonance. Thus, this procedure implements the following gate $|00\rangle \rightarrow |00\rangle$, $|01\rangle \rightarrow -|01\rangle$, $|10\rangle \rightarrow -|10\rangle$, $|11\rangle \rightarrow -|11\rangle$, where the first atom is the Cs atom and the second atom is the Na atom. This can be notated as $|0\rangle_{\text{Na}}\langle 0|_{\text{Na}} \otimes Z_{\text{Cs}} - |1\rangle_{\text{Na}}\langle 1|_{\text{Na}} \otimes I_{\text{Cs}}$ and is an entangling gate.

This procedure can be extended to having multiple cesium atoms within a blockade radius of sodium (protocol shown in figure 5.9). If we assume that sodium Rydberg atoms blockade cesium Rydberg atoms, but the cesium atoms are far enough apart to not influence each other, then the two cesium atoms act independently, and the implemented gate is $|0\rangle_{\text{Na}}\langle 0|_{\text{Na}} \otimes Z_{\text{Cs1}} Z_{\text{Cs2}} - |1\rangle_{\text{Na}}\langle 1|_{\text{Na}} \otimes I_{\text{Cs1}} I_{\text{Cs2}}$, which maps the ZZ operator on the two cesium atoms to the sodium hyperfine state $|0\rangle$, which can subsequently be read out. These assumptions apply in the ideal case, and figure 5.10 runs a simple 3 atom (1 sodium, 2 cesium) calculation assessing the error due to extraneous interaction. When the Na atom is in $|0\rangle$, it needs to allow for the cesium atoms to interact. Since it will never be excited to the Rydberg state, the interspecies interaction is irrelevant here. Figure 5.10a shows how the fidelity depends on the intraspecies cesium nearest-neighbor interaction (the actual interaction

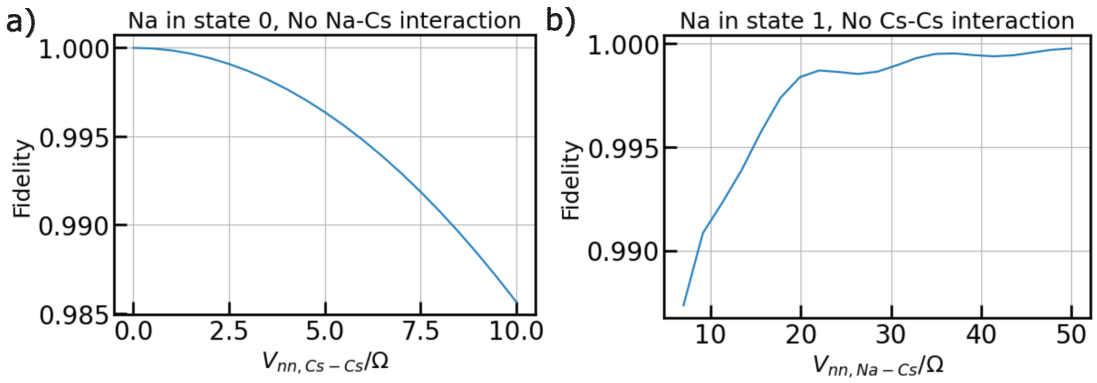

Figure 5.10: Fidelity calculation for the protocol described in figure 5.9 and the text. (a) Fidelity when the sodium atom is in state 0 as a function of the intraspecies cesium interaction. The interspecies interaction is irrelevant for this fidelity. (b) Fidelity when the sodium atom is in state 1 as a function of the interspecies interaction. Any intraspecies cesium interaction actually increases the fidelity of this initial state of the protocol.

between the two cesium atoms in the scheme is smaller than this due to the distance dependence of the interaction) in units of the Rabi frequency. When the sodium atom is in state $|1\rangle$, it needs to blockade all cesium activity, so the intraspecies cesium interaction only assists in the fidelity of this step. Figure 5.10b shows the gate fidelity as a function of the interspecies interaction in units of the Rabi frequency. While this scheme has individual value as a gate, it can easily be extended to perform a ZZ measurement on two cesium atoms using a single sodium atom. Consider the following procedure:

1. Prepare a sodium atom in the hyperfine state $\frac{1}{\sqrt{2}}(|0\rangle + |1\rangle)$.

2. Apply the aforementioned gate procedure implementing the operation $|0\rangle_{\mathrm{Na}}\langle 0|_{\mathrm{Na}} \otimes Z_{\mathrm{Cs1}}Z_{\mathrm{Cs2}} - |1\rangle_{\mathrm{Na}}\langle 1|_{\mathrm{Na}} \otimes I_{\mathrm{Cs1}}I_{\mathrm{Cs2}}$ mapping the $Z_{\mathrm{Cs1}}Z_{\mathrm{Cs2}}$ operator value as a relative phase.

3. Read out this phase by performing a Hadamard operation in the hyperfine manifold of sodium, and then projectively measuring the sodium atom in the $|0\rangle$, $|1\rangle$ basis.

State of Cesium atoms	Three atom state after step 2	Final readout of sodium atom
$\|00\rangle$	$\|000\rangle - \|100\rangle$	$\|1\rangle$
$\|01\rangle$	$-\|001\rangle - \|101\rangle$	$\|0\rangle$
$\|10\rangle$	$-\|010\rangle - \|110\rangle$	$\|0\rangle$
$\|11\rangle$	$\|011\rangle - \|111\rangle$	$\|1\rangle$

Table 5.1: The implementation of a $Z_{\mathrm{Cs1}}Z_{\mathrm{Cs2}}$ measurement on two cesium atoms by a sodium atom. The three atom state after step 2 refers to the in-text enumerated measurement procedure and the state is in the order of the sodium atom followed by the two cesium atoms.

The way this procedure affects the four computational basis states of two cesium atoms is tabulated in table 5.1. This measurement scheme can also be used to generate entangled states of cesium atoms. For instance, if the product state $\frac{1}{2}(|00\rangle + |01\rangle + |10\rangle + |11\rangle)$ is prepared, a measurement of the $Z_{\mathrm{Cs1}}Z_{\mathrm{Cs2}}$ operator will prepare either the $\frac{1}{\sqrt{2}}(|00\rangle + |11\rangle)$ or the $\frac{1}{\sqrt{2}}(|01\rangle + |10\rangle)$ Bell states depending on the measurement result. This gate can be generalized to any dynamics on the cesjh atoms, not necessarily just this ZZ operation. Other schemes involving step wise excitation have also been proposed [158] and can be used for universal digital quantum simulation [233].

5.5.2 Future Prospects in Quantum Simulation

For quantum simulation, dual-species Rydberg atom arrays provide a rich, controllable platform naturally suited for studying bipartite lattices, where each part of the lattice can be filled by each atom. In the ground-Rydberg encoding we have been using to implement transverse field Ising models (see section 4.2), the dual-species atom array naturally implements, with global driving, the Hamiltonian

$$H = \sum_{i_A} \left(\frac{\hbar\Omega_A}{2} \sigma^x_{i_A} - \hbar\Delta_A n_{i_A} \right) + \sum_{i_B} \left(\frac{\hbar\Omega_B}{2} \sigma^x_{i_B} - \hbar\Delta_B n_{i_B} \right)$$
$$+ \sum_{i_A<j_A} V^{AA}_{i_A j_A} n_{i_A} n_{j_A} + \sum_{i_B<j_B} V^{BB}_{i_B j_B} n_{i_B} n_{j_B} + \sum_{i_A<j_B} V^{AB}_{i_A j_B} n_{i_A} n_{j_B} \tag{5.2}$$

where the indices i_A, i_B label sites with atom A and atom B, Ω_A, Δ_A are the Rabi frequency and detuning for the driving laser for atom A, Ω_B, Δ_B are the Rabi frequency and detuning for the driving laser for atom B, and V^{AA}_{ij}, V^{BB}_{ij}, V^{AB}_{ij} are the two intraspecies interactions and one interspecies interactions. 4 of these parameters can be tuned easily and continuously with lasers. The continuous tuning of these drive parameters can nominally place the two species in different regions of their single species phase diagrams. The interaction terms can be tuned discretely with the choice of Rydberg state and continuously using external fields. As discussed in section 5.2, while the intraspecies interactions tend to be repulsive, based on the choice of state, the interspecies interactions can be attractive, which is a new feature compared to single-species atom arrays. The geometries of the two lattices can also be freely tuned with individual spatial light modulators of both species. A particular two ladder geometry with carefully tuned interaction strengths has been proposed for the observation of emergent spacetime supersymmetry [140].

In addition to ground state physics, dual-species atom arrays are well suited for dynamical experiments. The individual addressability of a sublattice (with still a global drive) can quench the system into a non-eigenstate with non-trivial dynamics. These ideas make these atom arrays ideal for studying central spin models surrounded by a bath [71] or studying defects in phases, where one species can be prepared in a phase, but the other species is interspersed as an interacting defect. One of the species can also be used as a probe for the other. For instance, species A can be prepared in a particular phase (or state), and species B (which interacts with A) can be driven to investigate the

spectrum of species A. Floquet engineering can also open possibilities for new Hamiltonians derived from equation 5.2.

6

Rydberg mediated quantum gates between polar molecules

6.1 Introduction

In the last chapter, we focused on the possibilities of dual-species neutral atom arrays that interact via promoting both species to the Rydberg state. Another possibility for obtaining interactions

between particles in the array is to assemble the two atoms into a polar molecule, which have a permanent molecular-frame dipole moment. Polar molecules then interact with each other via the dipole-dipole interaction. Tweezer arrays of ultracold molecules have recently been created primarily via two methods: direct laser cooling and assembly of ultracold atoms[133]. Direct laser cooling takes the approach of finding a special set of molecules[68,221] which contain nearly closed cycling transitions. These transitions can cycle over a thousand photons or so with a reasonable number (around 10) of repump lasers. In this way, typical laser cooling techniques on atoms work reasonably well for these molecules. These molecules are typically of the form MX, where M is an alkaline-earth-like metal and X is an electronegative radical with a single unpaired electron. In the compound MX, one of the two valence electrons in M forms a covalent bond with X, while the other is predominantly located on the M atom. Thus, photon cycling of the electron on the M atom can be performed with minimal energy transfer to the relatively uncoupled vibrational and rotational degrees of freedom, since the electron never interacts much with the atoms that form X. Examples of such molecules include CaF[7,104] and CaOH[228], both of which have been loaded into optical tweezer arrays. MOTs of SrF[16], YO[57] and SrOH[134] have been formed, and tweezer loading is the very next step.

Assembly of ultracold atoms into molecules starts from ultracold atoms, which can be reliably created utilizing laser cooling techniques. Then, molecules can be created (utilizing the proper techniques) from the atoms with minimal heating. Assembled molecules typically are formed from laser coolable atoms, making bialkali molecules a natural candidate for such techniques. Molecules such as Cs_2[62], KRb[162], Rb_2[132], RbCs[219,156], NaK[171,229], NaRb[96], NaLi[190] and NaCs[23] have been formed in their ground states with high fidelity. Others containing alkaline earth atoms such as Sr_2[137] have also been assembled while more esoteric combinations (FrAg[151]) are also actively being explored.

Another benefit of the assembly approach is the convenient availability of a reservoir of atoms without the need to introduce additional lasers or infrastructure. These atoms, as a quantum re-

source, have been used to determine the successful creation of a molecule for purposes of rearrangement[177], and for the observation of interactions[97,145] between Rydberg atoms and molecules. Given the development of Rydberg atom techniques detailed in this thesis and our group's expertise in molecular assembly, we are naturally poised to explore the prospects of a hybrid system consisting of tweezer arrays of molecules and atoms.

In this chapter, we briefly highlight our expertise in forming ultracold molecules and propose to use the atom-molecule interaction to enhance the capabilities of a molecule-based quantum computer. Section 6.2 describes our efforts towards a generic all-optical path to the assembly of molecules. Then section 6.3 summarizes the current prospects of using molecules for quantum computing along with their current limitations. Section 6.4 details our main proposal to utilize the interaction between Rydberg atoms and molecules to drive a faster sub-microsecond gate between molecules. Section 6.5 then describes a specific implementation in NaCs molecules utilizing cesium Rydberg atoms. Section 6.6 extends our approach to the application of non-destructive state-selective measurement of molecules using Rydberg atoms. Lastly section 6.7 details the complications of our method when extending it to larger arrays.

6.2 A General All-Optical Approach to Assembling Molecules

Assembly of ultracold atoms into molecules has been one of the most reliable methods of creating ultracold molecules with full quantum-state control. Due to the small interatomic distances present in a molecule, a two-step assembly procedure is typically employed. The two steps help bridge the large spatial wavefunction difference between two free atoms and a ground state molecule.

First, a weakly-bound molecule is created typically via a Feshbach resonance[52] followed by stimulated Raman adiabatic passage (STIRAP) to the rovibrational ground state. This approach has been successfully used in both bulk gas[62,162,132,219,156,171,96,229] and optical tweezers[42,213]. Whereas the

STIRAP procedure is rather general, magnetic Feshbach resonances may not always be available. These resonances typically arise from atoms that have magnetically sensitive states and can be an issue for alkaline earth atoms. Furthermore, the magnetic fields at which these Feshbach resonances are located may pose technical challenges.

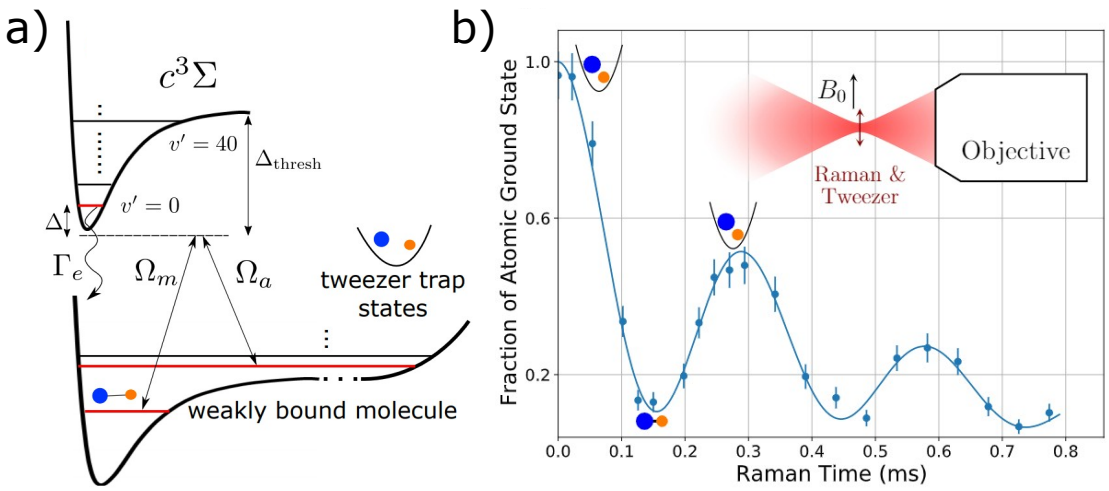

Figure 6.1: (a) The optical Raman transfer scheme from a free atom state in a harmonic trap to a weakly bound molecule via a molecular intermediate state. (b) Rabi oscillations between the free atom and weakly bound molecule state.

Here, we describe a general approach of forming weakly-bound molecules and its proof-of-principle demonstration on our dual-species platform [244]. The setup of our scheme is depicted in figure 6.1a. This method creates a weakly bound NaCs molecule from a pair of sodium and cesium atoms in a harmonic trap. The Raman transfer between the two states utilizes two laser beams that are detuned from an intermediate excited state by a detuning Δ. The Rabi frequencies for the transition between the free atom (weakly-bound molecular) state and the intermediate state is $\Omega_{\text{a}}(\Omega_{\text{m}})$. When the detuning is the largest energy scale of the system, the dynamics of the system can be described by an effective two level system which was described in detail in section 3.3 for a ladder system (when the intermediate state's energy is in between the two other states). The mathematics is

equivalent for our lambda system (when the intermediate state's energy is higher than both of the other states), where the effective Raman Rabi frequency is given by

$$\Omega = \frac{\Omega_{\mathrm{a}}\Omega_{\mathrm{m}}}{2\Delta}. \tag{6.1}$$

While the AC Stark shift and the scattering rate nominally follow the same formulas as discussed in section 3.3, this particular application has an additional layer of complexity, arising from the small energy spacing (typically 100s of MHz) between the free atoms state (tweezer trap ground state) and the weakly-bound molecular state relative to the intermediate state detuning. Hence, there exists cross-coupling, where the laser beam meant for the free atoms state also couples to the weakly-bound molecule state and vice versa. Assuming the power in each beam is the same, this approximately doubles both the AC Stark shift and the scattering rate resulting in a Stark shift of

$$\omega_{\mathrm{AC}} = \frac{\Omega_m^2}{2\Delta}, \tag{6.2}$$

and a scattering rate of

$$\Gamma = \Gamma_e \frac{\Omega_m^2}{2\Delta^2}, \tag{6.3}$$

where we have also assumed that $\Omega_m \gg \Omega_a$ so that the contribution to the Stark shift and scattering rate from the free atoms state is negligible. This assumption is quite valid, since the intermediate state is a deeply-bound molecular state, which has minimal overlap with the free atoms state.

The ratio of the Rabi frequency (representing the coherent process) to the AC Stark shift is

$$\frac{\Omega}{\omega_{\mathrm{AC}}} = \frac{\Omega_a}{\Omega_m} \ll 1 \tag{6.4}$$

resulting in a strict requirement on the intensity stability of the drive lasers. Namely, if the drive lasers fluctuate at the Ω_a/Ω_m level, the Stark shift would shift the resonance about a Rabi frequency amount leading to decoherence. The stark imbalance between the two coupling strengths leads to these strict technical requirements.

To help increase the ratio Ω_a/Ω_m, we need to increase the amplitude of the tweezer trap wavefunction at short distance. This can be achieved by using the highly interacting hyperfine state combination [106] $|F_{\mathrm{Na}} = 2, m_{F_{\mathrm{Na}}} = 2, F_{\mathrm{Cs}} = 3, m_{F_{\mathrm{Cs}}} = 3\rangle$, which increases the Ω_a/Ω_m ratio from 0.003 to 0.05. Note that this improvement not only relaxes the technical requirement of intensity stability, but also increases the coherent coupling between the atom and molecule state.

To decrease excess scattering from affecting our molecule creation process, we use the tweezer itself to drive the Raman transfer process. In particular, the tweezer may contain two frequency components, and the transfer only occurs when the second component (controlled by an AOM) is turned on. Additionally, since we are contending with excited molecular states, a wide range of resonances can be driven by our laser. Thus, the laser needs to have a clean frequency spectrum. We found much higher molecular creation efficiency (through reduction of scattering) by filtering our light with a 3D Bragg grating (Ondax 114-ER407-015) that has a full width half maximum of about 50 GHz.

The result of our efforts is depicted in figure 6.1b where coherent oscillations between a free atom and weakly bound molecular state are observed at a Rabi frequency of around 300 kHz. The transfer efficiency is 69%. With a weakly-bound molecule successfully created, STIRAP can follow to create a deeply-bound molecule for further study.

6.3 Quantum Computing with Molecules

Individually trapped ultracold polar molecules [142,42,7,101,188,157,183] are a promising candidate system for scalable quantum computing due to their long-lived internal states and intrinsic tunable interactions. Long coherence times have been demonstrated for many molecular degrees of freedom, including nuclear spin [90,172], rotation [39,203,45,170], and vibration [129]. Molecular-frame dipole moments allow molecules to interact via the dipole-dipole interaction, which has been observed for molecular gases prepared in opposite parity rotational states [239,225]. Early proposals of two-qubit gate schemes required external fields to polarize the molecules. In these cases, field stability imposes a practical constraint to their viability [66,241,103,120]. Recently, robust schemes with the potential for greater than 99.99% fidelity have been proposed. These schemes directly take advantage of the intrinsic dipolar interaction between two field-free molecular rotors, using a dipolar exchange [163,107] or energy shifts created by the interaction [108]. The former has been realized in optical tweezer experiments [104,13,176] of molecules. However, the millisecond gate times in these schemes are long compared to what has been realized in superconducting [128], trapped ion [38], or trapped atom systems [138,89,77]. A path to achieving molecule dipolar interaction strengths larger than a kHz by reducing molecular separation to below the trap light wavelength in an optical tweezer system has been outlined, but is technically demanding [44].

We present an approach which uses an atom to speed up molecular two-qubit gate times by several orders of magnitude. By transferring atoms to highly excited Rydberg states, they can be made to interact with polar molecules (1-5 Debye) through the dipole-dipole interaction. When an atomic transition is brought into resonance with a molecule's rotational transition, the Rydberg atom can mediate the interaction between molecules via its large transition dipole moment ($\sim$ 10 kDebye), which amplifies this interaction by several orders of magnitude. This amplified interaction strength can be used to implement Rydberg-mediated entangling gates between molecules. Because one

of the most widely-used schemes to create ultracold molecules is association of the constituent atoms[62,162,132], atoms are a readily available resource in many molecule experiments, making this scheme feasible to implement.

6.4 Driven exchange gate

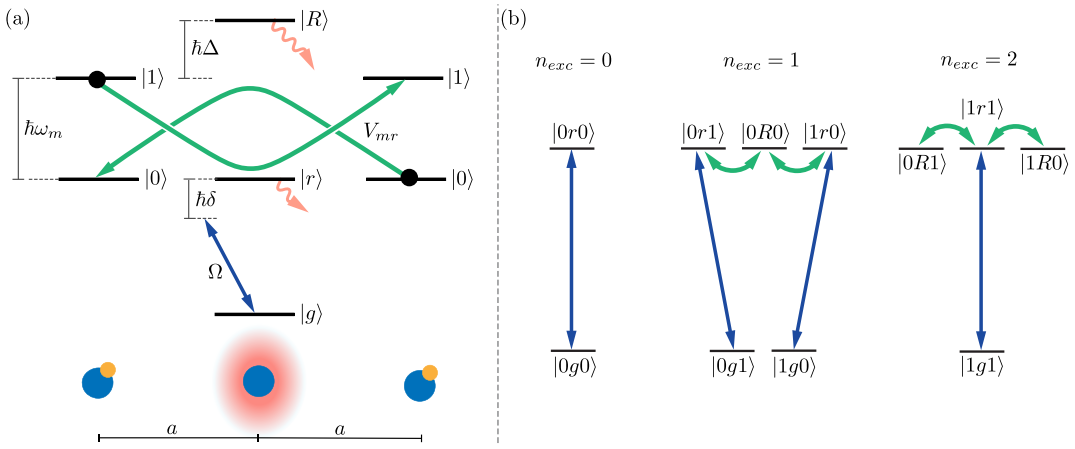

Figure 6.2: Relevant level structure for a driven Rydberg-mediated exchange between two molecules. (a) The relevant energy levels for the molecules (left and right) and the Rydberg atom (center). The energy spacing between the computational basis states for the molecule is $\hbar\omega_{\mathrm{m}}$, and the spacing between Rydberg states $|r\rangle$ and $|R\rangle$ differs from the molecule spacing by $\hbar\Delta$. The excitation laser, which excites an atom from $|g\rangle$ to $|r\rangle$, has Rabi frequency Ω, and its detuning is denoted by $\hbar\delta$. (b) The separation of the three-body Hilbert space (12 states) into distinct subspaces. The blue lines indicate the Rydberg excitation laser coupling, and the green lines depict the strong Rydberg-molecule interaction.

We first describe the fast entangling gate resulting from a Rydberg-mediated interaction between two molecules. We consider a three-particle system, consisting of two molecules with an atom placed in between them, as shown in figure 6.2a. To capture the essence of the gate, the molecules are treated as two-level systems ($|0\rangle$ and $|1\rangle$) which have a transition dipole moment d_m between them. In the atomic system, three states ($|g\rangle$, $|r\rangle$ and $|R\rangle$) are considered, where $|g\rangle$ is a ground electronic

state of the atom, and $|r\rangle$ and $|R\rangle$ are opposite parity Rydberg states which have a large transition dipole moment d_r between them.

The interaction Hamiltonian arises from the dipole-dipole interaction[231,239] between the particles separated by an interparticle spacing of a:

$$H_{\text{int}} = \frac{1}{2}[V_{\text{mr}}(\sigma_1^+ S^- + \sigma_1^- S^+ + S^+\sigma_2^- + S^-\sigma_2^+) + V_{\text{mm}}(\sigma_1^+\sigma_2^- + \sigma_1^-\sigma_2^+)] \tag{6.5}$$

where $\sigma_i^{\pm}$ are the Pauli ladder operators for molecules in the basis $\{|0\rangle, |1\rangle\}$, and $S^{\pm}$ are the Pauli ladder operators for the Rydberg atom in the basis $\{|r\rangle, |R\rangle\}$. The molecule-Rydberg interaction and the molecule-molecule interaction are given by $V_{\text{mr}} = d_m d_r/(4\pi\varepsilon_0 a^3)$ and $V_{\text{mm}} = d_m^2/(32\pi\varepsilon_0 a^3)$, respectively. The ground state atom, $|g\rangle$, is far off-resonance, and does not participate in the exchange interaction. Furthermore, we denote the molecular energy spacing as $\hbar\omega_{\text{m}}$, and the difference between the Rydberg energy spacing and the molecular energy spacing as $\hbar\Delta$. The energy spacing between the atomic ground state and Rydberg state $|r\rangle$ is denoted $\hbar\omega_{\text{gr}}$.

In addition to the intrinsic Hamiltonian arising from the dipolar interaction, we add a drive of the atom from $|g\rangle$ to $|r\rangle$ with Rabi frequency Ω, and detuning $\delta = \omega_{\text{L}} - \omega_{\text{gr}}$, where ω_{L} is the angular frequency of the laser. There are a total of twelve states, but the Hamiltonian is block diagonal in the sectors $\{|0g0\rangle, |0r0\rangle\}$, $\{|0g1\rangle, |0r1\rangle, |1g0\rangle, |1r0\rangle, |0R0\rangle\}$, $\{|1g1\rangle, |1r1\rangle, |0R1\rangle, |1R0\rangle\}$, and $\{|1R1\rangle\}$. These sectors can be characterized by the number of dipolar excitations

$$n_{\text{exc}} = \frac{1}{4}(\sigma_1^+\sigma_1^- + S^+S^- + \sigma_2^+\sigma_2^-). \tag{6.6}$$

Neither dipole-dipole interaction nor laser driving couple between these manifolds, and the dynamics within each sector are thus independent, with Hamiltonians given by:

$$H_{n_{\text{exc}=0}} = \hbar \begin{pmatrix} 0 & \Omega/2 \\ \Omega/2 & \delta \end{pmatrix}, \tag{6.7}$$

$$H_{n_{\text{exc}=1}} = \begin{pmatrix} -\hbar\delta & \hbar\Omega/2 & V_{\text{mm}}/2 & 0 & 0 \\ \hbar\Omega/2 & 0 & 0 & V_{\text{mm}}/2 & V_{\text{mr}}/2 \\ V_{\text{mm}}/2 & 0 & -\hbar\delta & \hbar\Omega/2 & 0 \\ 0 & V_{\text{mm}}/2 & \hbar\Omega/2 & 0 & V_{\text{mr}}/2 \\ 0 & V_{\text{mr}}/2 & 0 & V_{\text{mr}}/2 & \hbar\Delta \end{pmatrix} \tag{6.8}$$

$$H_{n_{\text{exc}=2}} = \begin{pmatrix} -\hbar\delta & \hbar\Omega/2 & 0 & 0 \\ \hbar\Omega/2 & 0 & V_{\text{mr}}/2 & V_{\text{mr}}/2 \\ 0 & V_{\text{mr}}/2 & \hbar\Delta & V_{\text{mm}}/2 \\ 0 & V_{\text{mr}}/2 & V_{\text{mm}}/2 & \hbar\Delta \end{pmatrix} \tag{6.9}$$

We first explore the case where the laser detuning is zero ($\delta = 0$) and the Rydberg transition is resonant with the molecule transition ($\Delta = 0$). The gate is performed by driving the atom from the ground state for a time $T = 2\pi/\Omega$. At the end of the drive, the $|0g0\rangle$ state returns to itself with a phase of -1. For this particular T, it can be shown analytically, ignoring the much smaller molecule-molecule interaction, that the entangling gate

$$\begin{pmatrix} -1 & 0 & 0 & 0 \\ 0 & 0 & 1 & 0 \\ 0 & 1 & 0 & 0 \\ 0 & 0 & 0 & 1 \end{pmatrix} \tag{6.10}$$

in the basis $\{|0g0\rangle, |0g1\rangle, |1g0\rangle, |1g1\rangle\}$ can be realized for a specific Rabi frequency of the drive, related to the molecule-Rydberg interaction by

$$\Omega = \sqrt{\frac{2}{4k^2-1}} V_{\mathrm{mr}}/\hbar \tag{6.11}$$

where k is an integer larger than 0. For $k = 1$, this corresponds to a Rabi frequency of $\sqrt{\frac{2}{3}} V_{\mathrm{mr}}$, allowing this gate to take advantage of the fast molecule-Rydberg interaction. To understand equation 6.11, we analyze the 5 state $n_{\mathrm{exc}} = 1$ manifold and 4 state $n_{\mathrm{exc}} = 2$ manifold separately.

Diagonalizing the Hamiltonian for the $n_{\mathrm{exc}} = 1$ manifold (equation 6.8), when $\delta = \Delta = V_{\mathrm{mm}} = 0$, the eigenvalues $0, \hbar\Omega/2, -\hbar\Omega/2, -\sqrt{\hbar^2\Omega^2 + 2V_{\mathrm{mr}}^2}/2, \sqrt{\hbar^2\Omega^2 + 2V_{\mathrm{mr}}^2}/2$ are obtained, and the states of interest $|0g1\rangle$ and $|1g0\rangle$ can be written in the eigenbasis

$$|0g1\rangle = \begin{pmatrix} \frac{V_{\mathrm{mr}}}{\sqrt{\hbar^2\Omega^2+2V_{\mathrm{mr}}^2}} \\ -1/2 \\ -1/2 \\ \frac{\hbar\Omega}{2\sqrt{\hbar^2\Omega^2+2V_{\mathrm{mr}}^2}} \\ \frac{\hbar\Omega}{2\sqrt{\hbar^2\Omega^2+2V_{\mathrm{mr}}^2}} \end{pmatrix}, |1g0\rangle = \begin{pmatrix} \frac{V_{\mathrm{mr}}}{\sqrt{\hbar^2\Omega^2+2V_{\mathrm{mr}}^2}} \\ 1/2 \\ 1/2 \\ \frac{\hbar\Omega}{2\sqrt{\hbar^2\Omega^2+2V_{\mathrm{mr}}^2}} \\ \frac{\hbar\Omega}{2\sqrt{\hbar^2\Omega^2+2V_{\mathrm{mr}}^2}} \end{pmatrix}. \tag{6.12}$$

These two states only differ in the sign of their second and third component. In order to get a swap between these two in the time evolution, we need the second and third components to flip sign, while keeping the other components the same. After a time $T = 2\pi/\Omega$, the first component keeps its phase, while the second and third component flip their sign (acquire a π phase shift) due to their phase evolution at a rate of $\Omega/2$. In this time, the fourth and fifth components need to acquire a 2π (or multiple of 2π) phase shift leading to the requirement

$$\frac{\sqrt{\hbar^2\Omega^2 + 2V_{\mathrm{mr}}^2}}{2} = k\hbar\Omega \tag{6.13}$$

where k is an integer. Solving this equation for Ω yields the result in equation 6.11.

We also need to verify that the Ω found above also works in the $n_{\text{exc}} = 2$ manifold. Diagonalizing the Hamiltonian of this manifold in equation 6.9 when $\delta = \Delta = V_{\text{mm}} = 0$, the eigenvalues $0, 0, -\sqrt{\hbar^2\Omega^2 + 2V_{\text{mr}}^2}/2, \sqrt{\hbar^2\Omega^2 + 2V_{\text{mr}}^2}/2$ are obtained, and the state of interest $|1g1\rangle$ can be written in the eigenbasis

$$|1g1\rangle = \begin{pmatrix} -\frac{V_{\text{mr}}\sqrt{\hbar^2\Omega^2+V_{\text{mr}}^2}}{\hbar^2\Omega^2+2V_{\text{mr}}^2} \\ -\frac{V_{\text{mr}}\sqrt{\hbar^2\Omega^2+V_{\text{mr}}^2}}{\hbar^2\Omega^2+2V_{\text{mr}}^2} \\ \frac{\hbar\Omega}{\sqrt{2\hbar^2\Omega^2+4V_{\text{mr}}^2}} \\ \frac{\hbar\Omega}{\sqrt{2\hbar^2\Omega^2+4V_{\text{mr}}^2}} \end{pmatrix} \tag{6.14}$$

With the constraint found in equation 6.13, all 4 components will remain the same, and the state is unchanged as needed.

The dynamics of this gate for $k = 1$ in each manifold is shown in figure 6.3. In the limit of large k, corresponding to $\hbar\Omega \ll V_{\text{mr}}$, the locations of these resonant exchange drives get closer together, indicating a scheme robust to the exact drive Rabi frequency. In this limit, for the $n_{\text{exc}} = 1$ manifold, the intermediate system consisting of $\{|0r1\rangle, |0R0\rangle, |1r0\rangle\}$ can be diagonalized, where a zero energy mode will emerge[240]. The two edge states $|1g0\rangle$ and $|0g1\rangle$ will then be coupled through this mode and their states can swap after a particular time of unitary evolution. In the 2 excitation manifold, a zero energy mode in the $\{|0R1\rangle, |1R0\rangle, |1r1\rangle\}$ manifold is also created, but consists only of a combination of the $|0R1\rangle$ and $|1R0\rangle$ states which has no matrix element with the $|1g1\rangle$ ground state. Thus, no excitation is allowed and the system remains in the ground state with no phase accumulation. The full landscape of the fidelity as a function of $\hbar\Omega/V_{\text{mr}}$ is shown in figure 6.4.

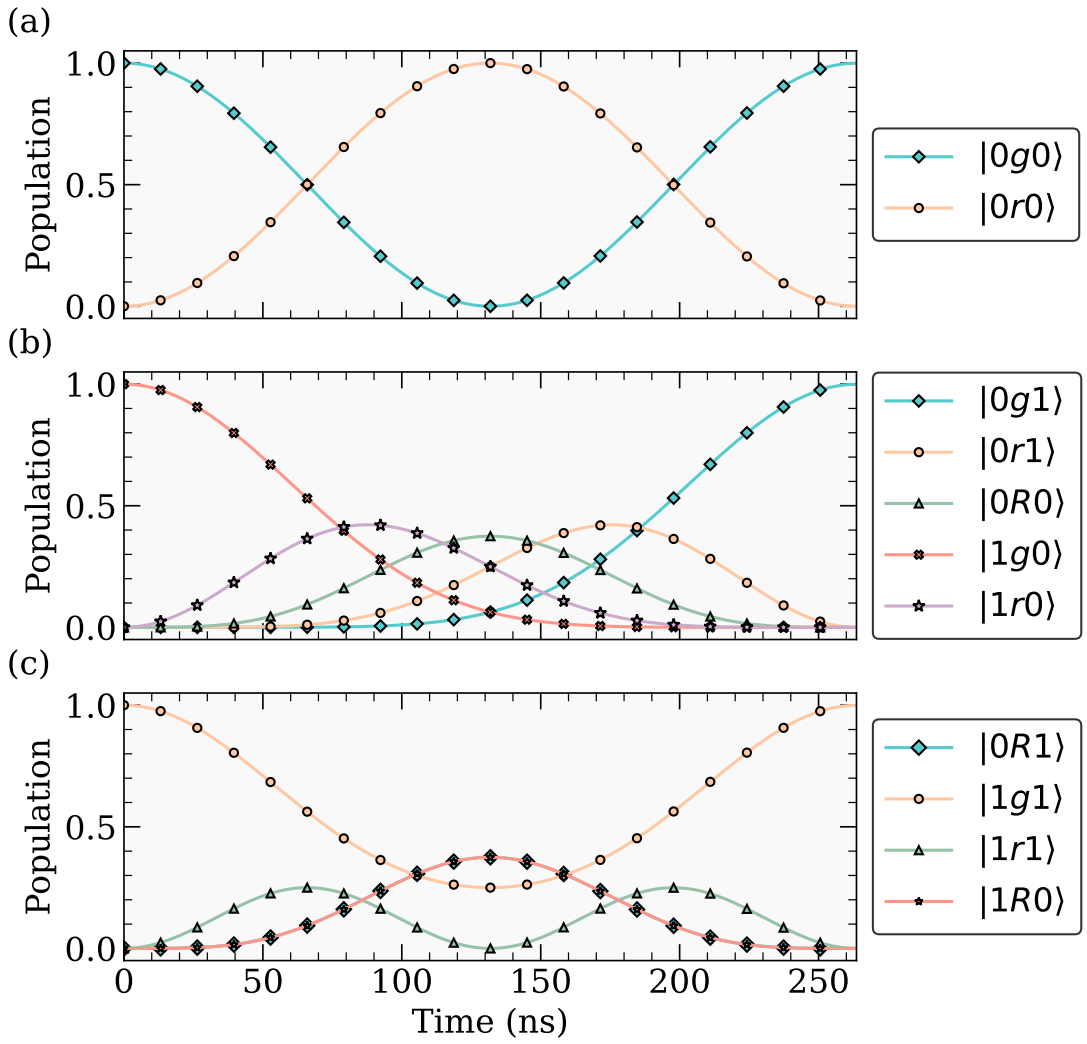

Figure 6.3: Population evolution through the driven exchange gate, starting in (a) $|0g0\rangle$, (b) $|1g0\rangle$, and (c) $|1g1\rangle$ for $\Omega = \sqrt{2/3}V_{\mathrm{mr}}/\hbar$. While molecule-molecule interaction is included in the evolution, we note that $d_r \gg d_m$, such that it only introduces a perturbation to the molecule-Rydberg interaction of magnitude $< 10^{-9}$.

6.4.1 Calculating Fidelities with Rydberg Decay

Before proceeding, let's discuss how we calculate fidelities for this chapter. We use the following definition for the gate fidelity [179,164]

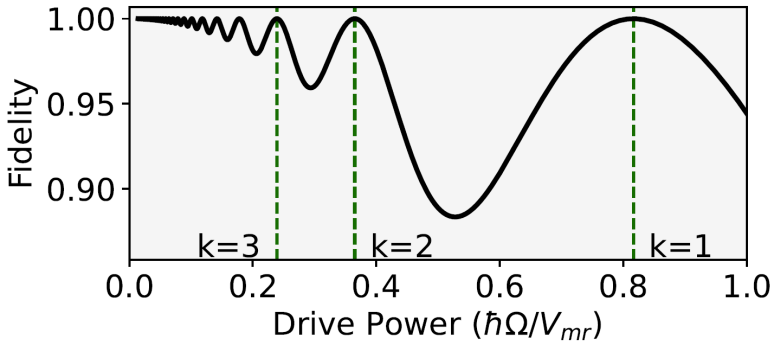

Figure 6.4: Demonstration of driven exchange resonances at various integer k, as defined in equation 6.11. As k increases, the resonances become closer and shallower, leading to insensitivity to the exact drive Rabi frequency.

$$F = \mathrm{Tr}(U_i U_p^\dagger / n) \tag{6.15}$$

where U_p is the gate unitary as calculated with no error sources, and n is the size of the relevant Hilbert space. U_i is the unitary of the operation with the error of interest, and the matrix elements $(U_i)_{A,B}$ are generated by applying a Hamiltonian with the error to a state A and using the coefficient of the resulting state B. For U_i with no error, $U_i = U_p$ and $F = 1$.

An error source, which fundamentally limits the performance of this gate, is the decay of the Rydberg atom which facilitates our exchange between the molecules. Lifetimes at typical Rydberg levels used for quantum information are approximately 100 μs, and are discussed in more detail in section 3.2. Typical Rydberg blockade gates skirt around this error by minimizing the population in the Rydberg state, advantages that our scheme does not have.

This gate, by operating outside the blockade regime, allows the excitation laser to pump to Rydberg levels and back faster than blockade based gates. The driven-exchange gate is therefore faster and less error from decay can occur. This advantage is twofold, as the gate only uses one Rydberg

atom, rather than two. In the NaCs with cesium system, decay limits the gate to a fidelity of 0.9997.

This number is calculated by adding non-Hermitian decay terms to our excitation-manifold Hamiltonians:

$$H'_{n_{\text{exc}=0}} = H_{n_{\text{exc}=0}} + \begin{pmatrix} 0 & 0 \\ 0 & -i\hbar\Gamma_r/2 \end{pmatrix}, \tag{6.16}$$

$$H'_{n_{\text{exc}=1}} = H_{n_{\text{exc}=1}} + \begin{pmatrix} 0 & 0 & 0 & 0 & 0 \\ 0 & -i\hbar\Gamma_r/2 & 0 & 0 & 0 \\ 0 & 0 & 0 & 0 & 0 \\ 0 & 0 & 0 & -i\hbar\Gamma_r/2 & 0 \\ 0 & 0 & 0 & 0 & -i\hbar\Gamma_R/2 \end{pmatrix}, \tag{6.17}$$

$$H'_{n_{\text{exc}=2}} = H_{n_{\text{exc}=2}} + \begin{pmatrix} 0 & 0 & 0 & 0 \\ 0 & -i\hbar\Gamma_r/2 & 0 & 0 \\ 0 & 0 & -i\hbar\Gamma_R/2 & 0 \\ 0 & 0 & 0 & -i\hbar\Gamma_R/2 \end{pmatrix}, \tag{6.18}$$

where Γ_r and Γ_R are the decay rates of the two chosen Rydberg levels.

6.5 Implementation in NaCs + Cs

We now consider the implementation of this gate in a system of ground state NaCs molecules and cesium Rydberg atoms. The key requirement is to find a pair of Rydberg states that match the energy gap of a dipole-allowed transition in the molecule, typically a rotational transition. In NaCs, the measured $N = 0$ to $N = 1$ rotational energy splitting is $h \times 3471.3203(7)$MHz[170]. Since Rydberg states are extremely sensitive to electric fields, and to a lesser extent, magnetic fields, external fields may be used to tune these states into resonance. Formation of ground state molecules from

their constituent atoms is a well-established technique that has been successful both in bulk gasses and in optical tweezers, and often relies on magnetic field control to access Feshbach resonances. A Feshbach resonance at 865 G is used to form NaCs molecules[247], and at magnetic fields of this order, Rydberg states can be tuned to be in resonance with the rotational transition in the molecule, as shown in table 6.1.

B(G)	Transition($\|r\rangle \rightarrow \|R\rangle$)	Δ(MHz)	$\|d_r\|$(D)
0	$64P_{1/2} \rightarrow 63D_{3/2}$	-12.6	6488
859.3	$72P_{3/2,3/2} \rightarrow 71D_{5/2,5/2}$	≈ 0	11220
769.9	$57P_{3/2,3/2} \rightarrow 56D_{5/2,3/2}$	≈ 0	4329
908.4	$49P_{3/2,3/2} \rightarrow 48D_{3/2,1/2}$	≈ 0	1280

Table 6.1: List of possible Cs Rydberg states to use for a near-resonant interaction with the NaCs $N = 0$ to $N = 1$ rotational transition at zero magnetic field and various magnetic fields near the NaCs Feshbach resonance at 865 G. The notation used for the atomic states are nL_{j,m_J}, where the m_J is particularly relevant for states at high magnetic field. For the high field states, three different polarization options are listed. Dipole moments are calculated with the Alkali Rydberg Calculator[208], and energy spacings include the quadratic Zeeman shift.

To calculate Rydberg transitions at high magnetic fields and large principal quantum numbers, we need to account for the quadratic Zeeman shift, which can be quite significant. The Hamiltonian for this effect is given by

$$H_{\text{QZeeman}} = \frac{e^2B^2}{8m}(x^2 + y^2) = \frac{e^2B^2}{8m}r^2 \sin^2\theta, \tag{6.19}$$

where θ is the polar angle[195,30]. In the basis $|n, l, j, m_j\rangle$, the matrix element

$$\langle n', l', j', m_j'|H_{\text{QZeeman}}|n, l, j, m_j\rangle \tag{6.20}$$

is nonzero when $l' = l$ or $l' = l \pm 2$, and $m_j' = m_j$. The diagonal contributions are relevant and can shift energy levels significantly. These terms consist of a radial integral and an angular integral.

The radial integral is performed for a state $|n, l, j, m_j\rangle$ with the wavefunctions in the Alkali Rydberg Calculator, which account for spin-orbit coupling[208]. The angular integral is performed by decomposing the state into the uncoupled $|n, l, m_l, s, m_s\rangle$ basis, where the matrix elements of $\sin^2\theta$ in this basis are known analytically[30]. These diagonal matrix elements are taken into account in the selection of states in table 6.1.

The off-diagonal contributions can mix different states, however they are only relevant when the coupling strength is on the same order as the energy separation between the states. Fortunately in cesium, the energy of the nearest states with $l' = l \pm 2$ to the states of interest ($|72P_{3/2,3/2}\rangle$ and $|71D_{5/2,5/2}\rangle$) are about an order of magnitude larger than the coupling strength between them. We note that for higher Rydberg states, these contributions are likely to grow larger and a full diagonalization may be required.

6.5.1 Molecular hyperfine and rotation structure

NaCs is a diatomic polar molecule, consisting of two alkali atoms, with a molecular-frame dipole moment around 4.6 Debye[11] in the rovibrational ground state. The NaCs ground electronic state is $X^1\Sigma$, where X is a conventional notation to label the state, superscript 1 indicates that the total electron spin state is a singlet* (i.e. the quantum number for operator $\mathbf{S} = \mathbf{S}_{\mathrm{Na}} + \mathbf{S}_{\mathrm{Cs}}$ is 0, and $\mathbf{S}_{\mathrm{Na}}, \mathbf{S}_{\mathrm{Cs}}$ are electronic spin operators). Σ indicates that the projection of the orbital angular momentum on the internuclear axis is zero. This has to be the case, because this molecular state arises from a 3S Na atom and a 6S Cs atom, both of which have no orbital angular momentum.

With the electron intrinsic spin and orbital angular momentum zero, the only angular momenta in the problem are the nuclear spins for sodium ($I_{\mathrm{Na}} = I_1 = 3/2$), and cesium ($I_{\mathrm{Cs}} = I_2 = 7/2$) and molecular rotation N. The full Hamiltonian governing the molecular structure of the electronic

*The total spin is a good quantum number for deeply bound states, since the splitting between singlet and triplet ($S = 1$) is given by the Coulomb interaction, since the symmetry of the spin wavefunction translates directly to the symmetry of the spatial wavefunction of the two electrons

and vibrational ground state in the presence of an external magnetic (**B**) and electric field (**E**):

$$H = B_v \mathbf{N}^2 + \sum_{i=1}^{2} eqQ_i \frac{3(\mathbf{I}_i \cdot \mathbf{N})^2 + \frac{3}{2}(\mathbf{I}_i \cdot \mathbf{N}) - \mathbf{I}_i^2 \mathbf{N}^2}{2I_i(2I_i-1)(2N-1)(2N+3)} + \sum_{i=1}^{2} c_i \mathbf{N} \cdot \mathbf{I}_i$$
$$+ c_4 \mathbf{I}_1 \cdot \mathbf{I}_2 - \boldsymbol{\mu} \cdot \mathbf{E} + \frac{1}{2}\mathbf{E} \cdot \boldsymbol{\alpha} \cdot \mathbf{E} - g_r \mu_N \mathbf{N} \cdot \mathbf{B} - \sum_{i=1}^{2} g_i \mu_N (1-\sigma_i) \mathbf{I}_i \cdot \mathbf{B} \tag{6.21}$$

where the first term is the rotational part of the Hamiltonian parameterized with the rotational constant B_v; the second term is the interaction between the nuclear electric quadrupole [3,76] and the electric field gradient at the nucleus due to the electrons, which is parameterized by constants eqQ_1, eqQ_2; the third term is the spin rotation coupling parameterized by constants c_1, c_2; the fourth term is spin-spin coupling parameterized by constant c_4; the 5th term is a DC Stark effect, which includes the dipole moment, μ; the 6th term is mainly used for calculating the light shift due to the trap, and depends on the molecular polarizability tensor [187] α; the 7th term is a nuclear rotation-magnetic field coupling parameterized by g factor g_r and nuclear magneton μ_N; the 8th term is a nuclear spin-magnetic field coupling parameterized by g factor g_i and a shielding factor σ_i. The constants for NaCs are listed in table 6.5.1 [2]

6.5.2 Analyzing the fidelities and robustness of the gate

For the molecule, the states $|0\rangle = |m_{I_{\mathrm{Na}}}, m_{I_{\mathrm{Cs}}}, N, m_N\rangle = |3/2, 5/2, 0, 0\rangle$ and $|1\rangle = |3/2, 5/2, 1, 1\rangle$ are chosen to be the qubit states. To maximize dipolar interaction, we choose the resonant pair $|72P_{3/2,3/2}\rangle$ and $|71D_{5/2,5/2}\rangle$ as our Rydberg states in a 859.3 G magnetic field. At 1 μm separation, this state choice results in interaction strengths $V_{\mathrm{mr}} = 2\pi \times 4.64$ MHz, compared to the molecule-molecule interaction strength of $V_{\mathrm{mm}} = 2\pi \times 142$ Hz.

A gate time of 263ns is achieved, with a fidelity of 0.9997, when accounting for the finite life-

Parameter	Value
B_v(GHz)	1.7396
eqQ_1(MHz)	−0.097
eqQ_2(MHz)	0.150
c_1(Hz)	14.2
c_2(Hz)	854.5
c_4(Hz)	3941.8
g_r	0
g_1	1.478
g_2	0.738
σ_1(ppm)	639.2
σ_2(ppm)	6278.7
μ_N(Hz/G)	762.2593285

Table 6.2: The molecular constants of NaCs. The variable names are defined by the Hamiltonian in equation 6.21

times of 221 μs and 118 μs for the Rydberg states. This is four orders of magnitude faster than the molecule-molecule gate time of 3.5 ms without the enhancement of the coupling via the Rydberg atom.

Hyperfine state leakage

Leakage to the many hyperfine states in the $N = 0$ and $N = 1$ rotational manifolds needs to be considered. The closest rotational excited states are in the same hyperfine state, but with different m_N, and are separated by only a few kHz. Exchange into these states is suppressed because the dipolar interaction preserves the total magnetic quantum number[86]. Excitation into a different m_N of the final molecular state would require an exchange to a different Rydberg state, which is highly off-resonant at high magnetic field.

Another leakage channel is other hyperfine states in the ground and excited rotational state manifolds, which at high field are separated by 100s of kHz. Transitions to these states are allowed, since the internal molecular Hamiltonian contains coupling between the nuclear spin and rotation

Transition	Detuning (kHz)	Relative coupling strength
$\|0\rangle \rightarrow \|1\rangle$	0	1
$\|0\rangle \rightarrow \|3/2, 7/2, 1, 0\rangle$	-475	0.022
$\|0\rangle \rightarrow \|1/2, 7/2, 1, 1\rangle$	464	0.00033
$\|1\rangle \rightarrow \|1/2, 7/2, 0, 0\rangle$	479	0.000055

Table 6.3: Possible states that may be accessed from the $|0\rangle = |m_{I_{\mathrm{Na}}}, m_{I_{\mathrm{Cs}}}, N, m_N\rangle = |3/2, 5/2, 0, 0\rangle$ and $|1\rangle = |3/2, 5/2, 1, 1\rangle$ computational basis states with a σ^+ polarization from $N = 0$ to $N = 1$ at 859.3 G. The energies of these transitions are also given, where a positive detuning is a transition which has larger energy separation. The relative strength of these transitions are also listed.

through the electric quadrupole moment [2,36]. However, at high magnetic fields, these transitions are suppressed, since the Zeeman term in the internal molecular Hamiltonian begins to dominate the aforementioned mixing terms. The strongest polarization-allowed couplings to the states $|0\rangle$ and $|1\rangle$ are enumerated in Table 6.3 along with their detuning from the primary $|0\rangle \leftrightarrow |1\rangle$ transition.

To account for this possible leakage, we perform a unitary simulation with an enlarged Hilbert space including the extra states. For instance, the Hilbert space of the $n_{\mathrm{exc}=1}$ manifold is given by $\{|0R0\rangle, |1r0\rangle, |0r1\rangle, |2r0\rangle, |0r2\rangle, |1g0\rangle, |0g1\rangle, |2g0\rangle, |0g2\rangle\}$. Then, the dynamics follow a Hamiltonian that includes coupling to the extra state and also includes the detuning of the extra state. To calculate the fidelity, the unitary U_i in equation 6.15 is calculated for the computational basis states $\{|0g0\rangle, |0g1\rangle, |1g0\rangle, |1g1\rangle\}$. The effect of leakage into the unwanted $|3/2, 7/2, 1, 0\rangle$ state caps the fidelity to 0.9996 at the current gate time.

Although coupling to unwanted states limits our fidelity, this coupling can also be used for a hyperfine encoding of quantum information for enlarged coherence times [90,172], similar to the previously proposed iSWAP gate scheme in molecules [163]. In particular, the hyperfine qubit states $|0_{\mathrm{h}}\rangle = |0\rangle = |3/2, 5/2, 0, 0\rangle$ and $|1_{\mathrm{h}}\rangle = |1/2, 7/2, 0, 0\rangle$ can be used, and a π pulse from $|1_{\mathrm{h}}\rangle$ to $|1\rangle$ starts the driven exchange gate. The gate then proceeds in the $\{|0_{\mathrm{h}}\rangle, |1\rangle\}$ basis as described in section 6.4, and finally the population from $|1\rangle$ is returned to the $|1_{\mathrm{h}}\rangle$ state with another π pulse.

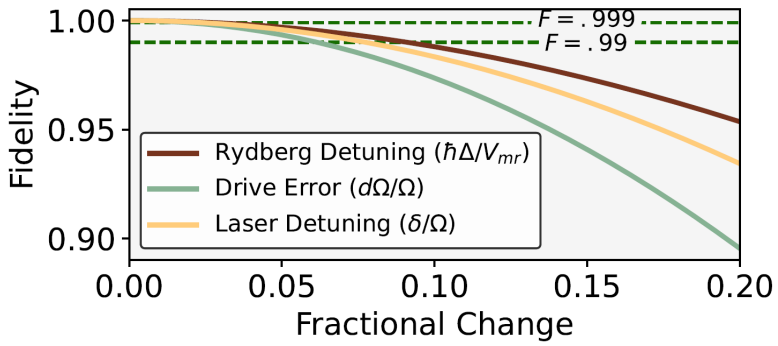

Figure 6.5: Fidelity loss due to fractional errors in detuning and drive Rabi frequency for $k = 1$. In this figure, $d\Omega$ refers to the error in Rabi frequency of the driving laser.

We now analyze the sensitivity of this gate to various parameters. Since Rydberg atoms are extremely sensitive to external fields, especially electric and magnetic fields. Thee excitation laser can also exhibit intensity and frequency error. Each source results in different errors in the Hamiltonian parameters: field amplitude changes Δ and ∂, laser intensity changes Ω, and laser frequency changes ∂.

To understand the worst-case effects of these errors, we simulate our gate evolution with a constant error over the entire gate time. These results are presented in figure 6.5. The noise arising from detuning is dominated by phase error, while intensity will change the population still in the Rydberg state. At 3 mG magnetic field fluctuation, Δ changes by $2\pi \times 5$ kHz and ∂ changes by $2\pi \times 4$ kHz, which gives a gate fidelity of 0.99998. To stay above 0.999, a fluctuation of up to 20 mG can be tolerated. For electric field fluctuations around zero field, this tolerance is 2mV/cm.

One note to consider is that this system is most sensitive to excitation drive Rabi frequency, and greater than 0.9999 fidelity requires greater than 1.94% stability. However, due to the dual-species nature of the array, it is possible to measure the Rydberg atoms without measuring the correspond-

ing qubits. This free measurement allows us to detect error-created Rydberg population and project into the correct ground state otherwise. At 10% drive Rabi frequency error, this error detection allows us to project from a 94.3% fidelity Hilbert space to a 99.9% fidelity subspace.

Additional Sources of Error

Since Rydberg atoms are typically anti-trapped by their tweezers, the trapping light is turned off during Rydberg excitation. During this period, the atomic motional wavefunction $\Psi_a(\mathbf{r}, t)$ can evolve and thus lead to a time-varying interaction strength given by

$$V_{\mathrm{mr}}(t) = \frac{d_m d_r}{4\pi\varepsilon_0} \int d^3\mathbf{r} |\Psi_a(\mathbf{r}, t)|^2 \frac{1}{|(\mathbf{r} - \mathbf{r}_m)|^3}, \tag{6.22}$$

where $\mathbf{r}_m$ is a fixed position of a motional ground-state cooled and trapped molecule. The atomic wavefunction is assumed to start in the ground state of a harmonic oscillator with trapping frequency $\omega = 2\pi \times 80$ kHz, and then evolved under a free-particle Hamiltonian. We recalculate 6.22 at each different time step and the time-dependent problem is solved with a Lindblad master equation solver from the Quantum Toolbox in Python [117]. The resulting gate fidelity is 0.99997.

Next, we consider van der Waals interactions in addition to resonant interactions. The degeneracy of the $|0R\rangle$ and $|1r\rangle$ states leads to a strong resonant-exchange. In principle, off-resonant exchange processes exist for these states as well as for $|0r\rangle$ and $|1R\rangle$. This leads to a $1/r^6$ van der Waals interaction, which can affect the gate dynamics, especially when atom motion is considered.

The contribution from nearby pair states is given by $V_{mr}^2/4(\Delta E)$, where V_{mr} is the interaction strength and ΔE is the energy gained or lost in the exchange process. We consider interacting pair states with $\Delta E \leq h \times 100$ GHz [58,21]. In addition, we also include off-resonant coupling to the second rotational state of the molecule.

Adding all these contributions at $a = 1\,\mu m$, the van der Waals interaction strength for each pair

state is $V_{vdW,0r} = h \times 2.3\,\text{kHz}$, $V_{vdW,1r} = h \times 1.25\,\text{kHz}$, $V_{vdW,0R} = h \times 863\,\text{Hz}$, $V_{vdW,1R} = h \times 2.84\,\text{kHz}$. These interactions can be calibrated away at a particular interparticle spacing by carefully tuning the Rydberg resonance. If there are fluctuations in this interaction due to atom motion, errors will be introduced into the gate. Since these interaction strengths are much smaller than the MHz scale on-resonant interactions, they can be neglected.

6.6 Nondestructive Molecule Detection

Next, we turn to the challenge of state detection and measurement of molecular qubits.

In order to use molecules as part of a scalable quantum computing platform, it is also necessary to implement reliable state preparation and measurement schemes for the molecules themselves. Furthermore, detecting the state of the molecule nondestructively and projecting it into that state is important for use in quantum error correction [222] and measurement-based quantum computing [32]. Nondestructive state-sensitive detection of molecules, however, remains a major challenge, since most molecules, including bialkalis, do not have closed cycling transitions, so direct imaging of them is difficult. To detect bialkali molecules, they are dissociated into atoms, which can then be directly imaged [62,162,132,219,156,171,96,129,229,137]. This technique is sensitive to the fidelity of the dissociation process and is also destructive, so it cannot be used for rearrangement in optical tweezer systems [127,75,14,15], which is important for realizing defect-free arrays of molecules. We note that rearrangement has been realized for CaF, which has a closed cycling transition [104,13]. Recently, rearrangement has been performed on bialkali molecules [177,189] by detecting the presence of an unformed molecule via its leftover atom, which can optically cycle photons. Nevertheless, in these works, the atom can only be detected if the magnetoassociation step fails, but is not sensitive to infidelity in the ground state transfer from the weakly-bound Feshbach state.

A general route to overcoming such detection challenges is to perform indirect detection through

state-sensitive coupling of a molecule to another quantum system such as an atom [236,55,131,246,113] or an optical cavity [250] which can then be optically detected. Building upon these ideas and the framework built in this chapter, we discuss a detection method of molecular states via a Rydberg atom.

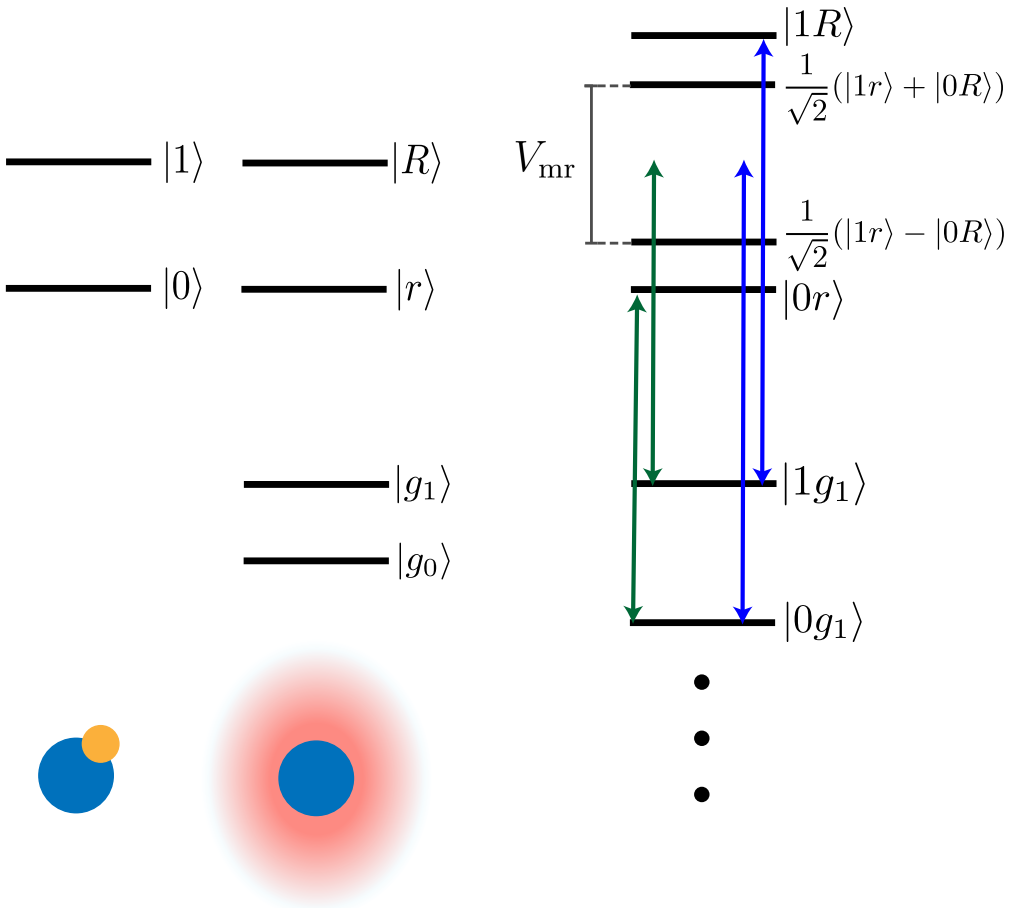

Figure 6.6: The relevant energy levels for a blockade based detection of the molecule. The energy levels for the molecule and Rydberg atom individually are shown on the left, with the two body states shown on the right. The dipolar interaction mixes the $|0R\rangle$ and $|1r\rangle$ states and results in an energy difference. The green (blue) arrows show the result of a laser attempting to drive the $|g_1\rangle \rightarrow |r\rangle$ ($|R\rangle$) transition, where the drive is off-resonant if the molecule is in the $|1\rangle$ ($|0\rangle$) state.

A hybrid system of molecules and atoms that can interact suggests the potential to perform non-

destructive quantum state detection of the molecules via the atoms. Bringing a Rydberg atom transition into resonance with a molecular rotational transition as discussed in this chapter will create an energy shift due to the molecule-atom interaction. Consider a pair of Rydberg states $|r\rangle$ and $|R\rangle$ that are resonant with the $N = 0$ to $N = 1$ rotational transition of a molecule, as shown in figure 6.6. In the two-body basis, the states $|0R\rangle$ and $|1r\rangle$ are coupled via the dipolar interaction and acquire an energy splitting of V_{mr}. Thus, in the presence of a molecule in state $|0\rangle$ ($|1\rangle$), the $|g\rangle \rightarrow |R\rangle$ ($|r\rangle$) will be blockaded[112], where $|g\rangle$ is a ground state of the atom, as long as the drive power is much weaker than the interaction strength, $\hbar\Omega_{\mathrm{drive}} \ll V_{\mathrm{mr}}$.

Using this energy shift, the state of a molecular qubit in $\alpha|0\rangle + \beta|1\rangle$ can be mapped onto the hyperfine states of the atom. Consider two hyperfine ground states of the atom $|g_0\rangle$, and $|g_1\rangle$ that can be selectively read out, where only state $|g_1\rangle$ is coupled to the Rydberg states. The molecule is detected by preparing the atom in state $\frac{1}{\sqrt{2}}(|g_0\rangle + |g_1\rangle)$, and then driving a 2π pulse from $|g_1\rangle$ to $|R\rangle$, resulting in the state $\frac{1}{\sqrt{2}}(\alpha|0\rangle \otimes (|g_0\rangle - |g_1\rangle) + \beta|1\rangle \otimes (|g_0\rangle + |g_1\rangle))$. A Hadamard gate can then be performed on the atom in the $\{|g_0\rangle , |g_1\rangle\}$ basis to obtain the state $\alpha|0g_1\rangle + \beta|1g_0\rangle$. A state selective atom measurement will then project the molecule into state $|0\rangle$ or $|1\rangle$. Repeated measurements of this form allow for state tomography to determine the populations $|\alpha|^2$ and $|\beta|^2$.

First Measurement	Second Measurement	Interpretation
$\|g_0\rangle$	$\|g_0\rangle$	No molecule
$\|g_0\rangle$	$\|g_1\rangle$	Molecule in $\|1\rangle$
$\|g_1\rangle$	-	Molecule in $\|0\rangle$

Table 6.4: Interpretation of measurement results of the atom in the blockade detection scheme. For an initial measurement result of $|g_1\rangle$ no further information can be gained from a second measurement of the same atom-molecule system.

In the case where there is no molecule, this procedure results in an atom in state $|g_0\rangle$, making it indistinguishable from having a molecule in state $|1\rangle$. To distinguish these cases, the same detection procedure can be performed again, but instead using a 2π pulse from $|g_1\rangle$ to $|r\rangle$. If the molecule

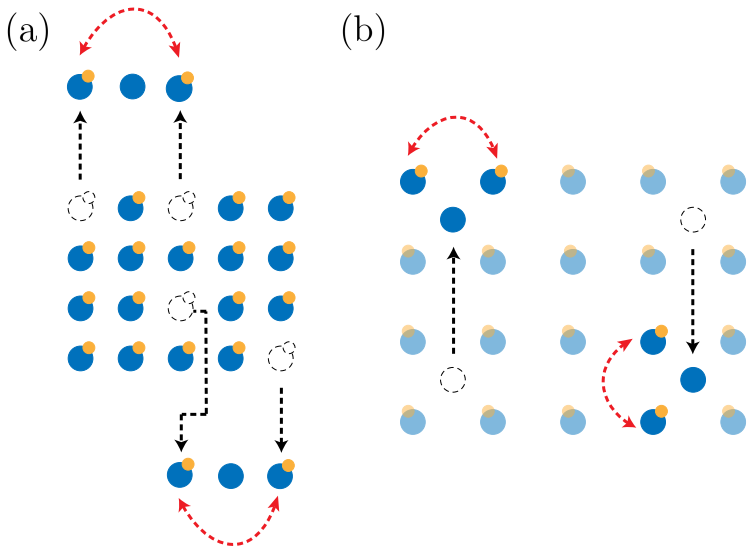

Figure 6.7: Two possible extensions of the molecule-Rydberg gate to larger arrays. (a) Using optical tweezers, molecules can be transported to positions next to atoms. At these locations, the gate scheme can proceed without involving other molecules. If atoms are placed far enough away, multiple gates can proceed in parallel. (b) Movable atoms can be placed sparsely throughout the array to mediate interactions between molecules of interest. The molecules that should not interact are placed in other rotational states, that are off resonant with the Rydberg atom transition.

were present, this would result in the atom state $|g_1\rangle$, in contrast to $|g_0\rangle$ if there were no molecule. This second measurement can be used for post-selection on the data for a background-free measurement of $|\beta|^2$. The logic of this procedure is summarized in table 6.4.

6.7 Extension to larger arrays

Extending the schemes in this chapter to larger arrays is non-trivial due to the Rydberg atom's interaction with other molecules or atoms in the array. The resonant Rydberg-Rydberg interaction, which is enhanced by a factor of d_r/d_m, is much stronger than the molecule-Rydberg interaction.

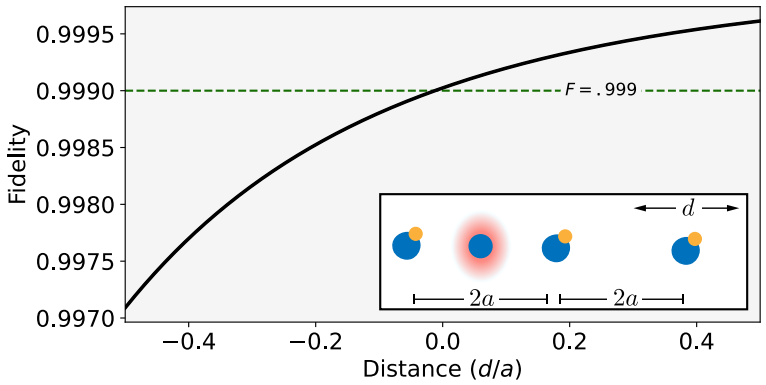

Figure 6.8: In extending to larger arrays, neighboring molecules will affect the gate due to interaction with the distant molecule. In a uniform array, fidelities of just above 0.999 can be achieved

.

This interaction can only be suppressed by distance, which limits the number of Rydberg atoms that may be used at the same time to entangle separate pairs of molecules. One possible method of extending to larger arrays is to utilize the mobility of an optical tweezer platform, as has been recently demonstrated for neutral atom systems[28], selectively moving molecules to interact with distant Rydberg atoms, as shown in figure 6.7a.

Another limitation is the interaction between a Rydberg atom and the next-nearest neighboring molecule. Figure 6.8 shows the effect of this distant molecule on the gate fidelity as a function of distance. A more robust method to ensure that only targeted molecules can interact with the Rydberg atom is to take advantage of the many internal states of molecules, particularly other rotational states, shown schematically in figure 6.7b. For example, if the Rydberg atom is made resonant with the $N = 1$ to $N = 2$ rotational transition, molecules can be stored in the $N = 0$ and $N = 3$ states to avoid interaction with the Rydberg. It is critical for the non-interacting states to be off-resonant with the Rydberg atom, which is possible due to the unequal and large spacing between rotational levels in molecules.

The exchange rate of the gate is at the MHz level, so different hyperfine states in the same rotational manifold of a $^1\Sigma$ molecule may not be used to prevent interaction, as they are only off-resonant by only tens of kHz. However, polarization offers a constraint and allows hyperfine shelving starting from the $N = 1$ manifold. If the Rydberg atom transition from $|r\rangle \rightarrow |R\rangle$ is σ^+ and is resonant with the $N = 0$ to $N = 1$ transition then the $|N = 1, m_N = 0\rangle$ and $|N = 1, m_N = -1\rangle$ molecule states will not interact with the Rydberg atom and can store the quantum information of non-interacting molecules.

6.8 Summary and Outlook

By introducing Rydberg atoms into a molecular system, it is possible to realize both high fidelity sub-microsecond entangling gates and nondestructive molecule detection. The large transition dipole moments in Rydberg atoms are used to facilitate dipolar exchange between two polar molecules. The gate only requires driving the Rydberg atom with a precise strength for a specific time and is general for all polar molecules with dipole-allowed GHz scale transitions, including diatomic and polyatomic species[246,221]. We detailed an implementation of the scheme with the bialkali NaCs molecule and cesium atoms, and analyzed its sensitivities to various experimental parameters, while also taking molecular hyperfine structure into account. Nondestructive projective measurement of the molecules can be performed via a blockade scheme, where detection ultimately occurs on the atoms. Using the atom as an ancillary qubit to detect gate errors shows promise and warrants further investigation.

When compared to purely molecular systems, the spontaneous decay and Doppler effects of the untrapped Rydberg atom limit the fidelity of gates in this scheme. These limitations are common to Rydberg-Rydberg systems, but this scheme benefits from having only one particle subject to these loss mechanisms during each entangling gate rather than two. Other benefits of using molecular

qubits include relatively long coherence times of greater than 5 seconds in hyperfine states[90], and of around 100 ms in the interacting rotational states[39]. The molecule-Rydberg gates presented here can also be natively combined with higher fidelity, but slower, molecule-molecule gates[163], depending on the application.

Molecules also offer a large number of internal states to selectively interact molecules in a larger array. These internal states can also be used as qudits[159] or as lattice sites in a synthetic dimension[218]. For the case of a synthetic dimension using rotational states, the Rydberg atom can be tuned to a particular rotational resonance enhancing excitation hopping between particular sites in the synthetic dimension. Using physical displacement, the enhancement of hopping is spatially-tunable and also allows for site-dependent interactions. Introducing neutral atoms into a molecular platform adds to the toolbox of polar molecule systems, enriching their potential for quantum science applications.

7

Conclusion

In this thesis, I have told the journey of how we converted our lab's molecule-making apparatus into a complete dual-species Rydberg atom apparatus. To that end, we have greatly increased the number of sodium and cesium atoms that can be trapped in our system to the hundreds using spatial light modulators. Along the way, we have learned how to effectively use such technologies and their inherent subtleties. Working with a many-body system required capabilities to rearrange atoms to particular locations and create defect-free arrays. Thus, we incorporated real-time feedback into our

computer control systems. We employed an arbitrary waveform generator to drive acousto-optical deflectors to perform the rearrangement task.

While one main thrust was to scale up our tweezer arrays, another thrust centered on gaining Rydberg excitation capabilities on our apparatus. The technical challenge centered around adding 4 more lasers (and delivering them to the experiment) to our already packed experimental setup. We also had to take extra care to characterize and mitigate any sources of laser noise that could affect our Rabi coherence times.

We successfully implemented cesium Rydberg excitations with up to 20 μs Rabi coherence times. Using this capability, we took a dive into a quantum simulation experiment, probing critical physics. Our adiabatic preparation method of the ground state wavefunction at the Ising critical point properly measured a σ-field scaling dimension (in 1D) of $\Delta_\sigma^{\mathrm{1D}} = 0.127(37)$ in agreement with the expectation of $1/8$. However, this result was not simple to obtain, and we needed to account for the effect of decoherence on our critical state preparation. We were pleased to find that decoherence could be neatly described by an exponential length scale. This work thus laid out a general framework for studying criticality in open quantum systems.

After our not-so-brief splash into critical physics, we returned to the task at hand of creating a dual-species Rydberg atom apparatus. We brought sodium Rydberg excitation to fruition, despite the technical challenges posed by our experimental apparatus. During the writing of this thesis, we were able to observe, for the first time, interactions between sodium and cesium Rydberg atoms! This observation is the first step to many exciting experiments in both quantum computing and quantum simulation that are especially enabled with two atomic species.

Lastly, as an ode to the past, we combined our expertise in molecules with our newly acquired Rydberg atom capabilities to craft a proposal where Rydberg atoms can be used to solve some of the outstanding problems of molecule-based quantum computers. Our proposal lays out a scheme to obtain sub-microsecond gates between molecules and also to perform non-destructive measure-

ment on molecules using atoms. This hybrid system is also very natural for systems of assembled molecules, where atoms are a plentiful resource.

For more details on all these points, please refer to their respective chapters, especially the summary and outlook sections at the end of each chapter. For now, I will close with some final, personal thoughts.

7.1 Final Thoughts

While single-species neutral atom platforms[27,150,47,148] and molecule platforms[176,13,104] have made great advances in recent years, I believe that the greater flexibility of a dual-species array will find its use cases. If needed, all single-species techniques can easily be implemented, and yet the platform can also take advantage of molecular assembly techniques to incorporate molecules into the platform. Viewed in another light, a fully functional dual-species Rydberg atom apparatus adds Rydberg capabilities to a molecule apparatus.

In quantum simulation, I believe the second species, and the tunable parameters it adds to the Hamiltonian, can simulate a strictly larger class of systems. The main challenge is to find interesting systems in nature to simulate. Here, I believe in the creativity of our theorist friends, and believe that they will be quite pleased to play around with the Hamiltonians that our system can implement.

However, as experimentalists, it is our job to deliver a highly-capable and easy-to-use apparatus. Although our retrofitted apparatus has been a fantastic platform to learn about Rydberg physics and to investigate criticality, it has become clear to us that it is in need of upgrades. Being designed as a molecule apparatus, it has gone quite far as a dual-species Rydberg apparatus! The most pressing changes center around a vacuum system change, where we can increase the vacuum-limited lifetime of our atoms, add electric field control and allow most of our Rydberg (especially for sodium) light

to transmit through. Of course all our surrounding and supporting laser technologies are here to stay! I would love to automate most laser tasks, such as laser alignment and laser locking, both of which are huge time sinks and occasionally a drag on group morale. Automation requires an initial time investment, but I strongly believe it will be worth it. The future is bright for our dual-species atom array and two is always better than one!

A

Data Processing and Analysis for Extracting Critical Exponents

In chapter 4, we discussed experiments relating to preparing ground states at critical points and measuring their correlations. In this appendix, we describe the data processing techniques we use to ensure that our data is reliable and also how we obtain error bars for quantities that are obtained in quite complex ways. These discussions are general and used for most of the data presented in

chapter 4.

A.1 Data Postselection

Critical correlations are very sensitive to experimental errors, especially missing atoms. In our experiment, we post-select all our data on successful rearrangement. However, there is approximately 3% loss per trap from the fluorescence imaging, and an additional 2% loss per trap from collisions with the background gas during Raman sideband cooling, resulting in a total 5% loss per trap during state initialization before performing our Rydberg experiments. This loss introduces unknown holes into the perfect 1D ring or 2D rectangular array. The unknown holes in the perfect 1D ring actually changes the boundary conditions of our system from periodic to open. These defects are hard to distinguish from Rydberg atoms, which are also detected as loss. However, we note that when Rydberg atoms are created in our sequences, they are more likely to be created at edges or where there are fewer neighboring atoms. Thus, holes due to atom loss are more likely to have neighboring holes that result from an atom being promoted to a Rydberg state. In our data analysis, this creates an atom configuration which violates the so-called Rydberg blockade; namely, there appear to be two or more Rydberg excitations within a blockade radius. To reduce the impact of loss on our data, we postselect on snapshots that do not contain any blockade violations.

To justify the above approach, we confirm numerically that postselection of blockade-violating snapshots does not bias our results. We first calculate the percentage of snapshots in the critical state to contain blockade violations to be 8% (24-atom ring), 10% (40-atom ring), 35% (7×7 array), and 52% (9×9 array). Although the percentage is high in 2D, the effect is smaller compared to 1D where holes change the boundary conditions. We calculate the σ field correlation of both the entire wavefunction and the portion that contains no blockade-violations. Comparing these two indicates only a minor deviation, suggesting that blockade-violating snapshots do not contribute significantly

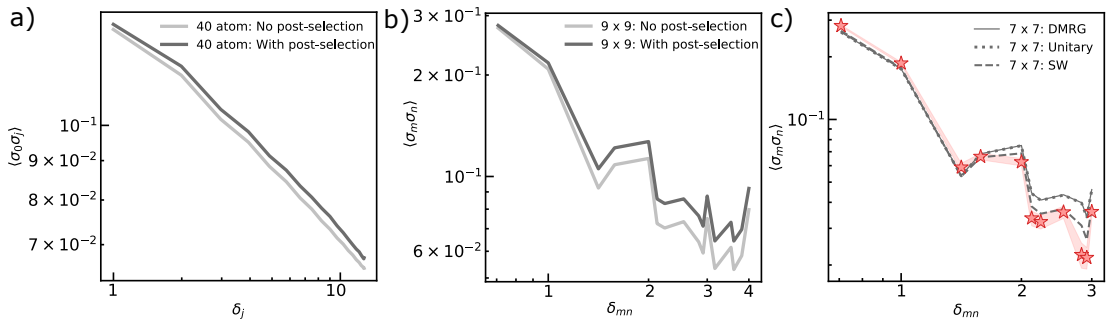

Figure A.1: Data post-selection. Stars denote experimental measurements, with the shaded region representing 1-σ bootstrap error. Gray solid, dotted, and dashed lines indicate ground (DMRG), unitary, and stochastic wave-function simulation results using experimental parameters. (a) and (b) Ground state simulations with and without blockade violation post-selection for 40-atom ring (a) and 9×9 rectangular array (b). (c) Raw measurement of the critical σ-field correlation with loss-inclusive simulations in the 7×7 rectangular array.

to this particular observable (figure A.1 a, b). Furthermore, we can account for atom loss in simulations by averaging over arrays with defects. These simulations agree well our raw data without blockade-violation post-selection, verifying our understanding of the impact of holes on our critical state (figure A.1 c). All data reported in the main text has been post-selected to exclude blockade violations, with the exception of data used for locating the critical point via linear ramps.

A.2 Bootstrap Error Bars

Since the extracted quantities in chapter 4 can be rather complicated (for instance arising from smoothing, interpolation and numerical differentiation), we use bootstrap methods[160] to estimate errorbars. From N snapshots of a particular experiment, we sample N times with replacement. We then proceed to calculate all observables, such as σ field correlators, and perform all required fits. We repeat this procedure for B (typically ≥ 1000) bootstrap samples, and enumerate the calculated

values. The reported value for the quantity is then taken to be the mean of the bootstrapped values with an errorbar given by the standard deviation. If the distribution of the bootstrapped values is asymmetric, we report the median value as our best estimate of the quantity with an errorbar determined by the 15.8th and 84th percentile of the distribution. This procedure results in the asymmetric errorbar in ξ_d/a reported in the main text, extracted from the power-law exponential fits (figure 4.10b and figure 4.13a,b). For all quantities reported in this work, including Δ_σ^{1D}, Δ_σ^{2D} and ξ_d/a, we incorporate both the bootstrap and fitting errorbars.

B

Numerical Simulations for Critical Physics

The results in chapter 4 require many numerical simulations. These simulations roughly fall in 3 categories of increasing computational cost: ground state methods, unitary time evolution methods and stochastic wavefunction methods. Ground state simulations are useful for understanding how an ideal system would behave. Without observing the correct physics in ground state simulations, one does not have any hope of observing the correct physics in an experiment. We use ground state simulations to answer questions such as whether finite-size and boundary effects are prohibitive.

These simulation results are also the key for crafting our LILA ramps, which require the gap at the starting detuning and the critical detuning. Unitary time evolution simulations are most useful for determining the effect of non-adiabaticity on our results. If our achievable ramp times (accounting for decoherence) are not enough to ensure adiabaticity, then we know that the procedure could not work. These are useful simulations in order to answer questions such as what are the largest-size systems we could access before the gap closes too much. It also informs us when we might be able to get away with a non-optimized, say linear, ramp. Lastly, stochastic wavefunction simulations are used to incorporate effects of decoherence. These simulations help us validate our extraction procedure of the critical exponent. The simulations described in this appendix were mostly performed by Vincent Liu, but I include it here for completeness.

We utilize matrix product state (MPS) methods for all 3 categories of numerical simulations, using the finite-size density matrix renormalization group (DMRG) algorithm for ground state studies and the two-site time-dependent variational principle (TDVP) method for time dynamics [100,201,99].

To capture the openness of our quantum system, we perform simulations of its time dynamics incorporating the two most relevant sources of single-body decoherence in our experiment, intermediate-state scattering and Rydberg state decay. This is generically described by the Lindblad master equation,

$$\frac{d\rho}{dt} = -\frac{i}{\hbar}[H,\rho] + \sum_j \left(c_j \rho c_j^\dagger - \frac{1}{2}\left\{ c_j^\dagger c_j \right\} \right), \tag{B.1}$$

where ρ is the density matrix, H is the system Hamiltonian, and the c_j are the jump operators describing the decoherence channels.

We model the Rydberg decay process using the jump operators $c_i^{\text{decay}} = \sqrt{\gamma_{\text{decay}}}\,|g\rangle_{i\,i}\langle r|$ for each atom i, where $1/\gamma_{\text{decay}} = 71.44\,\mu s$ is the lifetime of the Rydberg state. To model intermediate-state scattering, we first quantify the two-photon excitation process as a driving field $\Omega_{\text{blue}} =$

$2\pi \times 80.04\,\text{MHz}$ from the ground state $|g\rangle$ to an intermediate state $|e\rangle$ with a detuning $\delta = 2\pi \times 1.058\,\text{GHz}$, and a second driving field $\Omega_{\text{IR}} = 2\pi \times 42.3\,\text{MHz}$ from $|e\rangle$ to the Rydberg state $|r\rangle$. The intermediate state decays at a rate $\gamma_e = 2\pi \times 1.23\,\text{MHz}$, which we then model with the jump operators $\sqrt{\gamma_e}\,|g\rangle_{i\,i}\langle e|$ for each atom i. Next, we perform adiabatic elimination on the intermediate state $|e\rangle$, leading to an effective Lindbladian with a two-photon Rabi frequency $\Omega = \frac{\Omega_{\text{blue}}\Omega_{\text{IR}}}{2\delta} = 2\pi \times 1.6\,\text{MHz}$ and effective jump operators $c_i^{\text{scatt}} = \sqrt{\frac{\gamma_e}{4\delta^2}}\left(\Omega_{\text{blue}}\,|g\rangle_{i\,i}\langle g| + \Omega_{\text{IR}}\,|g\rangle_{i\,i}\langle r|\right)$ for each atom i. The intermediate-state scattering process can be summarized using an effective rate $\gamma_{\text{scatt}} = \frac{\gamma_e}{4\delta^2}\left(\Omega_{\text{blue}}^2 + \Omega_{\text{IR}}^2\right) = 1/70.69\,\mu s$, which is of a similar timescale to the Rydberg lifetime. We note that the presence of these two decoherence channels has a significant effect on the dynamics of the system, which occurs within a time period of $7\,\mu s$.

We implement open-system time evolution using the stochastic wavefunction framework, where we stochastically generate quantum trajectories of the system to produce an ensemble of pure states that can be averaged over to recover the behavior of the density matrix obtained using the Lindblad master equation. Under decoherence, quantum state evolution is modified from the Schrödinger equation such that the system evolves under a non-Hermitian effective Hamiltonian $H_{\text{eff}} = H - \frac{i\hbar}{2}\sum_j c_j^\dagger c_j$ and, for every jump operator c_j, the wavefunction $|\psi\rangle$ stochastically "jumps" to $\frac{c_j|\psi\rangle}{\langle\psi|c_j^\dagger c_j|\psi\rangle}$ with probability density $\langle\psi|\,c_j^\dagger c_j\,|\psi\rangle$ in time. In our numerics, we average over $O(100)$ such trajectories per simulation.

References

[1] Aeppli, A., Kim, K., Warfield, W., Safronova, M. S., & Ye, J. (2024). Clock with 8×10^{-19} systematic uncertainty. *Phys. Rev. Lett.*, 133(2), 023401.

[2] Aldegunde, J. & Hutson, J. M. (2017). Hyperfine structure of alkali-metal diatomic molecules. *Phys. Rev. A*, 96, 042506.

[3] Aldegunde, J., Rivington, B. A., Żuchowski, P. S., & Hutson, J. M. (2008). Hyperfine energy levels of alkali-metal dimers: Ground-state polar molecules in electric and magnetic fields. *Phys. Rev. A*, 78(3), 033434.

[4] Aliyu, M. M., Zhao, L., Quek, X. Q., Yellapragada, K. C., & Loh, H. (2021). D1 magic wavelength tweezers for scaling atom arrays. *Physical Review Research*, 3(4), 043059.

[5] Amin, M. H. S. (2009). Consistency of the adiabatic theorem. *Phys. Rev. Lett.*, 102, 220401.

[6] Anand, S., Bradley, C. E., White, R., Ramesh, V., Singh, K., & Bernien, H. (2024). A dual-species Rydberg array. *Nature Physics*, (pp. 1–7).

[7] Anderegg, L., Cheuk, L. W., Bao, Y., Burchesky, S., Ketterle, W., Ni, K.-K., & Doyle, J. M. (2019). An optical tweezer array of ultracold molecules. *Science*, 365, 1156–1158.

[8] Anderson, M. H., Ensher, J. R., Matthews, M. R., Wieman, C. E., & Cornell, E. A. (1995). Observation of Bose-Einstein condensation in a dilute atomic vapor. *Science*, 269(5221), 198–201.

[9] Anquez, M., Robbins, B. A., Bharath, H. M., Boguslawski, M., Hoang, T. M., & Chapman, M. S. (2016). Quantum Kibble-Zurek mechanism in a spin-1 Bose-Einstein condensate. *Phys. Rev. Lett.*, 116, 155301.

[10] Asbóth, J. K., Oroszlány, L., Pályi, A., Asbóth, J. K., Oroszlány, L., & Pályi, A. (2016). The Su-Schrieffer-Heeger (SSH) model. *A Short Course on Topological Insulators: Band Structure and Edge States in One and Two Dimensions*, (pp. 1–22).

[11] Aymar, M. & Dulieu, O. (2005). Calculation of accurate permanent dipole moments of the lowest $^{1,3}\sigma^+$ states of heteronuclear alkali dimers using extended basis sets. *The Journal of Chemical Physics*, 122(20).

[12] Bakr, W. S., Peng, A., Tai, M. E., Ma, R., Simon, J., Gillen, J. I., Foelling, S., Pollet, L., & Greiner, M. (2010). Probing the superfluid-to-Mott insulator transition at the single-atom level. *Science*, 329(5991), 547–550.

[13] Bao, Y., Yu, S. S., Anderegg, L., Chae, E., Ketterle, W., Ni, K.-K., & Doyle, J. M. (2023). Dipolar spin-exchange and entanglement between molecules in an optical tweezer array. *Science*, 382(6675), 1138–1143.

[14] Barredo, D., De Léséleuc, S., Lienhard, V., Lahaye, T., & Browaeys, A. (2016). An atom-by-atom assembler of defect-free arbitrary two-dimensional atomic arrays. *Science*, 354(6315), 1021–1023.

[15] Barredo, D., Lienhard, V., de Léséleuc, S., Lahaye, T., & Browaeys, A. (2018). Synthetic three-dimensional atomic structures assembled atom by atom. *Nature*, 561(7721), 79–82.

[16] Barry, J., McCarron, D., Norrgard, E., Steinecker, M., & DeMille, D. (2014). Magneto-optical trapping of a diatomic molecule. *Nature*, 512(7514), 286–289.

[17] Bartenstein, M., Altmeyer, A., Riedl, S., Jochim, S., Chin, C., Denschlag, J. H., & Grimm, R. (2004). Crossover from a molecular Bose-Einstein condensate to a degenerate Fermi gas. *Phys. Rev. Lett.*, 92(12), 120401.

[18] Berdanier, W., Kolodrubetz, M., Vasseur, R., & Moore, J. E. (2017). Floquet dynamics of boundary-driven systems at criticality. *Phys. Rev. Lett.*, 118, 260602.

[19] Bernien, H., Schwartz, S., Keesling, A., Levine, H., Omran, A., Pichler, H., Choi, S., Zibrov, A. S., Endres, M., Greiner, M., Vuletić, V., & Lukin, M. D. (2017). Probing many-body dynamics on a 51-atom quantum simulator. *Nature*, 551, 579.

[20] Beterov, I., Ryabtsev, I., Tretyakov, D., & Entin, V. (2009). Quasiclassical calculations of blackbody-radiation-induced depopulation rates and effective lifetimes of Rydberg nS, nP, and nD alkali-metal atoms with $n \leq 80$. *Phys. Rev. A*, 79(5), 052504.

[21] Beterov, I. I. & Saffman, M. (2015). Rydberg blockade, Förster resonances, and quantum state measurements with different atomic species. *Phys. Rev. A*, 92(4), 042710.

[22] Białończyk, M. & Damski, B. (2020). Locating quantum critical points with Kibble-Zurek quenches. *Phys. Rev. B*, 102, 134302.

[23] Bigagli, N., Yuan, W., Zhang, S., Bulatovic, B., Karman, T., Stevenson, I., & Will, S. (2024). Observation of Bose-Einstein condensation of dipolar molecules. *Nature*, (pp. 1–5).

[24] Black, E. D. (2001). An introduction to Pound-Drever-Hall laser frequency stabilization. *American Journal of Physics*, 69(1), 79–87.

[25] Bloch, I., Dalibard, J., & Nascimbene, S. (2012). Quantum simulations with ultracold quantum gases. *Nature Physics*, 8(4), 267–276.

[26] Blodgett, K. N., Peana, D., Phatak, S. S., Terry, L. M., Montes, M. P., & Hood, J. D. (2023). Imaging a ^{6}Li atom in an optical tweezer 2000 times with Λ-enhanced gray molasses. *Phys. Rev. Lett.*, 131(8), 083001.

[27] Bluvstein, D., Evered, S. J., Geim, A. A., Li, S. H., Zhou, H., Manovitz, T., Ebadi, S., Cain, M., Kalinowski, M., Hangleiter, D., et al. (2024). Logical quantum processor based on reconfigurable atom arrays. *Nature*, 626(7997), 58–65.

[28] Bluvstein, D., Levine, H., Semeghini, G., Wang, T. T., Ebadi, S., Kalinowski, M., Keesling, A., Maskara, N., Pichler, H., Greiner, M., et al. (2022). A quantum processor based on coherent transport of entangled atom arrays. *Nature*, 604(7906), 451–456.

[29] Born, M. & Wolf, E. (2013). *Principles of optics: electromagnetic theory of propagation, interference and diffraction of light*. Elsevier.

[30] Braun, P. (1983). On the quadratic zeeman effect in highly excited states of hydrogen and alkali-metal atoms. *Journal of Physics B: Atomic and Molecular Physics (1968-1987)*, 16(23), 4323.

[31] Bray, A. J. & Moore, M. A. (1977). Critical behaviour of semi-infinite systems. *Journal of Physics A: Mathematical and General*, 10(11), 1927.

[32] Briegel, H. J., Browne, D. E., Dür, W., Raussendorf, R., & Van den Nest, M. (2009). Measurement-based quantum computation. *Nature Physics*, 5(1), 19–26.

[33] Brion, E., Pedersen, L. H., & Mølmer, K. (2007). Adiabatic elimination in a lambda system. *Journal of Physics A: Mathematical and Theoretical*, 40(5), 1033.

[34] Browaeys, A., Barredo, D., & Lahaye, T. (2016). Experimental investigations of dipole-dipole interactions between a few Rydberg atoms. *Journal of Physics B: Atomic, Molecular and Optical Physics*, 49(15), 152001.

[35] Browaeys, A. & Lahaye, T. (2020). Many-body physics with individually controlled Rydberg atoms. *Nature Physics*, 16(2), 132–142.

[36] Brown, J. M. & Carrington, A. (2003). *Rotational spectroscopy of diatomic molecules*. Cambridge Univ.: Cambridge, UK.

[37] Brown, M., Thiele, T., Kiehl, C., Hsu, T.-W., & Regal, C. (2019). Gray-molasses optical-tweezer loading: controlling collisions for scaling atom-array assembly. *Phys. Rev. X*, 9(1), 011057.

[38] Bruzewicz, C. D., Chiaverini, J., McConnell, R., & Sage, J. M. (2019). Trapped-ion quantum computing: Progress and challenges. *Applied Physics Reviews*, 6(2), 021314.

[39] Burchesky, S., Anderegg, L., Bao, Y., Yu, S. S., Chae, E., Ketterle, W., Ni, K.-K., & Doyle, J. M. (2021). Rotational coherence times of polar molecules in optical tweezers. *Phys. Rev. Lett.*, 127(12), 123202.

[40] Burkhardt, T. W. & Diehl, H. W. (1994). Ordinary, extraordinary, and normal surface transitions: Extraordinary-normal equivalence and simple explanation of $|T - T_c|^{2-\alpha}$ singularities. *Phys. Rev. B*, 50, 3894–3898.

[41] Busch, T., Englert, B.-G., Rzażewski, K., & Wilkens, M. (1998). Two cold atoms in a harmonic trap. *Foundations of Physics*, 28(4), 549–559.

[42] Cairncross, W. B., Zhang, J. T., Picard, L. R., Yu, Y., Wang, K., & Ni, K.-K. (2021). Assembly of a rovibrational ground state molecule in an optical tweezer. *Phys. Rev. Lett.*, 126(12), 123402.

[43] Calabrese, P. & Cardy, J. (2016). Quantum quenches in 1+1 dimensional conformal field theories. *Journal of Statistical Mechanics: Theory and Experiment*, 2016(6), 064003.

[44] Caldwell, L. & Tarbutt, M. R. (2021). General approach to state-dependent optical-tweezer traps for polar molecules. *Physical Review Research*, 3(1), 013291.

[45] Caldwell, L., Williams, H. J., Fitch, N. J., Aldegunde, J., Hutson, J. M., Sauer, B. E., & Tarbutt, M. R. (2020). Long rotational coherence times of molecules in a magnetic trap. *Phys. Rev. Lett.*, 124, 063001.

[46] Cantat-Moltrecht, T., Cortiñas, R., Ravon, B., Méhaignerie, P., Haroche, S., Raimond, J.-M., Favier, M., Brune, M., & Sayrin, C. (2020). Long-lived circular Rydberg states of laser-cooled rubidium atoms in a cryostat. *Physical Review Research*, 2(2), 022032.

[47] Cao, A., Eckner, W. J., Lukin Yelin, T., Young, A. W., Jandura, S., Yan, L., Kim, K., Pupillo, G., Ye, J., Darkwah Oppong, N., et al. (2024). Multi-qubit gates and Schrödinger cat states in an optical clock. *Nature*, 634(8033), 315–320.

[48] Cardy, J. L. (1984). Conformal invariance and universality in finite-size scaling. *Journal of Physics A: Mathematical and General*, 17(7), L385.

[49] Cesa, F. & Pichler, H. (2023). Universal quantum computation in globally driven Rydberg atom arrays. *Phys. Rev. Lett.*, 131(17), 170601.

[50] Chao, Y.-X., Hua, Z.-X., Liang, X.-H., Yue, Z.-P., Jia, C., You, L., & Tey, M. K. (2024). Robust high-frequency laser phase noise suppression by adaptive Pound-Drever-Hall feedforward. *arXiv preprint arXiv:2407.19642*.

[51] Chen, C., Bornet, G., Bintz, M., Emperauger, G., Leclerc, L., Liu, V. S., Scholl, P., Barredo, D., Hauschild, J., Chatterjee, S., et al. (2023). Continuous symmetry breaking in a two-dimensional Rydberg array. *Nature*, 616(7958), 691–695.

[52] Chin, C., Grimm, R., Julienne, P., & Tiesinga, E. (2010). Feshbach resonances in ultracold gases. *Reviews of Modern Physics*, 82(2), 1225–1286.

[53] Choi, J., Zhou, H., Knowles, H. S., Landig, R., Choi, S., & Lukin, M. D. (2020). Robust dynamic Hamiltonian engineering of many-body spin systems. *Phys. Rev. X*, 10(3), 031002.

[54] Chomaz, L., Ferrier-Barbut, I., Ferlaino, F., Laburthe-Tolra, B., Lev, B. L., & Pfau, T. (2022). Dipolar physics: a review of experiments with magnetic quantum gases. *Reports on Progress in Physics*, 86(2), 026401.

[55] Chou, C.-W., Kurz, C., Hume, D. B., Plessow, P. N., Leibrandt, D. R., & Leibfried, D. (2017). Preparation and coherent manipulation of pure quantum states of a single molecular ion. *Nature*, 545(7653), 203–207.

[56] Cohen, S. R. & Thompson, J. D. (2021). Quantum computing with circular Rydberg atoms. *PRX Quantum*, 2(3), 030322.

[57] Collopy, A. L., Ding, S., Wu, Y., Finneran, I. A., Anderegg, L., Augenbraun, B. L., Doyle, J. M., & Ye, J. (2018). 3D magneto-optical trap of yttrium monoxide. *Phys. Rev. Lett.*, 121(21), 213201.

[58] Comparat, D. & Pillet, P. (2010). Dipole blockade in a cold Rydberg atomic sample. *JOSA B*, 27(6), A208–A232.

[59] Constantinides, N., Fahimniya, A., Devulapalli, D., Bluvstein, D., Gullans, M. J., Porto, J., Childs, A. M., & Gorshkov, A. V. (2024). Optimal routing protocols for reconfigurable atom arrays. *arXiv preprint arXiv:2411.05061*.

[60] Cui, J.-M., Huang, Y.-F., Wang, Z., Cao, D.-Y., Wang, J., Lv, W.-M., Luo, L., Del Campo, A., Han, Y.-J., Li, C.-F., et al. (2016). Experimental trapped-ion quantum simulation of the Kibble-Zurek dynamics in momentum space. *Scientific Reports*, 6(1), 33381.

[61] Dalibard, J. & Cohen-Tannoudji, C. (1989). Laser cooling below the doppler limit by polarization gradients: simple theoretical models. *JOSA B*, 6(11), 2023–2045.

[62] Danzl, J. G., Haller, E., Gustavsson, M., Mark, M. J., Hart, R., Bouloufa, N., Dulieu, O., Ritsch, H., & Nägerl, H.-C. (2008). Quantum gas of deeply bound ground state molecules. *Science*, 321(5892), 1062–1066.

[63] Davis, K. B., Mewes, M.-O., Andrews, M. R., van Druten, N. J., Durfee, D. S., Kurn, D., & Ketterle, W. (1995). Bose-Einstein condensation in a gas of sodium atoms. *Phys. Rev. Lett.*, 75(22), 3969.

[64] De Léséleuc, S., Lienhard, V., Scholl, P., Barredo, D., Weber, S., Lang, N., Büchler, H. P., Lahaye, T., & Browaeys, A. (2019). Observation of a symmetry-protected topological phase of interacting Bosons with Rydberg atoms. *Science*, 365(6455), 775–780.

[65] DeMarco, B. & Jin, D. S. (1999). Onset of Fermi degeneracy in a trapped atomic gas. *Science*, 285(5434), 1703–1706.

[66] DeMille, D. (2002). Quantum computation with trapped polar molecules. *Phys. Rev. Lett.*, 88(6), 067901.

[67] Denecker, T., Chew, Y. T., Guillemant, O., Watanabe, G., Tomita, T., Ohmori, K., & de Léséleuc, S. (2024). Measurement and feed-forward correction of the fast phase noise of lasers. *arXiv preprint arXiv:2411.10021*.

[68] Di Rosa, M. (2004). Laser-cooling molecules: Concept, candidates, and supporting hyperfine-resolved measurements of rotational lines in the A-X(0, 0) band of CaH. *The European Physical Journal D-Atomic, Molecular, Optical and Plasma Physics*, 31, 395–402.

[69] Dieckmann, K., Spreeuw, R., Weidemüller, M., & Walraven, J. (1998). Two-dimensional magneto-optical trap as a source of slow atoms. *Phys. Rev. A*, 58(5), 3891.

[70] Diehl, S., Micheli, A., Kantian, A., Kraus, B., Büchler, H. P., & Zoller, P. (2008). Quantum states and phases in driven open quantum systems with cold atoms. *Nature Physics*, 4(11), 878–883.

[71] Dobrzyniecki, J. & Tomza, M. (2023). Quantum simulation of the central spin model with a Rydberg atom and polar molecules in optical tweezers. *Phys. Rev. A*, 108(5), 052618.

[72] Dupont, M. & Moore, J. E. (2022). Quantum criticality using a superconducting quantum processor. *Phys. Rev. B*, 106, L041109.

[73] Ebadi, S., Keesling, A., Cain, M., Wang, T. T., Levine, H., Bluvstein, D., Semeghini, G., Omran, A., Liu, J.-G., Samajdar, R., et al. (2022). Quantum optimization of maximum independent set using Rydberg atom arrays. *Science*, 376(6598), 1209–1215.

[74] Ebadi, S., Wang, T. T., Levine, H., Keesling, A., Semeghini, G., Omran, A., Bluvstein, D., Samajdar, R., Pichler, H., Ho, W. W., Choi, S., Sachdev, S., Greiner, M., Vuletić, V., & Lukin, M. D. (2021). Quantum phases of matter on a 256-atom programmable quantum simulator. *Nature*, 595(7866), 227–232.

[75] Endres, M., Bernien, H., Keesling, A., Levine, H., Anschuetz, E. R., Krajenbrink, A., Senko, C., Vuletic, V., Greiner, M., & Lukin, M. D. (2016). Atom-by-atom assembly of defect-free one-dimensional cold atom arrays. *Science*, 354(6315), 1024–1027.

[76] English, T. C. & Zorn, J. C. (1967). Molecular beam measurement of the hyperfine structure of $^{133}Cs^{19}F$. *The Journal of Chemical Physics*, 47(10), 3896–3903.

[77] Evered, S. J., Bluvstein, D., Kalinowski, M., Ebadi, S., Manovitz, T., Zhou, H., Li, S. H., Geim, A. A., Wang, T. T., Maskara, N., et al. (2023). High-fidelity parallel entangling gates on a neutral-atom quantum computer. *Nature*, 622(7982), 268–272.

[78] Fendley, P., Sengupta, K., & Sachdev, S. (2004). Competing density-wave orders in a one-dimensional hard-Boson model. *Phys. Rev. B*, 69, 075106.

[79] Fisher, M. P., Weichman, P. B., Grinstein, G., & Fisher, D. S. (1989). Boson localization and the superfluid-insulator transition. *Phys. Rev. B*, 40(1), 546.

[80] Fowler, A. G., Mariantoni, M., Martinis, J. M., & Cleland, A. N. (2012). Surface codes: Towards practical large-scale quantum computation. *Phys. Rev. A*, 86(3), 032324.

[81] Gehm, M., O'hara, K., Savard, T., & Thomas, J. (1998). Dynamics of noise-induced heating in atom traps. *Phys. Rev. A*, 58(5), 3914.

[82] Gerchberg, R. W. (1972). A practical algorithm for the determination of plane from image and diffraction pictures. *Optik*, 35(2), 237–246.

[83] Glaetzle, A. W., Dalmonte, M., Nath, R., Gross, C., Bloch, I., & Zoller, P. (2015). Designing frustrated quantum magnets with laser-dressed Rydberg atoms. *Phys. Rev. Lett.*, 114(17), 173002.

[84] Gliozzi, F., Liendo, P., Meineri, M., & Rago, A. (2015). Boundary and interface CFTs from the conformal bootstrap. *Journal of High Energy Physics*, 2015(5), 36.

[85] Goldman, N. & Dalibard, J. (2014). Periodically driven quantum systems: effective Hamiltonians and engineered gauge fields. *Phys. Rev. X*, 4(3), 031027.

[86] Goldstein, E. V., Pax, P., & Meystre, P. (1996). Dipole-dipole interaction in three-dimensional optical lattices. *Phys. Rev. A*, 53(4), 2604.

[87] Goodman, J. W. (2005). *Introduction to Fourier optics*. Roberts and Company publishers.

[88] Gottesman, D. (1997). *Stabilizer codes and quantum error correction*. California Institute of Technology.

[89] Graham, T. M., Kwon, M., Grinkemeyer, B., Marra, Z., Jiang, X., Lichtman, M. T., Sun, Y., Ebert, M., & Saffman, M. (2019). Rydberg-mediated entanglement in a two-dimensional neutral atom qubit array. *Phys. Rev. Lett.*, 123(23), 230501.

[90] Gregory, P. D., Blackmore, J. A., Bromley, S. L., Hutson, J. M., & Cornish, S. L. (2021). Robust storage qubits in ultracold polar molecules. *Nature Physics*, 17(10), 1149–1153.

[91] Greiner, M., Mandel, O., Esslinger, T., Hänsch, T. W., & Bloch, I. (2002). Quantum phase transition from a superfluid to a Mott insulator in a gas of ultracold atoms. *nature*, 415(6867), 39–44.

[92] Gross, C. & Bakr, W. S. (2021). Quantum gas microscopy for single atom and spin detection. *Nature Physics*, 17(12), 1316–1323.

[93] Gross, C. & Bloch, I. (2017). Quantum simulations with ultracold atoms in optical lattices. *Science*, 357(6355), 995–1001.

[94] Grünzweig, T., Hilliard, A., McGovern, M., & Andersen, M. (2010). Near-deterministic preparation of a single atom in an optical microtrap. *Nature Physics*, 6(12), 951–954.

[95] Guggenheim, E. A. (1945). The principle of corresponding states. *The Journal of Chemical Physics*, 13(7), 253–261.

[96] Guo, M., Zhu, B., Lu, B., Ye, X., Wang, F., Vexiau, R., Bouloufa-Maafa, N., Quéméner, G., Dulieu, O., & Wang, D. (2016). Creation of an ultracold gas of ground-state dipolar $^{23}Na^{87}Rb$ molecules. *Phys. Rev. Lett.*, 116, 205303.

[97] Guttridge, A., Ruttley, D. K., Baldock, A. C., González-Férez, R., Sadeghpour, H., Adams, C., & Cornish, S. L. (2023). Observation of Rydberg blockade due to the charge-dipole interaction between an atom and a polar molecule. *Phys. Rev. Lett.*, 131(1), 013401.

[98] Haeberlen, U. & Waugh, J. S. (1968). Coherent averaging effects in magnetic resonance. *Physical Review*, 175(2), 453.

[99] Haegeman, J., Lubich, C., Oseledets, I., Vandereycken, B., & Verstraete, F. (2016). Unifying time evolution and optimization with matrix product states. *Phys. Rev. B*, 94, 165116.

[100] Hauschild, J. & Pollmann, F. (2018). Efficient numerical simulations with Tensor Networks: Tensor Network Python (TeNPy). *SciPost Phys. Lect. Notes*, (pp.5).

[101] He, X., Wang, K., Zhuang, J., Xu, P., Gao, X., Guo, R., Sheng, C., Liu, M., Wang, J., Li, J., Shlyapnikov, G. V., & Zhan, M. (2020). Coherently forming a single molecule in an optical trap. *Science*, 370(6514), 331–335.

[102] Heller, P. & Benedek, G. (1962). Nuclear magnetic resonance in MnF_2 near the critical point. *Phys. Rev. Lett.*, 8(11), 428.

[103] Herrera, F., Cao, Y., Kais, S., & Whaley, K. B. (2014). Infrared-dressed entanglement of cold open-shell polar molecules for universal matchgate quantum computing. *New Journal of Physics*, 16(7), 075001.

[104] Holland, C. M., Lu, Y., & Cheuk, L. W. (2023). On-demand entanglement of molecules in a reconfigurable optical tweezer array. *Science*, 382(6675), 1143–1147.

[105] Honer, J., Weimer, H., Pfau, T., & Büchler, H. P. (2010). Collective many-body interaction in Rydberg dressed atoms. *Phys. Rev. Lett.*, 105(16), 160404.

[106] Hood, J. D., Yu, Y., Lin, Y.-W., Zhang, J. T., Wang, K., Liu, L. R., Gao, B., & Ni, K.-K. (2020). Multichannel interactions of two atoms in an optical tweezer. *Physical Review Research*, 2(2), 023108.

[107] Hudson, E. R. & Campbell, W. C. (2018). Dipolar quantum logic for freely rotating trapped molecular ions. *Phys. Rev. A*, 98, 040302(R).

[108] Hughes, M., Frye, M. D., Sawant, R., Bhole, G., Jones, J. A., Cornish, S. L., Tarbutt, M. R., Hutson, J. M., Jaksch, D., & Mur-Petit, J. (2020). Robust entangling gate for polar molecules using magnetic and microwave fields. *Phys. Rev. A*, 101, 062308.

[109] Hulet, R. G. & Kleppner, D. (1983). Rydberg atoms in "circular" states. *Phys. Rev. Lett.*, 51(16), 1430.

[110] Hutzler, N. R., Liu, L. R., Yu, Y., & Ni, K.-K. (2017). Eliminating light shifts for single atom trapping. *New Journal of Physics*, 19(2), 023007.

[111] Ireland, P. M., Walker, D., & Pritchard, J. (2024). Interspecies Förster resonances for Rb-Cs Rydberg *d*-states for enhanced multi-qubit gate fidelities. *Physical Review Research*, 6(1), 013293.

[112] Jaksch, D., Cirac, J. I., Zoller, P., Rolston, S. L., Côté, R., & Lukin, M. D. (2000). Fast quantum gates for neutral atoms. *Phys. Rev. Lett.*, 85(10), 2208.

[113] Jamadagni, A., Ospelkaus, S., Santos, L., & Weimer, H. (2021). Quantum Zeno-based detection and state engineering of ultracold polar molecules. *Physical Review Research*, 3(3), 033208.

[114] Jandura, S., Thompson, J. D., & Pupillo, G. (2023). Optimizing Rydberg gates for logical-qubit performance. *PRX Quantum*, 4(2), 020336.

[115] Jarisch, F. & Zeppenfeld, M. (2018). State resolved investigation of Förster resonant energy transfer in collisions between polar molecules and Rydberg atoms. *New Journal of Physics*, 20(11), 113044.

[116] Jenkins, A., Lis, J. W., Senoo, A., McGrew, W. F., & Kaufman, A. M. (2022). Ytterbium nuclear-spin qubits in an optical tweezer array. *Phys. Rev. X*, 12(2), 021027.

[117] Johansson, J. R., Nation, P. D., & Nori, F. (2012). QuTiP: An open-source Python framework for the dynamics of open quantum systems. *Computer Physics Communications*, 183(8), 1760–1772.

[118] Johnson, J. & Rolston, S. (2010). Interactions between Rydberg-dressed atoms. *Phys. Rev. A*, 82(3), 033412.

[119] Kalinowski, M., Samajdar, R., Melko, R. G., Lukin, M. D., Sachdev, S., & Choi, S. (2022). Bulk and boundary quantum phase transitions in a square Rydberg atom array. *Phys. Rev. B*, 105, 174417.

[120] Karra, M., Sharma, K., Friedrich, B., Kais, S., & Herschbach, D. (2016). Prospects for quantum computing with an array of ultracold polar paramagnetic molecules. *J. Chem. Phys.*, 144(9), 094301.

[121] Kaufman, A., Lester, B., Foss-Feig, M., Wall, M., Rey, A., & Regal, C. (2015). Entangling two transportable neutral atoms via local spin exchange. *Nature*, 527(7577), 208–211.

[122] Kaufman, A. M., Lester, B. J., Reynolds, C. M., Wall, M. L., Foss-Feig, M., Hazzard, K., Rey, A., & Regal, C. (2014). Two-particle quantum interference in tunnel-coupled optical tweezers. *Science*, 345(6194), 306–309.

[123] Kaufman, A. M. & Ni, K.-K. (2021). Quantum science with optical tweezer arrays of ultracold atoms and molecules. *Nature Physics*, 17(12), 1324–1333.

[124] Keesling, A., Omran, A., Levine, H., Bernien, H., Pichler, H., Choi, S., Samajdar, R., Schwartz, S., Silvi, P., Sachdev, S., Zoller, P., Endres, M., Greiner, M., Vuletić, V., & Lukin, M. D. (2019). Quantum Kibble-Zurek mechanism and critical dynamics on a programmable Rydberg simulator. *Nature*, 568(7751), 207–211.

[125] Kibble, T. W. B. (1976). Topology of cosmic domains and strings. *Journal of Physics A: Mathematical and General*, 9(8), 1387.

[126] Kim, D., Keesling, A., Omran, A., Levine, H., Bernien, H., Greiner, M., Lukin, M. D., & Englund, D. R. (2019). Large-scale uniform optical focus array generation with a phase spatial light modulator. *Optics Letters*, 44(12), 3178–3181.

[127] Kim, H., Lee, W., Lee, H.-g., Jo, H., Song, Y., & Ahn, J. (2016). In situ single-atom array synthesis using dynamic holographic optical tweezers. *Nature Communications*, 7(1), 1–8.

[128] Kjaergaard, M., Schwartz, M. E., Braumüller, J., Krantz, P., Wang, J. I.-J., Gustavsson, S., & Oliver, W. D. (2020). Superconducting qubits: Current state of play. *Annual Review of Condensed Matter Physics*, 11, 369–395.

[129] Kondov, S. S., Lee, C.-H., Leung, K. H., Liedl, C., Majewska, I., Moszynski, R., & Zelevinsky, T. (2019). Molecular lattice clock with long vibrational coherence. *Nature Physics*, 15(11), 1118–1122.

[130] Kos, F., Poland, D., Simmons-Duffin, D., & Vichi, A. (2016). Precision islands in the Ising and $O(N)$ models. *Journal of High Energy Physics*, 2016(8), 36.

[131] Kuznetsova, E., Rittenhouse, S. T., Sadeghpour, H. R., & Yelin, S. F. (2016). Rydberg-atom-mediated nondestructive readout of collective rotational states in polar-molecule arrays. *Phys. Rev. A*, 94(3), 032325.

[132] Lang, F., Winkler, K., Strauss, C., Grimm, R., & Denschlag, J. H. (2008). Ultracold triplet molecules in the rovibrational ground state. *Phys. Rev. Lett.*, 101(13), 133005.

[133] Langen, T., Valtolina, G., Wang, D., & Ye, J. (2024). Quantum state manipulation and cooling of ultracold molecules. *Nature Physics*, (pp. 1–11).

[134] Lasner, Z. D., Frenett, A., Sawaoka, H., Anderegg, L., Augenbraun, B., Lampson, H., Li, M., Lunstad, A., Mango, J., Nasir, A., et al. (2024). Magneto-optical trapping of a heavy polyatomic molecule for precision measurement. *arXiv preprint arXiv:2409.04948*.

[135] Lee, W., Kim, H., & Ahn, J. (2016). Three-dimensional rearrangement of single atoms using actively controlled optical microtraps. *Optics Express*, 24(9), 9816–9825.

[136] Lepers, M., Vexiau, R., Aymar, M., Bouloufa-Maafa, N., & Dulieu, O. (2013). Long-range interactions between polar alkali-metal diatoms in external electric fields. *Phys. Rev. A*, 88(3), 032709.

[137] Leung, K., Tiberi, E., Iritani, B., Majewska, I., Moszynski, R., & Zelevinsky, T. (2021). Ultracold $^{88}Sr_2$ molecules in the absolute ground state. *New Journal of Physics*, 23(11), 115002.

[138] Levine, H., Keesling, A., Semeghini, G., Omran, A., Wang, T. T., Ebadi, S., Bernien, H., Greiner, M., Vuletić, V., Pichler, H., & Lukin, M. D. (2019). Parallel implementation of high-fidelity multiqubit gates with neutral atoms. *Phys. Rev. Lett.*, 123(17), 170503.

[139] Li, B.-W., Wu, Y.-K., Mei, Q.-X., Yao, R., Lian, W.-Q., Cai, M.-L., Wang, Y., Qi, B.-X., Yao, L., He, L., et al. (2023). Probing critical behavior of long-range transverse-field Ising model through quantum Kibble-Zurek mechanism. *PRX Quantum*, 4(1), 010302.

[140] Li, C., Liu, S., Wang, H., Zhang, W., Li, Z.-X., Zhai, H., & Gu, Y. (2024). Uncovering emergent spacetime supersymmetry with Rydberg atom arrays. *Phys. Rev. Lett.*, 133(22), 223401.

[141] Li, L., Huie, W., Chen, N., DeMarco, B., & Covey, J. P. (2022). Active cancellation of servo-induced noise on stabilized lasers via feedforward. *Physical Review Applied*, 18(6), 064005.

[142] Lin, Y., Leibrandt, D. R., Leibfried, D., & Chou, C.-W. (2020). Quantum entanglement between an atom and a molecule. *Nature*, 581, 273–277.

[143] Liu, L. R. (2019). *Building Single Molecules-Reactions, Collisions, and Spectroscopy of Two Atoms*. PhD thesis, Harvard University.

[144] Liu, L. R., Hood, J. D., Yu, Y., Zhang, J. T., Wang, K., Lin, Y.-W., Rosenband, T., & Ni, K.-K. (2019). Molecular assembly of ground-state cooled single atoms. *Phys. Rev. X*, 9, 021039.

[145] Liu, Y.-X., Zhu, L., Luke, J., Babin, M. C., Tscherbul, T. V., Gronowski, M., Ladjimi, H., Tomza, M., Bohn, J. L., & Ni, K.-K. (2024). Hyperfine-to-rotational energy transfer in ultracold atom-molecule collisions. *arXiv preprint arXiv:2407.08891*.

[146] Lorenzen, C. & Niemax, K. (1983). Quantum defects of the $n^2P_{1/2,3/2}$ levels in ^{39}K I and ^{85}Rb I. *Physica Scripta*, 27(4), 300.

[147] Ludlow, A. D., Boyd, M. M., Ye, J., Peik, E., & Schmidt, P. O. (2015). Optical atomic clocks. *Reviews of Modern Physics*, 87(2), 637–701.

[148] Ma, S., Liu, G., Peng, P., Zhang, B., Jandura, S., Claes, J., Burgers, A. P., Pupillo, G., Puri, S., & Thompson, J. D. (2023). High-fidelity gates and mid-circuit erasure conversion in an atomic qubit. *Nature*, 622(7982), 279–284.

[149] Maghrebi, M. F. & Gorshkov, A. V. (2016). Nonequilibrium many-body steady states via Keldysh formalism. *Phys. Rev. B*, 93, 014307.

[150] Manetsch, H. J., Nomura, G., Bataille, E., Leung, K. H., Lv, X., & Endres, M. (2024). A tweezer array with 6100 highly coherent atomic qubits. *arXiv preprint arXiv:2403.12021*.

[151] Marc, A., Hubert, M., & Fleig, T. (2023). Candidate molecules for next-generation searches of hadronic charge-parity violation. *Phys. Rev. A*, 108(6), 062815.

[152] Marinescu, M., Sadeghpour, H., & Dalgarno, A. (1994). Dispersion coefficients for alkali-metal dimers. *Phys. Rev. A*, 49(2), 982.

[153] McCarron, D., King, S., & Cornish, S. (2008). Modulation transfer spectroscopy in atomic rubidium. *Measurement Science and Technology*, 19(10), 105601.

[154] Metcalf, H. J. & Van der Straten, P. (1999). *Laser cooling and trapping*. Springer Science & Business Media.

[155] Mitra, A., Takei, S., Kim, Y. B., & Millis, A. J. (2006). Nonequilibrium quantum criticality in open electronic systems. *Phys. Rev. Lett.*, 97, 236808.

[156] Molony, P. K., Gregory, P. D., Ji, Z., Lu, B., Köppinger, M. P., Le Sueur, C. R., Blackley, C. L., Hutson, J. M., & Cornish, S. L. (2014). Creation of ultracold ^{87}Rb^{133}Cs molecules in the rovibrational ground state. *Phys. Rev. Lett.*, 113, 255301.

[157] Moses, S. A., Covey, J. P., Miecnikowski, M. T., Yan, B., Gadway, B., Ye, J., & Jin, D. S. (2015). Creation of a low-entropy quantum gas of polar molecules in an optical lattice. *Science*, 350(6261), 659–662.

[158] Müller, M., Lesanovsky, I., Weimer, H., Büchler, H., & Zoller, P. (2009). Mesoscopic Rydberg gate based on electromagnetically induced transparency. *Phys. Rev. Lett.*, 102(17), 170502.

[159] Mur-Petit, J., Sawant, R., Blackmore, J., Gregory, P., Hutson, J., Jaksch, D., Aldegunde, J., Tarbutt, M., & Cornish, S. L. (2020). Ultracold polar molecules as qudits. *New Journal of Physics*, 22(1).

[160] Narsky, I. & Porter, F. C. (2013). *Statistical analysis techniques in particle physics: Fits, density estimation and supervised learning*. John Wiley & Sons.

[161] Nguyen, T. L., Raimond, J.-M., Sayrin, C., Cortinas, R., Cantat-Moltrecht, T., Assemat, F., Dotsenko, I., Gleyzes, S., Haroche, S., Roux, G., et al. (2018). Towards quantum simulation with circular Rydberg atoms. *Phys. Rev. X*, 8(1), 011032.

[162] Ni, K.-K., Ospelkaus, S., de Miranda, M. H. G., Pe'er, A., Neyenhuis, B., Zirbel, J. J., Kotochigova, S., Julienne, P. S., Jin, D. S., & Ye, J. (2008). A high phase-space-density gas of polar molecules. *Science*, 322(5899), 231–235.

[163] Ni, K.-K., Rosenband, T., & Grimes, D. D. (2018). Dipolar exchange quantum logic gate with polar molecules. *Chem. Sci.*, 9, 6830–6838.

[164] Nielsen, M. & Chuang, I. (2000). *Quantum Computation and Quantum Information*. Cambridge University Press.

[165] Nogrette, F., Labuhn, H., Ravets, S., Barredo, D., Béguin, L., Vernier, A., Lahaye, T., & Browaeys, A. (2014). Single-atom trapping in holographic 2d arrays of microtraps with arbitrary geometries. *Phys. Rev. X*, 4(2), 021034.

[166] Norcia, M. A., Young, A. W., Eckner, W. J., Oelker, E., Ye, J., & Kaufman, A. M. (2019). Seconds-scale coherence on an optical clock transition in a tweezer array. *Science*, 366(6461), 93–97.

[167] Nozieres, P. & Schmitt-Rink, S. (1985). Bose condensation in an attractive Fermion gas: From weak to strong coupling superconductivity. *Journal of Low Temperature Physics*, 59, 195–211.

[168] Odavić, J., Haug, T., Torre, G., Hamma, A., Franchini, F., & Giampaolo, S. M. (2023). Complexity of frustration: A new source of non-local non-stabilizerness. *SciPost Phys.*, 15, 131.

[169] Padayasi, J., Krishnan, A., Metlitski, M. A., Gruzberg, I. A., & Meineri, M. (2022). The extraordinary boundary transition in the 3D $O(N)$ model via conformal bootstrap. *SciPost Phys.*, 12, 190.

[170] Park, A. J., Picard, L. R., Patenotte, G. E., Zhang, J. T., Rosenband, T., & Ni, K.-K. (2023). Extended rotational coherence of polar molecules in an elliptically polarized trap. *Phys. Rev. Lett.*, 131(18), 183401.

[171] Park, J. W., Will, S. A., & Zwierlein, M. W. (2015). Ultracold dipolar gas of Fermionic $^{23}Na^{40}K$ molecules in their absolute ground state. *Phys. Rev. Lett.*, 114, 205302.

[172] Park, J. W., Yan, Z. Z., Loh, H., Will, S. A., & Zwierlein, M. W. (2017). Second-scale nuclear spin coherence time of ultracold $^{23}Na^{40}K$ molecules. *Science*, 357(6349), 372–375.

[173] Parsons, M. F., Mazurenko, A., Chiu, C. S., Ji, G., Greif, D., & Greiner, M. (2016). Site-resolved measurement of the spin-correlation function in the Fermi-Hubbard model. *Science*, 353(6305), 1253–1256.

[174] Paz, D. A. & Maghrebi, M. F. (2021). Driven-dissipative Ising model: An exact field-theoretical analysis. *Phys. Rev. A*, 104, 023713.

[175] Pethick, C. J. & Smith, H. (2008). *Bose-Einstein condensation in dilute gases*. Cambridge university press.

[176] Picard, L. R., Park, A. J., Patenotte, G. E., Gebretsadkan, S., Wellnitz, D., Rey, A. M., & Ni, K.-K. (2024a). Entanglement and iSWAP gate between molecular qubits. *Nature*, (pp. 1–6).

[177] Picard, L. R., Patenotte, G. E., Park, A. J., Gebretsadkan, S. F., & Ni, K.-K. (2024b). Site-selective preparation and multistate readout of molecules in optical tweezers. *PRX Quantum*, 5(2), 020344.

[178] Pichard, G., Lim, D., Bloch, É., Vaneecloo, J., Bourachot, L., Both, G.-J., Mériaux, G., Dutartre, S., Hostein, R., Paris, J., et al. (2024). Rearrangement of individual atoms in a 2000-site optical-tweezer array at cryogenic temperatures. *Physical Review Applied*, 22(2), 024073.

[179] Poyatos, J. F., Cirac, J. I., & Zoller, P. (1997). Complete characterization of a quantum process: the two-bit quantum gate. *Phys. Rev. Lett.*, 78(2), 390.

[180] Rau, A. & Inokuti, M. (1997). The quantum defect: Early history and recent developments. *American Journal of Physics*, 65(3), 221–225.

[181] Ravets, S., Labuhn, H., Barredo, D., Béguin, L., Lahaye, T., & Browaeys, A. (2014). Coherent dipole–dipole coupling between two single Rydberg atoms at an electrically-tuned Förster resonance. *Nature Physics*, 10(12), 914–917.

[182] Ravon, B., Méhaignerie, P., Machu, Y., Hernández, A. D., Favier, M., Raimond, J.-M., Brune, M., & Sayrin, C. (2023). Array of individual circular Rydberg atoms trapped in optical tweezers. *Phys. Rev. Lett.*, 131(9), 093401.

[183] Reichsöllner, L., Schindewolf, A., Takekoshi, T., Grimm, R., & Nägerl, H.-C. (2017). Quantum engineering of a low-entropy gas of heteronuclear Bosonic molecules in an optical lattice. *Phys. Rev. Lett.*, 118, 073201.

[184] Richerme, P., Senko, C., Smith, J., Lee, A., Korenblit, S., & Monroe, C. (2013). Experimental performance of a quantum simulator: Optimizing adiabatic evolution and identifying many-body ground states. *Phys. Rev. A*, 88(1), 012334.

[185] Roland, J. & Cerf, N. J. (2002). Quantum search by local adiabatic evolution. *Phys. Rev. A*, 65, 042308.

[186] Ronzitti, E., Guillon, M., de Sars, V., & Emiliani, V. (2012). LCoS nematic SLM characterization and modeling for diffraction efficiency optimization, zero and ghost orders suppression. *Optics Express*, 20(16), 17843–17855.

[187] Rosenband, T., Grimes, D. D., & Ni, K.-K. (2018). Elliptical polarization for molecular Stark shift compensation in deep optical traps. *Optics Express*, 26(16), 19821–19825.

[188] Rosenberg, J. S., Christakis, L., Guardado-Sanchez, E., Yan, Z. Z., & Bakr, W. S. (2022). Observation of the Hanbury-Brown-Twiss effect with ultracold molecules. *Nature Physics*, 18(9), 1062–1066.

[189] Ruttley, D. K., Guttridge, A., Hepworth, T. R., & Cornish, S. L. (2024). Enhanced quantum control of individual ultracold molecules using optical tweezer arrays. *PRX Quantum*, 5(2), 020333.

[190] Rvachov, T. M., Son, H., Sommer, A. T., Ebadi, S., Park, J. J., Zwierlein, M. W., Ketterle, W., & Jamison, A. O. (2017). Long-lived ultracold molecules with electric and magnetic dipole moments. *Phys. Rev. Lett.*, 119(14), 143001.

[191] Sachdev, S. (2011). *Quantum Phase Transitions*. Cambridge University Press, 2 edition.

[192] Sahay, R., Lukin, M. D., & Cotler, J. (2024). Emergent holographic forces from tensor networks and criticality.

[193] Saleh, B. E. & Teich, M. C. (2019). *Fundamentals of Photonics*. John Wiley & Sons.

[194] Savitzky, A. & Golay, M. J. (1964). Smoothing and differentiation of data by simplified least squares procedures. *Analytical chemistry*, 36(8), 1627–1639.

[195] Schiff, L. & Snyder, H. (1939). Theory of the quadratic Zeeman effect. *Physical Review*, 55(1), 59.

[196] Schlosser, N., Reymond, G., & Grangier, P. (2002). Collisional blockade in microscopic optical dipole traps. *Phys. Rev. Lett.*, 89(2), 023005.

[197] Schlosser, N., Reymond, G., Protsenko, I., & Grangier, P. (2001). Sub-Poissonian loading of single atoms in a microscopic dipole trap. *Nature*, 411(6841), 1024–1027.

[198] Scholl, P., Schuler, M., Williams, H. J., Eberharter, A. A., Barredo, D., Schymik, K.-N., Lienhard, V., Henry, L.-P., Lang, T. C., Lahaye, T., et al. (2021). Quantum simulation of 2d antiferromagnets with hundreds of Rydberg atoms. *Nature*, 595(7866), 233–238.

[199] Scholl, P., Shaw, A. L., Tsai, R. B.-S., Finkelstein, R., Choi, J., & Endres, M. (2023). Erasure conversion in a high-fidelity Rydberg quantum simulator. *Nature*, 622(7982), 273–278.

[200] Scholl, P., Williams, H. J., Bornet, G., Wallner, F., Barredo, D., Henriet, L., Signoles, A., Hainaut, C., Franz, T., Geier, S., et al. (2022). Microwave engineering of programmable XXZ Hamiltonians in arrays of Rydberg atoms. *PRX Quantum*, 3(2), 020303.

[201] Schollwöck, U. (2011). The density-matrix renormalization group in the age of matrix product states. *Annals of Physics*, 326(1), 96–192. January 2011 Special Issue.

[202] Schymik, K.-N., Pancaldi, S., Nogrette, F., Barredo, D., Paris, J., Browaeys, A., & Lahaye, T. (2021). Single atoms with 6000-second trapping lifetimes in optical-tweezer arrays at cryogenic temperatures. *Physical Review Applied*, 16(3), 034013.

[203] Seeßelberg, F., Luo, X.-Y., Li, M., Bause, R., Kotochigova, S., Bloch, I., & Gohle, C. (2018). Extending rotational coherence of interacting polar molecules in a spin-decoupled magic trap. *Phys. Rev. Lett.*, 121, 253401.

[204] Semeghini, G., Levine, H., Keesling, A., Ebadi, S., Wang, T. T., Bluvstein, D., Verresen, R., Pichler, H., Kalinowski, M., Samajdar, R., Omran, A., Sachdev, S., Vishwanath, A., Greiner, M., Vuletić, V., & Lukin, M. D. (2021). Probing topological spin liquids on a programmable quantum simulator. *Science*, 374(6572), 1242–1247.

[205] Shaw, A. L., Scholl, P., Finklestein, R., Madjarov, I. S., Grinkemeyer, B., & Endres, M. (2023). Dark-state enhanced loading of an optical tweezer array. *Phys. Rev. Lett.*, 130(19), 193402.

[206] Sheng, C., Hou, J., He, X., Wang, K., Guo, R., Zhuang, J., Mamat, B., Xu, P., Liu, M., Wang, J., et al. (2022). Defect-free arbitrary-geometry assembly of mixed-species atom arrays. *Phys. Rev. Lett.*, 128(8), 083202.

[207] Šibalic, N. & Adams, C. S. (2018). *Rydberg Physics*. 2399-2891. IOP Publishing.

[208] Šibalić, N., Pritchard, J. D., Adams, C. S., & Weatherill, K. J. (2017). ARC: An open-source library for calculating properties of alkali Rydberg atoms. *Computer Physics Communications*, 220, 319–331.

[209] Singh, K., Anand, S., Pocklington, A., Kemp, J. T., & Bernien, H. (2022). Dual-element, two-dimensional atom array with continuous-mode operation. *Phys. Rev. X*, 12(1), 011040.

[210] Singh, K., Bradley, C. E., Anand, S., Ramesh, V., White, R., & Bernien, H. (2023). Mid-circuit correction of correlated phase errors using an array of spectator qubits. *Science*, 380(6651), 1265–1269.

[211] Slagle, K., Aasen, D., Pichler, H., Mong, R. S. K., Fendley, P., Chen, X., Endres, M., & Alicea, J. (2021). Microscopic characterization of Ising conformal field theory in Rydberg chains. *Phys. Rev. B*, 104, 235109.

[212] Sondhi, S. L., Girvin, S., Carini, J., & Shahar, D. (1997). Continuous quantum phase transitions. *Reviews of Modern Physics*, 69(1), 315.

[213] Spence, S., Brooks, R., Ruttley, D., Guttridge, A., & Cornish, S. L. (2022). Preparation of ^{87}Rb and ^{133}Cs in the motional ground state of a single optical tweezer. *New Journal of Physics*, 24(10), 103022.

[214] Stanley, H. E. (1999). Scaling, universality, and renormalization: Three pillars of modern critical phenomena. *Reviews of Modern Physics*, 71(2), S358.

[215] Steinert, L.-M., Osterholz, P., Eberhard, R., Festa, L., Lorenz, N., Chen, Z., Trautmann, A., & Gross, C. (2023). Spatially tunable spin interactions in neutral atom arrays. *Phys. Rev. Lett.*, 130(24), 243001.

[216] Su, L., Douglas, A., Szurek, M., Groth, R., Ozturk, S. F., Krahn, A., Hébert, A. H., Phelps, G. A., Ebadi, S., Dickerson, S., et al. (2023). Dipolar quantum solids emerging in a Hubbard quantum simulator. *Nature*, 622(7984), 724–729.

[217] Su, W.-P., Schrieffer, J. R., & Heeger, A. J. (1979). Solitons in polyacetylene. *Phys. Rev. Lett.*, 42(25), 1698.

[218] Sundar, B., Gadway, B., & Hazzard, K. R. (2018). Synthetic dimensions in ultracold polar molecules. *Scientific Reports*, 8(1), 1–7.

[219] Takekoshi, T., Reichsöllner, L., Schindewolf, A., Hutson, J. M., Le Sueur, C. R., Dulieu, O., Ferlaino, F., Grimm, R., & Nägerl, H.-C. (2014). Ultracold dense samples of dipolar RbCs molecules in the rovibrational and hyperfine ground state. *Phys. Rev. Lett.*, 113, 205301.

[220] Tan, D. B., Bluvstein, D., Lukin, M. D., & Cong, J. (2024). Compiling quantum circuits for dynamically field-programmable neutral atoms array processors. *Quantum*, 8, 1281.

[221] Tarbutt, M. (2019). Laser cooling of molecules. *Contemporary Physics*.

[222] Terhal, B. M. (2015). Quantum error correction for quantum memories. *Reviews of Modern Physics*, 87(2), 307.

[223] Thompson, D. R. & Rice, O. (1964). Shape of the coexistence curve in the perfluoromethylcyclohexane-carbon tetrachloride system. II. Measurements accurate to 0.0001. *Journal of the American Chemical Society*, 86(17), 3547–3553.

[224] Thompson, J. D., Tiecke, T., Zibrov, A. S., Vuletić, V., & Lukin, M. D. (2013). Coherence and Raman sideband cooling of a single atom in an optical tweezer. *Phys. Rev. Lett.*, 110(13), 133001.

[225] Tobias, W. G., Matsuda, K., Li, J.-R., Miller, C., Carroll, A. N., Bilitewski, T., Rey, A. M., & Ye, J. (2022). Reactions between layer-resolved molecules mediated by dipolar spin exchange. *Science*, 375(6586), 1299–1303.

[226] Vandersypen, L. M. & Chuang, I. L. (2004). NMR techniques for quantum control and computation. *Reviews of Modern Physics*, 76(4), 1037–1069.

[227] Verresen, R., Tantivasadakarn, N., & Vishwanath, A. (2021). Efficiently preparing Schrödinger's cat, fractons and non-abelian topological order in quantum devices. *arXiv preprint arXiv:2112.03061*.

[228] Vilas, N. B., Robichaud, P., Hallas, C., Li, G. K., Anderegg, L., & Doyle, J. M. (2024). An optical tweezer array of ultracold polyatomic molecules. *Nature*, 628(8007), 282–286.

[229] Voges, K. K., Gersema, P., Meyer zum Alten Borgloh, M., Schulze, T. A., Hartmann, T., Zenesini, A., & Ospelkaus, S. (2020). Ultracold gas of bosonic $^{23}Na^{39}K$ ground-state molecules. *Phys. Rev. Lett.*, 125, 083401.

[230] Vojta, M. (2003). Quantum phase transitions. *Reports on Progress in Physics*, 66(12), 2069.

[231] Wall, M. L., Hazzard, K. R. A., & Rey, A. M. (2015). *From atomic to mesoscale: The Role of Quantum Coherence in Systems of Various Complexities*, chapter Quantum magnetism with ultracold molecules. World Scientific.

[232] Weber, S., Tresp, C., Menke, H., Urvoy, A., Firstenberg, O., Büchler, H. P., & Hofferberth, S. (2017). Calculation of Rydberg interaction potentials. *Journal of Physics B: Atomic, Molecular and Optical Physics*, 50(13), 133001.

[233] Weimer, H., Müller, M., Lesanovsky, I., Zoller, P., & Büchler, H. P. (2010). A Rydberg quantum simulator. *Nature Physics*, 6(5), 382–388.

[234] Weisskopf, V. F. & Wigner, E. P. (1930). Calculation of the natural brightness of spectral lines on the basis of Dirac's theory. *Z. Phys.*, 63, 54–73.

[235] Windpassinger, P. & Sengstock, K. (2013). Engineering novel optical lattices. *Reports on Progress in Physics*, 76(8), 086401.

[236] Wolf, F., Wan, Y., Heip, J. C., Gebert, F., Shi, C., & Schmidt, P. O. (2016). Non-destructive state detection for quantum logic spectroscopy of molecular ions. *Nature*, 530(7591), 457–460.

[237] Wu, H., Richaud, R., Raimond, J.-M., Brune, M., & Gleyzes, S. (2023). Millisecond-lived circular Rydberg atoms in a room-temperature experiment. *Phys. Rev. Lett.*, 130(2), 023202.

[238] Wu, Z. & Xia, G. (2003). Transmission of a Gaussian beam after incidenting nonnormally on a Fabry-Perot etalon: a nonresonant case. *Optics and Laser Technology*, 35(2), 123–126.

[239] Yan, B., Moses, S. A., Gadway, B., Covey, J. P., Hazzard, K. R. A., Rey, A. M., Jin, D. S., & Ye, J. (2013). Observation of dipolar spin-exchange interactions with lattice-confined polar molecules. *Nature*, 501(7468), 521–525.

[240] Yao, N. Y., Jiang, L., Gorshkov, A. V., Gong, Z.-X., Zhai, A., Duan, L.-M., & Lukin, M. D. (2011). Robust quantum state transfer in random unpolarized spin chains. *Phys. Rev. Lett.*, 106(4), 040505.

[241] Yelin, S. F., Kirby, K., & Côté, R. (2006). Schemes for robust quantum computation with polar molecules. *Phys. Rev. A*, 74(5), 050301(R).

[242] Yeomans, J. M. (1992). *Statistical Mechanics of Phase Transitions*. Clarendon Press.

[243] Yu, Y. (2021). *Coherent Creation of Single Molecules from Single Atoms*. PhD thesis, Harvard University.

[244] Yu, Y., Wang, K., Hood, J. D., Picard, L. R., Zhang, J. T., Cairncross, W. B., Hutson, J. M., Gonzalez-Ferez, R., Rosenband, T., & Ni, K.-K. (2021). Coherent optical creation of a single molecule. *Phys. Rev. X*, 11(3), 031061.

[245] Zeiher, J., Choi, J.-y., Rubio-Abadal, A., Pohl, T., Van Bijnen, R., Bloch, I., & Gross, C. (2017). Coherent many-body spin dynamics in a long-range interacting Ising chain. *Phys. Rev. X*, 7(4), 041063.

[246] Zeppenfeld, M. (2017). Nondestructive detection of polar molecules via Rydberg atoms. *EPL (Europhysics Letters)*, 118(1), 13002.

[247] Zhang, J. T., Yu, Y., Cairncross, W. B., Wang, K., Picard, L. R. B., Hood, J. D., Lin, Y.-W., Hutson, J. M., & Ni, K.-K. (2020). Forming a single molecule by magnetoassociation in an optical tweezer. *Phys. Rev. Lett.*, 124, 253401.

[248] Zhao, L., Lee, M. D. K., Aliyu, M. M., & Loh, H. (2023). Floquet-tailored Rydberg interactions. *Nature Communications*, 14(1), 7128.

[249] Zhelyazkova, V. & Hogan, S. (2017). Electrically tuned Förster resonances in collisions of NH_3 with Rydberg He atoms. *Phys. Rev. A*, 95(4), 042710.

[250] Zhu, M., Wei, Y.-C., & Hung, C.-L. (2020). Resonator-assisted single-molecule quantum state detection. *Phys. Rev. A*, 102(2), 023716.

[251] Zou, J. & Hogan, S. (2022). Probing van der Waals interactions and detecting polar molecules by Förster-resonance energy transfer with Rydberg atoms at temperatures below 100 mk. *Phys. Rev. A*, 106(4), 043111.

[252] Zurek, W. H. (1985). Cosmological experiments in superfluid helium? *Nature*, 317(6037), 505–508.

[253] Zwierlein, M., Stan, C., Schunck, C., Raupach, S., Kerman, A., & Ketterle, W. (2004). Condensation of pairs of Fermionic atoms near a Feshbach resonance. *Phys. Rev. Lett.*, 92(12), 120403.

[254] Zwierlein, M. W., Abo-Shaeer, J. R., Schirotzek, A., Schunck, C. H., & Ketterle, W. (2005). Vortices and superfluidity in a strongly interacting Fermi gas. *Nature*, 435(7045), 1047–1051.

This thesis was typeset using LaTeX, originally developed by Leslie Lamport and based on Donald Knuth's TeX. The body text is set in 11 point Egenolff-Berner Garamond, a revival of Claude Garamont's humanist typeface. The above illustration, "Science Experiment 02", was created by Ben Schlitter and released under CC BY-NC-ND 3.0. A template that can be used to format a PhD thesis with this look and feel has been released under the permissive MIT (X11) license, and can be found online at github.com/suchow/Dissertate or from its author, Jordan Suchow, at suchow@post.harvard.edu.